Modifying and Controlling Diffusion Properties of Molecular Dopants in Organic Semiconductors

Zur Erlangung des akademischen Grades Doktor-Ingenieur (Dr.-Ing.)
genehmigte Dissertation von Patrick N. Reiser aus Heidelberg
Tag der Einreichung: 23.07.2019, Tag der Prüfung: 13.11.2019
Darmstadt — D 17

1. Gutachten: Prof. Dr. Wolfram Jaegermann
2. Gutachten: Prof. Dr. Annemarie Pucci

TECHNISCHE UNIVERSITÄT DARMSTADT

Fachbereich 11 Material- und Geowissenschaften
Fachgebiet Oberflächenforschung

Modifying and Controlling Diffusion Properties of Molecular Dopants in Organic Semiconductors

Genehmigte Dissertation von Patrick N. Reiser aus Heidelberg

1. Gutachten: Prof. Dr. Wolfram Jaegermann
2. Gutachten: Prof. Dr. Annemarie Pucci

Tag der Einreichung: 23.07.2019
Tag der Prüfung: 13.11.2019

Darmstadt — D 17

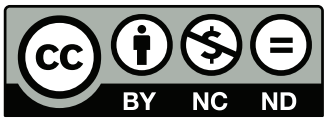

Contents

1 Introduction

The materials science field of organic electronics is comparably young, although the first report on organic conductive materials dates back to the 19th century, and constitutes the oxidation of polyaniline described by Henry Letheby in 1862.[1,2] The research on organic materials with regard to their semiconducting properties and potential for optoelectronics, as it is known today, rather started in the 1960s for example with the high conductivity of a tetraiodopyrrole derivative or the electroluminescent properties of anthrazene.[3–5] Most importantly, Heeger, MacDiarmid und Shirakawa demonstrated in 1977 that polyacetylene can be doped or oxidized with halogens, causing a controlled change in conductivity reaching from insulating to a quasi-metallic state.[6] Since doping is the key-technology for electronics built from semiconductors like silicon, this discovery is considered to be the foundation of organic electronics and was rewarded with the Nobel Prize in 2000. The most successful application are organic light emitting diodes (OLED) which are presently employed in display manufacturing and reached a considerable market share in consumer electronics of phones, computer or television screens. Among the first OLED devices built by Ching Tang in 1987,[7] doping of organic layers was not required, but charge recombination and light emission occurred at the hetero-contact between separate electron and hole transport layers. The same can be said about organic photovoltaics (OPV) with regard to charge separation at a donor/acceptor interface.[8] The fact that doping was not used is partially due to stability issues and to the high mobility of dopants, since in early studies doping was realized with volatile halogens or diffusive alkali-metals.[9,10] Today, small molecular OLEDs consist of multiple functional layers including a transparent electrode, luminescent and phosphorescent dyes embedded in an organic matrix as well as blocking, transport or injection layers.[11] In modern devices doping is employed to improve contact properties and to reduce ohmic losses of organic charge transport layers.[12] For this purpose, small molecular dopants have been developed, which act as an oxidizing or reducing agent and show increased morphological stability.[13] However, there are still material systems reported, especially polymers, in which a considerable diffusion of molecular dopants is observed.[14,15] Since molecular dopants are known to cause exciton quenching,[16] a suppression of diffusion is of interest for the future design of strong dopants for organic semiconductors. A more detailed review on literature about doping and dopant diffusion can be found in Section 3.1 and 6.1. Possible strategies to prevent inter-diffusion of dopants are discussed in Section 7.1 with regard to successful attempts in literature.

The goal of this work is to first investigate diffusion in a known dopant-host system and to identify properties that can impact or control the diffusion. In a second step, strategies of immobilization are considered with the prospect to synthesize a dopant that can be universally employed with any organic host matrix and activated after blending, in order to engage an immobilizing reaction with its host. Accordingly, this thesis is structured into three parts: in the first part basic and principles on the subject are summarized from literature, the second part deals with characterization of a host-dopant system with which diffusion is investigated in a sequential doping scheme, and the third part covers immobilization of a novel synthesized n-dopant bearing an anchor group.

More specifically, Chapter 2 tries to briefly explain the electronic structure of organic semiconductors present in the solid phase, and how energetic states are affected if an additional charge or polaron is present. As in inorganic semiconductors, the charge carrier density can be controlled by doping, causing a change in electrical conductivity and shift of the Fermi level position. In Chapter 3 two prominent models for doping followed by a detailed statistical description are summarized from literature. Using semi-empirical corrections of the text-book formalism in Chapter 3, the position of the Fermi level can be estimated for silicon used as substrate in Section 9.3. Experimental techniques utilized in this work and special methods of data analysis are presented in Chapter 4 and 5. A survey of literature about diffusion of dopants in organic semiconductors is given in Chapter 6 introducing the system of poly(3-hexylthiophene) (P3HT) doped with the soluble molybdenum complex Mo(tfd-CO_2Me)$_3$, which is used in the second part of this thesis. In Chapter 9 electrical and spectral characteristics of doped P3HT are investigated for the purpose of identifying charge transfer and diffusion in a sequential doping process, in which the dopant is deposited on a pristine P3HT film and subsequently diffuses into the polymer. The diffusion of sequentially doped P3HT is then thoroughly studied in Chapter 10 and fitted by a numeric model that describes the absorption, charging and diffusion of dopant molecules. Also desorption is discussed for comparison but which is unable to sufficiently explain the data. A short summary on the drift of ionic molecular dopants in an externally applied field can be found in Chapter 11. Strategies to suppress diffusion are introduced in Chapter 7 comparing different approaches pursued in literature. The immobilization scheme in this work is based on organic azides, which can be activated by UV-light, inducing photolysis and potentially generating reactive singlet nitrenes that can undergo an insertion reaction with neighbouring molecules (see Section 7.2). A phenyl azide has been succefully introduced to the n-dopant DMBI in the group of of Prof. Bunz at the Institute for Organic Chemistry in Heidelberg and is shown in Section 8.2. Its reaction and doping properties are tested with PCBM as matrix in Chapter 13. An increase in thermal stability and a reduction of volatility at room temperature is demonstrated by photoelectron spectroscopy after reaction of the azide group. A counter-doping effect of the n-dopant in unintentionally p-doped polymer P3HT is observed in Chapter 14. Details about the azide reaction and processing properties were initially studied in Chapter 12 by means of a simplified model system. Finally, a summary and discussion of the main results of this thesis is presented in Chapter 15. A list of publications related to this work can be found in Section A.

Part I
Basics and Principles

2 Organic Semiconductors

2.1 Structure and Classification

In general, organic materials are electrically insulating, i.e. the energy difference between highest occupied molecular orbital (HOMO) and lowest unoccupied molecular orbital (LUMO) is larger than 3 eV. Semiconducting properties can be observed for the class of organic materials, which feature an extensive π-conjugated system.[17] The carbon atom in its ground state has six electrons in the electron configuration $1s^2\ 2s^2\ 2p^2$ or [He] $2s^2\ 2p^2$. Depending on the covalent bond, electrons from the 2s orbital are promoted and can form sp, sp^2 or sp^3 hybridization. For organic electronics the sp^2 hybrid orbitals are crucial for their electronic properties. In this hybridization, a total of three $2sp^2$ hybrid orbitals are formed with one remaining $2p_z$ orbital. By overlapping of $2sp^2$ hybrid orbitals, σ-bonds are created between two carbon atoms or in a C-H bond with the 1s orbital of hydrogen. The σ-bonds are strong covalent bonds with a high electron localization and large splitting between bonding σ and anti-bonding σ^* orbitals. In double bonds the remaining $2p_z$ orbital overlap laterally and form usually weaker π-bonds, which are more diffuse and exhibit a lower splitting between binding π and anti-bonding π^*-orbitals. A so-called conjugated π-system is formed from alternating single and double bonds, which are interchangeable in the case of e.g. benzene, leading to a large delocalized π system. As a consequence, the HOMO and LUMO level are built up from π and π^* orbitals reducing the gap to around 1.5 to 3 eV, which in principle leads to semiconducting properties and light absorption in the visible range.[17] Organic semiconductors classification distinguishes between conjugated molecules with a molar mass around 100 g mol^{-1} and polymers in the order of 10000 g mol^{-1}. They differ in morphology but also in processing methods. Small molecules can be thermally deposited under vacuum conditions, which is not possible for polymers as they likely decompose before evaporation. Thin films of conjugated polymer are obtained either by spin-coating, as it is mainly done in this work, or by printing from solution.

2.2 Electronic Properties

Organic molecules form weakly-interacting molecular solids, in which intermolecular attraction is mainly given by van-der-Waals or dipole-dipole interactions. Small molecules can form a highly ordered single crystal, which is often monoclinic or triclinic and displays anisotropy of physical properties like carrier mobility or refractive index.[18] However, due to weak interactions and exchange energies, the splitting of energy levels in the solid is very small and consequently the band width amounts to only 10 - 300 meV compared to inorganic solids with a band width of 2 - 8 eV. The small band width in combination with thermal motion yields a high effective mass of charge carriers and causes Bloch waves to be scattered. In literature, the charge transport in molecular crystals is often referred to as "band-like" transport and sometimes to hopping of strongly localized charge carriers.[19]
In practice, most organic films processed for devices are amorphous or semi-crystalline, which

usually yields localized states limited to a single molecule. For partially crystalline films, delocalization can extend within the crystalline regions but breaks at distortions and defects. The disorder in amorphous films causes a variation in polarization of the molecular environment leading to a broadening of the distribution of states as depicted in Figure 2.1. They are usually assumed to follow a Gaussian distribution.[20]
The charge carrier transport in amorphous organic solids is described by the thermally stimulated tunnelling based on the Miller-Abraham model of hopping in disordered materials.[21,22] Here, the transport takes place via tunnelling between an initial and final state under the absorption or emission of a phonon. Usually the probability of phonon emission is set to one and the absorption probability is approximated by Boltzmann statistics. The mobilities in amorphous organic semiconductors are typically 10^{-6} to 10^{-3} cm^2 V^{-1} s^{-1} which is considerably lower than for example silicon with 1340 cm^2 V^{-1} s^{-1}, see e.g. in Section 3.2.[23]

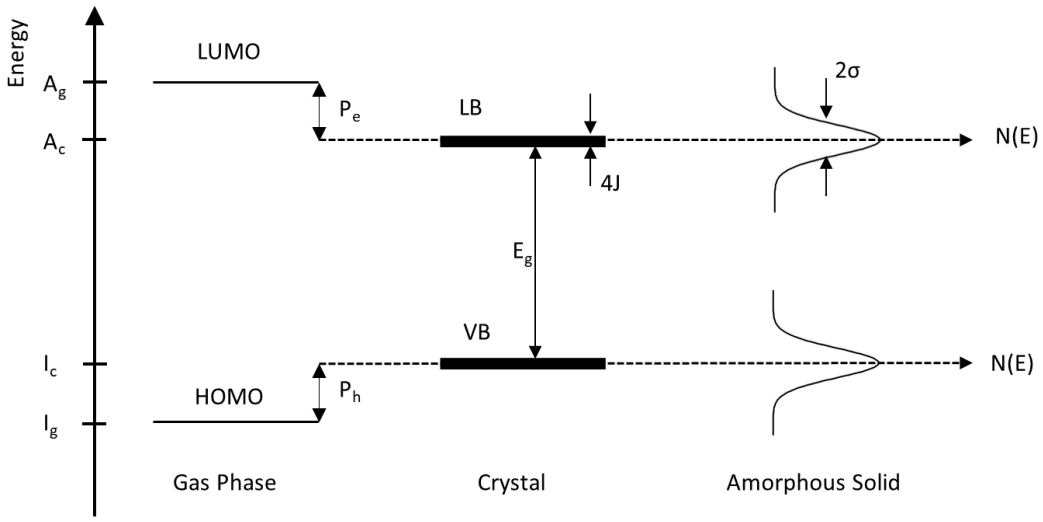

Figure 2.1: Energy level diagram of (polaronic) molecular states from the gas phase, crystal to amorphous solid. The polarization energies of cation and anion are denoted by P_h and P_e. The width of the disorder state distribution is given by 2σ and the band width in the crystal by the exchange energy J. (Based on Bässler[20])

2.3 Band Gap in Organic Semiconductors

Whereas the band gap in inorganic semiconductors is a characteristic quantity that describes the energy difference between top of the valence band and bottom of the conduction band, a corresponding definition for organic semiconductors is more complex. In analogy, the distance between HOMO and LUMO level can be regarded as band gap, however, the position of energy levels in soft organic materials depends on polarization, relaxation and electronic excitation. Therefore reported values for the band gap in OSC may differ with respect to their intended application and measurement technique. In general, one can distinguish four types of band gaps following Figure 2.2, which are named adiabatic, photoemission, transport and optical band gap.[24]
The *adiabatic band gap* is the largest energy gap and is calculated in thermodynamic equilibrium for the ionization potential and electron affinity of an isolated non-ionized molecule but which

is difficult to asses experimentally.
The *photoemission band gap* refers to the band gap estimated from HOMO and LUMO levels measured by ultraviolet photoelectron spectroscopy (UPS) and inverse photoelectron spectroscopy (IPES). The resulting energy gap is smaller than the adiabatic band gap due to final state relaxation effects of the generated charge in electron emission or capture process. Details about photoelectron spectroscopy can be found in Section 4.1. With regard to relevant timescales, possible relaxation processes include electronic (ca. 10^{-16} s), molecular (ca. 10^{-14} s) and lattice relaxations (ca. 10^{-13} - 10^{-14}s). The electronic relaxation holds the biggest contribution of the order of 1 eV compared to molecular (ca. 200 meV) and lattice relaxation (ca. 10 meV).[24,25] Given the time-scale of the photoemission process of ca. 10^{-14} s, electronic relaxation is accounted for in the measured energy gap, but molecular relaxation contributions are difficult to assess as they are approximately on the same time-scale.

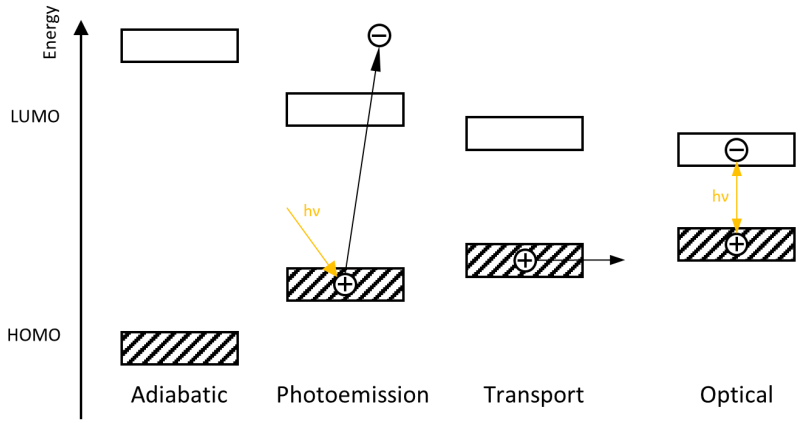

Figure 2.2: Schematic drawing of different band gaps definitions.

The *transport gap* represents the energy gap of those levels, at which electrons or holes are transported. Since charge transport can be considered to be a comparably slow process, all of the above mentioned relaxation phenomena are included in the transport gap. The fully relaxed charged state is referred to as polaron and defines the transport gap. Since lattice relaxation effects are normally small, the photoemission band gap can be regarded as a good representative for the transport gap up to an error of ca. 200 meV.[26] However, the transport level is not necessarily located at the maximum or onset of the state distribution. In a theoretical description of Schmechel et al. the transport level is defined as the centre of the differential conductivity, which is calculated from the combination of density of states (DOS), occupation statistics and differential mobilities.[21] As a consequence, the transport level is generally located somewhere below the maximum and above the onset of the density of states. In summary, the transport gap relevant for device operation may be about 0.2 to 0.5 eV smaller than predicted by UPS/IPES.[24,27,28]
Finally, the *optical band gap* is measured by light absorption spectroscopy, and represents the binding energy of a Frenkel or charge-transfer exciton, which is located on a single or on neighbouring molecules, respectively. In case of inorganic semiconductor the delocalized Mott-Wannier excition has a low binding energy (ca. 0.01 eV) due to a higher dielectric constant and lower effective mass. In contrast, Frenkel excitons in organic matter feature a low dielectric constant and have a binding energy in the order of 0.1 to 1 eV.[24] The observed optical band gap

is typically lower than the measured photoemission band gap, and has been empirically studied by Sworakowski showing a larger deviation for larger band gaps.[29]

2.4 Optical Properties of Polarons

Originally, the term polaron defines a quasiparticle of an electron or charged particle moving through a dielectric crystal causing a distortion or change in bond length of the lattice due to polarization, screening the charge with a "phonon-cloud". In organic semiconductors (OSC) the definition applies to molecular crystals, whereas for amorphous OSC it is adapted to intermolecular and, with a larger contribution, intra-molecular reorganization.[27] Adding a charge to a molecule leads to relaxation and reorganisation of molecular orbitals with a corresponding shift in the respective energy levels. Additionally, the charge causes a polarization of its surrounding further stabilizing the charged state. The energy levels of polarons according to the Su-Schrieffer-Heeger (SSH) model are depicted for a positively charged molecule in Figure 2.3 together with the energy position of the neutral molecule or polymer.[30] In this model and its extensions, polaronic states are predicted in the band gap with optical absorption lines P1 and P2 as sketched in Figure 2.3.[31] For certain polymers a polaron delocalization can not only occur along the backbone but also across π-π stacked chains, which is referred to as 2D polarons with transitions DP1 and DP2.[32,33] In fact, the SSH model was developed for an ideal conjugated polymer with the assumption that electronic interactions such as the coulomb interaction of π-electrons are negligible. The model is further used for amorphous solids of small molecules, but the range of its applicability is still under discussion.[34] Winkler et al. and Heimel include intersite Coulomb interaction and propose an energy scheme depicted in Figure 2.3, which suggests a slightly different origin of the charge-induced optical transitions.[35,36]

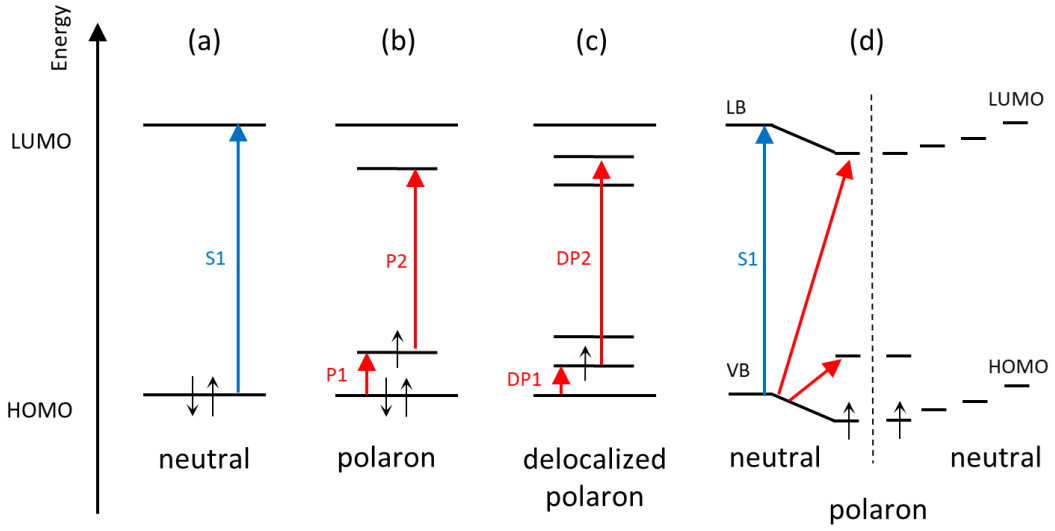

Figure 2.3: Scheme of energy levels with optical transition S1 of a neutral molecule in (a). Traditional scheme for positively charged polymer in (b) with two polaronic states in the band gap that are probed by transitions P1 and P2. The situation of (b) in the case of a two-dimensional delocalized polaron in (c). Recently proposed states of small molecules and polymers in (d) which feature similar transitions P1 and P2. The graphic is based on Kahmann et al.[31]

3 Doping of Organic Semiconductors

3.1 Doping Mechanism

In the context of this work, the expression *doping* always refers to electrical or electrochemical doping, which describes the introduction of impurities to modify electrical properties of semiconductors. This is indeed possible for organic semiconductors (OSC), which enhances the conductivity of the bulk material by several orders of magnitude. This is mainly due to an increase in the charge carrier concentration n which relates to the conductivity σ according to:[37]

$$\sigma = en\mu \ . \tag{3.1}$$

The mobility μ in OSC also depends on the charge carrier concentration and the doping level. For example, broadening of the density of states (DOS), dopant-induced coulomb traps and filling of intrinsic trap states is known to influence the observed carrier mobility.[38] Since the discovery of polyacetylene doped by iodine, which dates back to the year 1977, a large variety of dopants is investigated today. Compared to halogens and alkali metals used in early studies,[10] molecular dopants offer better morphological stability, which is discussed with regard to diffusion in Section 6.1. For p-dopants organic molecules, transition-metal-oxides and organometallic complexes have been reported in literature, summarized in Section 3.4. Due to their inherent air-instability, the synthesis of molecular n-dopants was not successful for many years and is discussed in more detail in Section 8.1. When introducing a molecular dopant to the OSC, a charge transfer occurs between host and dopant. One distinguishes the integer charge transfer (ICT) model and the generation of charge transfer complexes (CTC), which are detailed below. In comparison to inorganic semiconductors, dopant-ions and the charged OSC are usually closely bound, causing strong localization of charge carriers and consequently low doping efficiencies. For OSC doping concentrations of 10^{-3} to 10^{-1} mol% are typically applied, opposed to 10^{-6} to 10^{-3} mol% for inorganic semiconductors.[39] The binding energy of e.g. a hole at an ionized acceptor site can be estimated using the analogy of a hydrogen atom for inorganic semiconductors, which gives approximately 30 meV in case of silicon.[37] The coulomb energy of the organic equivalent is significantly higher, being several 100 meV as inferred from a distance of ca. 1 nm and a low dielectric constant of $\epsilon_r = 3-4$.[40]

3.1.1 Integer Charge Transfer Model (ICT)

The generation of charge carriers can be achieved by either chemical oxidation or reduction of the organic host molecule. In case of p-doping, the acceptor impurity must have an electron affinity (EA) which is higher than the ionization potential (IE) of the organic semiconductor (OSC).[41] For n-doping the roles are reversed and the dopant acts as a donor with an extremely low ionization potential. Under these conditions an integer charge is transferred between OSC

and dopant, resulting in a polaron on the OSC and an ionized donor or acceptor molecule. For molecular dopants this picture directly translates to the respective positions of highest occupied molecular orbital (HOMO) and the lowest unoccupied molecular orbital (LUMO) in Figure 3.1a. Consequently, for p-doping the HOMO level of the host must be positioned higher, i.e. at lower binding energies, than the LUMO-level of the acceptor to allow for an electron transfer to the dopant, see Figure 3.1. As mentioned before, due to the low dielectric constant of OSC in the order of 3-4 Coulomb interactions are strong and can give electron-hole binding energies of several 100 meV.[34] Therefore, the energetic landscape after electron transfer is important to describe the transport of free charge carriers. Because of its charge, the cation experiences relaxation of frontier orbitals with energy λ. Compared to the neutral molecule, the cation features a higher second IE and a lower EA, which splits into occupied and un-occupied HOMO derived sub-levels by the so-called Hubbard energy U.[35] This is depicted in Figure 3.1b. However, the situation is more complex, if molecular anion and cation are lying close together as for the ion pair formed after ICT. It is presumed that disorder is an important factor for the final dissociation of the charge transfer complex resulting in free holes.[42] There are many dopant-matrix systems for which an ICT is experimentally verified by optical and infrared spectroscopy.[43–45] For ideal crystalline polymers a singly occupied positive polaron state within the neutral OSC gap is suspected but which is still under discussion.[30,46,47] For example, Salzmann et al. stated that such an intragap polaron level has not yet been identified unambiguously using photoelectron spectroscopy and concluded on a more "molecular" nature of commonly doped conjugated polymers.[34] For more information please refer to Section 2.4.

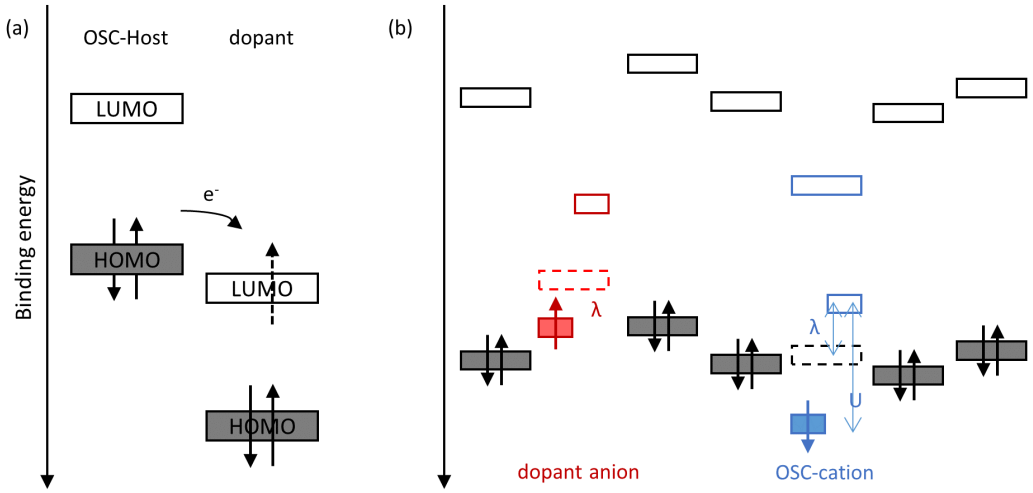

Figure 3.1: Schematic drawing of ICT for p-doping in (a) and energy levels of neutral OSC and charged dopant anion in (b). The situation for n-type doping is analogous. The reorganisation and Hubbard energy is denoted by λ and U, respectively. The diagram is based on Salzmann et al.[34]

3.1.2 Charge Transfer Complex (CTC)

A second doping mechanism is the hybrid charge transfer complex (CTC) model, proposed by Salzmann et al.[34] Here dopant and host are in close vicinity and form supra-molecular hybrid orbitals due to an overlap of electron wave functions. In case of p-doping, the frontier orbitals of

the host HOMO and the dopant LUMO develop new hybrid states in the band gap that consist of occupied bonding and unoccupied anti-bonding orbitals. The relative contribution of the parent states defines the de-occupation of the organic semiconductors (OSC) HOMO and the amount of charge transfer δ which then takes non-integer values. Using a Hückel-type model, the CTC's is given according to Salzmann et al.:[34]

$$E_{\mathrm{CPX,H/L}} = \frac{H_{\mathrm{OSC}} + L_{\mathrm{dop}}}{2} \pm \sqrt{(H_{\mathrm{OSC}} - L_{\mathrm{dop}})^2 + 4\beta^2} \tag{3.2}$$

Here, the OSCs HOMO is denoted by H_{OSC} and the dopant LUMO level by L_{dop}. The resonance integral β is an important parameter that influences the energy gap between bonding and anti-bonding orbitals upon interaction and consequently the doping efficiency. A bonding effect and thus partial charge transfer can occur even if H_{OSC} and L_{dop} are not in resonance or even if L_{dop} is higher, in which case an ICT is energetically forbidden. The unoccupied hybrid state L_{CPX} is accessible for electrons from the neutral OSC via thermal activation, but depending on the energy difference compared to $k_B T$, its occupation is not favoured. This situation is depicted in Figure 3.2. The are several studies on CTC formation using density functional theory and spectroscopy techniques to identify hybrid states and a non-integer charge on the dopant.[48,49] In conclusion, the neutral CTC state can act as a dopant, but is usually not as effective as ICT doping.

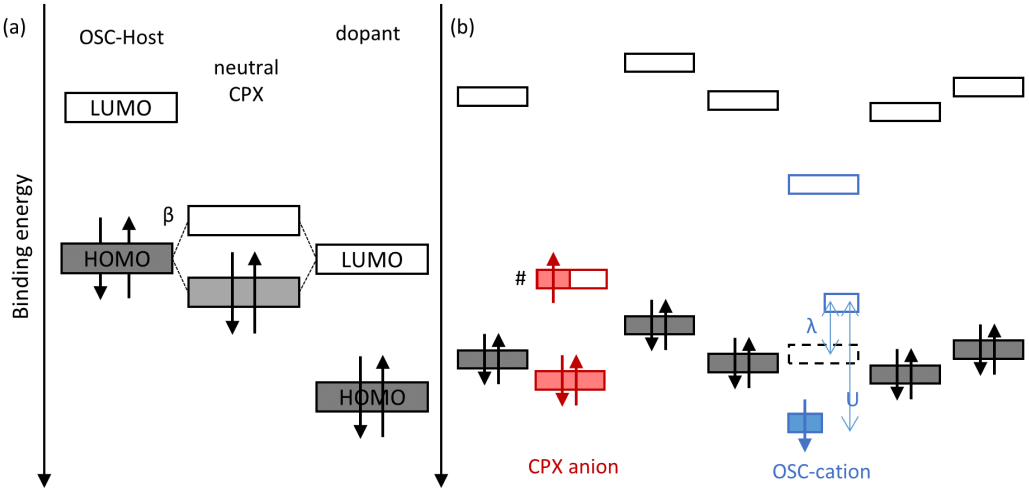

Figure 3.2: Schematic drawing of CTC for p-doping in (a) and energy levels of neutral OSC and partially charged CTC state in (b). The situation for n-type doping is analogous. The reorganisation and Hubbard energy is denoted by λ and U, respectively. The diagram is based on Salzmann et al.[34]

3.2 Theoretical Description: Inorganic Semiconductors

The theoretical description of doping in Organic Semiconductors can be approached from the established classical semiconductor theory. In the following, important characteristics and formula for intrinsic and extrinsic inorganic semiconductors are summarized. These can be directly applied to silicon, which is certainly the most important semiconducting material in present-day industry. Another goal of this derivation is to comprehensively establish the necessary semi-empirical equations connecting the Fermi level position in silicon with its conductivity. For Section 9.3 the doping concentration and Fermi level position of silicon as a substrate is of interest for band alignment experiments with doped organic materials. Therefore, it is sought to calculate Fermi level position from a measured electrical conductivity or data provided from the wafer manufacturer. Electronic properties are generally determined by band structure and occupation of electron states. An energy gap above the valence band of a few eV with no electron state in between (for clean and defect free materials) is the defining feature of semiconductors, in which the gap is generally much larger than $k_B T$. In the intrinsic case, a conduction of electrons is only possible if they are thermally excited into the conduction band across the band gap. Conducting electron n and hole concentration p can be calculated from the density of states at the band edges D_C, D_V and its occupation given by Fermi-Dirac statistics $f(E,T;E_F)$:[37]

$$n = \int_{E_C}^{\infty} D_C(E)\, f(E,T;E_F)\, dE \quad \text{and} \quad p = \int_{-\infty}^{E_V} D_V(E)\, [1 - f(E,T;E_F)]\, dE\,. \tag{3.3}$$

The limits of integration reflect the band gap E_g between valence band maximum E_V and conduction band gap minimum $E_C = E_V + E_g$. For intrinsic semiconductors at low temperatures, the Fermi level E_F is located nearly in the middle of the band-gap and there are only few free charge carriers $n_i = p_i$ rendered by the tail of the Fermi-Dirac distribution. For further calculations, it is common to approximate the band extrema by a parabola and use the definition of the effective mass for electrons m_n and holes m_p, respectively. This resembles the simple case of a free electron gas in a box. The density of states in three dimension then yields:[37]

$$D_C(E) = \frac{(2m_n^*)^{3/2}}{2\pi^2\hbar^3}\sqrt{E - E_C} \qquad \text{for } E > E_C \tag{3.4}$$

$$D_V(E) = \frac{(2m_p^*)^{3/2}}{2\pi^2\hbar^3}\sqrt{E_V - E} \qquad \text{for } E < E_V \tag{3.5}$$

Values for the effective electron and hole mass can be found in literature and are determined by the corresponding band curvature of the band dispersion. For silicon one typically finds values like $m_n = 1.09\, m_e$ and $m_p = 0.81\, m_e$ with the free electron mass m_e. In order to solve the integral in Eq. 3.3 analytically using the density of states in Eq. 3.5, the Fermi-Dirac distribution has to be approximated by Boltzmann distribution in Eq. 3.7. This is a reasonable approach if the Fermi level lies within the band gap (ca. $3k_B T$ from the band edges) and only the tail of Fermi distribution is considered.[37]

$$f(E,T;E_F) = \frac{1}{e^{(E-E_F)/k_B T}+1} \approx e^{-(E-E_F)/k_B T} \quad \text{for } E > E_F \tag{3.6}$$

$$1 - f(E,T;E_F) = \frac{1}{e^{(E_F-E)/k_B T}+1} \approx e^{-(E_F-E)/k_B T} \quad \text{for } E < E_F \tag{3.7}$$

With Eq. 3.7 and Eq. 3.5 a closed expression for electron and hole density can be derived, which is written in terms of the effective density of states $\mathcal{N}_n$ and $\mathcal{N}_p$.[37] However, since Eq. 3.3 is to be solved for strongly doped semiconductors, Eq. 3.3 is carried out numerically and not reverted to Boltzmann approximation in Eq. 3.7. Demanding charge neutrality $n_i = p_i$ then determines the position of the Fermi level, which lies directly in the middle of the band gap for $T = 0$ or for identical effective mass of electrons and holes. For doped semiconductors similar considerations define the position of the Fermi level. In case of low doping concentrations, impurities and defects introduce electron states within the band gap that can either donate or receive an electron from bands of the host crystal. One distinguishes between density of donors n_D, with energy level E_D close to E_C and density of acceptors n_A, with energy level E_A close to E_V. Effective dopants will induce shallow states close to the band edges, e.g. in silicon typically Boron and Phosphorus are used with an ionization energy of around 45 meV. The density of donors n_D can be divided in neutral n_D^0 and charged donors n_D^+, which are in total $n_D = n_D^0 + n_D^+$. The same holds for acceptors $n_A = n_A^0 + n_A^-$ with neutral n_A^0 and negatively charged acceptors n_A^-. Their energetic distance with respect to the Fermi level determines if defects are ionized or remain neutral. The probability of occupying the dopant ground state, not being ionized, can also be calculated by Fermi-Dirac statistics:

$$\frac{n_D^+}{n_D} = \left[1 + g_D\, e^{(E_F - E_D)/k_B T}\right]^{-1} \quad \text{and} \quad \frac{n_A^-}{n_A} = \left[1 + g_A\, e^{(E_A - E_F)/k_B T}\right]^{-1} \tag{3.8}$$

The statistics are weighted with degeneracy factors associated with the ratio of initial and accessible free states. For silicon and donors like Phosphor it is $g_D = 2$, which directly reflects the spin degeneracy of occupation. For acceptors in silicon also the double splitting of the valence band has to be considered, e.g. for Boron $g_A = 4$. If one now includes donors and acceptors, charge neutrality demands:

$$n + n_A^- = p + n_D^+ \tag{3.9}$$

In equilibrium charge neutrality has to be fulfilled, which allows to calculate the Fermi level position using Eq. 3.8, 3.5 and 3.3 if the doping concentration is known. This has to be carried out numerically, since there is no simple analytical solution for Eq. 3.9. Finally for the conductivity both electrons and holes are considered as charge carriers and contribute with their respective mobilities μ_e, μ_p. In a simple picture, scattering time and effective mass are characterizing the mobility $\mu = e\tau/m^*$. Typically the average scattering time is similar for holes and electrons but the effective mass may differ. The total conductivity σ then reads:

$$\sigma = en\mu_n + ep\mu_p \tag{3.10}$$

Corrections for Silicon

The above description holds for very low doping concentrations. For higher doping, donor and acceptor levels can further extend and form bands within the host semiconductor, which is referred to as degenerate semiconductors. In order to obtain reasonable predictions for higher doping concentration, further corrections and improvements have to be taken into account. In

order to avoid a full band calculation for each doping level, compact correction terms or semi-empirical formula are sought to improve quantities given in Eq. 3.8, 3.5 and 3.3. It is known that the band gap in silicon decreases upon increasing the temperature or doping level due to changes in the band structure. The dependence on temperature is governed by electron-phonon coupling in general and can be approximated using several models. Beside the Bose-Einstein model,[50] and a phonon related model proposed by Pässler et al.,[51] the Varshni equation is a very commonly used fitting with parameter A, B to describe the band gap $E_g(T)$:[52]

$$E_g(T) = E_g(0) - \frac{AT^2}{T+B} \tag{3.11}$$

The parameters *A*,*B* are documented for silicon. Its dependence on doping is known as band gap narrowing and has been of importance for vertical integrated bipolar transistor structures and contact doping for solar cells. In literature, one distinguishes the real band gap ΔE_G and the apparent band gap reduction ΔE_g^{app}.[53,54] The band gap narrowing leads to an increase in the *np* product beyond the normal equilibrium value of n_i^2. This has been electrically measured and related to the *np* product following Boltzmann statistics according to $np = n_{eff}^2 = n_i^2 \exp(\Delta E_g^{app}/k_B T)$.[55,56] The apparent band gap therefore holds both degeneracy and density of states effects (including nonparabolicity contributions).[54] Since Fermi-Dirac statistics is used, a fit of calculated ΔE_G from Schenk et al.[57] seems reasonable in this case:[53,54]

$$\Delta E_g(N_D) = A\left[ln\left(\frac{N_D}{N_{\text{eff}}}\right)\right]^b + C\ , \tag{3.12}$$

where *A*,*b*,*C* are fitting constants and N_{eff} denotes the relevant doping concentration N_D at which band gap narrowing effects start to occur. The constant C is often not needed and only improves the result for low doping concentrations. Typical values for N_{eff} are about 10^{17} cm^{-3} and $b = 1$ for the apparent band gap narrowing. Here, $N_{\text{eff}} = 10^{14}$ cm^{-3}, $b = 3$ and a somewhat lower *A* for the real band gap narrowing is used in connection with Fermi-Dirac statistics.[54] For this calculation the centre of the band gap is set to zero yielding a conduction and valence band position of $E_C = E_g/2$ and $E_V = -E_g/2$, respectively. Without further considerations, the energy levels of donors and acceptors are affected by ΔE_G. Since donors and acceptors can form conducting bands in degenerate semiconductors, it is reasonable to assume that also the ionization energy will be reduced. In a simple picture, the decrease in activation energy can be explained by a reduced average potential energy of an electron or hole at higher doping concentrations. In the semiconductor ionic impurities are shielded on average by charge carriers, which leads to a lowering of potential energy.[58] An overlapping or distribution effect will be inversely proportional to the distance which is governed by $N_D^{1/3}$. A theoretically motivated expression for e.g. E_A is written in terms of acceptor density N_A and isolated ionization energy E_I as:[58]

$$E_A = E_I - aN_A^{1/3} \tag{3.13}$$

The values E_A are determined from Hall data of doped silicon at lower temperatures and lead, to a fit of a of the order of $4 \cdot 10^{-8}$ eV cm.[58] The consequence is a vanishing ionization energy at very high doping levels. This is only a very rough estimate[59] but can be used to improve the applicability of Eq. 3.8 towards high doping concentration. Finally, in order to connect

calculations of charge carrier concentrations with conductivity, the effect of impurities on the charge carrier mobility has to be taken into account. There is a study of Arora et al.[60] using combined theoretical and experimental data on the mobility of electrons and holes to derive a fit which holds for doping concentration up to 10^{20} cm^{-3} and a temperature between 250 K - 500 K within 13% of errors. They used a fitting expression of the mobility:[60]

$$\mu = \mu_{\min} + \frac{\mu_0}{1 + (N_D/N_{reff})^{\alpha}} \tag{3.14}$$

where $\mu_{\min}$ is the minimum mobility and N_{reff} denotes a reference concentration marking the onset of the impact of doping concentration N_D controlled via the exponential α. Experimental data on the lattice scattering mobility yield a temperature dependence for electrons and holes given by $\mu_L = 8.56 \cdot 10^8\, T^{-2.33}$ and $\mu_L = 1.58 \cdot 10^8\, T^{-2.33}$, respectively.[61–63] The ionized impurity scattering was estimated by a modified Brooks-Herring formulation,[64] taking anisotropic scattering effects into account, and combined with the lattice mobility by a mixed scattering formula.[59] At high doping concentrations the mobilities were found to depend on the dopant type as well. Their numeric fits then read with $T_n = T/300$:[60]

$$\mu_e = 88\, T_n^{-0.57} + \frac{7.4 \cdot 10^8\, T^{-2.33}}{1 + [N_D/(1.26 \cdot 10^{17} T_N^{2.4})]\, 0.88\, T_N^{-0.146}} \tag{3.15}$$

$$\mu_h = 54.3\, T_n^{-0.57} + \frac{1.36 \cdot 10^8\, T^{-2.33}}{1 + [N_D/(2.35 \cdot 10^{17} T_N^{2.4})]\, 0.88\, T_N^{-0.146}} \tag{3.16}$$

Putting the above corrections of Eq. 3.16, Eq. 3.13 and Eq. 3.12 into the equations derived previously with the parameters for silicon, it is possible to calculate the Fermi level position for given resistivity and doping type (being either Boron or Phosphorous). In Figure 3.3 they have been plotted using above equations for various cases. In order to account for different crystal growth methods and impurities an opposite donor or acceptor concentration is assumed for compensation. In the case of Czochralski process (CZ) $N_{d,a} = 10^{14}$ cm^{-3} is chosen and a concentration of $N_{d,a} = 10^{11}$ cm^{-3} for floating zone purification (FZ). In Figure 3.3e, f the temperature behaviour of charge carrier concentration and Fermi level position is depicted. For doped silicon at moderate temperatures, e.g. room temperature, there is a plateau where charge carrier concentration equals $n = n_D$ since $k_B T \approx E_d$. If the temperature increases, the Fermi level approaches the middle of the band gap since electrons can be thermally excited from the valence into the conduction band, which is referred to as intrinsic conduction. This results in a rise in charge carrier concentration in Figure 3.3f at low $1/T$. For this simplified description, a very high doping concentration requires the temperature to be further increased to render intrinsic conduction dominant leading to a shift of the Fermi level towards centre of the band gap expected for electron and hole symmetry provided comparable effective mass. For very low temperatures the charge carrier concentration decreases with inverse temperature due to disabled ionization of donors since $k_B T < E_D$. The Fermi level is then determined by the donor state E_D, which remains partially ionized from compensation of acceptors. The mobilities in Figure 3.3h, i show a decrease with both temperature and doping concentration as expected from Eq. 3.16 originating from scattering with phonons generated at high temperatures and impurities caused by doping. In Figure 3.16k a high resistivity can only be reached for low doping concentrations which are usually achieved using floating zone (FZ) process since standard Czochralski grown

silicon has a higher impurity density of dopants. Nowadays it is possible to produce Czochralski grown silicon with higher purity too. For the study in this work several silicon wafers of 100 $\pm 0.5^{\circ}$ orientation have been ordered from Sil'tronix silicon technologies. With nominal resistivity data the Fermi level position is calculated as explained above and compared to XPS data in Section 9.3. All wafer surfaces are covered with a native oxygen layer of ca. 2 nm, which is not taken into account in this description, especially with regard to surface states recorded in literature[65–67]. In addition, conductivity was measured experimentally yielding similar values.

Label	Resistivity [Ω cm]	Doping concentration calculated [cm^{-3}]	Band Gap calculated [eV]	Fermi level - VB calculated[ev]
n++	0.003	$3 \cdot 10^{19}$	1.02	1.04
n+	0.013	$1 \cdot 10^{18}$	1.07	1.02
n	0.9	$5 \cdot 10^{15}$	1.12	0.90
n	4	$1 \cdot 10^{15}$	1.12	0.86
i	3000	$2 \cdot 10^{12}$	1.13	0.69
i	10000	$5 \cdot 10^{11}$	1.13	0.66
p	2	$7 \cdot 10^{15}$	1.12	0.20
p+	0.0015	$3 \cdot 10^{20}$	0.89	-0.07

Table 3.1: Calculated charge carrier concentration and Fermi level position at room temperature from conductivity data of silicon wafers of 100 $\pm 0.5^{\circ}$ orientation doped with either Boron or Phosphorous. The resistivity is provided from the retailer, but was additionally measured in Section 9.3. The label is chosen arbitrarily to mark the individual wafer batch. The highest doped wafers n++ and p+ can be considered degenerate.

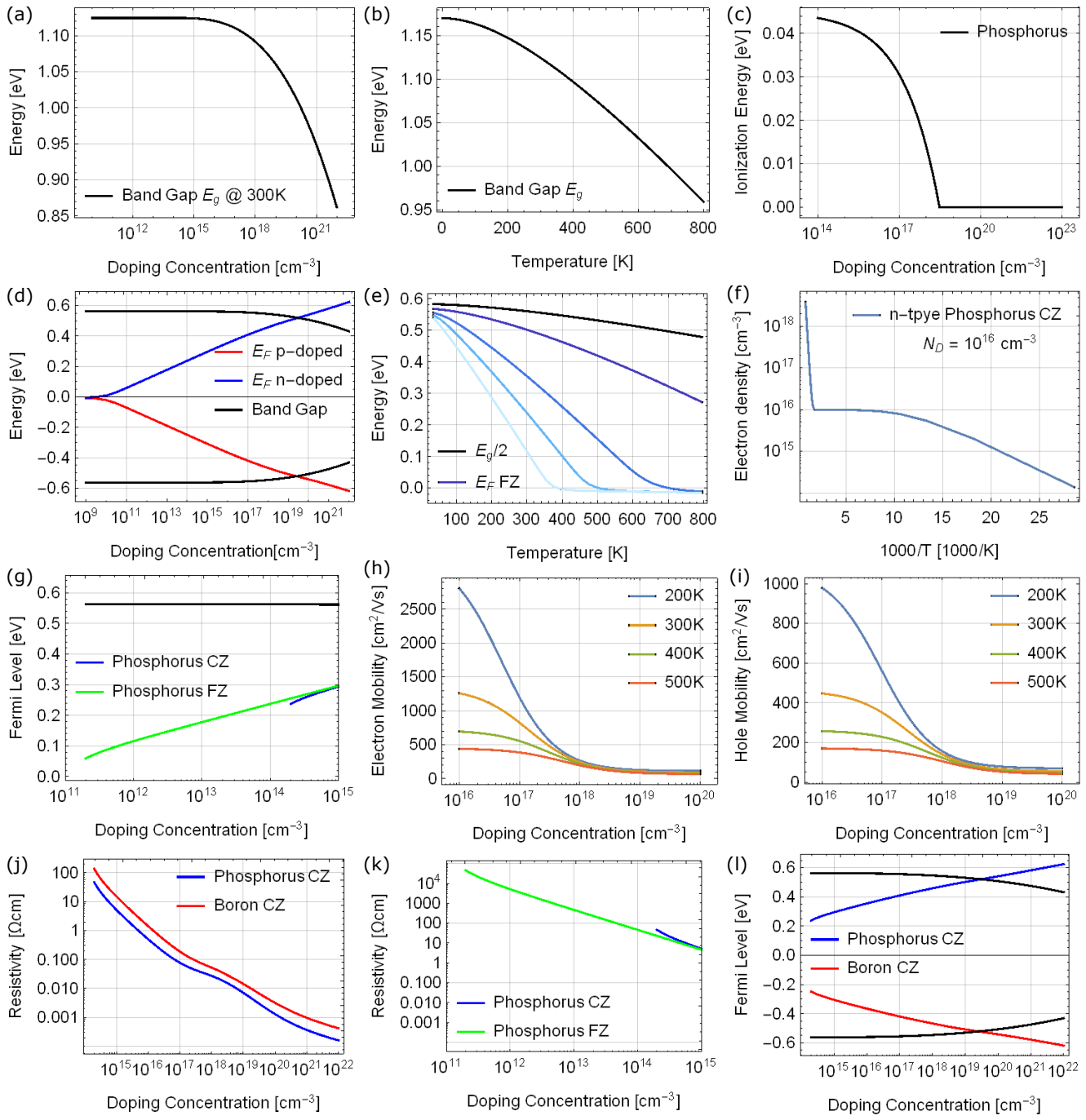

Figure 3.3: All Figures are plotted with parameters of silicon, where Boron and Phosphorus denote p- and n-type doping. Figure (a) and (b) show the doping and temperature dependence of the band gap reduction according to Eq. 3.12 and Eq. 3.11. Decrease of ionization energy in (c). In (d) and (e) changes in the Fermi level position E_F versus doping concentration and temperature. The electron density is given in (f) as a function of inverse temperature. Electron and hole mobility for different temperatures versus doping concentration in (h) and (i). The Fermi level for Phosphorus and Boron doped silicon in (g) and (l). Their resistivity versus doping concentration in (j) and (k). The label CZ and FZ stands for silicon crystals grown by Czochralski and Floating Zone method, for which a low opposite impurity concentration of donors and acceptors of $N_{d,a} = 10^{14}$ cm^{-3} (CZ) and $N_{d,a} = 10^{11}$ cm^{-3} (FZ) is assumed. To achieve high resistivity in (k) a FZ method becomes necessary.

3.3 Theoretical Description: Organic Semiconductors

A theoretical description of molecular doping in organic semiconductors as presented in literature is typically approached by common statistical models of inorganic semiconductor theory, detailed in the previous section.[13,68] Such a model is adapted to organic semiconductors by applying modifications to the density of states and introducing deep traps in the band gap. Even though doping in Organic semiconductors is not yet fully understood, an effective statistical description based on classical semiconductors physics was found to nicely match experimental data of the Fermi level position as shown by Tietze et al.[13] in a wide doping range. Also conductivity and thermoelectric power could be analysed by Schmechel et al.[21] using the Miller-Abraham model of hopping transport to describe data from Maenning et al.[69] on p-doped Zinc-phthalocyanine (ZnPc). Recently, doping induced changes in the density of states for charge transfer complexes were further studied by Salzmann et al.[34,70] in a statistical picture being also able to quantitatively reproduce experimental data. There may be few points that are not fully understood or accounted for and which need to be resolved in future studies, however, the model of Tietze et al. does effectively describe experimental data surprisingly well and therefore it will be summarized in the following.[13,68] Unlike inorganic semiconductors forming large bands of several eV in size, organic semiconductors can only have sharp bands of ca. 100 meV due to weak intermolecular coupling or rather localized states which follow a Gaussian distribution, generated by disorder and polarization effects.[71,72] It is to mention, that a local spatial correlation is not taken into account in a Gaussian disorder model, but is necessary to explain the electrical field dependence.[73] The Gaussian is then superimposed with an exponential tail of defect states reaching into the gap.[13,74,75]

$$g_{\mathrm{DOS}}(E) = \begin{cases} \frac{N_0}{\sqrt{2\pi}\sigma}\, e^{-\frac{(E-E_0)^2}{2\sigma^2}}, & \text{if } E < E_\beta. \\ \frac{N_\beta}{\beta}\, e^{-\frac{E-E_\beta}{\beta}}, & \text{if } E > E_\beta. \end{cases} \tag{3.17}$$

Centre of the Gaussian representing a HOMO level in Eq. 3.17 is marked by E_0 with a typical width of $\sigma \approx 0.2$ eV. The transition between Gaussian and exponential tail is controlled by E_β. Usually a definition of a transport energy as maximum of conductivity is commonly used since the relevant energies for transport are located in the outer end of the Gaussian or the exponential tail of $g_{\mathrm{DOS}}(E)$. The maximum conductivity derives from a product of mobility and charge carrier concentrations, i.e. the density of states convoluted with Fermi-Dirac function. In literature, a trap density is usually introduced by Gaussian shaped distribution:[68]

$$g_{\mathrm{T}}(E) = \frac{N_{\mathrm{T}}}{\sqrt{2\pi}\sigma_{\mathrm{T}}}\, e^{-\frac{(E-E_{\mathrm{T}})^2}{2\sigma_{\mathrm{T}}^2}} \tag{3.18}$$

The trap density is not directly measured and may have an arbitrary shape. The parameters are fitted by Tietze et al. and situated in the centre of the band gap.[13,74,76] In case of p-doping, neglecting free electrons, charge neutrality equation demands with hole density p, trap density N_{T} and dopant or acceptor density N_A:[68]

$$p + N_{\mathrm{T}}^{+} \approx N_A^{-} \ . \tag{3.19}$$

The occupation of states in the HOMO and traps are governed by Fermi-Dirac statistics $f(E;E_F)$ with a suitable degeneracy, according to:[70]

$$p = \int_{-\infty}^{\infty} g_{\mathrm{DOS}}(E)[1-f(E,E_F)]\ dE \tag{3.20}$$

$$N_{\mathrm{T}}^{+} = \int_{-\infty}^{\infty} g_{\mathrm{T}}(E)[1-f(E,E_F)]\ dE\ . \tag{3.21}$$

The acceptor is not introduced in terms of a density but as a single level E_A by Tietze et al.[13] The acceptor state is defined in a statistical context but is not directly connected to an accessible level like the LUMO state of the dopant. Identical to Eq. 3.8 the ionization of the single acceptor level is derived by:

$$\frac{N_A^-}{N_A} = \left[1 + e^{(E_A - E_F)/k_B T}\right]^{-1} \tag{3.22}$$

This is different to the model of Salzmann et al.[34] in which a density of states is assumed for the dopant instead of a single effective level in order to take new states from charge transfer crystals into account.[49] Salzmann et al. then derive the fraction of charged dopants or occupied acceptor states similar to Eq. 3.21. For strong p-type doping the Fermi level will be pinned or saturated about 0.35 eV above the HOMO level, which requires the acceptor states in this description to be located above the HOMO as well.[68] This is also the case for very strong dopants, which possess a high electron affinity locating their LUMO below the host's HOMO. Given low doping concentrations the activation energy of dopants can be estimated from a temperature dependent impedance spectroscopy measurement at a Schottky contact linking the width of the depletion region to the amount of space charges N_A: with the hole transport material and the dopant an ITO/MeO-TPD:C60F36/Al Schottky diode was build by Tietze et al.[13] Its capacity-voltage dependence suggested $\Delta E_A = 32$ meV in the temperature range 178 - 313 K at 0.5 wt% doping.[13] To resolve this discrepancy Tietze et al. concluded that a virtual acceptor state represents rather the generation of free charge carriers for the statistical analysis. It is assumed that strong dopants have a high charge transfer efficiency of close to 100% at moderate doping. However, they form bound charge transfer complexes $[M^+A^-]$ of matrix M and acceptor A,[38] where charges are closely bound due to Coulomb interaction and a low dielectric background. For contributing to free charge carriers they have to overcome Coulomb attraction and dissociate to $A^-[M^+M]$ decreasing the overall doping efficiency p/N_A.[13] More precisely, an equilibrium of hole release and recapture at negatively charged acceptors sites has to be considered. Assuming the hole release does not strongly depend on the doping concentration, the capture of free holes is expected to increase with N_A as the density of acceptor sites increases.[68] The Fermi level being below the dopant states reflects this situation as acceptor states are occupied and correspondingly holes are captured. At high doping concentration Olthof et al.[47] measured a Fermi level pinned closer to the HOMO for a more crystalline material having a higher permittivity, which agrees with the interpretation of hole release from Tietze et al.[13] On the basis of this arguing the situation should be similar for n-type doping, however, other measurements[68,74] indicate that the Fermi level may not necessarily be pinned as for p-doping and can even cross the LUMO

level of the matrix. It is to be mentioned that for this statement to be valid, the LUMO position has to be indirectly inferred from IPES or transport measurements, which may hold systematic errors. Nonetheless, this is a curious finding and may require further investigations on the fundamental doping mechanism.
Tietze et al.[68] measured the dependence curve of the Fermi level position versus doping concentration by UPS, which shows three different slopes on a log-scale. In their model, these regimes are explained by trap-filling, dopant saturation and reserve. At very low concentration, deep traps get occupied and the Fermi level position E_F is affected by the trap density $g_{\mathrm{T}}(E)$. After all traps are filled the Fermi level E_F is rapidly moving towards E_A.[68] In the dopant saturation regime, all dopants are ionized and the charge carrier density directly increases with the dopant concentrations. This is the region with highest slope of Fermi level shift versus doping ratio, determined by E_A and $g_{\mathrm{DOS}}(E)$ in the charge neutrality relation of Eq. 3.19.[68] If E_F exceeds E_A, there will be more uncharged dopants reducing the doping efficiency and ultimately causing the Fermi level to be pinned above the HOMO-Level. This is then labelled as dopant reserve regime[68] in resemblance with inorganic semiconductor theory, in which usually the temperature regions of E_F are described.[37] These classifications can be found in the corresponding electrical measurements of doping efficiency and conductivity.[68,75] It is to be mentioned, that all models do not take morphology effects into account. Especially, for high doping concentrations dopants are likely to form clusters and transfer charges across a dopant matrix interface. This is an alternative mechanism for the reduced doping efficiency at high concentrations, too. Additionally, changes in the density of states due to polaron formation of the mobile excess charge of ca. 0.1 eV is either neglected or incorporated by simply shifting HOMO/LUMO states effectively reducing the gap.[70]

3.4 Overview of Materials

Even though it is not a straight-forward criterion for efficient p-doping, as a rule of thumb, the LUMO of the dopant has to be located below the HOMO of the organic semiconductor. There is a discussion in literature on how to determine the proper HOMO and LUMO levels in the blend in order to best predict ICT. The direct measurement with photoelectron spectroscopy (PES) and inverse photoemission spectroscopy (IPS) yield the HOMO/LUMO values of a pure dopant or matrix film. Additionally HOMO/LUMO levels of isolated molecules can be derived by density functional theory (DFT) calculation or in solution by cyclic voltammetry (CV).[29] Often there is a certain discrepancy between HOMO/LUMO values, which depends on the measurement technique and film properties. A list of energy levels reported in literature of common materials is given in Table 3.2.

	HOMO [eV]	LUMO [eV]	Band Gap [eV]
rr-P3HT	4.65[77]	2.13[77]	
rra-P3HT	5.25[78]		2.25[78]
CBP	6.23[79], 6.3[80]	2.23[79]	3.1[80,81]
NPB, α-NPD	5.47[79], 5.5[80], 5.6[82], 5.7[83]	0.85[84], 1.52[79]	3.1[80–83]
CuPC	5.0[80], 5.2[85], 4.95[82]		1.7[80,82]
Alq_3	6.1[80], 5.95[83], 5.8[85]		2.7[80,81,83]
Pentacene	5.2[84]	3[84]	
ZnPC	5.07[86]		1.6[86], 2.42[87]
F4ZnPC	5.46[86]		2.42[87]
Spiro-OMeTAD	5[88], 5.22[89]	2.24[89]	2.98[89]
MoO_3	9.68[79]	6.7[79]	
$Mo(tfd)_3$	7.84[90]	5.59[90]	
$Mo(tfd\text{-}CO_2Me)_3$	7.2[91]	5[91]	
F4TCNQ	8.34[14]	5.24[14], 5.24[92]	
F6TCNNQ		5.0[13], 5.37[92]	

Table 3.2: HOMO and LUMO values reported in literature for several p-dopant and matrix molecules: Poly(3-hexylthiophen-2,5-diyl) (P3HT), 4-4'-N,N'-dicarbazolyl-biphenyl (CBP), N,N'-diphenyl-N,N'- bis(1-naphthyl)- 1,1'biphenyl-4,4" diamine (α-NPD), copper phthalocyanine (CuPc), tris(8-hydroxy-quinoline)aluminum (Alq_3), zinc phthalocyanine (ZnPc), fluorinated zinc phthalocyanine (F4ZnPc), N^2,N^2,$N^{2\prime}$,$N^{2\prime}$, N^7,N^7,$N^{7\prime}$,$N^{7\prime}$ -octakis(4-methoxyphenyl)-9,9' -spirobi[9H-fluorene]-2,2',7,7'-tetramine (Spiro-OMeTAD), molybdenum trioxide (MoO_3), molybdenum tris-[1,2-bis(trifluoromethyl)ethane-1,2-dithiolene] ($Mo(tfd)_3$), molybdenum tris-[1-(methoxycarbonyl)- 2-(trifluoromethyl) ethane-1,2-dithiolene ($Mo(tfd\text{-}CO_2Me)_3$), tetrafluorotetracyanoquinodimethane (F4TCNQ), 2,2-(perfluoronaphthalene-2,6-diylidene)-dimalononitrile (F6TCNNQ). The HOMO values or the ionization potential are directly taken from literature and were mostly measured with UPS. Ideally the LUMO level is determined by IPES or by CV. If only the optical gap is used to derive the LUMO level for energy diagrams, the literature vales are sorted in the band gap column. It is to note, that this list is not complete nor does it contain all literature on that matter.

4 Experimental Methods

4.1 Photoelectron Spectroscopy

4.1.1 Principle of Photoelectron Spectroscopy

Photoelectron or photoemission spectroscopy (PES) is an important tool in surface science and interface characterization. The analysis method is based on the photoelectric effect, which describes the emission of electrons from the surface of a material if irradiated with light of sufficiently high energy. If X-rays are used as light source, electron from core-level shells can be excited. X-ray photoemission spectroscopy (XPS) is often applied for determining chemical composition and oxidation states at the surface. Electrons from the valence region are typically excited with lower-energy radiation from UV-light sources. In ultra-violet photoemission spectroscopy (UPS) the density of states in the valence region, ionization potential, work function and the respective position of the Fermi level is detected. A mapping of the band structure at the surface can be approached by angle-resolved photoemission spectroscopy (AR-XPS), which holds additional information on the scattering process of valence electrons and their direction. For primary photoelectrons the binding energy $E_{\mathbf{B}}$ can be calculated if the light energy $h\nu$ is known and their kinetic energy $E_{\mathbf{kin}}$ is measured, assuming a complete absorption of the photon and no secondary scattering processes. Conservation of energy therefore dictates:

$$E_{\mathbf{B}} = h\nu - E_{\mathbf{kin}} - \phi \ , \tag{4.1}$$

where in fact $\tilde{E}_{\mathbf{kin}}$, as defined in Figure 4.1, is measured instead of $E_{\mathbf{kin}}$, which depends on the work function of the sample ϕ and the detector $\phi_{\mathbf{D}}$. In practice, the contact potential difference has to be determined by calibration of, for example, a clean metal surface to set the zero reference point for the binding energy axis, provided that the spectrometer is in electrical contact with the sample. The work function can be inferred from the difference in binding energy between excitation energy and the secondary-electron cutoff (SEC). Direct photoelectrons inelastically scatter when escaping the surface generating a background of electrons appearing at higher binding energies. Those secondary electrons that just manage to leave the sample have to overcome the work function and are left with zero kinetic energy detected as the SEC. With $E_{\mathbf{kin}}(\mathrm{SEC}) = 0$ the work function is given according to Eq. 4.1 by $\tilde{\phi} = h\nu - E_{\mathbf{B}}(\mathrm{SEC})$, requiring calibration of the spectrometer, since in practice an additional bias of -5 eV is applied to the sample in order to accelerate the slow electrons for better detectability. After photo excitation, the remaining hole is filled by an electron from higher shells, which can transfer its energy to an other electron getting excited and possibly emitted from the surface. The so-called Auger electrons leave the surface with constant kinetic energy irrespective of the light source. When using different excitation energies, Auger-lines therefore appear at variable binding energy. In XPS high resolution spectra, a spin-orbit splitting of core-level lines can be observed depending

on the energy of the final state of the atom. As a consequence core-level lines in XPS are labelled by nl_j with n the principal quantum number, l angular momentum and $j = l \pm s$ with $s = 1/2$ which can either align parallel or anti-parallel. The relative intensity of the doublet is then given by its degeneracy $g = |2j + 1|$.

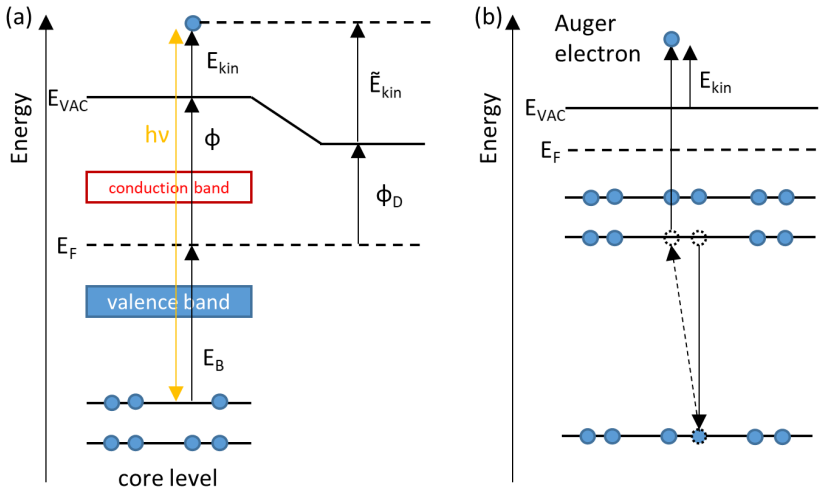

Figure 4.1: Sketch of the energy diagram of the photoemission process plus detector in (a). Schematics of the Auger effect in (b).

4.1.2 Inelastic Mean Free Path

Photoemission spectroscopy is a very surface sensitive method due to a low inelastic mean free path (IMFP) of electrons in solid state materials. The mean free path λ depends on both the material properties as well as on the kinetic energy of electrons. The overall dependence of λ on the kinetic electron energy is shown in Figure 4.2 and follows a "universal" curve, which has the same shape for many materials. Especially for metals the function $\lambda(E_{\text{kin}})$ has a very universal character. Given the mean free path at fixed E_{kin}, the intensity of primary electrons I_0 is reduced after travelling a distance d in the solid according to:

$$I(d) = I_0 e^{-\frac{d}{\lambda(E_{\text{kin}})}} \quad . \tag{4.2}$$

Then λ determines the distance for which an electron beam is reduced in intensity by a factor of $1/e$. To approximate the IMFP for organic materials, or to improve on the material specifications, certain semi-empirical equations can be used.[93–96] In this work, the predictive formula of Tanuma et al.[97] is used for calculating coverages on different substrates. Whereas the agreement with experimental values is large in the range 50 to 200 eV, a precision of about 13% is reported for the high energy range. Modified from the Bethe equation, the IMPF TPP-2 formula of Tanuma et al. reads:[97]

$$\lambda = \frac{E}{E_p^2 \left[\beta \ln(\gamma E) - (C/E) + (D/E)^2\right]} \quad , \tag{4.3}$$

where λ denotes the IMFP (in Å) as a function of electron energy E (in eV) with the free-electron plasmon energy $E_p = 28.8(N_v \rho / M)^{\frac{1}{2}}$ (in eV), the number of valence electrons per atom N_v, the

molar weight M and the bulk density ρ (in g cm^{-3}). The parameters γ, β, C, D are fitted based on theoretical or experimental data, further depending on the density, E_p, M, ρ, N_v and the band gap E_g. For composites mean values of M, N_v and E_p are taken from all atomic species and inserted into Eq. 4.3 to get the best estimation.

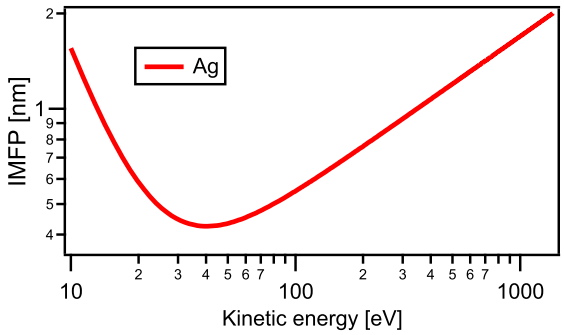

Figure 4.2: Plot of the Inelastic Mean Free Path (IMFP) of silver as a function of kinetic energy, calculated from Eq. 4.3.

4.1.3 Quantitative XPS

With XPS stoichiometric information can be obtained from different core-level emission lines taking into account their respective photo excitation cross-sections. However, in order to get quantitative information, the use of a reference method and database becomes necessary, that involves knowledge of the detection process like the detector system, sample properties, geometry and processing of the spectra. In general, the photoelectron signal I may be written in terms of kinetic energy E:[98]

$$I = \sigma\, D(E) \int_{\gamma} \int_{\phi} L(\gamma) \int_{y} \int_{x} J_0(x,y)\, T(x,y,\gamma,\phi,E) \int_{z} N(x,y,z)\, e^{\frac{-z}{\lambda(E)\cos\theta(\phi,\gamma)}}\, dV\, d\Omega\,. \tag{4.4}$$

Here, σ denotes the cross-section from the specific core-level shell, $D(E)$ the detector efficiency, $L(\gamma)$ the angular asymmetry of the intensity of the photoemission process, J_0 the X-ray flux intensity over the surface area (x,y), $T(x,y,\gamma,\phi,E)$ the analyser transmission function, $N(x,y,z)$ the atom density of the atom under consideration, $\lambda(E)$ inelastic electron mean free path in the matrix and θ is the angle between surface normal and detector. The angle between emission axis and incident X-rays is marked by γ, whereas ϕ is the rotational angle of emitted electrons. Assuming a homogeneous distribution of atoms and a single take-off angle, the integration over z can be carried out. Within the same probed area and photon flux, the ratio of intensities of atom A and B can then be connected to their molar ratio:

$$\frac{N_A}{N_B} = \frac{I_A}{I_B}\left(\frac{\sigma_A\, D(E_A)\, T(E_A)\, \lambda(E_A)}{\sigma_B\, D(E_B)\, T(E_B)\, \lambda(E_B)}\right)^{-1} \tag{4.5}$$

The remaining factors in Eq. 4.5 are often enclosed in the detector-specific atomic sensitivity factors ASF which then lead to Eq. 4.6. It is to note that an average inelastic mean free path has to be assumed which may differ for example in organic materials.

$$\frac{N_A}{N_B} = \frac{I_A}{I_B}\frac{\mathrm{ASF}_B}{\mathrm{ASF}_A} \tag{4.6}$$

4.1.4 Charging

During PES measurement photoelectrons are constantly emitted from the surface and leave a positive charge behind, which has to be compensated from within the bulk of the material. Consequently, there is a small current between the sample and the reference potential or ground of the spectrometer. If these positive charges at the surface can not be replenished fast enough, they will pile up and build a positive surface potential. Electrons leaving the surface are slowed down by the attractive potential and appear at higher binding energies compared to a neutral surface. This leads to wrongly assigned binding energies and false conclusions when investigating doping or performing interface experiments, which result from the sample not being in equilibrium.
The conductivity of the sample is an important criterion for charging effects to become apparent. If the resistivity is too high, electrons are not compensating the photo-generated holes at the same rate they are created by photoemission.[99] For strong charging and surface inhomogeneities, an additional broadening of peak shapes is observed. For intrinsic organic semiconductors with a band gap up to 2 eV and mobilities of down to 10^{-5} cm^2 V^{-1} s^{-1}, a high resistivity can be expected. Given a photo-current of 20 nA, a beam diameter of 200 μm and a film thickness of 100 nm, a potential drop of 0.2 eV occurs within the organic layer for a conductivity of $\sigma = 10^{-7}$ Ω^{-1} m^{-1}, where a full compensation is assumed. The amount of photoelectrons depend on the flux of the light source but also on the cross-section of the respective electron-shells, which is a function of photon energy. For organic materials, charging is much more severe in case of UPS, compared to XPS at comparable photon flux. The reason is a much higher cross-section for the C 2p orbitals (with UPS at 21.22 eV) than for the C 1s state (with XPS at 1486.7 eV). In addition, XPS produces a large number of secondary electrons distributed in vacuum which may also contribute to hole compensation.
Since this is a common problem in PES, there are several strategies to account for charging. Most modern spectrometers are equipped with a neutraliser composed of an electron flood gun and/or a soft ion beam, which can compensate surface charges but leaves the precise Fermi level position unknown. In principle, the application of very thin films can reduce the resistance and therefore charging, however, the influence of the e.g. metal substrate can become dominant for very low thickness. Alternatively a thin gold layer can be deposited on-top and the position of the Au 4f peak may be used as a reference in conjunction with the value of a clean gold sample. It is to be noted, that effects of gold cluster size and interactions with the metal need to be considered. Nonetheless, there are parameters that can be analysed which are not affected by charging like difference in binding energies or for example the modified Auger parameter.[99]

4.1.5 Setup and Settings

In this work, photoelectron spectroscopy (PES) measurements were carried out using a PHI5000 Versa Probe scanning photoelectron spectrometer attached to the clustertool, a fully integrated UHV system at InnovationLab (Heidelberg). The spectrometer was equipped with a monochromatic Al Kα X-ray source at 1486.7 eV photon energy for X-ray photoelectron spectroscopy (XPS). For ultra-violet photoelectron spectroscopy (UPS), a differentially pumped helium discharge lamp is attached to the spectrometer chamber, which is operated for He I emission at 21.2 eV with a current of 80 mA. To increase He II emission the partial pressure is lowered and

the set point for the current loop increased to 200 mA. The energy offset is regularly calibrated with the Fermi level edge of a sputter-cleaned silver sample distributed in vacuum. The focused X-ray spot is approximately 200 μm in diameter and can be narrowed down to 10 μm. The pass energy for measuring high resolution core-level lines was set to 11.75 or 23.5 eV.

4.2 Infrared Spectroscopy

In this work, infrared spectroscopy (IR) measurements are discussed to complement XPS analysis, since additional information on charge-transfer in the bulk, composition and molecular properties can be obtained from optical spectroscopy which are not accessible with XPS. All IR spectra shown in this work have been measured in the group of A. Pucci at the clustertool of InnovationLab Heidelberg. Since this work is not carried out by the author, only important experimental findings are mentioned, which support conclusions presented herein and which help to draw a more conclusive picture on the system under investigation. For more information the reader is referred to corresponding literature.[100,101]

4.2.1 Setup and Settings

For IR transmission measurements the FTIR-spectrometer Vertex80v from Bruker was used. The base pressure in the sample compartment was ca. 3 mbar to prevent absorption from ambient air. Most of the measurements were recorded near normal transmittance (7°) with a Mercury Cadmium Telluride (MCT) detector. In this spectrometer, a globar is used as a light source, which is a heated rod made from silicon carbide. The resolution can be estimated to about 4 cm^{-1} and an average of 200 scans is usually taken. To further obtain a good signal to noise ratio, the MCT detector has to be cooled to liquid nitrogen temperatures. Additionally, the spectrometer possesses a DLaTGS-detector (deuterated L-alanine doped triglycene sulphate), which does not require cooling and has a good linearity but worse sensitivity. The MCT detector (580 cm^{-1} - 6000 cm^{-1}) shows a linear response for low intensity and software corrections are possible. In standard measurements an aperture of 1 mm and a potassium bromide (KBr) beam splitter is used.

4.3 Vacuum Thermal Evaporation

Small molecules for organic electronics are usually deposited from heated crucibles at high vacuum (HV) to ultra high vacuum (UHV). Since organic materials are heated in UHV, they do not decompose but pass over into the gas phase from a liquid phase or they directly sublime, provided that the decomposition temperature is higher than the evaporation temperature at given pressure. Contaminations can only stem from impurities within the source material or residual gas molecules. With this technique stacks of multiple layers of different materials can be easily realized, since layers are grown molecule by molecule at an adjustable evaporation rate controlled by distance and temperature. Especially homogeneously doped layers can be fabricated by co-evaporation, in which both dopant and matrix molecule are simultaneously deposited.[102] The molecular beam can be stopped by a simple shutter and the rate is monitored by a quartz micro-balance.
For this work, a new preparation chamber was built up that is small enough to work with only

little amount of organic material. The initial goal was to characterize new dopant molecules with a set of common matrix materials. For a first successful synthesis there can be as little as <100 mg substance after purification. To run several experiments with one material batch, a small crucible and a short distance to the substrate is required. However, if the sample-to-source distance is chosen too small, the thin film will be inhomogeneous and a simultaneous monitoring with a micro-balance is difficult. For this purpose, an old (mostly organic contaminated) evaporation chamber was thoroughly cleaned and set-up as depicted in Figure 4.3. At the bottom a water-cooled metal source can be attached and a commercial 4-cell evaporator was mounted to the side. Since the individual cells are small, a shutter is not needed due to a fast heat-up and cool-down time. The sample enters the chamber horizontally on the transfer rod. At the connecting cross on the top a pressure sensor and a turbo-molecular pump is attached. A water-cooled micro-balance is introduce from a small flange at the upper 45° position to partially catch the molecular beam that does not hit the sample. A sensitivity check and tooling factor calibration was not jet conducted. A simple geometric consideration yields a thickness variation of 1.5% for a 1 cm sample from the central source positions ($\theta = 0°$) in Figure 4.3c (evaporated mass M, density ρ) but increases to ± 8% at the $\theta = 45°$ position, if the sample is kept horizontally:

$$d = \frac{M \cos\theta}{\rho 4\pi r^2} = \frac{Mh}{\rho 4\pi (h^2 + L^2)^{3/2}} \tag{4.7}$$

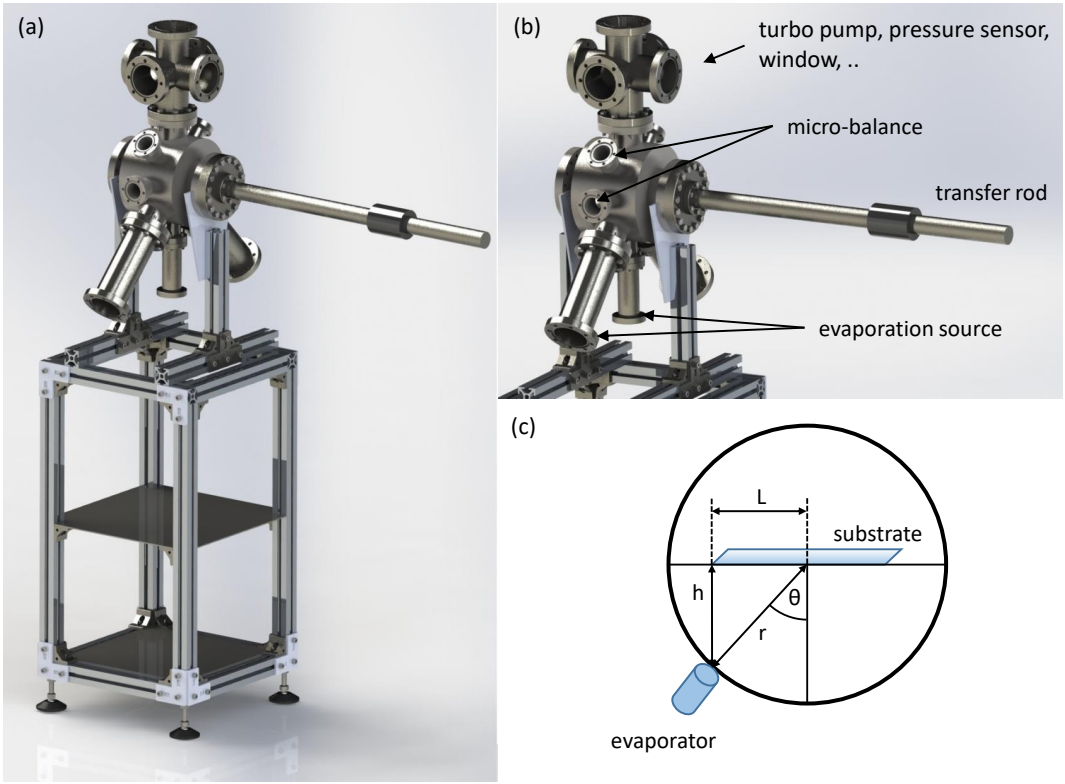

Figure 4.3: Computer designed model of the evaporation chamber (a) with intended configuration (b) and geometric properties in (c).

5 Methods in Data Analysis

5.1 Doping Concentration

As described in Section 4.1, it is possible to estimate stoichiometric element ratios with quantitative information in XPS. Here, a homogeneous distribution of the respective elements has to be assumed, because XPS is very surface sensitive and an element that originates from e.g. a top layer has a higher detection efficiency compared to an element that is only present in the bulk. Provided a homogeneous atomic distribution and benefiting from the comparably higher information depth in organic materials, the doping concentration can be calculated on the basis of atomic ratios. Additionally, the doping concentration needs to be high enough in order to detect dopant-related core-level emission lines, which is usually around >1%. However, for organic semiconductors a doping concentration in the order of a few vol% is often used to achieve high conductivity. If the number of atoms in each molecule is known from their structure, ratios of elements can be converted to molar ratios or to molar fractions of molecules. In case of p-doping, the dopant is commonly fluorinated, whereas the matrix is not. Hence, fluorine can be used as an unambiguous marker for the dopant. However, the matrix may not posses an exclusive core-level emission and in an extreme case (for example in n-doping of Section 8.1) all core-level lines bear contributions of both dopant and matrix, in which only their relative intensities change with doping concentration. In order to calculate the most probable doping ratio based on all available elements in XPS, the following method is proposed. Let $\tilde{I}_x$ be the ASF or transmission/cross-section corrected intensity of the relevant core-level emission line of element x and n_A be the molar concentration of molecular species A. Then, with the number of atoms of element x in A denoted by $N_{x,A}$, the intensity can be expressed for multiple molecular species according to:

$$\tilde{I}_x \sim \sum_A N_{x,A}\, n_A \tag{5.1}$$

$$\tilde{\mathbf{I}} \sim \mathbf{N}\,\mathbf{n}\ , \tag{5.2}$$

where $\mathbf{n} = (n_A, n_B, n_C, ...)$ is the vector of molar densities for molecular species A, B, C, ... and $\tilde{\mathbf{I}} = (\tilde{I}_x, \tilde{I}_y, \tilde{I}_z, ...)$ the vector of corrected core-level intensities for elements x, y, z, ... connected by the matrix $\mathbf{N} = (N_{x,A})$. There is a single unknown proportionality factor in Eq. 5.1 which cancels for ratios like n_A/n_B. Eq. 5.2 can be solved via $\mathbf{n} \sim \mathbf{N}^{-1}\tilde{\mathbf{I}}$ with the pseudo inverse of $\mathbf{N}$. However, errors for the intensity have to be taken into account, if the difference in absolute values is large. The noise level can be estimated by shot-noise with square-root dependence on intensity which leads to the weights $\mathbf{w} = \mathrm{diag}(\sqrt{\tilde{\mathbf{I}}})$. Consequently, the result can be improved by solving the weighted least square fit in Eq. 5.3 with a common numeric library, yielding also values for the standard error in n.

$$\min_n \left|\left|\mathbf{w}^{-1/2}\,(\tilde{\mathbf{I}} - \mathbf{N}\,\mathbf{n})\right|\right|_2 \tag{5.3}$$

5.2 Satellite Removal in UPS

For UPS measurements, the UV light source is often a non-monochromatized differentially-pumped cold cathode capillary discharge lamp which is filled with a low-pressured noble gas, typically Helium. The resonant fluorescence occurs when the noble gas is excited in the discharge process and subsequently decays to the ground state. Common choices of emission lines are Ne I (16.6 eV) and Ne II (26.8 eV) or He I (584 Å, 21.2eV) and He II (304 Å, 40.8 eV). In this work, a helium discharge lamp is used that can be adjusted to operate in He I and He II emission. Usually the transition from the first excited to the ground state is the most intense, but there are also other transition from e.g. higher excited states. The strongest emission of He I is at 584 Å but there are lines at 537 Å, 522 Å and 304 Å which can have intensities of about 2% of the main line. For heavier noble gases also a richer satellite structure can be expected. Since photoemission in UPS occurs mainly from the He I emission at 21.22 eV, the He I satellites generate ghost lines of the UPS spectra shifted in binding energy due to a variation in photon energy. These can be partially corrected by subtracting the scaled and shifted recorded spectrum according to the distribution and intensity of He I satellites. For most purposes this is a sufficiently good correction given the relative intensities of around 2%. However, when trying to investigate band gap states or using heavier noble gases, a more accurate satellite correction can be attempted. Assuming that the cross-section of photoemission does not change within the energy range of He I satellites, the measured spectrum $I(E)$ is derived from the pure or true spectrum $S(E)$ via convolution:

$$I(E) = \int S(E')\, t(E-E')\, dE' \ , \tag{5.4}$$

where $t(E)$ holds information on the exciting UV spectrum. In a simple approach $t(E)$ can be constructed from the sum of the main line plus individual satellites. Provided that their relative strength N_i and energy shift ΔE_i is known from calibration or calculation, the transfer function $t(E)$ can be expressed by:

$$t(E) = N_0\delta(E) + N_1\delta(E-\Delta E_1) + \ldots \ =: \sum_i N_i\delta(E-\Delta E_i) \tag{5.5}$$

With the above approximation for $t(E)$, the clean spectrum $S(E)$ can be inferred from Eq. 5.4 via deconvolution. In fact, if only a sum of delta peaks is considered in Eq. 5.5, the convolution matrix will be sparse and a direct inversion by singular value decomposition can be attempted if the data vector is not too large. Alternatively iterative deconvolution like Richardson-Lucy algorithm or Fourier-based methods are favoured. This can in principle also be applied to XPS for a non-monochromatized Al Kα source. With the expression in Eq. 5.4 also photoemission-induced charging (mentioned in Section 4.1) can be corrected for, if $t(E)$ describes a charging process that causes an energy shift and broadening. For example, the transfer function can be determined from deconvolution of a charged core-level line with its uncharged reference obtained by deposition of an additional conducting toplayer. With this transfer function, the charged XPS valence band can be recovered, which would not be possible with a conducting toplayer.

6 Diffusion in Organic Semiconductors

6.1 Overview Diffusion

Doping of organic semiconductors can be beneficial for many types of devices since it improves contact resistance to metals or metal-like oxides and reduces Ohmic losses in charge transport layers.[12,44,102–106] Ideally, the position of the Fermi level can be controlled with respect to the transport level of the semiconductor, that offers a powerful tool to engineer electrical properties of organic layers in a multi-stack device.[12,107] An increase in conductivity of 10 orders of magnitude has been reported, giving rise to almost metal-like doped polymers.[6,10] With highly increased conductivity, organic polymers also become promising candidates for thermo-electric applications featuring a low thermal conductivity.[108,109] However, in modern state-of-the-art devices electrical or electrochemical doping plays a minor role or is sometimes not used at all. Up to recently,[110] homo p-n-junctions still posed a challenge for organic devices and is still problematic for polymers.[111] The problems of stability are mainly due to reactivity and diffusion of dopants, since in early studies, halogens and alkali-metals have been used for doping.[9,10,112,113] As an example, dopants can diffusive into adjacent layers and cause exciton quenching, reducing the lifetime of optoelectronic devices.[16,114–116] This has been improved by introducing molecular dopants, which constitute of small molecules with a specifically high electron affinity or low ionization potential acting as electron acceptors or donors.[13] For example in case of p-doping, molecules like 2,3,5,6-tetrafluoro-7,7,8,8-tetracyanoquinodimethane (F4TCNQ) and molybdenum tris(1,2-bis(trifluoromethyl)-ethane-1,2-dithiolene) ($Mo(tfd)_3$) possess a high electron affinity and enable an integer or partial charge transfer.[43] Details about the charge transfer mechanism and the generation of free charge carriers is subject of intensive research. However, even for molecular dopants a strong diffusion and drift has been reported and gained more attention recently.[14,15,117–120] Generally speaking, a higher diffusivity can be expected for polymers as hosts in comparison to conjugated host molecules like fullerenes, since polymers offer a large free volume and lower density.[120] The host morphology plays an important role when considering diffusion, as for example stable doped layers have been reported with F4TCNQ and $Mo(tfd)_3$ in N,N'-di(1-naphthyl)-N,N'-diphenyl-(1,1'-biphenyl)-4,4'-diamine (α-NPD),[46,121] whereas F4TCNQ was found to diffuse in more crystalline materials like zincphthalocyanine (ZnPc) and 4,4'-bis(N-carbazolyl)-1,1'-bi-phenyl (CBP), causing migration to a metal electrode modifying its surface potential.[14,15] Moreover, the size and chemical properties of molecular dopants can determine their mobility in an organic matrix. Thermally activated diffusion of F4TCNQ and the fluorinated fullerene C60F36 was studied by Li et al. in N,N,N',N'-tetrakis(4-methoxyphenyl)benzidine (MeO-TPD) by means of photoluminescence spectroscopy, neutron reflectometry, and near-edge X-ray absorption finestructure spectroscopy, showing that the larger C60F36 provides an increased morphological stability than F4TCNQ.[117] The diffusion of small molecules was also quantitatively studied in literature: A series of work was focused on the diffusion of fullerene-derivatives in the polymer poly(3-hexylthiophene) (P3HT), which is of interest for bulk hetero-junctions made from PCBM:P3HT in solar cell applications, yield-

ing diffusion constants D of ca. 10^{-11} and 10^{-14} cm^2s^{-1} at around 140 °C.[122–124] Very recently, the diffusion of F4TCNQ and its monoester-substituted derivative, in which one of the cyano moieties is replaced by an alkyl ester, was measured quantitatively using confocal fluorescence microscopy, a measurement technique that enables analysis of spatial concentration profiles as a function of time.[125] The results of a two-component fit reveal that charged F4TCNQ ($D \approx 10^{-13}cm^2s^{-1}$) is less mobile than neutral F4TCNQ ($D \approx 10^{-11}cm^2s^{-1}$) and that the slightly more bulky derivative shows an order of magnitude reduced mobility than F4TCNQ.[125] As another example in this context, the diffusion of ions in polymers from electrolyte dielectrics used in organic thin-film transistors was measured to be 10^{-12} - 10^{-14} cm^2s^{-1} at room temperature.[126,127] On the other hand, the diffusivity of molecular dopants can be beneficially used in sequential doping, in which the pure polymer is processed to achieve optimal morphology, eg. crystallinity, and the dopant is introduced subsequently by vacuum or solution-based deposition.[128–130] Provided the dopant enters the film, this offers doped and, at least in some cases, highly ordered polymer films with coherent charge transport.[118,131] Parallel to this work, Li et al. reported that F4TCNQ diffuses more easily in crystalline P3HT, compared to fully amorphous P3HT, which causes a reduction in fidelity for dopant induced solubility control (DISC) patterning.[132] The DISC patterning method employs sequential deposition of dopants, which diffuse into the semiconducting polymer and render doped regions insoluble in nonpolar solvents due to the high polarity of charge transfer.[133] The diffusion of small molecules in rubbery or glassy polymers has been extensively studied in literature, but is mainly focused on the penetration of solvents and other liquids.[134,135] Theoretical descriptions of diffusion in such systems require concepts of free volume and partial immobilization to explain deviations from Fickian diffusion.[136–140] The temperature dependence of diffusion in such systems is modelled by Arrhenius law and involves an activation energy for transport.[134] These concepts may also play a role in the diffusion of molecular dopants in organic semiconductors.

This work is aimed at testing and investigating diffusion within a known system to further discuss and verify strategies of immobilization. In the first part of the chapter, the bulky dopant molybdenum tris(1-(methoxycarbonyl)-2-(trifluoromethyl)-ethane-1,2-dithiolene $Mo(tfd\text{-}CO_2Me)_3$ is studied in P3HT to characterize spectroscopic features used to identify diffusion, which is then discussed for sequentially doped P3HT with regard to its morphology in the second part.

6.2 Material System P3HT

In order to investigate the diffusion of molecular dopants in more detail, a suitable model system of dopant and matrix has to be chosen. A more elaborate literature reviews on recent studies, that focus on diffusion in common organic materials, are presented in Section 6.1 and 7.1. The materials used for this study are shown in Figure 6.1. By choosing a polymer as matrix, a higher diffusivity of dopants can be expected, being favourable for the context of this work. The polymer poly(3-hexylthiophene) (P3HT) is a very well known hole-transport and donor material for organic photovoltaics (OPV)[141,142] and organic field effect transistors (OFETS),[143] which found broad application in previous studies.[143–145] P3HT essentially contains a backbone of repeating thiophene units with attached hexyl side chains. The precise conformation of the polymer depends on the regioregularity of its hexyl side chains.[146] Ideally, an alternating alignment of thiophene (head) and side chains (tail), which is referred to as head-tail coupling, leads to high structural order and "straight" 2D-sheets of lamellar structures in a crystalline phase (see Figure 6.2b).[147] The percentage of head-tail coupling is considered as degree of regio-regularity and allows efficient π-π stacking of thiophene backbones. A completely random orientation of P3HT is referred to as regio-random P3HT (rra-P3HT) and results in isolated chains in a coiled conformation.[147] P3HT exhibits broad absorption bands in the visible range between 400 nm and 600 nm as depicted in Figure 12.4b.[145]

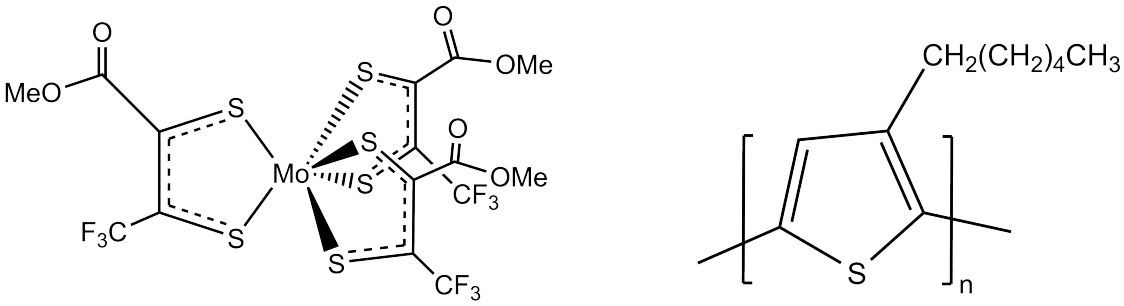

(a) $Mo(tfd\text{-}CO_2Me)_3$ **(b)** P3HT

Figure 6.1: The Figure shows the structural formula of the dopant molecule molybdenum tris-(1-(methoxycarbonyl)-2-(trifluoromethyl)ethane-1,2-dithiolene) ($Mo(tfd\text{-}CO_2Me)_3$) in (a) and the matrix poly(3-hexylthiophene) (P3HT) in (b). The dopant was provided by the group of S. Marder (Georgia Institute of Technology).

The energy levels of P3HT, i.e. the HOMO and LUMO levels are located around 5 eV and 3 eV with respect to the vacuum level.[148,149] The precise position of energy levels depends on the morphology of P3HT, as for example a stronger bound HOMO-level at 5.25 eV was reported for rra-P3HT, compared to regio-regular P3HT (rr-P3HT), and was possibly assigned to an increased backbone-twist.[78] For rr-P3HT a HOMO and LUMO level of 4.65 eV and 2.13 eV has been reported.[77] Additionally, the structural orientation of P3HT at the substrate's interface affects the determination of bulk energy levels. P3HT is known to exhibit large space charge regions in a Schottky diode configuration. The morphology of rr-P3HT is regarded to be semi-crystalline with a crystalline content of 40-70%, depending on molecular weight and regio-regularity.[150] For P3HT crystals two characteristic stacking distances are observed in electron diffraction measurements that are assigned to the π-π stacking of the thiophene backbone

at 0.38 nm in (010)-direction and the lamellar stacking at 1.68 nm in (100)-direction.[151–154] In P3HT OFETs the orientation of crystals at the gate strongly affects the observed mobility, since a edge-on orientation of the lamellar-stacked sheets enable a charge transport along the (010)-direction supported by π-π-interactions increasing the hole mobility.[155,156] For comparing the influence of morphology in this work, rr-P3HT was purchased from Merck KGaA (lisicon SP001) and rra-P3HT from Rieke Metals with material properties listed in Table 6.1. For this study,

	M_w [g mol^{-1}]	Regioregularity [%]	Polydispersity
rr-P3HT	24 320	93.7	2.1
rra-P3HT	57 000	-	2.9

Table 6.1: Material parameters of the utilized P3HT such as molar weight and regularity.

the dopant Molybdenum tris[1-(methoxycarbonyl)-2-(trifluoromethyl)-ethane-1,2-dithiolene] (Mo(tfd-CO_2Me)$_3$) was investigated, which is a derivative of Mo(tfd)$_3$ designed by Zhang et al. to increase solubility.[121,157] As a consequence Mo(tfd-CO_2Me)$_3$ can be both vacuum (UHV) and solution processed, which is necessary to compare effects of different processing methods (sequential or "in-solution" doping) on, for example, morphology, charge transfer efficiency and energy levels.[158] The dopant Mo(tfd-CO_2Me)$_3$ has an electron affinity of around 5 eV which is lower than for strong dopants like Mo(tfd)$_3$ or F4TCNQ.[91,121,159] Nonetheless, a high doping efficiency is observed with P3HT (see Section 9.1 and 9.2), although P3HT has a HOMO of around 5 eV as well.[77,148,149] Mo(tfd-CO_2Me)$_3$ undergoes integer charge transfer with P3HT and quantum calculations from Tenderholt et al. suggest, that the electron is mainly localized around the C_2S_2 portions of the dithiolene ligands.[91,160] A goal of this work is to test the impact of P3HT crystallinity on dopant diffusion. In principle, even a directional dependence of the dopant diffusion in P3HT crystallites may be possible provided that the lamellar or π-π plane is blocking the dopants in one direction. However, there is a discussion in literature whether large molecular dopants can actually enter P3HT crystallites or are only located in the amorphous regions of rr-P3HT. Liu et al. suggested that a reduction in π-π spacing upon doping is not due to intercalated dopants but due to charging itself.[161]

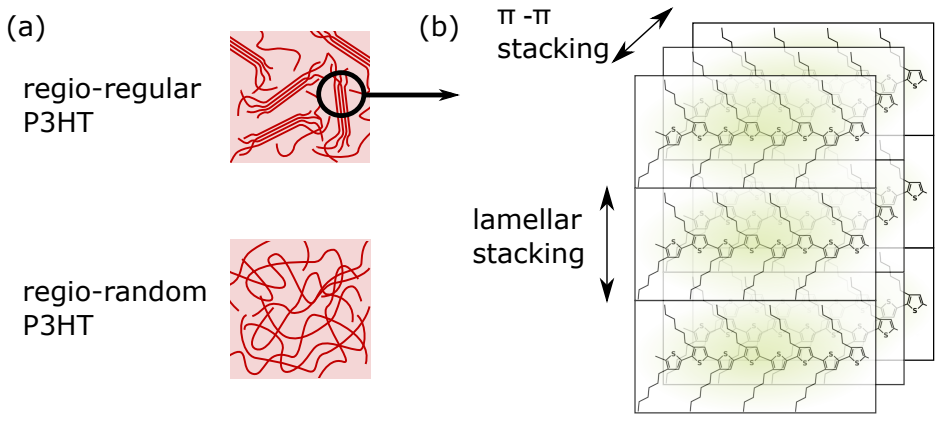

Figure 6.2: (a) Sketch of the morphology of regio-regular rr-P3HT and regio-random rra-P3HT. (b) Schematic of the P3HT crystallites with π-π and lamellar stacking order.

7 Immobilization Strategies

7.1 Overview of Immobilization Strategies and Molecule Design

The potential benefits of electrical or electrochemical doping in organic semiconductors are crucial for the development of devices and can be used in state of the art applications,[12,162] which was stated in the introduction in Section 6.1. In the previous chapter the volatility and diffusivity of dopants in low dense organic host materials like for example polymers was discussed. Since dopant migration has been identified as an important degradation mechanism for organic light emitting diodes[16] limiting lifetime and reducing performance for long-term operation, the prospect of suppressing or reducing any kind of molecular diffusion is of interest in the design routes for universally employable and strong dopants.[34] For example it is known that dopants entering adjacent layers can cause exciton quenching in optoelectronic devices.[16,114–116] Also stable p-n structures are not possible with halogens and alkali metals as oxidizing or reducing agent because of their high diffusivity.[9,10] Moreover they were found to cause problems in organic hole transport layers for planar n-i-p perovskite solar cells. In the previous chapter properties that influence the diffusion were identified. It is known in literature that the specific material combination determines if a dopant-host system is stable. In general, larger dopant molecules offer better thermal stability as they experience more hindrance when diffusing through the matrix.[117] Li et al. directly measured the diffusion constant of F4TCNQ ($D \approx 10^{-11}\mathrm{cm}^2\mathrm{s}^{-1}$) in P3HT and its bulkier monoester-substituted derivative, yielding more than an order of magnitude lower diffusivity.[125] Regarding the host material, polymers enable a generally higher dopant mobility than for example molecular glasses.[120,129] Although there is no direct proof for this conclusion, experimental observations may suggest that crystalline semiconductors may allow for a higher diffusivity than fully amorphous materials like α-NPD or C_{60}. For example, stable layers have been reported for F4TCNQ and $Mo(tfd)_3$ in α-NPD.[46,121] However, in similar-sized but more crystalline materials such as ZnPc and CBP, the same dopant F4TCNQ was observed to migrate towards a metal electrode changing its surface properties.[14,15] A possible explanation may include grain boundaries acting as dopant pathways. This idea can at least agree with the higher dopant-uptake in sequentially doped rr-P3HT found in this work (see Section 10.3). Moreover, Li et al. reported that charged F4TCNQ molecules in P3HT are much less mobile ($D \approx 10^{-13}\mathrm{cm}^2\mathrm{s}^{-1}$) than their neutral counterparts ($D \approx 10^{-11}\mathrm{cm}^2\mathrm{s}^{-1}$).[125] In modelling the diffusion in sequential doping, studied in Section 10.3, charged dopants were practically treated as immobile, because a change in surface concentration was only observed for neutral molecules. An explanation for this difference is given by increased electrostatic interactions of the charged dopant with its surrounding. Coulomb forces and polarization effects are considered to enhance the onsite binding energy, preventing the dopant from migrating.[163] In conclusion, suppressing diffusion can either focus on morphology, i.e. size and crystalline, or on increasing intermolecular interactions which is the case for charged molecules. There are some publications in literature addressing these two approaches to stabilize dopants in for example soft polymers. Dai et al. proposed an additional dopant blocking interlayer to hinder

dopant migration in adjacent layers, which was introduced by soft-contact transfer lamination.[91,158] It was shown via secondary ion mass spectrometry that dopants are not diffusive in the P3HT:ICBA bulk heterojunction suggesting that ICBA is filling up voids and thereby presumably blocking dopant pathways.[158] Li et al. investigated doping of the modified thiophene poly(thiophene-3-[2-(2-methoxy-ethoxy)ethoxy]-2,5-diyl) (S-P3MEET) bearing very polar side chains intended to increase the binding to F4TCNQ anions.[164] In fact, they found that the ethyloxy side-chains of S-P3MEET are capturing the F4TCNQ molecules and retain them up to an annealing temperature of 210 °C. In a stack of P3HT and S-P3MEET absorption and fluorescence spectroscopy revealed that F4TCNQ diffused into S-P3MEET, where it is more strongly bound, and little F4TCNQ was left in P3HT.[164] Interestingly, with regard to this study presented in Section 13.4, they found an increase in the melting temperature of S-P3MEET with 5 wt% doping suggesting that F4TCNQ further stabilizes the polymer film. A different approach was followed by Mor et al., where contact doping was achieved with strong polyelectrolytes, i.e. sulfonated poly(sulfone)s improving charge carrier injection.[119] Polymer strands incorporating acidic moieties aligned in ultra thin layers at the anode mimic doped transport layers for contact barrier reduction.[119] The advantage is, that in principle p-type polymer donors serve the same role as for example small molecular dopants like F4TCNQ, but resist diffusion due to their large size and can be employed within the electrode region. Usually most of these methods have some drawbacks or are only effective in a specific material configuration. For example, additional dopant blocking interlayer complicates the stack processing and induce possible problems for energy level alignment at its interfaces.[165] Also making dopants simply large probably causes problems concerning morphology. In this work, it is sought to increase intermolecular interactions between dopant and matrix in order to reduce diffusivity and create a more stable doped layer. In organic solids intermolecular interactions include dispersion force, dipole-dipole interactions, π-π interactions or even hybridization. Anchoring, i.e. thermally stable connections between dopant and host, are likely achieved via a covalent bond. A pre-modification of the host with a functional group that introduces self-doping was previously used to localize dopants in fabricated thin films.[166,167] In order to engage a bond after film formation or blending at desired concentration, host and dopant require complementary functional groups to trigger a specific chemical reaction such as amino, ester, epoxide or thiol groups.[168–170] This "click-chemistry" principle however requires to synthetically modify each organic semiconductor to fit the dopant which is not feasible given the scope of materials in use. Possible strategies are depicted in Figure 7.1. The goal is to functionalize a common dopant which possess an anchoring group being able to undergo covalent bonding to any organic semiconductor. In particular, this means the reactive group has to attach to aliphatic C-H or olefinic C=C bonds present in almost any organic semiconductor without introduction of severe degradation and traps by altering the electronic structure of the host molecule, caused by additional covalent bonds. Furthermore, a possible partial polymerization or interconnection among dopant molecules is also not excluded, if segregation occurs and they are not individually dispersed in the matrix. However, this tends to reduce the diffusivity as well and is initially not considered to be a problem. In the following organic azides are discussed to provide an universal anchoring mechanism and are applied as suitable dopants for immobilization.

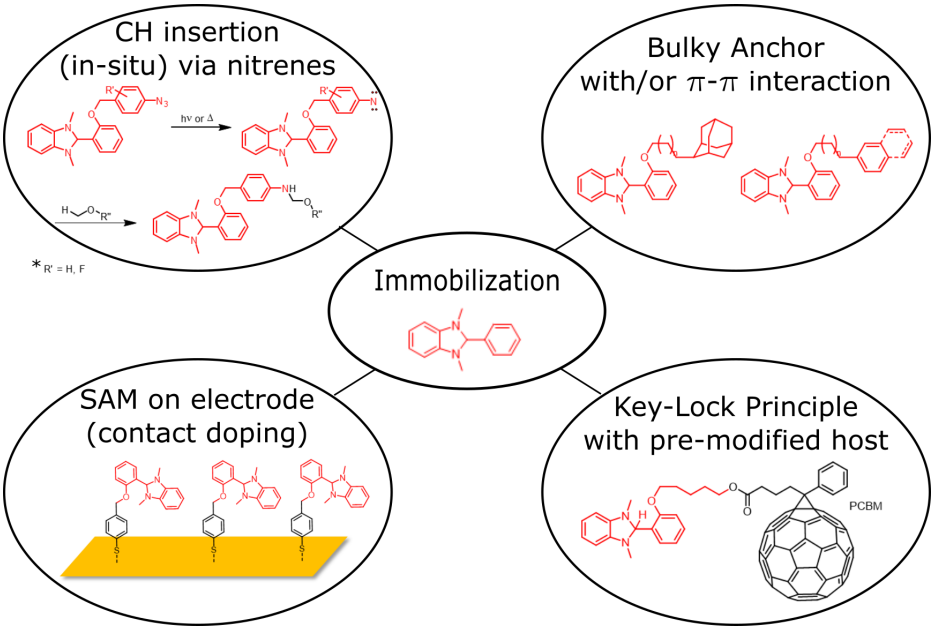

Figure 7.1: This schematic illustrates different immobilization approaches for the n-type dopant DMBI (in the centre) either by increasing intermolecular interaction with a bulky anchor that decreases diffusivity in low dense matrix or by creating covalent bonds to the host molecule or the electrode.

7.2 Chemistry of Organic Azides

As described in the previous chapter, organic azides are of interest for the purpose of binding molecular dopants to neighbouring matrix molecules. The class of organic azides is very diverse and includes aryl, acyl and alkyl azides. Their unique properties and applicabilities in synthetic chemistry is used for example in heterocycles or anilines, pharmaceuticals, explosives technology, biomarkers and peptides and photo-activation of polymers.[171,172] Bräse et al. counted more than 1000 publications and there are several reviews on the topic.[171,173–176] The first aromatic azide has been synthesized by P. Griess in 1866 and hydrogen azide was synthesized by Curtius in 1890.[71,177] In biochemistry azides are used for acetylation of proteins[178,179] and azidonucleosides like azidothymidin, which inhibits reverse transcriptase employed for antiretroviral medication in for example AIDS treatment.[180] Inorganic azides on the other hand often form explosives. In the case of heavy metal azides, e.g. lead azide, they serve as primary explosives for booster detonation since they easily trigger on impact or heat.[181] Sodium azide is used to inflate air bags of cars, since decomposition can be initiated by heat or an electrical impulse and rapidly releases nitrogen.[171] Organic azides are likely explosive, if the azido moieties are dominating, i.e. as a rule of thumb for compounds having (C+O)/N<3.[182] In general, azides are also very toxic and have to be handled with care. In the context of this work the photochemical cross-linking of spacers like bis-azides is of particular interest. This has received much attention lately as desolubilization is not limited to a specific polymer and may be very well be applied to any suitable material. As an example, Png et al. used a bis(fluorophenyl azide) (sFPA) for cross-linking,[183] thus protecting polymer strands from redissolution in solution-processed heterostructures. The cross-linker bis(perfluorophenyl) azide (bis-PFPA) has also been tested in conjunction with doped polymer films, however, not on the

dopants themselves but mixed in a doped film preserving the doping benefits.[184] FPA is investigated to be activated by deep-ultraviolet light (UV, 254 nm) inducing photolysis and generating reactive singlet nitrenes;[174,183] afterwards they potentially undergo a scope of reactions but depending on reaction partners preferably cross-linking. Another field of applications involves the modification of surfaces which is based on an azide click-chemistry to selectively bind organic molecules and in its principle proceeds by a functionalization via SAMs.[179,185–187] For example, carbon surfaces can be treated by gaseous iodine azide vapour yielding an azide terminated surface, which then selectively can be used in click chemistry: coupling them to terminal alkynes via copper-catalyzed azide-alkyne cycloaddition has been demonstrated by Stenehjem et al.[179] This approach was previously applied to graphitic surfaces in a solution based process.[186] The use of azide termination or as an intermediate connector for SAMs was demonstrated also for hydrogen terminated silicon surfaces in conjunction with diacetylene species or bifunctional short oligoethylene oxide spacers using azide-alkyne cycloaddition in order to attach biomolecules like e.g. glycans for sensing (specific) glycan binding protein absorption.[185,188] In fact, there is a broad application of azides for click-chemistry in surface science.[179,185,186,188]

7.2.1 Structure

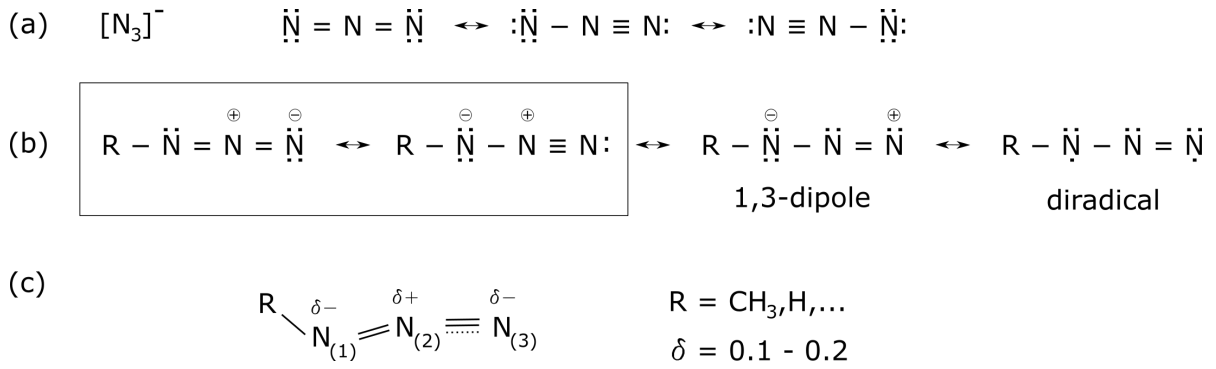

Figure 7.2: The Figure shows N_3^- Lewis-structures in (a) and exemplary for an organic azide in (b) possible resonance structures.[173] A schematic drawing of DFT results in (c) based on Chen et al.[189,190]

Azides form (metallic) salts of the anion N_3^- or of organic compounds of the hydrazoic acid (HN_3), which belong to the group of pseudohalogenes. The nitrogen atoms in the azide group are arranged linearly, and have a polar mesomeric structure.[171] Their corresponding resonance structures are depicted in Figure 7.2. For organic azides the bond length of for example CH_3N_3 are given by 1.47 Å in R-$N_{(1)}$, 1.23 Å in $N_{(1)}$-$N_{(2)}$ and 1.14 Å in $N_{(2)}$-$N_{(3)}$ provided the numbering in Figure 7.2c.[189,191,192] This means that the outer $N_{(2)}$-$N_{(3)}$ bond has the character of a triple bond whereas the inner $N_{(1)}$-$N_{(2)}$ bond is very close to an isolated nitrogen double bond. The structure of the azide chain then implies a pentavalent central nitrogen. Atomic distances between atoms were found to vary only little for different azide species.[189] The charge distribution however depends on the rest R connected to the azide R-$N_{(1)}$.[191] A density functional theory (DFT) calculation yields the Hirshfeld charges Q for particular nitrogen atoms.[193] Chen et al. calculated a rather symmetric charge distribution with a central electron deficient nitrogen provided the azide is bound to carbon which is sketched below in Figure 7.2c.[189] In case

of H-$N_{(1)}$ the nitrogen attracts more negative charge. Because of their polarity azides can react with electron-deficient (electrophiles) and electron-rich compounds (nucleophiles) at the different nitrogens bearing a partial negative and positive charge, respectively.[171] Furthermore, the azide chain is not perfectly linear but shows some bending with bond angles of 173.2° for $\measuredangle N_{(1)}$-$N_{(2)}$-$N_{(3)}$ sketched in Figure 7.2c.[189–191] The angle of course varies again with the organic moiety the azide is attached to.[191]

7.2.2 Spectroscopic characteristics

IR Spectroscopy: Due to its polar nature the azide group exhibits strong IR active vibrations bands. They have been measured and calculated for several azide species. The N_3 group has a symmetric and asymmetric stretching mode experimentally measured to be at ca. 1270 cm^{-1} and 2100 cm^{-1},[194–196] which shows slightly different values depending on the species. In addition, there is a torsion and bending vibration involving the organic rest and therefore being strongly dependent on the chemical compound. For example, the wavenumber of torsion and bending mode in HN_3 and CH_3N_3 are interchanged.[189] Due to the lighter hydrogen atom a torsional mode becomes easier whereas for the heavier CH_3 group the moment of inertia shifts and the bending mode is favoured.[189]

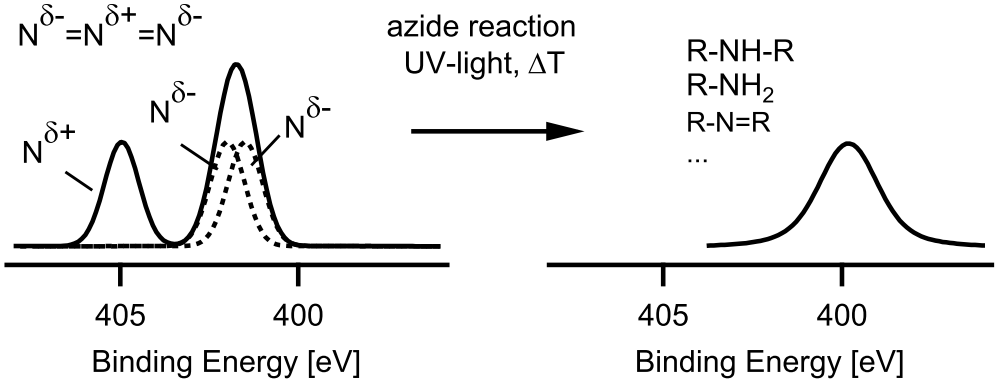

Figure 7.3: The Figure shows a schematic drawing of N 1s core level species from DFT results based on Chen et al.[189] The separation of the lateral nitrogen core level N_3 and N_1 depends on the organic rest group and may not be resolved in an experiment. This picture agrees with various experimental findings.[185]

Photoelectron Spectroscopy: The uneven charge distribution of the mesomeric azide bond significantly affects the N 1s core shell ionization energy which depends on the electrostatic surrounding and therefore on the chemical environment of the atom. N 1s spectra consist of three components and have been measured experimentally and calculated theoretically for several azide species.[189] The organic rest mainly alters the global peak position and the relative energy of the inner nitrogen atom $N_{(1)}$. For example in the case of HN_3 the energetic distance of $N_{(1)}$-$N_{(3)}$ is much larger than for CH_3N_3 because carbon is more electronegative than hydrogen.[189] As a general trend, the energetic ordering seems to be $E_B(N_{(1)}) < E_B(N_{(3)}) < E_B(N_{(2)})$ with the central nitrogen $N_{(2)}$ distinctively separated up to 2-3 eV to higher binding energies.[189] This agrees with a Hirshfeld charge distribution calculation for organic azides in which the central nitrogen

is found to be electron deficient.[189,193] Considering the valence electrons the HOMO/LUMO levels are only situated on the azide group for a small organic rest like e.g. HN_3 and CH_3N_3 otherwise the HOMO is dominated by the organic moiety. Azide orbitals can be identified to have σ bond character at ca. 30 eV ionization energy (from the nitrogen 2s orbitals) and π orbitals at ca. 15 eV (consist of $2p_x$ and $2p_y$ components).[195,197]

7.2.3 Possible Reactions

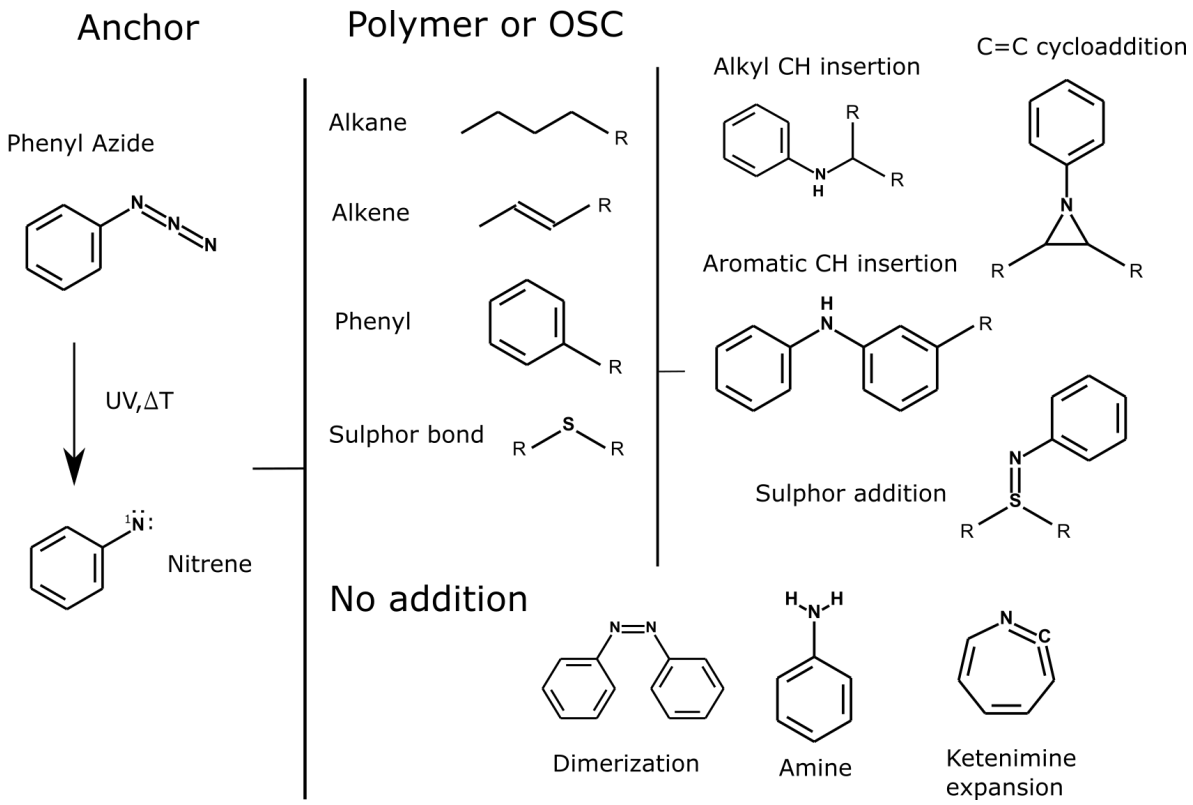

Figure 7.4: The Figure shows a schematic drawing of possible reaction adducts that can occur with a phenyl azide group activated by photolysis embedded in a matrix. There are favourable reactions like CH insertion that leads to an addition of the phenyl anchor and immobilization. But also reactions are possible like amine formation or triplet expansion, which do not form a covalent bond with the OSC host, in which case an immobilization of an attached dopant may not be successful.[183,198]

As it is previously mentioned, organic azides are explosive or at least unstable, meaning a reaction can be triggered by heat or photolysis (UV light) causing rapid azide decomposition accompanied by nitrogen release and possibly by a generation of (intermediate but long-lived) singlet nitrenes.[174] The term singlet refers to electrons in the nitrogen valence shell occupying low-energy orbitals in pairs opposed to triplet with one pair and two electrons with parallel spin.[174] This offers a handy tool to induce immobilization by cross-linking of azide containing molecules after for example processing and mixing. However, it is described in Section 7.2 that there are plenty of possible products arising from a nitrene radical embedded in matrix of suitable organic educts. An insertion into aliphatic C-H-bonds is favorable for the goal of this work but there are other possible undesired reactions involving triplet reactions, aro-

matic insertion, reactions with other functional groups or ketenimine ring expansion, which are sketched in Figure 7.4.[183,199] If properly substituted, nitrenes were found to preferably undergo insertion reactions in a solid state matrix or at very low temperatures.[199,200] Leyva et al. investigated the reaction of nitrene with frozen polycrystalline toluene, which yields insertion adducts of modest yield.[199] However, in solution a photolysis only results in trace amounts of azobenzenes and singlet nitrene rapidly undergoes ring expansion to form dehydroazepine, being captured by nucleophiles like amine and which may result in polymerization giving undefined red tar.[198] Ring expansion is found to be dominating only in solution for non-fluorinated aryl azides,[199,201,202] whereas in thin films or matrices, C-H insertion prevails.[200,203–205] For fluorinated perfluorophenyl azides a significantly higher yield of CH insertion products up to 57% was found in cyclohexane, which were intended for the use as photoaffinity labels.[198,206] The fluorine substitutes withdraw electrons and increase nitrene lifetime.[207] It was further reported that matrix effects and, interestingly, polymer rigidity has an effect on radical lifetimes, which is important for reaction kinetics and spin relaxation.[203] In a polymer matrix, Cai et al. developed bis(perfluorophenyl) azides (bisPFPAs) for cross-linking polystyrene under electron beam exposure or UV-light (250 nm) and demonstrated a high yield of bis-CH insertion of 45% (after purification).[205] Non-inserted phenylazides may be removed by an additional annealing step.[200]

8 N-dopant DMBI

The goal of this work, as explained in Section 7.2, is to attach a reactive functional azide group to an existing molecular dopant without diminishing its reducing or oxidizing capabilities. However, the synthesis or derivatization of p-dopants, having a phenyl azide attached, was not yet successful. The research was mainly focused on trying to modify F4TCNQ and F6TCNNQ. Molecular acceptors are designed to be electron poor, which is why hydrogen is often substituted by fluorine. This renders intermediate synthesis steps prone to radical-nucleophilic aromatic substitution and therefore purification of the desired product is challenging. A successful synthesis route was then found for the n-dopant 1,3-Dimethyl-2-phenyl-2,3-dihydro-1H-benzoimidazole (DMBI). There are several derivatives of DMBI synthesized by S. Benneckendorf from OCI Heidelberg, which are supposed to connect to organic host materials or bind to the surface of electrodes. A phenol group was attached to DMBI in ortho position yielding the non-reactive reference molecule *o*-BnO-DMBI and the desired functional representative 2-(2-((4-azidobenzyl)oxy)phenyl) -1,3-dimethyl-2,3-dihydro-1H -benzoimidazole (*o*-AzBnO-DMBI) by introduction of phenyl azide. Additionally 2-(2-methoxyphenyl) -1,3-dimethyl-2,3-dihydro-1H -benzoimidazole (*o*-MeO-DMBI) with a smaller methoxy group, known to literature, was synthesized for comparison. Instead of the functional azide group a phosphate or thiol group can be considered to form self-assembled monolayers on suitable substrates that can achieve a potential work function reduction or contact doping effects. For this goal the derivative *o*-PBnO-DMBI-I was designed. The synthesis and characterization was not performed by the author and is therefore only briefly mentioned for the sake of completeness and can be found in detail elsewhere.[208]

8.1 Air Stable Dopant DMBI

In principle, the synthesis of stable molecular n-dopants or donors has been elusive for many years due to their inherent problem of being unstable in air. A low ionization energy is required for charge transfer from the dopant HOMO to the host's LUMO, but also allows for easy oxidation causing degradation under ambient conditions. Doping of electron transport layers was formerly realized by alkali metals or injection layers like Lithium Fluoride (LiF) with the drawback of high diffusivity.[209] Larger molecular n-dopants like bis(cyclopentadienyl)cobalt(II) ($CoCp_2$),[210] decamethylcobaltocene (DMC)[211] or bis(terpyridine)ruthenium[212] $[Ru(terpy)_2]^0$ are less mobile but still suffer from stability issues.[44] The key to overcome this problem is to prepare the dopant in a non-doping but stable preliminary stage and activate the precursor via a chemical reaction facilitating the desired dopant or radical which is then able to donate an electron. This was achieved with organometallic dimers rhodocene $[RhCp_2]_2$, and ruthenium(pentamethylcyclopentadienyl)(1,3,5-triethylbenzene), $[Cp^*Ru(TEB)]_2$.[213] These precursors are neutral and comparably stable until processed, then they initiate a reaction with acceptors cleaving the dimer carbon bond and forming monomeric cations and acceptor radical anions.[212] Another class of molecules that can trigger a reaction upon processing is given by salts of cationic dyes like pyronin B and rhodamine B.[214–216] When

co-evaporating Pyronin B chloride, both the leuco and neutral radical form are present in the blended film, whereas the neutral radical form has been identified to cause doping. The contribution of intermediate leuco base in the course of doping was investigated by means of the triphenylmethane dye crystal violet (CV) and its leuco base, leucocrystal violet (LCV), whereas LCV is generated during evaporation of the cationic CV dye.[215] An irreversible electron-transfer can be induced by light or heating which excites LCV to form the radical ions $LCV^{+\bullet}$ together with the negative host and then decay to the non-radical CV cation by hydride transfer.[44] If met with a strong oxidant, LCV can be oxidized directly via hydride transfer with subsequent electron donation.[217] A similar doping mechanism was found for air-stable dopants based on 1,3-Dimethyl-2-phenyl-2,3-dihydro-1H-benzoimidazole (DMBI) developed by Bao et al.[218,219] The dopant DMBI is sufficiently stable in air and increases the conductivity of e.g. PCBM over 4 orders of magnitude, being applicable for n-channel organic thin-film transistors or electron transporting layers of perovskite solar cells.[220,221] Additionally, DMBI can be further derivatized in ortho or para position yielding for example the commonly used 4-(1,3-dimethyl-2,3-dihydro-1H-benzoimidazol-2-yl)phenyl)dimethylamine (N-DMBI).[222–224]

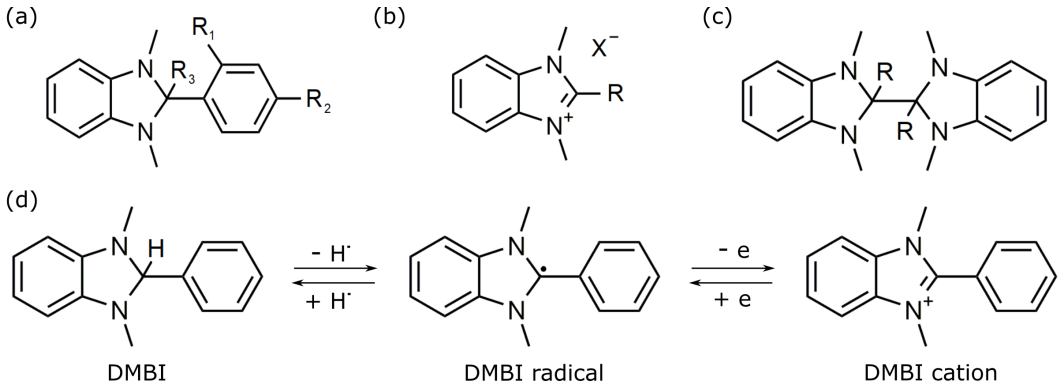

Figure 8.1: Structure of DMBI in (a) with nomenclature according to Naab et al.[225] of rest R_1 in o- (ortho) and R_2 in p- (para) position, for example with R_1 being a methoxy group gives o-MeO-DMBI. The ionic form with counter ion X^- in (b), e.g. DMBI-I with X being iodine. The DMBI dimer in (c) with different possible rest groups. The doping mechanism proposed by Wei et al.[218] depicted in (d) showing hydride and electron transfer. The hydrogen atom is assumed to be accepted by the host in the doping process.[225]

For vacuum processing DMBI is either used as the oxidized salt 1,3-dimethyl-2-phenyl-1H-benzoimidazol-3-ium iodide (DMBI-I) or as neutral benzimidazoline-radical dimers with cyclohexyl $(2\text{-Cyc-DMBI})_2$, ferrocenyl $(2\text{-Fc-DMBI})_2$ and ruthenocenyl $(2\text{-Rc-DMBI})_2$.[226,227] Here, the doping mechanism of DMBI proceeds via a hydride or hydrogen atom transfer similar to LCV, but its details are still under discussion. Recently, Naab et al. investigated the mechanism and reaction rates of DMBI in more detail, suggesting bimolecular hydride or hydrogen-atom transfer which leads to the generation of host radical anions with PCBM.[225] For the DMBI-I salt, the dopant has to be reduced during evaporation splitting from its halogen counter ion and enable n-doping as DMBI radical. This process does not occur in solution processing which is why no doping is found for PCBM mixed with DMBI-I. The DMBI dimers, on the other hand, were found to be effective solution- and vacuum-processable dopants, since a DMBI radical is formed after C-C homolysis ideally reducing the host to its radical anion. By design the doping efficiency of

DMBI dimers therefore should not depend on the C-H bond accepting strength of the host, like it is the case for DMBI-H.[226]

8.2 DMBI Derivatives

The novel derivatives of DMBI have been synthesized by S. Benneckendorf from OCI Heidelberg and are listed below. The dopants are then investigated with a suitable host material in the next section. We do not list detailed information about molecule characterization but refer to Benneckendorf et al.[208] It is to be mentioned that the following materials have been isolated after crystallization from petroleum ether/methanol or DCM/hexanes to yield colorless single crystals suitable for X-ray crystal analyses, which unambiguously prove their structure. Furthermore, it is important to know that DMBI derivatives are quite stable in air but only fairly stable in solution, meaning that after one day at ambient conditions in chloroform, the oxidized species is formed as evidenced by NMR spectroscopy. The dopants were stored under air in a fridge or freezer.

8.2.1 o-AzBnO-DMBI

In general, DMBI dopants can be accessed via a simple condensation reactions as shown in Figure 8.2b. Introduction of a phenylazide is achieved after etherification of salicylaldehyde with 1-azido-4-(bromomethyl)benzene in dimethylformamid (DMF) at room temperature in step 1 of Figure 8.2b. In the second step a condensation reaction with N^1,N^2-dimethylbenzene-1,2-diamine was performed to obtain *o*-AzBnO-DMBI with 47% yield. Its main UV-Vis absorption features are located at $\lambda = 221$ nm, 274 nm, 313 nm, and an additional absorption band appears at 253 nm which can be correlated with the azide. Thermogravimetric analysis (TGA) shows an irreversible mass loss at 117 °C for repeated cycles attributed to loss of nitrogen due to azide pyrolysis. Furthermore, a low melting point (86 °C) and a decomposition temperature at 240 °C were identified.

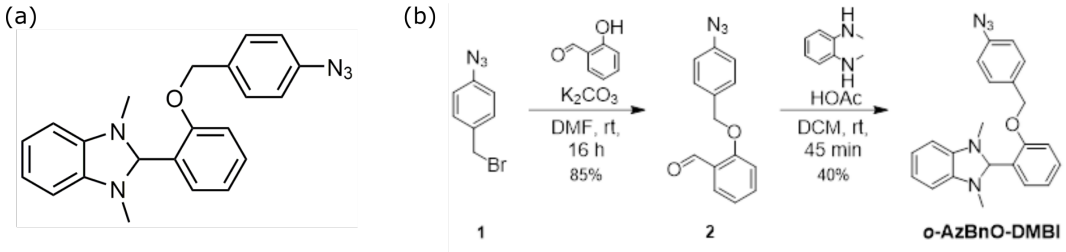

Figure 8.2: Structure of *o*-AzBnO-DMBI in (a) and synthesis scheme in (b). Provided by S. Benneckendorf (Univ. Heidelberg).[208]

8.2.2 o-BnO-DMBI

To compare the immobilizable *o*-AzBnO-DMBI with a similar but not functional dopant, the derivative *o*-BnO-DMBI was synthesized with a phenyl group employing benzyl bromide in the Williamson ether synthesis in step 1 of Figure 8.3. As measured by TGA, *o*-BnO-DMBI has a low

melting point at 108 °C and decomposes at 200 °C. In UV-Vis absorptions spectroscopy *o*-BnO-DMBI exhibits absorption features at λ = 221 nm, 274 nm and 313 nm but not at 254 nm as *o*-AzBnO-DMBI.[208]

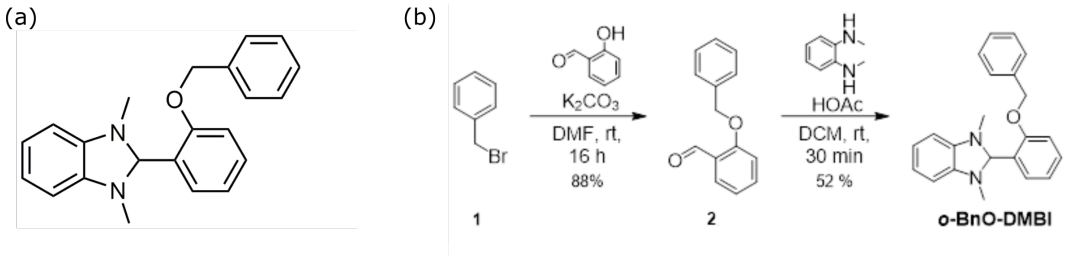

Figure 8.3: Structure of *o*-BnO-DMBI in (a) and synthesis scheme in (b). Provided by S. Benneckendorf (Univ. Heidelberg).[208]

8.2.3 o-MeO-DMBI

The DMBI derivative *o*-MeO-DMBI in Figure 8.4, which is known to literature,[219] only bears an ortho-methoxy group and therefore can be used for comparison to *o*-AzBnO-DMBI or *o*-BnO-DMBI and is investigated in Section 13.4 in terms of stability.

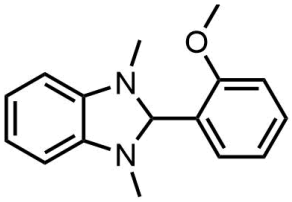

Figure 8.4: Structure of *o*-MeO-DMBI. Provided by S. Benneckendorf (Univ. Heidelberg).[208]

8.2.4 o-PBnO-DMBI

To realize attachment at the surface and achieve contact doping, i.e. charge transfer only at the interface between semiconductor and electrode, the dopant *o*-PBnO-DMBI-I was synthesized. Here, the dopant is existent as an Iodine salt, since synthesis of its neutral form was not successful. As a consequence, *o*-PBnO-DMBI-I has to be reduced with $NaBH_4$ after self assembled mono-layer (SAM) formation on oxidic substrates in order to arrive at the neutral species in the last step of Figure 8.5. For now, this is an intended route to employ DMBI for contact doping but has not been demonstrated yet.

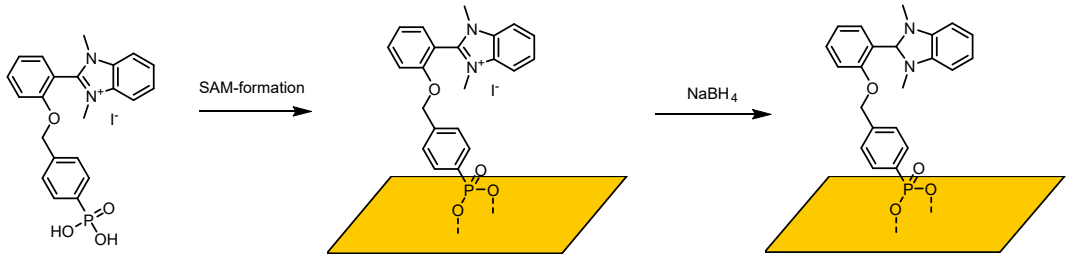

Figure 8.5: Structure of *o*-PBnO-DMBI-I with intended reaction mechanism. Provided by S. Benneckendorf (Univ. Heidelberg).[208]

Part II
Diffusion of Molecular Dopants

9 Doping Properties in Organic Semiconductors

9.1 Electrical Conductivities of P-Doped P3HT

When adding a dopant to P3HT with an electron affinity high enough, ideally below the HOMO level of P3HT, an electron transfer to the dopant becomes possible, generating charged species.[41,49,159] This is the case for dopants such as F4TCNQ and Mo(tfd-CO_2Me)$_3$, where an integer charge transfer is verified.[43,91,121] In this process free charge carriers or holes are created, increasing the carrier concentration and hence the conductivity by several orders of magnitude.[43,228] Details about the doping process are discussed in Section 3.1. Conductivity values of the system, which is studied in this thesis, are listed in Table 9.1 and have been measured by L. Müller (TU Braunschweig).[120,229,230]

Experimental Information: P3HT films were spin-cast from chloroform (CF) or chlorobenze (CB) on borosilicate glass substrates with a roughness down to 2 nm. Gold electrodes were evaporated to a thickness of 60 nm through a shadow mask of finger-like structures. Current measurements were then performed on different channel lengths. Alternatively four-point probe measurements have been performed on doped films without gold contacts.

Results: Since processing parameters, such as solvents, temperature, concentration, annealing, substrate treatment etc. strongly influence the observed electrical properties, a comparison with literature values in Table 9.1 is usually difficult.[229,231–233] For example, if dopant and P3HT are mixed in solution charge transfer causes aggregation and alters the morphology of the thin film.[129] As a consequence, a direct connection between measured sheet resistance and charge carrier concentration is generally not trivial. Although almost all F4TCNQ dopants are charged at moderate doping level, only about 5% F4TCNQ anions contribute to free holes.[43] Together with morphology related effects, electronic trap filling and broadening of the energetic distribution of transport sites by Coulomb potentials can change the carrier mobility at low and moderate doping, which impacts the doping-conductivity relation.[43] However, an increase in conductivity up to values listed in Table 9.1 usually suggests efficient doping. The data in Table 9.1 show that the solvent can affect conductivities of P3HT by influencing the morphology, i.e. the degree of crystallinity. For pure P3HT films the solvent of higher boiling point, i.e. chlorobenze (CB, 131°C) compared to chloroform (CF, 61°C), increases the drying time allowing P3HT chains to align.[229] However, this is different for films doped with F4TCNQ, where agglomerates may already occur in solution.[129,234] Moreover, the dopant Mo(tfd-CO_2Me)$_3$ displays a better conductivity of 49.3 S m^{-1} than F4TCNQ although F4TCNQ is expected to possess a higher electron affinity when blended with P3HT. It is to note that Mo(tfd-CO_2Me)$_3$ is designed in order to increase solubility, which could be the reason for improved conductivity due to a better mixing and higher structural order within the film.[91,130,231] Another possible explanation can result from the generation of free holes. The electron in Mo(tfd-CO_2Me)$_3$ cations is localized around the molybdenum core and, in a naive picture, shielded by the organic moieties

	concentration	solvent	conductivity [S m^{-1}]
P3HT	-	CB	$(2.3 \pm 0.6)\ 10^{-4}$
P3HT	-	CF	$(1.1 \pm 0.4)\ 10^{-4}$
P3HT:F4TCNQ	1:10 MR	CB	0.3 ± 0.1
P3HT:F4TCNQ	1:10 MR	CF	2.9 ± 1
P3HT:Mo(tfd-CO_2Me)$_3$	1:10 MR	CB	49.3 ± 9.7
Literature[91,129,153]			
P3HT:Mo(tfd-CO_2Me)$_3$	10 wt%	CB	ca. 22
P3HT:F4TCNQ	17.5 mol%	CB	1.82 ± 0.22
P3HT:F4TCNQ	17 mol%	CF	8

Table 9.1: Conductivities for P3HT and P3HT doped with F4TCNQ and Mo(tfd-CO_2Me)$_3$. The solvent for processing was either chloroform (CF) or chlorobenze (CB). The concentration is given in molar ratio (MR) or molar fraction (mol%) or weight percentage (wt%). Electrical measurement have been carried out by L. Müller (TU Braunschweig).

of the complex, reducing coulomb interaction allowing the hole to escape.[160] This has been identified to be an important mechanism in the generation of free charge carriers form theoretical considerations.[42] The analysis of electrical properties of doped P3HT films are not carried out by the author and, for further information, the reader is referred to Müller et al.[229,230]

9.2 IR Characteristics of doped P3HT

In order to estimate doping efficiencies, approaches in literature often rely on optical absorption spectra, analysing P3HT polaron and dopant cation contributions under usage of appropriate absorption cross-sections.[231,235–237] Since diffusion during sequential deposition can best be demonstrated with IR spectroscopy as outlined in Section 10.1, important doping characteristics in the Infra-red spectral range are briefly mentioned in the following.

Experimental Information: Thin films of P3HT and Mo(tfd-CO_2Me)$_3$ were spin-cast from a solution of chlorobenze on cut intrinsic silicon wafers, which were solvent-cleaned in an ultrasonic bath. The substrate's backside was cleaned after spin-coating.

Results: A typical IR-transmission spectrum of P3HT and Mo(tfd-CO_2Me)$_3$ is shown in Figure 9.1, measured by V. Sivanesan (Univ. Heidelberg). Pristine P3HT exhibit a series of vibration modes around 1500 and 3000 cm^{-1} that are mainly assigned to stretching modes of the thiophene ring and C-H vibrations in the hexyl side chain.[238,239] For doped P3HT, a broad electronic excitation between 3000 cm^{-1} and 5000 cm^{-1} emerges, which can be assigned to the polaronic optical transition P1, described in Section 2.4.[32] The P1 polaron absorption is expected to feature a 1-dimensional intra-chain delocalization.[33] Below 1500 cm^{-1} IR-active vibrations (IRAVs) modes are present for doped P3HT, which have a large oscillator strength.[238] Moreover, for (undoped) rr-P3HT a 2-dimensional DP1 polaron, that is defined by inter-chain delocalization, was measured between 500 and 1500 cm^{-1} and assumed to interfere or superimpose with IRAV modes.[32] For the dopant F4TCNQ, infra-red absorption studies are used in literature to identify the degree of charge transfer in P3HT. This is possible, since the C≡N stretching vibration of charged F4TCNQ is red-shifted compared to neutral F4TCNQ at 2228 cm^{-1}.[240] Furthermore, the red-shift was shown to linearly depend on the charge located on F4TCNQ

molecules, thereby offering a distinction between integer or partial charge transfer.[241–244] In a study of Méndez et al., F4TCNQ was demonstrated to undergo integer charge transfer with P3HT, but the non-fluorinated and weaker acceptor TCNQ only a partial charge transfer causing lower conductivities.[49] In contrast, the C=O stretching vibration of Mo(tfd-CO_2Me)$_3$ at 1737 cm^{-1} does not shift at a significant level. Thus, given the high doping efficiency of Mo(tfd-CO_2Me)$_3$, a reasonable conclusions can not be made by evaluating the stretching mode of Mo(tfd-CO_2Me)$_3$. As a possible explanation, the additional charge may not be located at the C=O moieties but on the metal centre of the dopant.[160] For a detailed analysis and peak fitting of the C=O fano line shape, the reader is referred to the master thesis of V. Sivanesan (Univ. Heidelberg).[101]

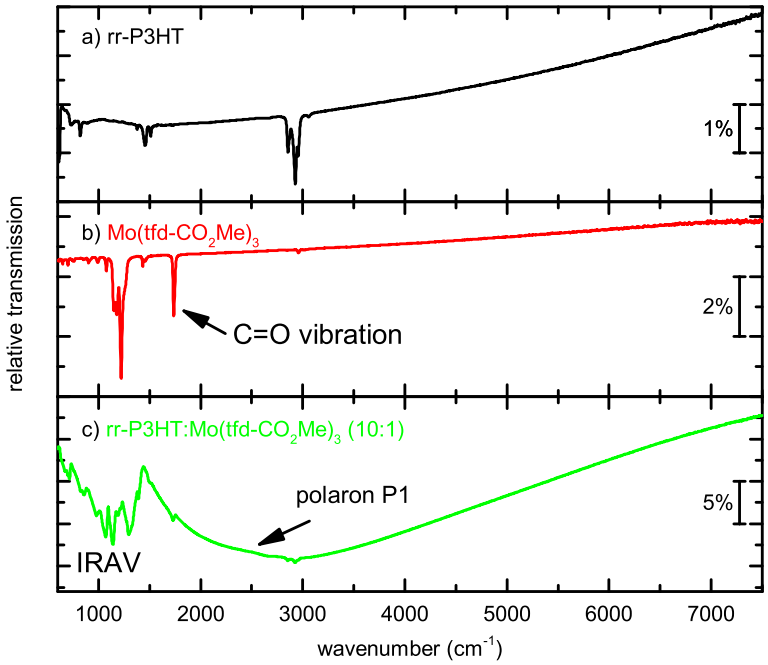

Figure 9.1: IR transmission spectra of pristine rr-P3HT in (a), pure Mo(tfd-CO_2Me)$_3$ in (b) and the doped P3HT film in (c) at a molar ration of 10:1 (P3HT:Mo(tfd-CO_2Me)$_3$). The broad polaronic optical transition P1 at 3000 cm^{-1} in (c) is a clear indicator of doping. Figure is adapted from Reiser et al.[245]

9.3 Fermi Level Shift and Charge-Transfer in P3HT

9.3.1 Photoemission of P3HT and MoCOMe

As a first step photoelectron spectra of pure P3HT and Mo(tfd-CO_2Me)$_3$ were recorded to study important core-level peak characteristics and energy levels of pure materials.

Experimental Information: Pure rr-P3HT and Mo(tfd-CO_2Me)$_3$ films were spin-cast from solution at 600 rpm and 1200 rpm, respectively. The materials were dissolved in chlorobenze at 7.5 g L^{-1} and stirred over night at 50 °C. Solvent-cleaned cut n-type silicon wafers were chosen as substrate for P3HT and ITO for Mo(tfd-CO_2Me)$_3$.

Analysis: XPS and UPS spectra of pristine P3HT and Mo(tfd-CO_2Me)$_3$ are presented in Figure 9.2. For pure P3HT there is obviously no F 1s emission detectable in Figure 9.2 within the limit of noise. For Mo(tfd-CO_2Me)$_3$, however, the F 1s emission in Figure 9.2f, l is the strongest XPS line and can be used to determine the dopant concentration in Section 10.2. Both P3HT and Mo(tfd-CO_2Me)$_3$ contain sulphur: The S $2p_{3/2}$ peak for Mo(tfd-CO_2Me)$_3$ in Figure 9.2e is located at lower binding energies of about 163 eV. The S $2p_{3/2}$ emission of P3HT is measured at 164 eV in Figure 9.2b agreeing with carbon-sulphur bonds in literature. The difference in energy may very well be explained by the different chemical binding conditions, since sulphur within the tfd-moieties of Mo(tfd-CO_2Me)$_3$ is involved in metal-complex formation. There is a single (broader) C 1s peak found for P3HT which is composed of the different carbon-carbon or carbon-hydrogen and carbon-sulphur bonds plus a shake-up satellite at ca. 287 eV. The individual components differ only slightly in binding energy but give rise to an asymmetric peak shape. A detailed peak component fit of the C 1s line based on DFT calculations can be found in literature[246,247] and is not carried out here. The situation is however very different for Mo(tfd-CO_2Me)$_3$, in which more electro-negative elements are bound to carbon such as oxygen and fluorine. In Figure 9.2d the emission at highest binding energy (292.5 eV) is assigned to CF_3 and the central component at 289 eV to carbon in the methoxy group. The main line at 285 eV shows a shoulder towards higher binding energies, indicating that two constituents are involved. The carbon not yet assigned is bound to sulphur in the tfd-group and in the methyl group, which occur at a ratio of 2:1 according to Figure 6.1. Therefore, the larger component at 285 eV is attributed to carbon-sulphur bonds and the methyl group to the shoulder at 286.5 eV, connected by an ether bond. The Mo 3d spectrum in Figure 9.2j overlaps with the S 2s emission, which is why a peak fitting has to be carried out to separate the Mo $3d_{5/2}$ from the S 2s line. Additionally, a small satellite structure is suspected, which is shifted about 2 eV to higher binding energies. The position of the Mo $3d_{5/2}$ line at ca. 230 eV lies in the middle of the extreme 6+ and 0 oxidation states and has been previously measured for Mo(tfd)$_3$ to be between Mo(III) and Mo(IV) coinciding with the binding energies of MoS_2 with an oxidation state of 4+.[121,248,249] The O 1s emission of Mo(tfd-CO_2Me)$_3$ shows two components at 533.5 eV from the methoxy group and at 531.7 eV from the carbonyl part. The ASF corrected XPS peak intensities match the expected element composition, which are derived from the structural formula in Figure 6.1. If they had not agree with the chemical structure, this could have indicated that the materials decompose during deposition or have major contaminations. The integrated intensities are given in Table Appendix B.2. Their corresponding ionization energy (IE) and work function can be deduced from UPS measurements of occupied states in the valence region in Figure 9.2g-i.

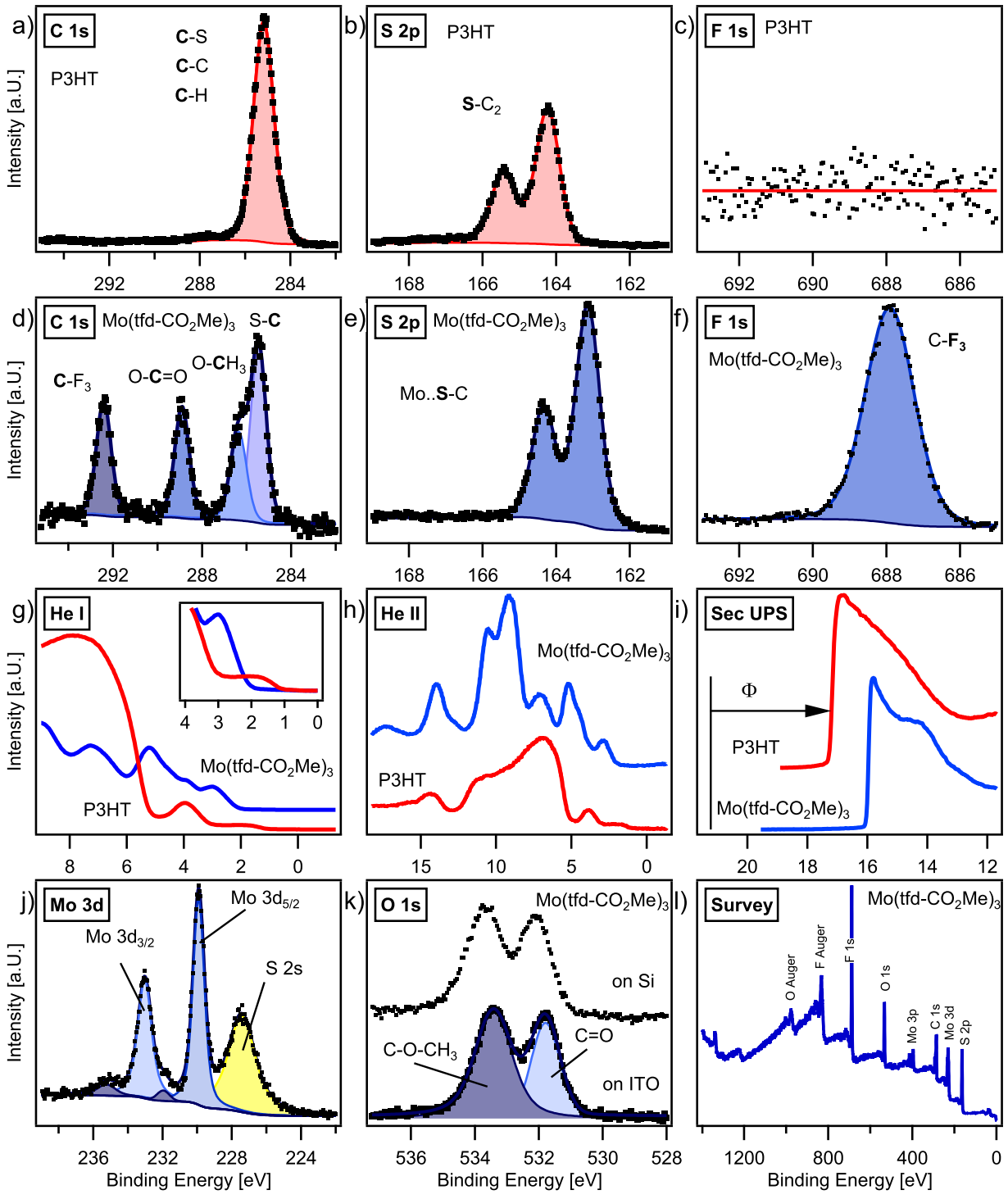

Figure 9.2: The figure shows C 1s, S 2p and F 1s core-level spectra of pure P3HT in (a)-(c) and the dopant Mo(tfd-CO_2Me)$_3$ in (d)-(f). The intensity scale for the S 2p emission in (b) and (c) is identical, but differs for (a),(b) and (c),(f). UPS measurements are given in (g)-(i) for P3HT in red and for Mo(tfd-CO_2Me)$_3$ in blue. Additionally the Mo 3d, O 1s and survey spectra of Mo(tfd-CO_2Me)$_3$ are presented in (j),(k),(l). For all core-level spectra, a peak fit is added to the graph including labels of their component assignment. Common Voigt-profiles are used for fitting and are represented with varying colour shades.

The UPS spectra of P3HT are studied in literature and feature a peak centred at around 4 eV that is attributed to the localised π-state of the thiophene units.[145] The delocalized π-states appear at lower binding energies and form a flat plateau with a HOMO at around 1 eV depicted in the inset of Figure 9.2g. The intense emissions in the region between 5 and 10 eV contain contributions from both σ- and π-bands but are dominated from σ states of the side chains.[145] As previously mentioned, spectral details and the HOMO position depend on morphology, conjugation length as well as the processing conditions.[250] We also find a strong dependence of the measured Fermi level position on the choice of substrate, which is discussed in connection with doping in the next section. Moreover, radiation induced changes are possible for P3HT under illumination.[251] Furthermore it has to be mentioned, that the thickness of P3HT films was measured with a profilometer to be around 50 nm which causes charging during UPS and (to a much lesser degree) in XPS. Consequently UPS is recorded under UV-illumination, which by itself affects the energy position of P3HT, leading to a considerable uncertainty in the determined HOMO onset. Nonetheless, the HOMO position of P3HT and Mo(tfd-CO_2Me)$_3$ have been estimated by linear extrapolation of spectral onset and are listed in Table 9.2, agreeing with values reported in literature within the systematic error margin of 0.2 - 0.5 eV for P3HT. The problems and estimation of charging by photo-excitation are discussed in more detail in Section 9.3 and 14. For Mo(tfd-CO_2Me)$_3$ a work function of 5 - 5.2 eV is found, which in turn means that Mo(tfd-CO_2Me)$_3$ is strongly n-type with a HOMO binding energy of ca. 2.1 eV if a band gap of ca. 2.2 eV is assumed.[91] Due to its high electron affinity, the dopant acts as an acceptor with electrons from either substrate or contaminations. A different Fermi level position of Mo(tfd-CO_2Me)$_3$ is found when processed on ITO or silicon, but a common IE of ca. 7.3 eV is measured.

Material	Φ [eV]	HOMO [eV]	F 1s [eV]	Mo $3d_{5/2}$ [eV]	IP [eV]
P3HT on Si	ca. 3.75	ca. 1	-	-	ca. 4.75
Mo(tfd-CO_2Me)$_3$ on ITO	5.2	2.15	687.85	229.9	7.3
Mo(tfd-CO_2Me)$_3$ on Si	4.9	2.4	688.2	230.1	7.3
Literature[91]					
Mo(tfd-CO_2Me)$_3$ on Au	5.2	2	-	-	7.2

Table 9.2: Energy levels determined from the spectra shown in Figure 9.2. The HOMO onset and secondary electron cutoff have been estimated from linear extrapolation. The ionization potential (IP) is given by the sum of work function Φ and HOMO level BE. Values reported in literature are given below. The precise energy levels of P3HT depend on various parameters and will be discussed in the next Section.

9.3.2 Substrate Characterization

In this study cut silicon wafers are used as substrates since they provide a smooth surface and can be purchased with controlled conductivity and surface treatment. Anticipating results from the next section, differently doped silicon wafers are chosen to investigate their influence of substrate properties on solution-processed organic thin films. In a first step, a set of purchased silicon wafers is characterized by XPS and UPS.

Experimental Information: A selection of silicon wafers was purchased from Sil'tronix Silicon Technologies (France) and shipped in a sealed container. All wafers had (100)-orientation and a native oxide layer as termination. The doping conditions were chosen from strong p- to n-doped silicon with a conductivity specified from the retailer in Table 9.3. The wafer were split with a glass cutter and broken by hand to obtain about 1-2 cm^2 large sample substrates. They were subsequently cleaned by acetone and isopropanol in a heated ultrasonic bath for 20 min, as it is the general cleaning procedure done before organic layer deposition.

Results: As a first step, silicon substrates were measured by a four-point probe sensing method to compare the sheet resistivity with resistivity values provided from the retailer. The results of this measurement is listed in Table 9.3. Within the limits of accuracy one finds a reasonably good agreement. From the resistivity values in Table 9.3, charge carrier concentration and Fermi level position can be estimated using the textbook formalism with semi-empirical corrections as described in Section 3.2. To characterize the substrate, XPS and UPS measurements

Sample	Polished	Thickness [μm]	Nom. resistivity [Ω cm]	Meas. resistivity [Ω cm]
p+	2s	525	0.0015	0.0012
p	1s	475	2	1.29
i	2s	1000	7000	6789
n	2s	375	4	4.25
n'	1s	675	0.9	0.77
n+	1s	650	0.013	0.017
n++	2s	265	0.003	0.0054

Table 9.3: Four point probe resistivity measurements of purchased silicon substrates in comparison to the nominal resistivity provided from the retailer. The nominal wafer thickness is used to calculate the resistivity from four point probe currents. The wafers were either one-side (1s) or two-side polished (2s) but all experiments were measured on the smooth surface. The trivial names i,n,p, etc. are self-chosen in this context for labelling the wafer types.

were done on multiple samples of each wafer class. For simplicity the silicon wafers are referred to as their doping type using the self-chosen trivial names in Table 9.3 for categorization. The recorded XPS and UPS spectra are presented in Figure 9.3 with a color-map from blue (n-type) to red (p-type). The Si 2p line in Figure 9.3b shows the Si 2p doublet with closely spaced spin-orbit components at around 99 eV and a component at ca. 103 eV from SiO_x of the native oxide layer. The oxygen at the surface leads to a strong O 1s emission at ca. 533 eV and an Auger line at around 900 eV in Figure 9.3a, e. As expected, a systematic shift to higher binding energies can be observed for both the O 1s and the S 2p level, when going from p-doped to n-doped silicon.

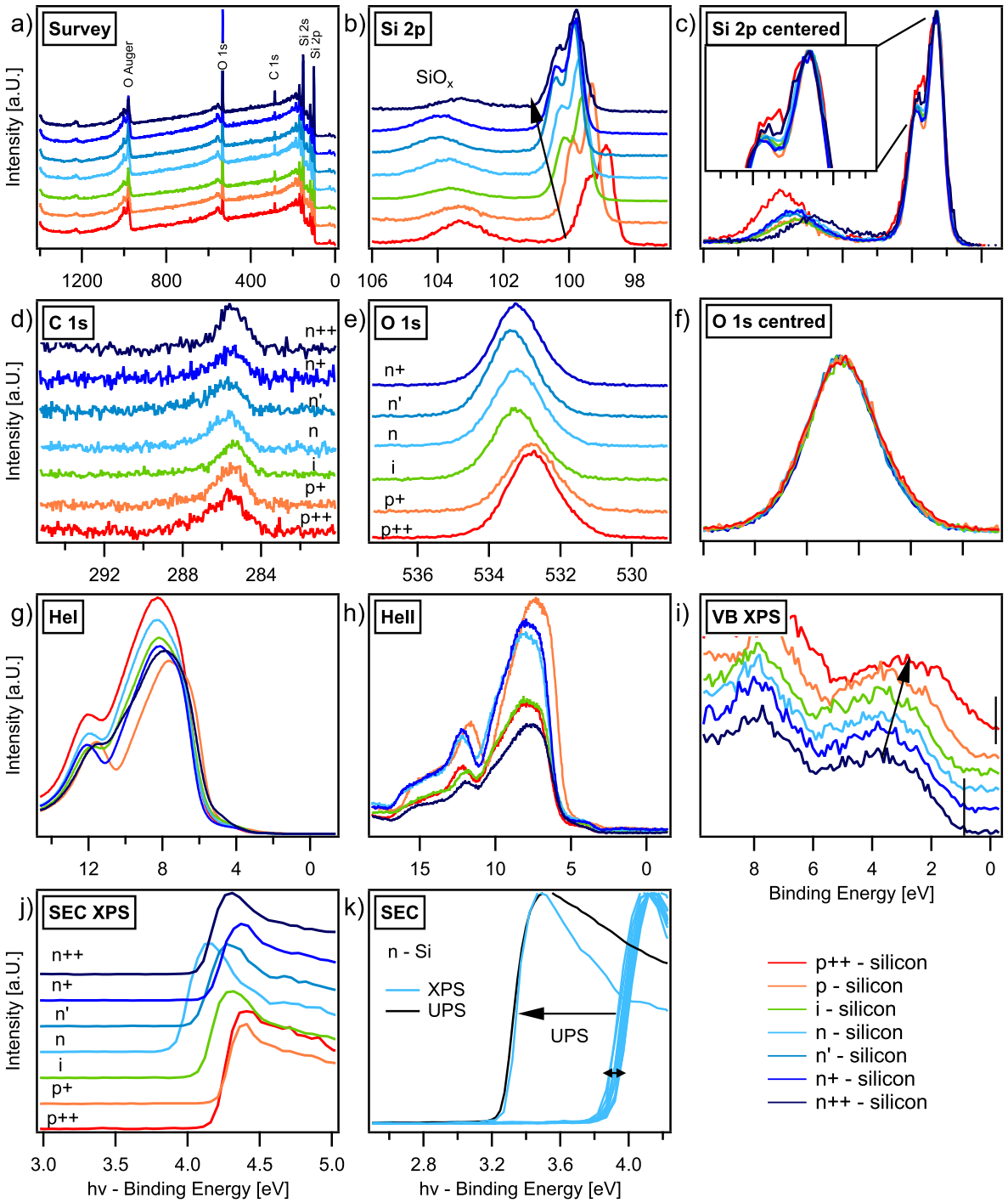

Figure 9.3: XPS and UPS spectra for differently doped silicon substrates from Table 9.3. The colour-legend is given for all figures at the bottom. The labels are trivial names to identify the wafer type. Si 2p and O 1s emission is given in (b) and (e) showing Fermi level shift from p- to n-doped silicon. Their normalized and centred spectra are given in (c) and (f), respectively. Carbon contaminations are plotted in (d). UPS spectra in (g) and (h) overemphasize contaminations. A reliable measurement of the valence region is plotted in (i) using XPS. Representative XPS secondary electron edges (SEC) are listed in (j), whereas the UPS SEC shows an irreversible shift to higher binding energies compared to XPS, which is not fully understood.

Upon doping the Fermi level moves to the valence or conduction band for either n- or p-doping. This can be verified by measuring the valence region with XPS in Figure 9.3i, where the total shift of about 1 eV is found when tracking the valence band maximum (VBM). For UPS spectra in Figure 9.3g, h we mainly measure contaminations, since the carbon valence electron in the 2p-orbitals feature a high cross-section for HeI (21.22 eV) excitation energy. The presence of carbon contaminations can also be confirmed by the C 1s spectra of Figure 9.3d, which are similar for all substrate types. However, the peak intensities of the Si 2p and O 1s emission varies for different spots on the substrate, suggesting inhomogeneous coverage of contaminations or the silicon's native oxygen layer. Therefore, the normalized and centred Si 2p and O 1s emission is plotted in Figure 9.3e, f which exhibit a common peak shape for the O 1s line but deviations for the Si 2p peak at highest doping levels. For n++ and p+ silicon substrates the visibility of spin-orbit splitting of the 2p state seems to be reduced and the component from SiO_x is shifted with respect to the Si $2p_{3/2}$ peak. This observation is not further investigated as it is not topic of this work. However, measurements of the secondary electron cut-off (SEC) with UPS show a considerable discrepancy in comparison to those measured with XPS in Figure 9.3k. The work function determined from UPS is likely not trustworthy since the UPS measurement seems to reduce the work function as derived from XPS in Figure 9.3k. This effect is not fully understood but is likely caused by the oxide layer. A similar effect was observed for oxide substrates in literature before.[252]

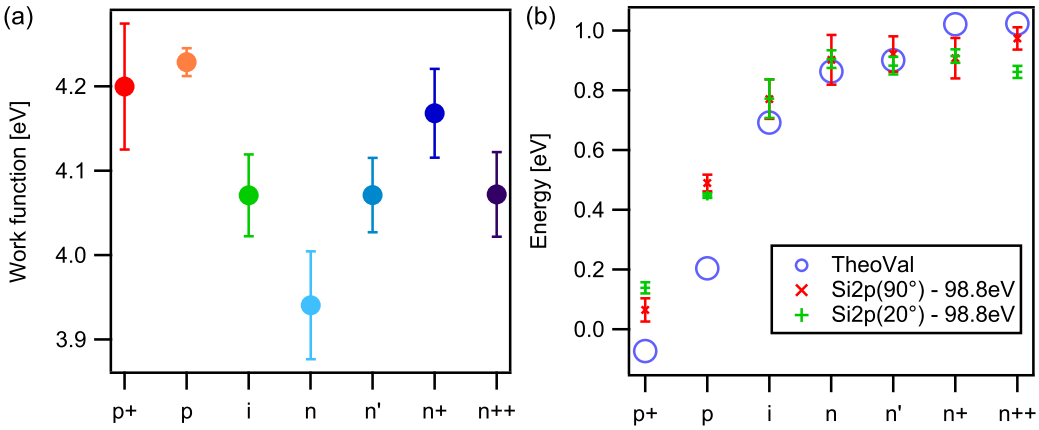

Figure 9.4: Mean values of measured XPS work function in (a) and Si 2p maximum in (b) for two different take-off angles. Standard deviation of the data set from multiple samples is given as error-bars. Theoretical estimations based on conductivities according to Section 3.2 are plotted as blue circles for comparison.

Consequently, work function values are deduced from XPS in Figure 9.4a as they are likely more reliable. Moreover, the work function derived from XPS does not depend on the doping level as it is observed for the silicon valence band and core-level lines. Since the position of the SEC varies for each sample, multiple samples were measured and the mean value including standard deviation are plotted in Figure 9.4a. Again, there is no systematic dependence of the doping-induced Fermi level shift on the work function in Figure 9.4a but a rather random distribution with n-Si having the lowest work function. As a conclusion, the work function is mostly determined by the oxide layer or carbon contamination on the surface. Even for atomically clean silicon a non-trivial dependence on the doping level is found in literature.[67] This already complicates the intended experimental study of energy alignment, since the work

function is not properly controlled and does not change in accordance with the substrate's Fermi level position. At least, the measured Fermi level shift can be nicely compared to calculated values in Figure 9.4b. For this purpose, the Si $2p_{3/2}$ peak maximum is extracted from Figure 9.3b and shifted by 98.8 eV to match the valence band position. The Si $2p_{3/2}$ peak can be determined more accurately, and the distance of 98.8 eV between the Si 2p level and VBM is reported in literature.[253,254] This may not hold for very high doping concentrations, but serves as an approximate reference point for comparison. Additionally, the Si 2p emission was recorded under a take-off angle of 20° in order be more surface sensitive. Within this measurement one can not find evidence for a difference in Fermi level position between the two take-off angles. In total, a nice overall agreement is found between calculated Fermi level position and measured Si 2p shifts. Deviations at high doping concentrations can also be ascribed to approximations made in calculating the density of states, which does not take into account the formation of doping-induced sub-bands in case of degenerate silicon. Additionally, the Si 2p position is compared to the shift of the O 1s level and the SiO_x satellite near the Si 2p main line in Figure Appendix B.4. The position of the O 1s emission roughly follows the trend of the Fermi level shift derived from the Si 2p line. However, there are deviations at higher doping levels which could be due a variation of the properties of the native oxide layer. Since this observation is not a main focus of this work, it is not further investigated. As a side remark, a former p-doped substrate was identified to be in-fact n-doped based on the position of its Si 2p level and wrongly labelled by the manufacturer. This was further proven by with Hall-measurements of the charge carrier type.

9.3.3 Photoemission of P3HT doped with MoCOMe

The photoemission study of doped P3HT, presented here, primarily serves to identify spectral changes originating from doping, to evaluate charge transfer and Fermi level shifts. To this end, a systematic parameter variation of doping concentration of both P3HT film and of the underlying silicon substrate was conducted. The idea to study energy level alignment at the interface of doped polymers on a fundamental level, could not be achieved, since substrate preparation, sample to sample variations during solution-processing and photoelectron-induced charging impeded drawing decisive conclusions about the energetic conditions at the Si-P3HT interface. Nonetheless the observations are stated in the following together with a brief discussion of errors and possible improvements of the experiment. The main spectral features emerging upon doping of P3HT agree with those reported in literature.[91] The measurements serve as a starting point for further experiments on diffusion in sequentially doped P3HT films discussed in Section 10.2.

Fermi Level Position in P3HT

In order to support electrical and optical measurements done on the system P3HT:Mo(tfd-$CO_2Me)_3$, processing parameters are chosen to match the same P3HT films used for these investigations with silicon substrates characterized as described in the previous section. However, the layer thickness was not ideal for photoelectron spectroscopy measurements since the undoped P3HT films were not conductive enough and photoelectron-induced charging occurred.

Experimental Information: The materials rr-P3HT and Mo(tfd-$CO_2Me)_3$ are stored and their sample weight is determined in air. They were separately dissolved in chlorobenze in a nitrogen glovebox. The respective solutions were stirred overnight at 50°C and mixed several hour before spin-coating with a solution of 7.5 g L^{-1} at 600 rpm for 60 s. The cut silicon wafers from the previous section were cut and cleaned in an ultrasonic bath with isopropanol and acetone for 20 min.

Results: The series of doped P3HT with a varying doping concentration prepared in solution, ranging from 1:100 to 1:5 molar ratio of Mo(tfd-$CO_2Me)_3$:P3HT, is shown in Figure 9.5. For increasing doping concentration, dopant related core-level lines start to become visible such as the F 1s emission in Figure 9.5c and the corresponding carbon emission component at 289 eV in Figure 9.5c. Also the oxygen and molybdenum spectra of Mo(tfd-$CO_2Me)_3$ can be identified for higher doping concentrations in Figure 9.5a, j, k. For the sulphur S 2p emission in Figure 9.5g, and the same spectra centered at the main S $2p_{3/2}$ line in 9.5h, a growth in overall peak intensity is observed with doping, which agrees with a higher sulphur content in Mo(tfd-$CO_2Me)_3$ versus P3HT. But most importantly, a distinct shoulder at 163 eV emerges with increasing dopant concentration, which is correlated to charged dopants, i.e. radical Mo(tfd-$CO_2Me)_3$ anions that have accepted an electron from P3HT. Charged species of Mo(tfd-$CO_2Me)_3$ may also be identified when the peak components of the Mo 3d emission in Figure 9.5k are explored. Assuming integer charge transfer, a more detailed analysis on doping ratios can be performed on the basis of the S 2p and Mo 3d line, which is postponed to the next section. Moreover, a doping related rise in carrier concentrations leads to a Fermi level shift observed for both XPS and UPS spectra in Figure 9.5. As expected for p-doping, the Fermi level moves by almost 1 eV towards the HOMO position of P3HT.

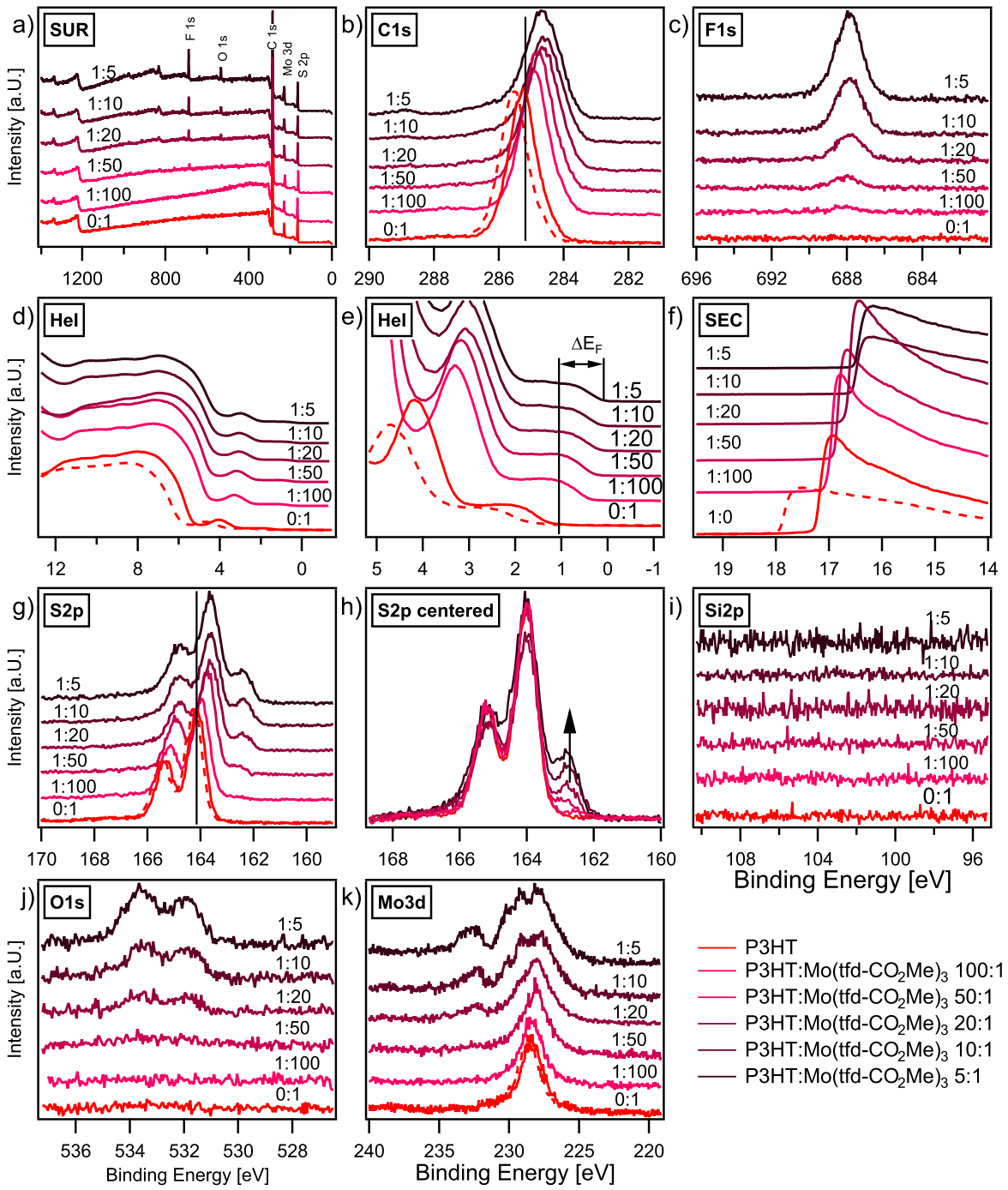

Figure 9.5: P3HT doped with Mo(tfd-CO_2Me)$_3$ at varying concentration. The molar ratio of dopants to P3HT monomers is given at each graph and in the legend (right corner). UPS spectra are shown in (d)-(f). The S 2p core level is centered in (h) to highlight changes in shape. UPS measurements of pure P3HT heavily suffer from charging effects, and are performed under UV illumination to increase conductivity by photo-generated charge carriers. For comparison, the dashed line in (d)-(f) is measured without UV-lamp. Also the C 1s level in XPS (b) seems to be affected by charging to a lesser degree. Fermi level shift due to doping amounts to almost 1 eV.

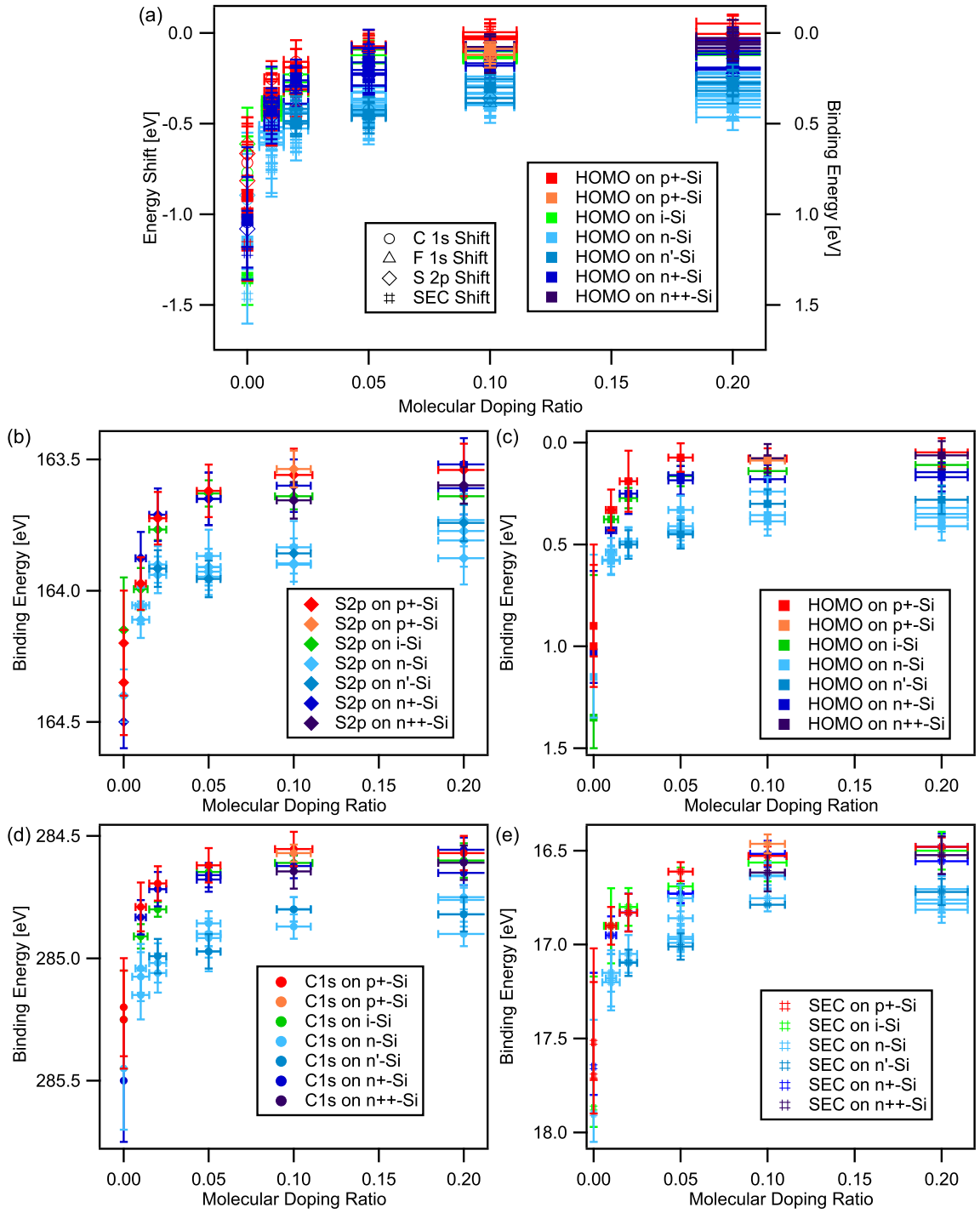

Figure 9.6: Binding energies extracted from the spectra in Figure 9.5 for differently doped silicon substrates (b)-(c). HOMO onset/SEC for pure P3HT are determined for spectra recorded under UV-illumination which still holds a uncompensated shift of ca. -0.3 eV in (c),(d). Errorbars are estimated based on statistical variations for multiple samples plus a systematic error-estimation for charge corrections. The error for preparing the desired doping concentration in solution is assumed to be 15%. The result in (b)-(e) are overlayed in (a) to highlight the Fermi level shift visible in both UPS and core-level spectra resulting from P3HT. The relative offset has been adjusted to roughly match the HOMO position at high doping concentration.

This is accompanied by a shift of core-level emission lines towards lower binding energies and an increase in work function, determined by the secondary electron cut-off (SEC) in Figure 9.5f. In order to investigate the Fermi level position as a function of doping concentration in more detail, the HOMO onset and the SEC are determined by linear extrapolation to zero intensity around the point of highest slope. Additionally, the C 1s and S $2p_{3/2}$ peak maximum position is approximated by a Gaussian fit to track Fermi level shifts. This has been carried out for all doping concentrations and available silicon substrates and is plotted in Figure 9.6b-e. It is noteworthy that at highest doping concentration the S $2p_{3/2}$ and, to a smaller degree also the C 1s contain contributions of the neutral dopant, slightly changing the peak shape/composition and therefore the position of its maximum. A large systematic error enters for UPS measurements of pure P3HT due to charging effects from photo-excitation. If the resistivity is too high, remaining positive charges from photoelectrons leaving the sample can not be fully compensated and build up an attractive surface potential. Photoelectrons then appear to have less kinetic energy and emission lines are shifted to higher binding energies, which can be confused with a Fermi level shift. The layer thickness of P3HT thin films was measured with a profilometer to be about 50 nm and slightly thinner for doped films of about 45 nm. The film thickness was chosen to match samples used for optical and electrical characterization, but is too large for UPS measurements in case of undoped P3HT. On the other hand, if it is chosen to be too small, the influence of the substrate is dominating the Fermi level position of the P3HT adlayer and material properties of bulk P3HT can not be correctly determined. To compensate for charging, a UV-LED diode was mounted on a transparent window, illuminating the sample during UPS and XPS measurements. The goal was to photo-generate charge carriers to improve the conductivity in P3HT to reduce positive surface charging from the photoemission process. This technique has been applied previously in XPS studies to measure band alignment of organic interfaces.[255] As described before, the UPS spectrum in Figure 9.5e and even the C 1s core-level emission shifts to lower binding energies under UV-illumination of 364 nm (solid versus dashed line in Figure 9.5b, e). To verify that indeed charging is causing the shift, XPS and UPS spectra can be alternately recorded with combinations of illumination from XPS (1486.7 eV), UPS (21.22 eV) and UV-LED (3.4 eV), revealing that the C 1s level moves to higher binding energies if the UPS lamp is turned on but shifts back if the UV-LED is switched on (exemplified in Figure 14.1). From this test, one can try to estimate charging effects and conclude that the UV-LED is largely compensating charging for XPS but in case of UPS, a remaining shift of about 0.2-0.4 eV remains when comparing to the XPS C 1s position. Consequently, the UPS spectra of pure P3HT were recorded using the UV-LED and fitted values for HOMO-level and SEC may still hold a charging-induced shift of -0.3 eV in Figure 9.5c, e. Moreover, it is known that UV-light may also permanently affect the band position in organic materials, which is difficult to account for.[251] This means that the energy values extracted for pure P3HT are facing large systematic errors of at least 0.35 eV for UPS and 0.2 eV for XPS which means that the HOMO BE can not be more precisely determined between 0.8 - 1.3 eV and the work function around 3.6 - 4.1 eV. Since all samples are solution-processed, a shot-to-shot variation and even variations within different positions of one sample give rise to statistical error in energy levels of around 0.2 eV. For doped samples charging from UPS measurement does not occur and the Fermi level moves to BE values of 0.1 - 0.2 eV close to the HOMO position. Even with a poorly defined HOMO-level for undoped P3HT, this amounts to a Fermi level shift of 0.5 - 1 eV in total. In Figure 9.6a the core-level and work function shifts are overlaid with the HOMO position via an arbitrary offset. Both follow the same trend as a function of concentration, indicating a doping induced Fermi level shift.

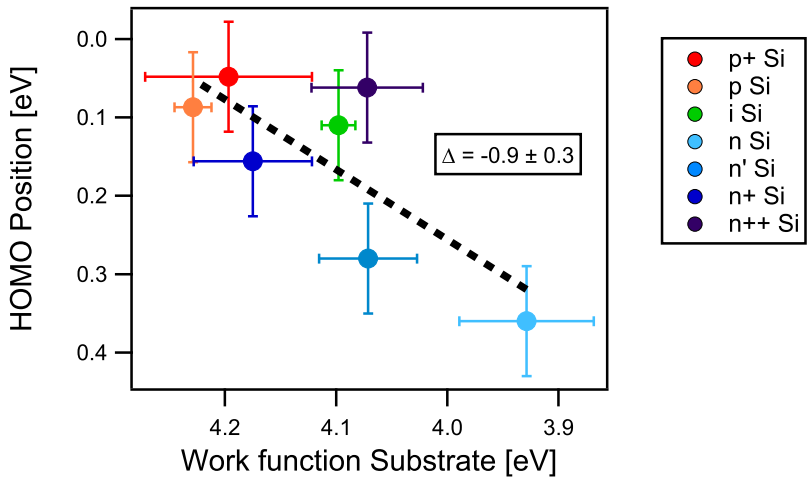

Figure 9.7: The determined HOMO onset for highest doping concentration from Figure 9.6 plotted versus the work function of the silicon substrate. The doping type of the substrate is encoded by color on the right-hand side.

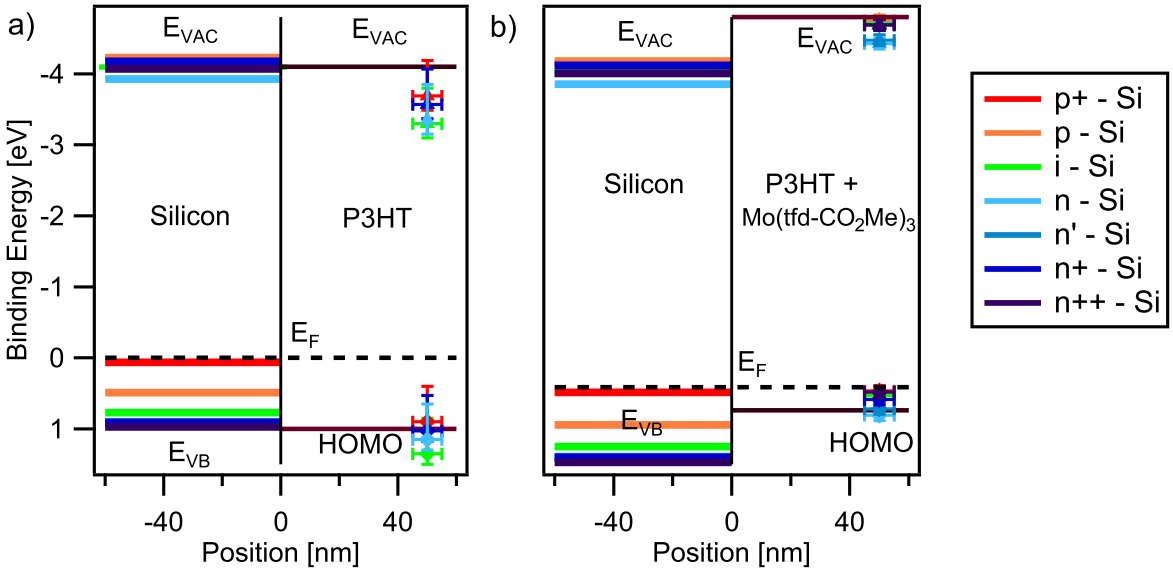

Figure 9.8: A simplified band diagram of P3HT in (a) and doped P3HT in (b) on silicon with aligned Fermi level. Only the energy level position of P3HT at 50 nm is measured. The brown line gives an approximate level of P3HT based on literature values.[91,148,149] Note the large error in (a) due to charging effects. The common Fermi level is marked by a dashed line.

The idea of this experiment was to change doping and Fermi level position of the substrate to find a direct dependence of the Fermi level in P3HT on the substrate's energetic conditions, which then disappears at high $Mo(tfd\text{-}CO_2Me)_3$ content due to a reduced space charge region and screening from charge carriers. However, this could not be demonstrated as undoped P3HT could not be measured without large systematic and statistical errors and the substrate's work function is not controlled by its doping level. Surprisingly there seems to be a statistically relevant difference of the HOMO-level for highest doping concentration between n-Si and quasi-

intrinsic or strongly doped silicon as substrate. This does not correlate with the hole or electron density in silicon but with the work function measured in Section 9.4. The HOMO position of strongly doped P3HT is plotted versus the silicon substrate's work function in Figure 9.7 yielding a slope close to one. A band diagram based on the UPS and XPS work function measurements is drawn in Figure 9.8. Here, bands in silicon are drawn as straight lines although there is no information on the conditions at the silicon surface. In fact, for intrinsic or low doped n-Si, a considerable band bending in silicon could be possible. However, a measurement of the Si 2p beneath the P3HT film, which could have given information on the Fermi level in silicon, was not possible in Figure 9.5i. For highly doped P3HT the band setup in Figure 9.8 suggest a downward band bending towards n-silicon in case of doped P3HT.

Charge Transfer of Mo(tfd-CO_2Me)$_3$

The spectra of Figure 9.5g, k can be analysed in more detail to derive an estimate for the charge transfer efficiency of Mo(tfd-CO_2Me)$_3$ in P3HT. For this purpose, a model fit was adjusted to the data of the S 2p and Mo 3d emission for each doping concentration and substrate. In the following discussion an integer charge transfer for Mo(tfd-CO_2Me)$_3$ in P3HT is assumed, which agrees with its strong doping capabilities and studies reported in literature.[91] The shoulder of the S 2p emission at 162.5 eV in Figure 9.9a can be assigned to the S $2p_{3/2}$ emission of charged radical Mo(tfd-CO_2Me)$_3$ anions. This agrees with a density functional theory calculation of Tenderholt et al. revealing that the additional electron is mostly located at the sulphur C_2S_2 portions of dithiolene ligands of the Mo(tfd-CO_2Me)$_3$ complex.[91,160] The corresponding polaron in rr-P3HT is delocalized over many thiophene units. Since the positive charge on rr-P3HT is not localized, a distinct peak component at higher binding energies in the S 2p emission is not observed.[33] For the fit of the S 2p emission the S 2p level of pure Mo(tfd-CO_2Me)$_3$ is used to model the charged species at lower binding energies. The main peak of the S 2p level in Figure 9.9a contains sulphur of both P3HT and Mo(tfd-CO_2Me)$_3$, each at slightly different binding energies. For simplicity these components were not separated, but a broader single peak model of adjustable width is used instead (consisting of two Voigt profiles for S $2p_{1/2}$ and $2p_{3/2}$). An exemplary fit is plotted in Figure 9.9a, showing the sum of combined neutral and partially charged S 2p in green and blue, respectively. The fraction of charged dopants can only be determined if the doping concentration is taking into account to separate the neutral S 2p peak contributions from P3HT and Mo(tfd-CO_2Me)$_3$ within the green fit component in Figure 9.9a. The amount of neutral n_{d^0} and charged dopants n_{d^-} add up to the total amount of dopants $n_d = n_{d^0} + n_{d^-}$, where the amount of P3HT shall be denoted by n_m. With this definition the molar ratio prepared in solution is given by n_d/n_m which equals $(n_{d^0} + n_{d^-})/n_m$. The quotient of integrated peak intensities I(S 2p) of different S 2p core-level species are expected to match their respective *atomic* molar ratios. As a consequence, the molar ration n_d/n_m can then also be expressed by:

$$\frac{n_d}{n_m} = \frac{I_d(\text{S 2p})/N_d(\text{S})}{I_m(\text{S 2p})/N_m(\text{S})} = \frac{(\,I_{d^0}(\text{S 2p}) + I_{d^-}(\text{S 2p})\,)/N_d(\text{S})}{I_m(\text{S 2p})/N_m(\text{S})} \tag{9.1}$$

where N_d(S) and N_m(S) denote the number of sulphur atoms in Mo(tfd-CO_2Me)$_3$ and the P3HT monomer. From the fit in Figure 9.9a, only the ratio of $I_{d^-}(\text{S 2p})/(I_{d^0}(\text{S 2p}) + I_m(\text{S 2p}))$ can be inferred. In this case, if one takes the molar doping ratio n_d/n_m to be known, the fit result can

be inserted into the above equation to solve for the fraction of charged dopants n_{d^-}/n_d which equals $I_{d^-}(\mathrm{S\ 2p})/I_d(\mathrm{S\ 2p})$, where $I_d(\mathrm{S\ 2p}) = I_{d^-}(\mathrm{S\ 2p}) + I_{d^0}(\mathrm{S\ 2p})$.

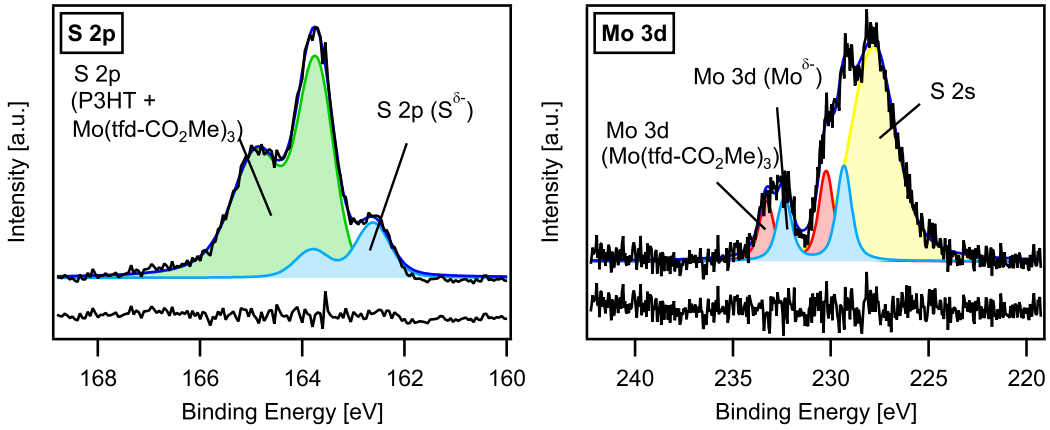

Figure 9.9: Figure shows two example fits of the S 2p and the Mo 3d core-level emission in (a) and (b), from which the charge transfer ratio can be determined. In both spectra a negatively charge species of $S^{\delta-}$ and $Mo^{\delta-}$ can be identified. The molar doping ratio for the fits in this Figure was set to 5:1 (P3HT:Mo(tfd-CO_2Me)$_3$).

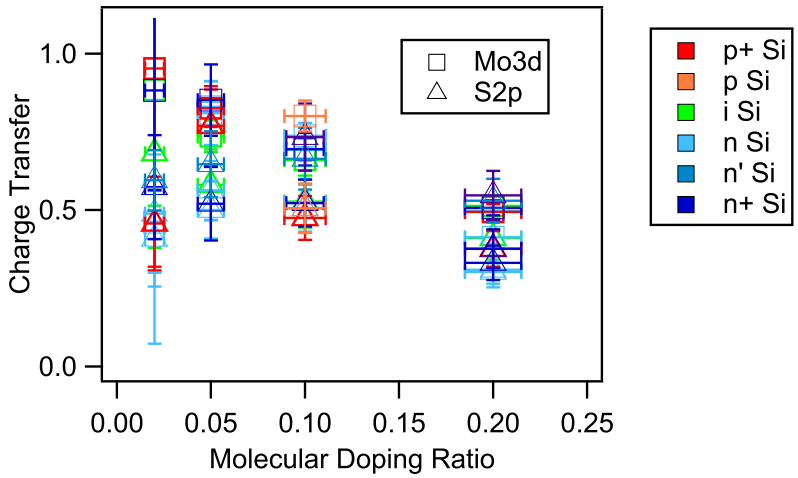

Figure 9.10: Fraction of dopants that undergoes charge transfer with P3HT as a function of molar doping ratio of Mo(tfd-CO_2Me)$_3$:P3HT, which is determined from S 2p (triangle) and Mo 3d (Squares) core-level spectra. Error-bars are calculated from fitting errors and are assumed to be 10% for the doping concentration prepared in solution. The silicon substrate is represented by colour with the legend on the right-hand side.

It should be noted again that this consideration only applies to an integer charge transfer, in which neutral and charged dopants can be clearly separated within their respective core-level emission lines. This is assumed to be also the case for the Mo 3d spectrum in Figure 9.9b. Although it is shown in literature that the additional electron is mainly located at the C_2S_2 portions of dithiolene ligands,[91,160] the Mo 3d spectrum shows two components in both the Mo $3d_{5/2}$ and the $3d_{3/2}$ region. For the fit in Figure 9.9b the Mo 3d part of pure Mo(tfd-CO_2Me)$_3$ and a single broad peak for the S 2s emission is chosen, which stems in this case from both P3HT

and Mo(tfd-CO_2Me)$_3$. The Mo 3d component towards lower binding energy is attributed to Mo(tfd-CO_2Me)$_3^-$ and the Mo 3d peak at 230 eV to neutral dopants as in Figure 9.5k. The ratio of charged to neutral dopants can be simply inferred from the quotient of the corresponding Mo 3d fit components in blue and red shown in Figure 9.9b. These fitting procedure has been done for all concentrations and substrates in Figure 9.10. For very low concentration a reliably fit is difficult, which leads to large error bars for a molar doping ratio of for example 1:100. The fraction of charge transfer derived from the Mo 3d spectrum does not significantly deviate from the values calculated from the S 2p level but seems to be slightly higher. This difference is not relevant, but could be explained by the indirect calculation of the neutral S 2p contribution. Overall one observes a decrease in the amount of charge transfer with concentration, meaning that for low dopant content most of the dopants can accept an electron, whereas for high doping concentration a successful charge transfer becomes unlikely. This behaviour is reported in literature and is ascribed to either agglomeration of dopants within the film or a reduced number of unoccupied doping sites due to coulomb interactions of dopant ions.[13,79] Furthermore, there is no dependence of the substrate on the doping efficiency found for the data in Figure 9.10.
In conclusion, this investigation serves to analyse doping related spectral features that indicated charge transfer and verify an increase in carrier concentration causing a Fermi level shift towards the HOMO level of P3HT. However, a further-reaching study on band alignment with respect to substrate properties could not be achieved since intrinsic P3HT layers suffer from charging and the substrate surface properties are not sufficiently controlled. Additional conceptual considerations on improving the experiment are also expressed in the final discussion. In principle, charging can be reduced by choosing a lower P3HT film thickness as it is done in Section 14. However, if the film thickness is chosen to low, charge carrier exchange with the substrate and a possible band bending at the interface may not be saturated. To fully reveal the energetic conditions at the interface, a step-wise variation of the organic film thickness has to be conducted with repeated photoemission measurements. Furthermore, band bending in the substrate and the contribution of the interface dipole can be better evaluated in such an experiment. However, this is typically not possible for polymers such as P3HT, since processing parameters determine the morphology of the P3HT film, which impacts the position of energy levels. As a compromise, one could choose only two carefully selected processing parameters to obtain a low and high film thickness to evaluate the extent of the interface dipole. To guarantee a similar film quality, the samples need to be cross-validated with structural analysis, e.g. transmission electron microscopy (TEM) or grazing-incidence wide-angle X-ray scattering (GIWAXS).

9.4 Metal-Semiconductor Interface

Using photoelectron spectroscopy, many interface studies for organic electronics rely on thermally evaporated small molecules on electrode materials to step-wise build up the contact and consecutively measure energy level positions. For polymers this is not possible because of their high molecular weight. In this section, silver is thermally evaporated onto a doped P3HT film to investigate band alignment and possible charge transfer at the metal contact. This experiment was carried out as a preliminary study to prepare and characterize a system, with which a drift of molecular dopants can be studied. Details about previous experiments that demonstrate a drift can be found in Section 11.

Experimental Information: $Mo(tfd\text{-}CO_2Me)_3$ and P3HT were dissolved in chlorobenzene and mixed at a molar ratio of 1:10. The solutions were stirred over night at 50°C and mixed several hours before processing. Thin films were spin-cast from a 13.5 g L^{-1} solution at 1200 rpm on solvent-cleaned cut p^+-Si silicon wafers. The samples were then directly transferred to the vacuum system. Silver was thermally evaporated without breaking the vacuum. The evaporation rate for silver was set to ca. 1 nm min^{-1}, which is lower as it is used for device fabrication, and was monitored by a micro-balance.

Results: XPS and UPS spectra of step-wise deposited silver on doped P3HT are shown in Figure 9.11. With increasing coverage damping of organic-related core-level lines can be found for the F 1s, C 1s, O1s and S 2p emission. As expected, an increase of the Ag 3d line and all silver related core-level features in the survey spectrum in Figure 9.11a can be confirmed. The nominal coverage derived from the micro-balance during deposition is written at each graph and is encoded by colour, going from red to grey, as listed in the legend of Figure 9.11. Even at a coverage of ca. 18 nm, carbon and fluorine traces can still be detected, which would not be possible if a dense layer and the small inelastic electron mean free path (IMFP) of silver is considered. This discrepancy can either be explained by intercalation of silver into the polymer, formation of islands or lighter organic contaminations "floating" on top of the growing silver layer. Intercalation into the polymer is certainly possible and is difficult to rule out completely,[256] but is not expected to be the dominating factor in this system. In a similar study, Hirose et al. found an abrupt, unreacted interface of silver, but within the same experiment e.g. aluminium was seen to react and intercalate into the organic semiconductor during deposition.[257] Here, the formation of islands can be directly verified by Scanning Electron Microscopy (SEM) images in Figure 9.13. The surface-image of doped P3HT clearly changes when a nominal 5 nm silver layer is deposited, showing small 5 - 10 nm grains that are already connected. For coverages above 200 nm large structures can be seen in Figure 9.13d easily reaching 100 nm in size. This correlates with a control experiment performed with the bare silicon substrate. The coverage derived from damping of respective core-level emission lines is plotted versus the nominal thickness in Figure 9.12d, using an estimated calculated electron mean free path (IMFP) for silver. For coverages below 10 nm they roughly agree regardless of the chosen substrate line but are considerably lower than the nominal thickness. As it can be inferred from Figure 9.11k, the Si 2p emission can still be detected at nominal coverage of 10 nm, whereas for 50 nm a dense silver layer was found (there are no data points in between). On the other hand, even for silicon, carbon contaminations appear at the surface when reaching dense silver layers, although the C 1s is smaller than for P3HT as sublayer. The C 1s signal further persists to much higher silver coverage.

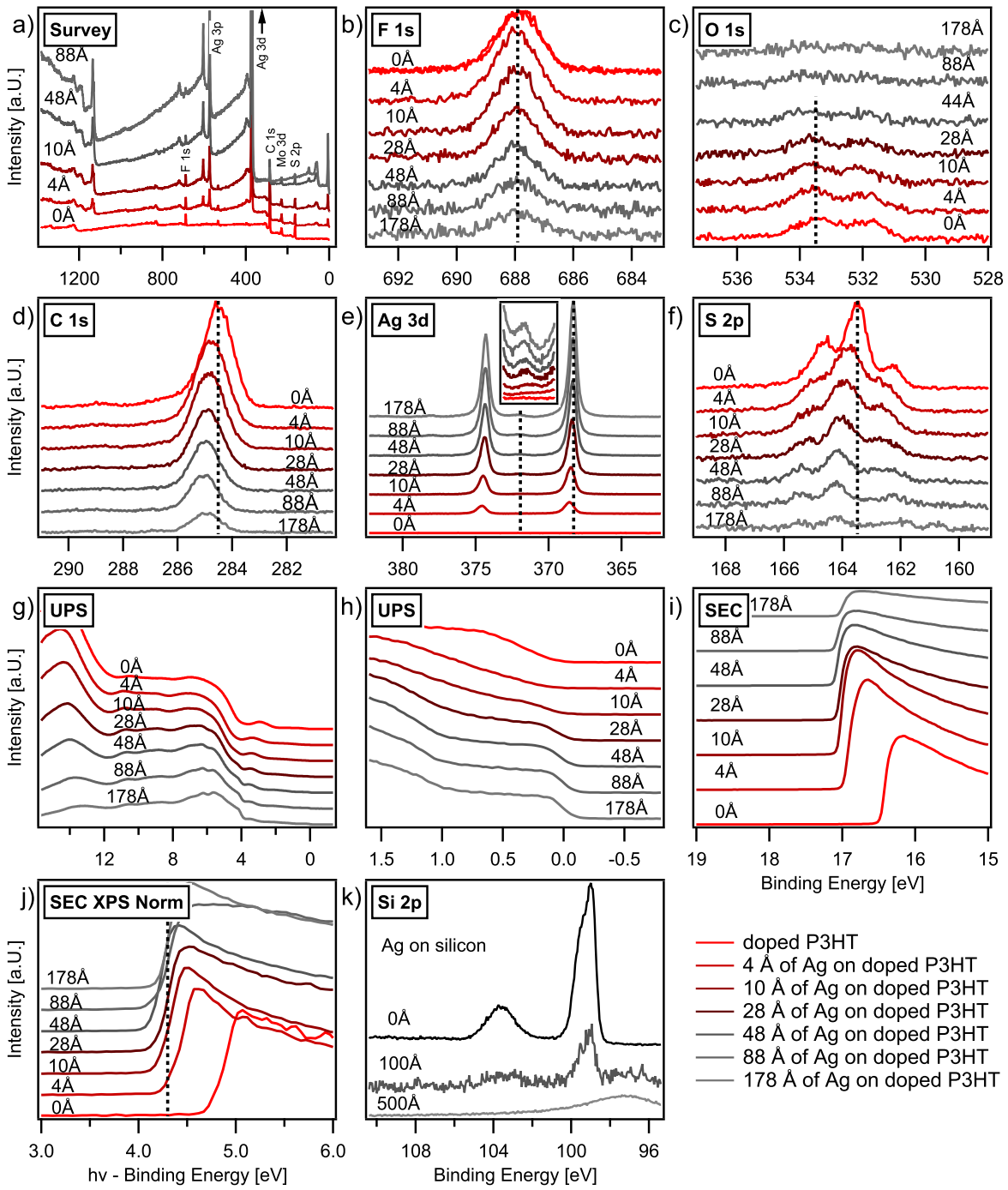

Figure 9.11: Figure shows XPS and UPS spectra for step-wise evaporated Silver on P3HT doped with Mo(tfd-CO_2Me)$_3$. In the legend and at each graph the nominal coverage is provided, as determined by a quartz micro-balance. A reduction in peak intensity with increasing silver coverage is visible for the F 1s, O 1s, C 1s and S 2p emission in (b),(c),(d) and (f). UPS (HeI) spectra are plotted in (g) and its zoom at the Fermi-level in (h). The secondary electron cut-off (SEC) is depicted in (i) and (j) measured with UPS and XPS. The Si 2p emission of a silicon substrate, on which silver is directly deposited is given in (k).

If silver is deposited on doped P3HT, additionally the fluorine and sulphur related emission of the S 2p and F 1s level can be observed at very high coverage. The organic contaminations therefore have to originate from the substrate and seem to "float" on the heavier silver layer. In fact, also the more surface-sensitive UPS measurements in Figure 9.11 do not show the spectrum of sputter-cleaned silver. Even at highest coverage, there is considerable contribution of either P3HT or the dopant. A linear combination of the UPS spectra of P3HT and sputter-cleaned silver is fitted to the data in Figure 9.12a showing a good overall match. However, the π-state of P3HT is more likely situated at around 3.5 eV, which leaves the shoulder at 2 eV unexplained. The UPS spectra may contain further contributions of the dopant or organic fragments, which can be located at 2 eV. The formation of islands and the possibility of surface contaminations from the organic layer, complicates the analysis of the interface diagram. Nonetheless, a Fermi level shift is observed in Figure 9.11, marked for the C 1s and the S2p emission by a dashed line.

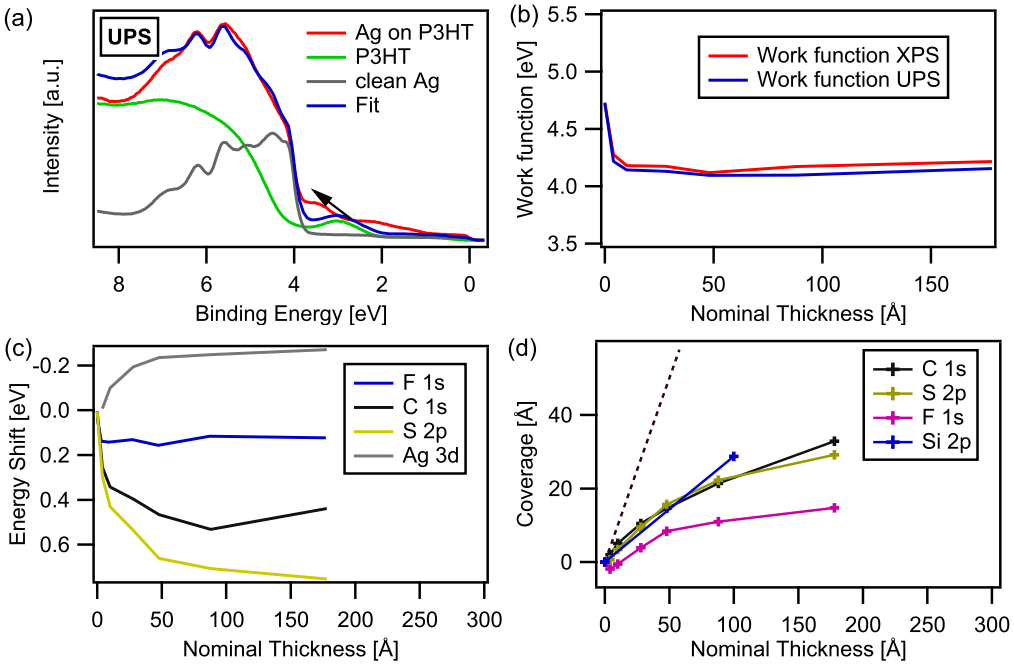

Figure 9.12: Fitted UPS spectra of high Ag-coverage on doped P3HT from Figure 9.11g in (a). The dependence of the work function with silver coverage is presented in (b). Changes of core-level as a function of nominal silver layer thickness is plotted in (b). The nominal layer thickness is obtained from a calibrated quartz-balance and is compared to an estimated coverage based on damping of photoemission from the underlying layer in (d).

There is a small shift of the Ag 3d line up to a coverage of 5 nm, which may be caused by small metallic islands which show a size-dependent hole screening or may indicate intercalation for low coverage and metallic Ag formation at high coverage. Within the first deposition step, the secondary electron cout-off (SEC) quickly drops close to the position of silver, yielding a work function of ca. 4.2 eV. With further deposition, the work function stays constant as shown in Figure 9.12b. When plotting the energy position of the C 1s or the S 2p line in Figure 9.12, a band bending of up to 0.5 eV within the organic layer can be expected. However, this can occur over a short distance which can not be determined, since the metal is deposited onto the

semiconductor. Moreover, silver is exhibiting inhomogeneous growth conditions that do not allow for concluding the spatial extension of band alignment. Interestingly, the F 1s level and the S 2p component, which is attributed to charged dopants, do not shift accordingly but besides an initial shift of 0.13 eV stays constant regardless of the deposited silver. This suggests that isolated dopants or clusters of Mo(tfd-CO_2Me)$_3$ at the metal interface stay charged and do not follow the band bending measured for P3HT. With the information acquired by this experiment, the band alignment for P3HT is anticipated as sketched in Figure 9.14. Admittedly, there is a certain margin of interpretation, since one does not evaporate the organic semiconductor and measure its energetic progression, but rather track P3HT between growing silver islands. For higher coverage the signal is likely dominated from P3HT fragments "floating" on top of the metal layer and is therefore not meaningful for the P3HT film.

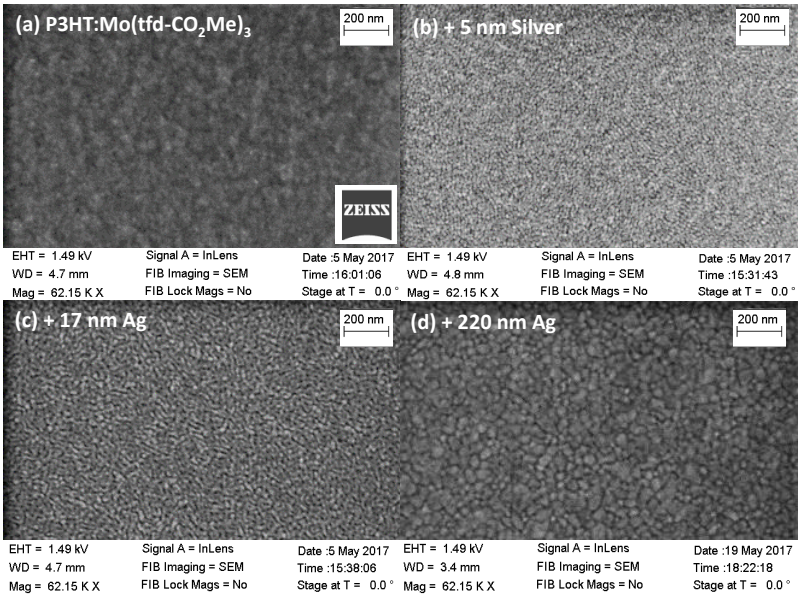

Figure 9.13: Scanning electron microscopy (SEM) images of silver deposited on P3HT with increasing coverage. Data was recorded and provided by L. Müller (TU Braunschweig).

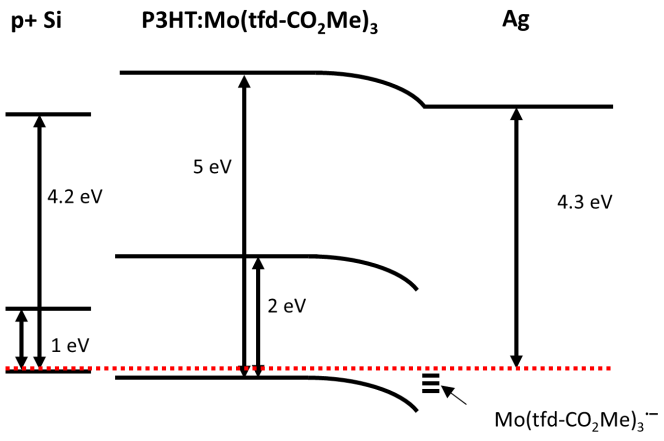

Figure 9.14: Schematic band diagram of the interface of doped P3HT with silver anticipated from XPS measurements in Figure 9.11.

10 Diffusion in Sequentially Doped P3HT

It is mentioned in the beginning of this chapter that sequential doping offers the potential of doped and highly crystalline polymer films with coherent charge transport.[118] In this section, the diffusion of thermally evaporated Mo(tfd-CO_2Me)$_3$ is studied in a sequential doping process of P3HT with varying crystallinity. In order to obtain a complete picture of the diffusion process, in-situ IR spectroscopy during sequential dopant deposition and subsequent photoelectron spectroscopy after evaporation are applied, since they differentially probe both bulk and the surface region of the P3HT film. With these techniques it is also possible to estimate charge transfer and its efficiency as a function of the nominal dopant coverage, allowing to optimize the doping process. Moreover, it is attempted to model the doping concentration versus time from XPS core-level spectra. Because Mo(tfd-CO_2Me)$_3$ is considered to be a bulky dopant, it is not expected to enter the π-π stacking of P3HT crystallites, which may cause a difference in the diffusion behaviour when comparing semi-crystalline and fully amorphous P3HT. In fact, there has been some controversy in literature, whether F4TCNQ is entering the P3HT crystal based on refractometry data and lattice spacing.[153,161]

Materials and Sample Preparation: Samples for XPS and IR spectroscopy have been prepared identically. For this study rr-P3HT (>93% regularity, $M_W = 24$ kg mol^{-1}) and rra-P3HT ($M_W = 57$ kg mol^{-1}) was used without further treatment as described in Section 6.2. The dopant Mo(tfd-CO_2Me)$_3$ was provided by the group of S. Marder (Georgia Institute of Technology) and synthesized according to Zhang et al.[121,157] Both P3HT materials were dissolved in chlorobenzene and stirred on a hot-plate overnight at 50°C with a concentration of 11 and 13.5 mg/mL for rr-P3HT and rra-P3HT, respectively. Thin films were spin-cast at 1200 rpm for 30 s in a nitrogen glovebox on cut ca. 1.5 cm^2 silicon i-Si wafers (intrinsic, σ >5000 Ω). Silicon substrates were cleaned with acetone and isopropanol in an ultra-sonic bath prior to spin-coating. The resulting film thickness $L_0 = 50 \pm 6$ nm was determined by ellipsometry and a DEKTAK profilometer. The samples were then shortly exposed to ambient conditions when transported to the UHV evaporation chamber. After deposition, UHV conditions were not interrupted for further XPS and IR measurements. Dopant evaporation was carried out at ca. 130 °C and a pressure of 10^{-8} mbar.

10.1 IR-Spectroscopy Measurements During Deposition

Experimental Information: IR spectra were recorded in transmission geometry during dopant deposition in UHV. Therefore, the backside of the silicon substrate was cleaned with chlorobenze in the glovebox. The evaporation rate was monitored by a quartz micro-balance and chosen to be between 0.1 and 1 nm min^{-1}. The nominal layer thickness L_d determined from the evaporation rate provides a measure for the amount of deposited molecules.

Discussion: Relative IR transmission spectra measured by S. Beck (Univ. Heidelberg) of the thermal deposition of Mo(tfd-CO_2Me)$_3$ on P3HT thin films are shown in Figure 10.1. The reference spectra of pure P3HT and Mo(tfd-CO_2Me)$_3$ can be found in Section 9.2. The nominal dopant coverage ranges up to 11 nm and refers to the equivalent layer thickness L_d of pure Mo(tfd-CO_2Me)$_3$, which was measured by the micro-balance. As it can be inferred from Figure

10.1, doping-induced spectral features immediately emerge with increasing Mo(tfd-CO_2Me)$_3$ coverage. These are the strong IR-active vibrational (IRAV) modes below 1500 cm^{-1} and the broad polaronic P1 absorption around 3200 cm^{-1} for rr-P3HT and at 5000 cm^{-1} for rra-P3HT, which are caused by an electron transfer from Mo(tfd-CO_2Me)$_3$ to P3HT resulting in a positive charge on the polymer backbone.[32,238] The blue-shift in binding energy between rr-P3HT and rra-P3HT can be explained by a stronger polaron localization in rra-P3HT due to a lower effective conjugation length and reduced π-π stacking that is caused by disorder.

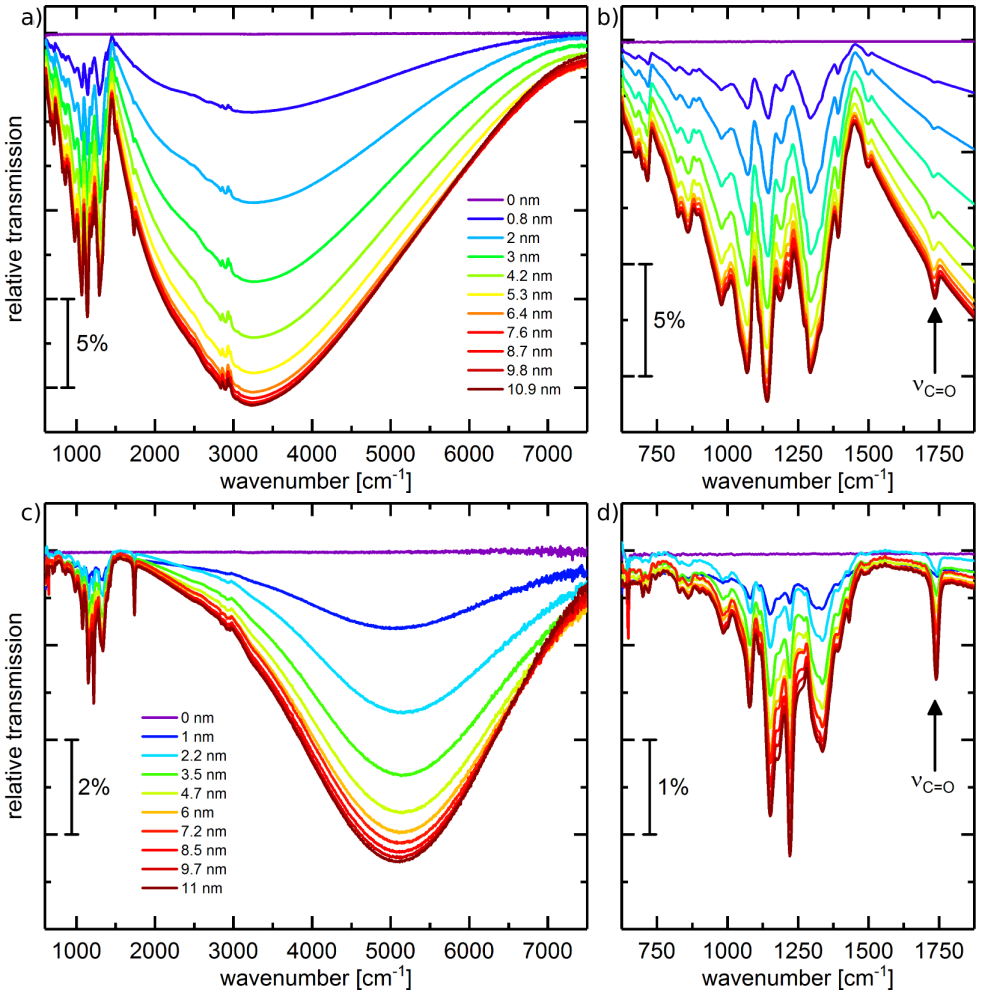

Figure 10.1: Relative transmission spectra of a sequentially doped rr-P3HT layer in (a),(b) and ra-P3HT in (c),(d) for varying dopant coverage from 0 nm to 11 nm. The whole MIR range is depicted in (a),(c) and the fingerprint range zoomed in (b),(d). The characteristic C=O stretching vibration of Mo(tfd-CO_2Me)$_3$ is marked on the right. There is a different ordinate scale in (a) and (c). The data have been measured and provided by S. Beck (Univ. Heidelberg).

Although most of the vibrations modes are comparably weak with respect to the strong IRAV modes, the C=O stretching vibration at 1735 cm^{-1} is well separated and can be used as an indicator for the presence of dopants. The relative spectral change is largest at small coverage and saturate above 8 nm for both rr-P3HT and rra-P3HT, suggesting that further deposition does not introduce additional charge transfer. The growth of polaronic absorption bands reveal that both charge transfer and diffusion starts immediately with dopant deposition, whereas only a

much smaller increase was measured when evaporation has stopped. During the deposition process, dopants are expected to carry thermal energy, allowing a fast immersion into the P3HT film. As a control experiment, and in order to verify that it is not a matter of surface doping, Mo(tfd-CO_2Me)$_3$ was evaporated on a cooled P3HT film and subsequently annealed. Since this experiment was also not done by the author, the reader is referred for details to Reiser et al.[245] However, the experiment shows, that on a cooled substrate only vibrational modes attributed to neutral Mo(tfd-CO_2Me)$_3$ with the characteristic C=O stretching vibration at 1735 cm^{-1} are observed (beside a small initial charge transfer at the interface for 0.3 nm coverage). When the substrate warms up to room temperature, diffusion sets in at 5-10 °C and doping related absorption features (IRAV modes + polaron) drastically changes the spectrum. These feature slowly increase and saturate at room temperature within several hours, much slower than those observed during thermal evaporation. The final saturated spectrum of doped P3HT is comparable for both samples, which are either kept at -20 °C or room temperature during dopant deposition. With higher coverage further deposition of dopant molecules does not induce additional electron transfer, and presumably a dopant adlayer is formed. However, since IR spectroscopy probes the whole layer stack, the method is not able to distinguish the diffusion profile of neutral dopants, which is considered to be an important mechanism for device degradation.[114] Here, XPS can distinguish the chemical composition at the surface and how it is related to diffusion.

10.2 Photoelectron Spectroscopy after Deposition

Experimental Information: The evaporation rate was chosen to be ca. 1 nm min^{-1}. The samples were transferred after evaporation to the XPS chamber in UHV conditions. Core-level spectra were recorded over the course of several hours, while moving the focused X-ray beam (200 μm) along the surface within one data series to avoid radiation damage.

Results: Complementary to IR spectroscopic data, XPS is a surface sensitive technique for chemical states, which can distinguish charged and neutral dopants within the inelastic mean free path of ca. 3 nm for organic materials. In Figure 10.2a,c the S 2p core-level spectra of rr-P3HT and rra-P3HT are shown for different dopant coverages, which are quantified by the nominal layer thickness L_d measured by the micro-balance. An overall increase in S 2p intensity is observed with dopant deposition, which is due to the higher relative sulphur content in Mo(tfd-CO_2Me)$_3$ compared to P3HT and consequently the molar density of sulphur increases with increasing dopant concentration. An electron transfer from P3HT to the dopant gives rise to a charged Mo(tfd-CO_2Me)$_3^{\cdot-}$ species bearing a negative charge located on its functional core and particularly on the C_2S_2 portions of dithiolene ligands.[160] This causes a shift to lower binding energies of the S 2p core-level line of the dopant and has been studied by a peak deconvolution in Section 9.3. Especially for rr-P3HT in Figure 10.2a and when comparing the upper graphs in Figure 10.2a, the shoulder towards lower binding energies can be clearly recognized. For lower dopant deposition up to a nominal Mo(tfd-CO_2Me)$_3$ layer thickness of $L_d = 5$ nm, there is only an increase of charged species at lower binding energies (162.5 eV). This means that most dopants at the surface seem to be charged in case of low dopant coverage. For higher deposition, additional electron transfer does not occur and neutral dopants are accumulating at the surface. For neutral Mo(tfd-CO_2Me)$_3$ the position of the S 2p$_{3/2}$ is located at ca. 163 eV which is about 1 eV lower than for pure P3HT at about 164 eV in Figure 9.2b. Therefore, at high coverage the maximum of the S 2p$_{3/2}$ broadens and shifts from the position of doped P3HT to the binding energy measured for neutral Mo(tfd-CO_2Me)$_3$ at 163 eV. A similar situation

is found for rra-P3HT in Figure 10.2c, although the amount of charged dopants is lower than for rr-P3HT (determined by the S $2p_{3/2}$ peak at ca. 162.5 eV). At a high coverage of $L_d = 15$ nm, the S 2p intensity for rra-P3HT is larger than for rr-P3HT, suggesting that there are more neutral dopants accumulating on the surface in case of rra-P3HT. The position of the S $2p_{3/2}$ peak of P3HT, Mo(tfd-CO_2Me)$_3$ and Mo(tfd-CO_2Me)$_3^-$ is marked by a red dotted line in Figure 10.2. In order to study the diffusion and changes in dopant surface concentration, XPS measurements were performed after various waiting times with the sample being at room temperature. In Figure 10.2b, d the spectra are plotted separately after evaporation together with a spectrum recorded for a 10 h waiting time with the sample kept in UHV at room temperature. For low doping concentrations with a majority of charged dopants, there is no change in the amount of dopants found with waiting time. For a coverage of $L_d = 8$ nm, a considerable decrease of the neutral dopant fraction is observed after 10 h, whereas the amount of Mo(tfd-CO_2Me)$_3^-$ at 162.5 eV mainly stays unperturbed. In fact, the shoulder towards lower binding energies does not decrease regardless of the type of P3HT or the dopant concentration for the probed information depth, even though an even distribution of dopants in the whole film is not expected. In contrast to rra-P3HT, a significant decline in the amount of neutral dopants after 10 h can be identified for rr-P3HT and coverages $L_d = 10$ - 15 nm. This suggests that neutral dopants are more mobile than charged dopants, which are likely coulombically bound to the host matrix. For rra-P3HT, such a decrease is not seen above $L_d = 11$ nm and the total S 2p peak stays roughly constant for 10 h, which is dominated by neutral Mo(tfd-CO_2Me)$_3$, probably forming a dopant layer.

The changes in surface concentration as a function of time, which are due to neutral dopants, can be further quantified in Figure 10.3. From C 1s and F 1s core-level spectra, recorded together with the S 2p emission in Figure 10.2, the molar ratio of dopants to P3HT monomers can be calculated. For this purpose, the background-subtracted core-level spectra have to be integrated and weighted with atomic sensitivity factors (ASF), which are specific to the spectrometer and account for analyzer transmission, cross-section, and average electron mean free path, as described in Section 4.1. The correctly scaled intensity $\tilde{I}$ is then derived from the measured peak intensity I according to: $\tilde{I} = I/\mathrm{ASF}$ and its ratios correspond to the ratio of respective atomic densities. However, because both dopant and matrix contain sulphur and carbon, the molar ratio n_d/n_m of dopants n_d to matrix monomers n_m has to be inferred from rearranging:

$$\frac{\tilde{I}(\mathrm{F\ 1s})}{\tilde{I}(\mathrm{C\ 1s,\ S\ 2p})} = \frac{N_d(\mathrm{F})n_d}{N_d(\mathrm{C,\ S})n_d + N_m(\mathrm{C,\ S})n_m} \tag{10.1}$$

where N_d(C,F,S) and N_m(C,S) denote the number of atoms (C, F, S) in dopant and matrix monomers, respectively. Alternatively the most probable doping concentration can be calculated using the formalism in Section 5. For very high doping concentration, Eq. 10.1 is not accurate and leads to big errors when the carbon intensity is mainly dominated by Mo(tfd-CO_2Me)$_3$ because of division close to zero. As a consequence, a peak component fit of the C 1s emission as depicted in Figure 9.2d is used instead, attributing the main C 1s line to P3HT plus dopant, whereas the components toward higher binding energies are only from Mo(tfd-CO_2Me)$_3$. Molar fractions in Figure 10.3 are then simply derived from molar rations n_d/n_m by:

$$\frac{n_d}{n_d + n_m} = \frac{n_d/n_m}{n_d/n_m + 1} \tag{10.2}$$

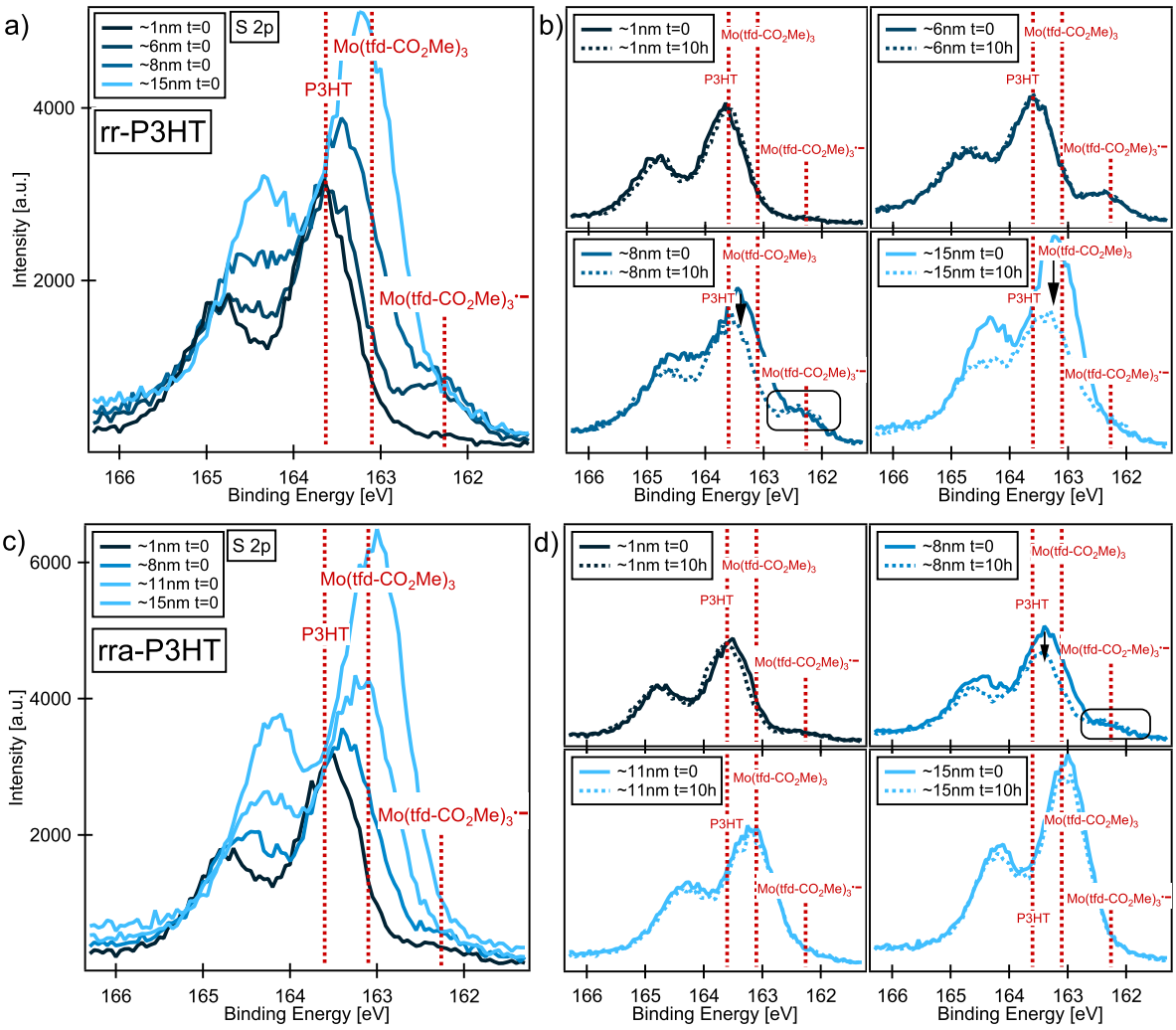

Figure 10.2: S 2p spectra for varying dopant coverage measured directly after dopant evaporation on rr-P3HT (a) and rra-P3HT (c). Each spectrum is remeasured after 10 hours for rr-PH3HT in (b) and rra-P3HT (d). For (b), (d) the solid lines show the spectra recorded directly after evaporation from (a), (c), and the dashed lines show the spectra recorded 10 h later. The assignment of the S $2p_{3/2}$ emission line for different chemical components is marked by a red dashed line in each plot. The intensity scale in (a) and (b), (c) and (d) is similar but differs between (a) and (c). Adapted from Reiser et al.[245]

Finally, in Figure 10.3, the dopant fraction at the surface is plotted versus waiting time on a logscale for the various nominal dopant coverages, given by the nominal layer thickness L_d. Each sample represents one data series with a fixed deposited coverage encoded by colour. It can be seen that the decrease in surface concentration is continuous and not strictly exponential. For low molar fractions of < 0.05, the surface concentrations seems to be constant with time and, provided that almost all Mo(tfd-CO_2Me)$_3$ is charged, this agrees with the hypothesis that charged dopants are less mobile than neutral dopants. For extremely high coverage there is also no change in the molar fraction, which can be explained by a saturated P3HT film and a dense dopant toplayer. On the other hand, an opaque dopant layer would be expected at a nominal coverage of $L_d = 10$ nm, if no diffusion had occurred (provided an IMPF of around

3nm). However, the molar fraction shows there is indeed no dense adlayer of Mo(tfd-CO_2Me)$_3$ present at the surface (already at the first XPS measurement) up to a nominal dopant layer thickness of 18 nm for rr-P3HT and 14nm for rra-P3HT. This agrees with IR spectroscopy data, which find a diffusion into the P3HT film already during deposition. Further deposition beyond 18 nm will hold a molar fraction of one, meaning a pure dopant contribution on the surface. To understand the data in Figure 10.3 in more detail, a numerical model is constructed in the next section.

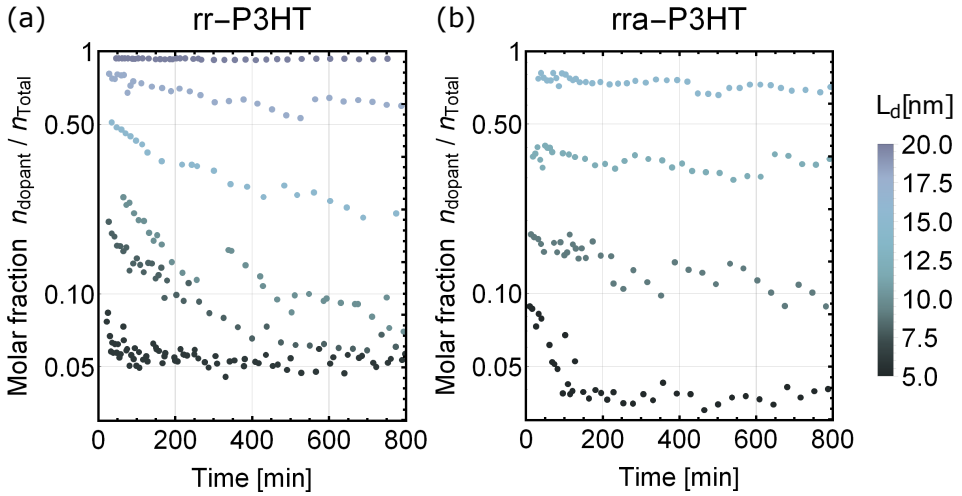

Figure 10.3: Molar fractions of Mo(tfd-CO_2Me)$_3$ to P3HTmonomers for rr-P3HT (a) and rra-P3HT (b) as determined in the surface region. The color legend on the right side shows the approximate nominal layer thickness L_d of Mo(tfd-CO_2Me)$_3$ as measured by the micro-balance. Relative errors for molar ratios can be estimated to be as high as 15%.

10.3 Theoretical Modeling of Photoemission Data

After thermal evaporation has ended, there is a slow decrease of the amount of neutral dopants at the surface observed with XPS in Figure 10.3, which can either be explained by desorption or further diffusion of the dopant into the P3HT film. To evaluate the contribution of these processes, a quantitative analysis and theoretical modelling is carried out in the following. For this purpose, the amount of Mo(tfd-CO_2Me)$_3$ and P3HT has to be estimated from their respective layer thickness in order to calculate molar ratios or fractions derived from XPS measurements. The amount of dopants shall be denoted by n_d and the amount of P3HT monomers by n_m. The length of the total thin film after evaporation is assumed to be $L = L_d + L_0$, where L_d describes the nominal dopant coverage, measured by the micro-balance, and L_0 is the initial thickness of the pure P3HT film $L_0 = 50 \pm 6$ nm. Furthermore, for a given area A the amount of dopants and polymer monomers can be calculated from the nominal dopant coverage $n_d = \frac{\rho_d}{M_d} A L_d$ and pure P3HT film thickness $n_m = \frac{\rho_m}{M_m} A L_0$. The molar weight $M_d = 744.54$ g mol^{-1} of Mo(tfd-CO_2Me)$_3$ and $M_m = 166.28$ g mol^{-1} of P3HT is known from their chemical structure, whereas their respective densities must be estimated based on literature values of similar materials.[258,259] For this calculation a generic density of $\rho_d = 1.6$ g cm^{-3} and $\rho_m = 1.1$ g cm^{-3} is used, respectively. With the definition of the density $\rho = \frac{m}{V} = \frac{m}{AL}$ and molar weight $M = \frac{m}{n}$, one therefore obtains $n = \frac{\rho}{M} AL$ by substitution the mass m. The total average molar fraction X for each data series is

then inferred from $X = n_d/(n_d + n_m)$, which is used to set the initial conditions and distribution for the calculation.

10.3.1 Desorption estimate

In general Mo(tfd-CO_2Me)$_3$ is stable under UHV conditions and was evaporated at ca. 130 ° C for this process and adsorbs on P3HT and on silicon. However, small amounts can still desorb from the surface in UHV conditions. In order to quantify the desorption rate, a pure film of Mo(tfd-CO_2Me)$_3$ was deposited on a silicon substrate with a layer thickness thin enough to measure the Si 2p core-level signal of the substrate. The Si 2p emission was then recorded in UHV over the course of days. The layer thickness was calculated according to Beer's law with an empirically estimated electron mean free path of $\lambda = 3.4$nm for the pure Mo(tfd-CO_2Me)$_3$ layer. The results of this control experiment is shown in Figure 10.4. An increase of the Si 2p intensity corresponds to a decrease of the nominal coverage and gives a decline in the calculated layer thickness in Figure 10.4. At the same time the F 1s and C 1s core-level intensity does not change significantly, which excludes a steady drift in X-ray power as the cause for the rise in Si 2p peak intensity. The linear decrease in coverage is attributed to desorption at a constant rate of $r < 0.05$ nm h^{-1}, which is obtained from the linear fit in Figure 10.4. With this desorption rate, the decrease in surface dopant concentration can be estimated and compared to the data in Figure 10.3. For this purpose, a simplified but extreme situation is assumed, in which there is a pure dopant toplayer on pure P3HT, meaning no intermixing.

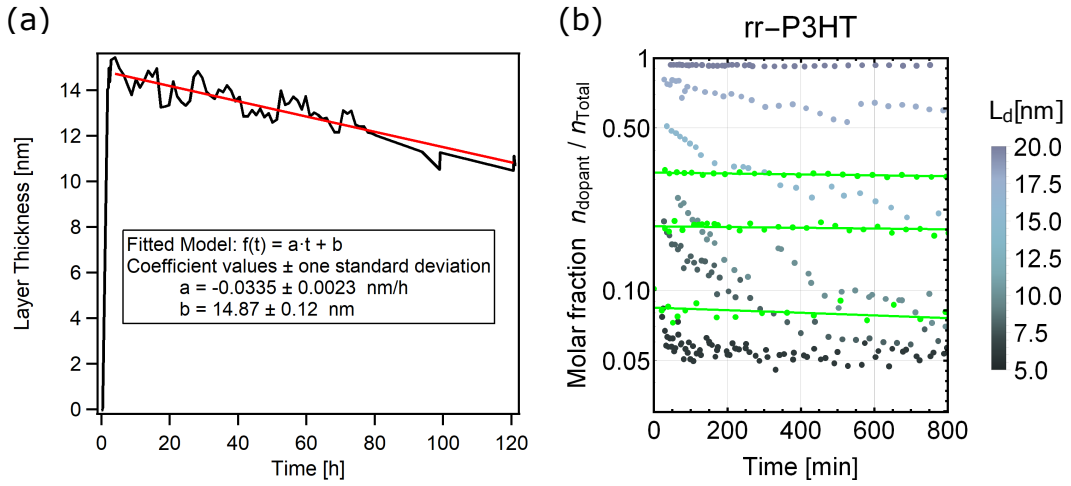

Figure 10.4: The nominal layer thickness of Mo(tfd-CO_2Me)$_3$ on silicon versus time in (a). A linear fit is added in red with the fit results listed in the inset. Molar surface fraction of dopants is plotted over time in (b). The blue data points are taken from the data in Figure 10.3 for rr-P3HT. The green data points, together with a linear fit to guide the eye, are from a solution-doped rr-P3HT film with homogeneous but similar overall concentration.

In this case a maximum desorption rate $r = 0.05$ nm h^{-1} causes the dopant layer to decrease at the surface with r until all dopants have left the P3HT film. The inelastic electron mean free path λ gives a measure for the information depth. For this simplification, it is assumed that a fixed one-dimensional volume of length λ is probed by XPS, which generates a signal of the dopant layer of thickness l_d and the remaining P3HT volume of $\lambda - l_d$. If the dopant thickness

is larger than λ, only dopants can be detected with XPS. The molar fraction measured from the combined dopant and P3HT volume is given by $X = n_d/(n_d + n_m)$, where in this case n_d is the amount of dopants in the adlayer l_d and n_m the amount of P3HT in the rest volume $\lambda - l_d$. As explained in the beginning of this section, the amount n_d and n_m can be calculated with the layer thickness l_d for a certain area A via $n_d = \frac{\rho_d}{M_d} A l_d$ and correspondingly $n_m = \frac{\rho_m}{M_m} A(\lambda - l_d)$, using the numerical values: $M_d = 744.54$ g mol^{-1}, $M_m = 166.28$ g mol^{-1}, $\rho_d = 1.6$ g cm^{-3}, $\rho_m = 1.1$ g cm^{-3}. The time dependence for the molar fraction $X(t)$ enters with the decreasing layer thickness due to desorption $l(t) = l(0) - rt$ with the rate from Figure 10.4. The initial layer thickness is adjusted to fit the first data point in Figure 10.3. The time-dependence of the desorption estimate is plotted in Figure 10.5 in comparison to the data and an extended model based on absorption and diffusion. For very high dopant coverage, the decrease in surface concentration predicted by desorption is actually higher than observed by XPS. Whereas for intermediate coverage, the desorption estimate can not explain the steep decrease in dopant concentration at the surface. It should be noted that charged dopants, which dominate at fraction of ca. 0.05 and are considered to be less mobile, are not taken into account in this desorption model. In order to verify that desorption is indeed not the dominating mechanism and that it is not different for P3HT than for a pure Mo(tfd-CO_2Me)$_3$ film, a doped P3HT film is prepared from solution with homogeneous but similar overall concentrations. The measured surface concentration is plotted (green) in Figure 10.4 together with the data of Figure 10.3, which does not show a comparable decline given the same timescales.

10.3.2 Absorption and Diffusion model

The more detailed model to describe the data in Figure 10.3 is formulated in terms of concentrations c and takes dopant absorption, bulk diffusion of dopants, charging of dopants, and a finite sorption capacity of the P3HT film into account.[260] With the assumption of a locally constant average density $\bar{\rho}$ and molar mass $\bar{M}$, the approximate concentration reads: $c \approx \frac{n_d}{n_d + n_m} \frac{\bar{\rho}}{\bar{M}}$. Since molar concentrations c can be related to molar fractions, which are derived from XPS measurements, the here presented model is applied to the data in Figure 10.5. For the course of the following description, the model is given in concentrations but molar fractions are inserted to fit the data. For this description, one distinguishes between the concentration of charged dopants c_c, neutral dopants c_n and dopants adsorbed on the surface c_a. The concentration of adsorbed dopants is only defined within a surface region that in this case is set to 3 nm, which approximately matches the XPS information depth and the surface roughness of P3HT. In this region, dopants can be absorbed by the film, and in this model, transformed into neutral dopants c_n which can subsequently diffuse through the P3HT bulk. In a simple image, dopants at the surface have to find a diffusion pathway to enter the P3HT film. To model the transition, neutral dopants c_n are defined with the whole film, including the surface region. Additionally neutral dopants can undergo a charge transfer and transform into charged dopants c_c. Because changes in surface coverage are mainly due to neutral dopants, see Figure 10.2, charged dopants c_c are considered to be immobile in this model. Consequently, the bulk diffusion is only related to neutral dopants and is modelled by Fickian diffusion that is independent of concentration with diffusion constant D_c. To match the finite thickness of the thin film, the diffusion current $J_c = -D_c \partial_x c_n(x,t)$ is set to zero at the surface ($x = 0$) and towards the substrate ($x = L$), which defines the boundary conditions for the system. For this calculation, the length (thickness) of

the thin film after evaporation is set to $L = L_d + L_0$, with the nominal dopant coverage L_d, measured by a micro-balance, and $L_0 = 50 \pm 5$ nm the initial P3HT film thickness. For simplicity, both absorption or uptake of dopants and charging of neutral dopants are modelled by linear isothermal sorption in Eq. 10.4, 10.5. Here, the sorption constants k_c and k_a for charged and adsorbed dopants are introduced, respectively. The finite dopant capacity (the volume that dopants can occupy in the P3HT film) enters by a multiplier in the differential equation in Eq. 10.5 which yields the saturation capacity S_{tot} for both charged and neutral dopants. The upper limit for charged dopants is realized analogously and is given by S_c, representing the maximum number of available doping sites. Assuming that the number of sites does not differ between bulk and surface, S_c can be estimated based on the XPS data in Figure 10.2 or 10.3. The system of differential equations to solve in terms of c_a, c_n, c_c then reads:

$$\partial_t c_n(x,t) = D_c \partial_x^2 c_n(x,t) - \partial_t c_c(x,t) - \partial_t c_a(x,t) \tag{10.3}$$

$$\partial_t c_c(x,t) = k_c c_n(x,t)\left(1 - \frac{c_c(x,t)}{S_c}\right) \tag{10.4}$$

$$\partial_t c_a(x,t) = -k_a c_a(x,t)\left(1 - \frac{c_c(x,t) + c_n(x,t)}{S_{\text{tot}}}\right) \tag{10.5}$$

The total concentration at the surface is simply given by $c(0,t) = c_n(0,t) + c_c(0,t) + c_a(0,t)$ and is assumed to be representative for molar fractions, meaning that $c(0,t)$ is compared to the data in Figure 10.5 after solving the above differential equations. To do this, initial conditions has to be set up in a reasonable way to match the experimental situation, which is described in the following.

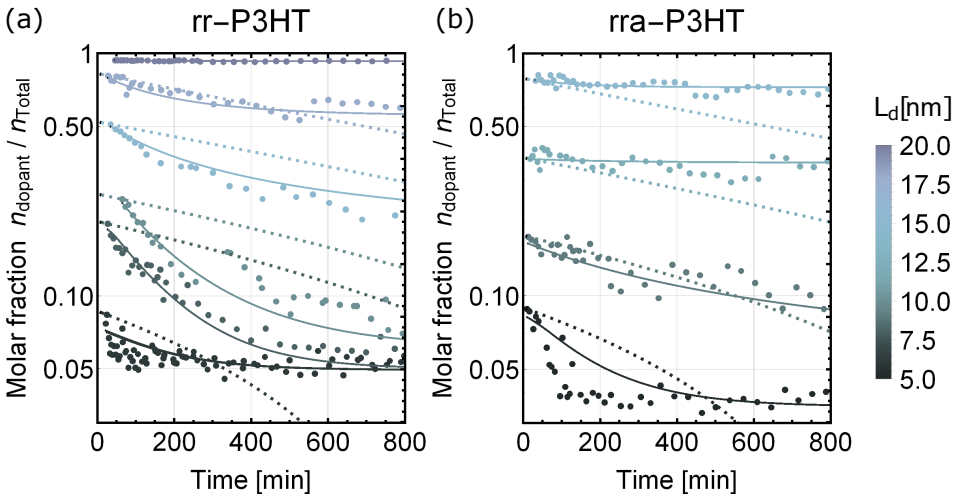

Figure 10.5: Measured molar surface fractions of Mo(tfd-CO_2Me)$_3$ in rr-P3HT (a) and rra-P3HT (b). The nominal layer thickness is encoded by colour for each data series with the bar legend on the right-hand side. The solid lines (also coloured) represent a fit of the discussed model, i.e. solving differential Eq. 10.3 - 10.5 with the proper initial conditions and constraint parameters. The dashed line shows the desorption estimate of the previous section for comparison with a rat of $r = 0.05$ nm h^{-1}. Adapted from Reiser et al.[245]

From IR spectroscopy measurements, it is known that there are dopants diffusing into the P3HT film already during thermal deposition. The slow decrease observed with XPS is mainly

due to remaining dopants at the surface, which are incorporated or absorbed by the P3HT over time at room temperature. Therefore, the amount of evaporated dopants is split, which is inferred from the nominal layer thickness L_d, into an equilibrated fraction and dopants remaining on the surface. In practice, one chooses an equilibrated molar fraction of neutral dopants X_n distributed in the entire film and an adsorbed fraction at the surface X_a. They are assigned to the concentrations $c_n(x,0)$ and $c_a(x,0)$ when solving the differential equations. The distribution between X_n and X_a has to match the total dopant fraction X, when treated as a density, according to $XL = X_n L + X_a \lambda$. Adsorbed dopants are defined in a surface region with length λ. The surface fraction X_a is then adjusted in a way that $X_a + X_n$ matches the first data points probed by XPS in Figure 10.5. The calculation of molar fraction X from the dopant layer thickness is described above and uses the numerical values: $M_d = 744.54$ g mol^{-1}, $M_m = 166.28$ g mol^{-1}, $\rho_d = 1.6$ g cm^{-3}, $\rho_m = 1.1$ g cm^{-3}.

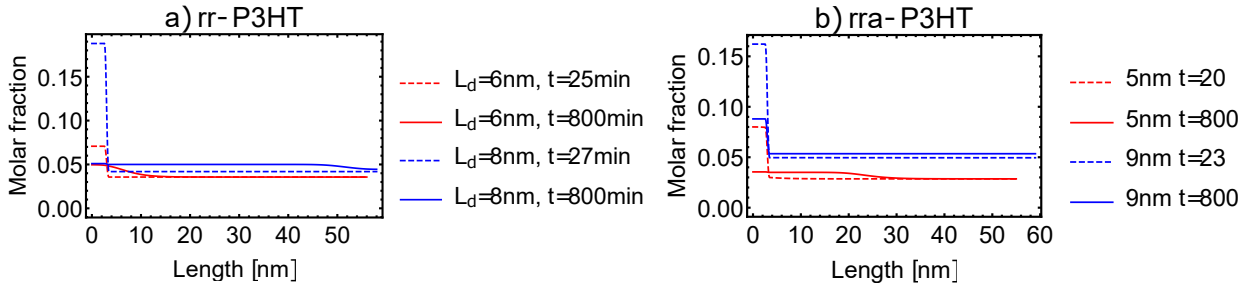

Figure 10.6: Calculated spatial distribution of the molar fraction of Mo(tfd-CO_2Me)$_3$ in rr-P3HT (a) and rra-P3HT (b) for two different coverages L_d in red and blue. The initial distribution is shown by a dotted line and the propagated solution at t = 800 min by a solid line. The region between 0 and 3 nm contains adsorbed dopants.

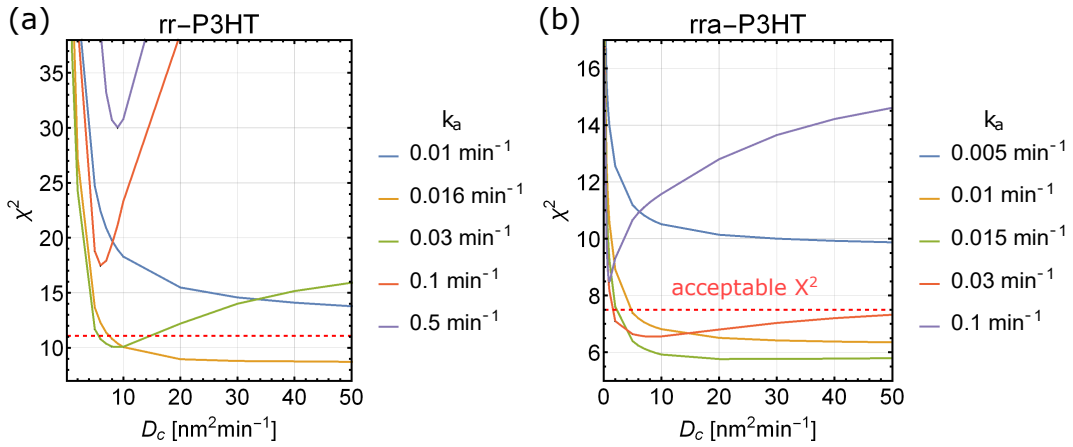

Figure 10.7: The sum of squared residuals X^2 of the fitting routine for the data in Figure 10.5 versus the diffusion constant D_c for rr-P3HT in (a) and rra-P3HT in (b). The coloured line represents different values for k_a chosen constant for the fit and given in the legend on the right. To find a lower limit for the diffusion constant in this model, a significant difference in X^2 from the optimal X^2_{min} is defined by $X^2/X^2_{\text{min}} = 1.3$ which yields a threshold of an acceptable X^2 as a function of D_c marked by a red dashed line. The overall difference of the X^2 value is due to a different number of data points.

An example of the initial dopant distribution is plotted in Figure 10.6 for two different coverages together with the propagated solution calculated from Eq. 10.3 - 10.5. For rr-P3HT, the changes in Figure 10.6 highlight adsorbed dopants at the surface ($x \in [0, 3\text{nm}]$) being absorbed and distributed in the film by diffusion, as it is intended by construction of the model. Ideally all data series in Figure 10.5 can be reproduced with one set of parameters for rr-P3HT and rra-P3HT. To reduce the number of degrees of freedom, some of the constants in Eq. 10.5 - 10.5 can be fixed based on experimental findings in Figure 10.2 and 10.3. With IR spectroscopy a fast charge transfer was observed during deposition, which is why the sorption constant for charged dopants is set sufficiently high ($k_c = 100\ \text{min}^{-1}$) to ensure an immediate charge transfer on the time scales relevant for fitting. From the S 2p core-level emission in Figure 10.2 the maximum number of charge dopants can be estimated, which is assumed to be also valid in the bulk of the P3HT film. Therefore the capacities are set constant and chosen manually to be $S_c = 0.05$ for rr-P3HT and $S_c = 0.035$ for rra-P3HT used in the fitting routine in Figure 10.5. The results of solving the differential equations Eq. 10.5 - 10.5 is fitted to the data in Figure 10.5 with k_a, S_{tot} and D_c as free parameters simultaneously to all data series. The best fit is obtained with $k_a \approx 0.015\ \text{min}^{-1}$ for both rr-P3HT and rra-P3HT and sufficiently high diffusion constant D_c.

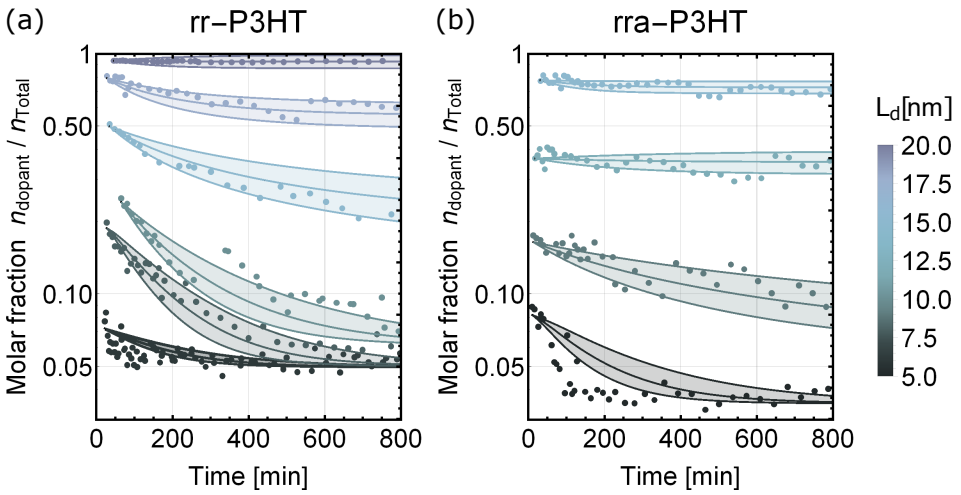

Figure 10.8: The figure shows molar surface fractions of Mo(tfd-CO_2Me)$_3$ versus time for rr-P3HT in a) and rra-P3HT in b) similar to Figure 10.5. In order to visualize the effect of variations in error margin of the parameters S_{tot}, k_a, they have been added with $k_a = 0.016 \pm 0.004$ and $S_{\text{tot}} = 0.084 \pm 0.003$ for rr-P3HT and $k_a = 0.015 \pm 0.005$ and $S_{\text{tot}} = 0.0580.002$ for rra-P3HT.

As a consequence, the diffusion constant is not a decisive factor and the time dependence in this model is mainly dominated by the incorporation or absorption rate k_c. However, the diffusion constant must not be chosen too small in order to get a good fit result. The sum of squared residuals X^2 is plotted in Figure 10.7, showing that for the best k_a, the dependence on D_c flattens out towards higher values, but increases if D_c is chosen too small. If a threshold for an acceptable X^2 is introduced based on the best X^2_{min}, a lower limit on the diffusion can be derived. Setting an acceptable tolerance requires a diffusion constant $D_c \geq 10^{-15}\ \text{cm}^2\ \text{s}^{-1}$ for rr-P3HT and $D_c \geq 3 \cdot 10^{-16}\ \text{cm}^2\ \text{s}^{-1}$ for rra-P3HT to sufficiently describe the data within this model. Although one obtains a similar k_a, a different total capacity of $S_{\text{tot}} = 0.084$ for rr-P3HT and $S_{\text{tot}} = 0.058$ for rra-P3HT is suggested by the model fit. The difference of S_{tot} is bigger than the error of

ca. 10% in L_0. Additionally, the dependence of variations in fitting parameters on the resulting concentration curves is illustrated in Figure 10.8. In general, the more complex diffusion model yields a better description of the data than the estimate only based on desorption. Within this model and to explain differences in Mo(tfd-CO_2Me)$_3$ capacity S_{tot} between rr- and rra-P3HT at high concentrations, the morphology of such thin films can be considered. Complementary electron diffraction measurements carried out by L. Müller on these samples reveal clear signal of a semi-crystalline morphology with crystallites being embedded in an amorphous matrix for rr-P3HT.[245] This is not found for rra-P3HT which agrees with previous studies.[261] The fully amorphous rra-P3HT has a slightly lower density than rr-P3HT, which suggests also a large free volume benefiting the diffusion of dopants. This does not agree with the observations of this study, however there is evidence that the rra-P3HT inter-crystalline regions in rr-P3HT have an even lower density than amorphous rra-P3HT.[258] Although there is no direct proof for this hypothesis, the low-density grain boundaries in rr-P3HT may play an important role in absorbing and improving the diffusion of dopants. For example, the mobility model of solvent molecules in polymers, which was derived from a statistical treatment, proposes a volatility:[134,137]

$$m_d \sim e^{-B_d/f} \ , \tag{10.6}$$

where m_d denotes the mobility, f the fractional free volume and B_d represents minimal void size that dopants need to perform a jump.[136] To shed further light on this hypothesis, imaging of dopant pathways could be attempted with scanning tunnelling or transmission electron microscopy, requiring molecular resolution and sufficient material contrast.

11 Drift of Molecular Dopants

Within this project, the mobility of molecular dopants was investigated by forcing the dopants to drift in an externally applied electrical field. If dopants undergo charge transfer, molecular ions are present in the organic host matrix that are sensitive to potential gradients. With a high enough applied electrical field, ionic migration becomes possible, if the potential barrier at the doping site is sufficiently lowered. This has been studied systematically by Müller et al. for p-doped P3HT in Figure 11.1.[120] The drift of F4TCNQ in P3HT can be observed with fluorescence microscopy on a laterally structured electrode setup having channels of ca. 125 μm length. If the electrical field reaches a certain threshold value, the dopant is pushed away from the cathode causing a change in contrast of the fluorescence signal in Figure 11.1a.

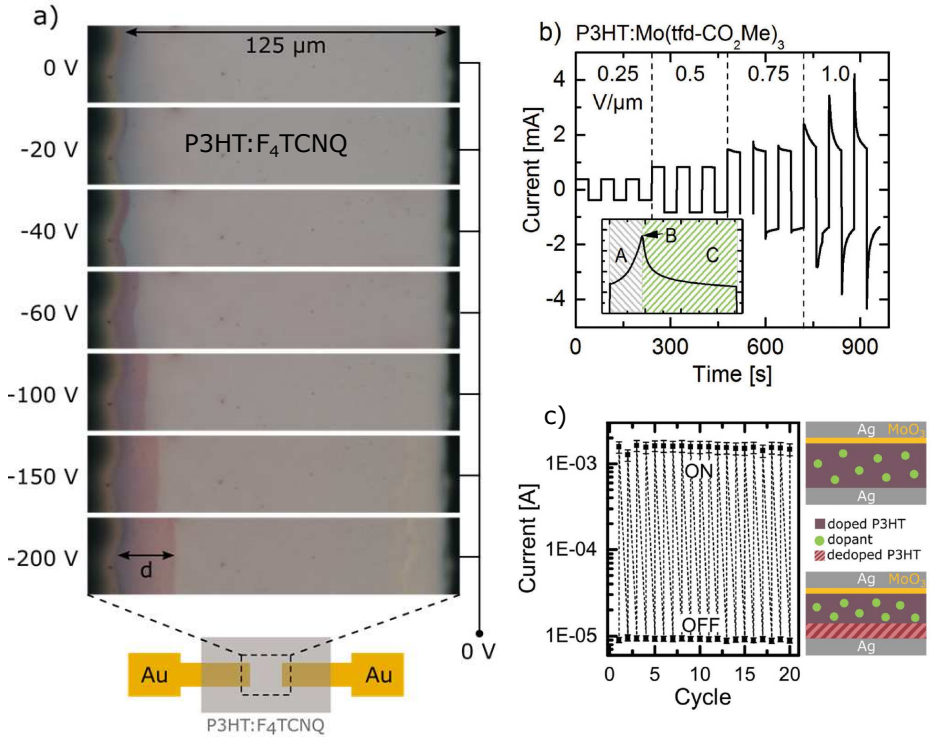

Figure 11.1: (a) Lateral micrographs of a P3HT:F4TCNQ channels between two gold electrodes (black) and an applied electrical field of strength between 0 and 1.6 V μm^{-1} for 30 s. Pure, undoped P3HT appears reddish/violet due to its absorption at 400 - 700 nm, whereas doped P3HT features a broader absorption and a greyish colour. (b) Current as a function of time for increasing constant electric fields of alternating polarity. At a field of ca. 0.75 V μm^{-1} the current decreases because an undoped region emerges from dopant drift. (c) Application of a memristor, which writes at high fields ($\geq$ 1V μm^{-1}) and reads out at low voltages. The difference in current is due to an undoped region at the silver contact. Modified from Müller et al.[120]

The emergence of an undoped region, which can be several microns in size, causes a subsequent fall-off in the current through the device. After reversing the bias, the doping distribution can be reversed as well, with the dopants subsequently drifting into the opposing direction. When choosing asymmetric contacts, a memristive device can be constructed based on the conductivity modulation that stems from a controlled dopant migration in Figure 11.1c. Since this work has not been done by the author, the reader is referred to Müller et al. for additional information.[120] Interestingly, for the small molecular transport material Spiro-MeOTAD a drift is not observed at comparable fields strengths. Furthermore, the drift in rra-P3HT seems to be less effective than in rr-P3HT. The drift of $Mo(tfd\text{-}CO_2Me)_3$ was additionally verified by IR microscopy. To run a similar experiment in UHV with XPS, a new sample holder was constructed, which allows an external voltage to be applied in-situ without breaking the vacuum. A doped P3HT film was spin-cast on a cleaned glass substrate and a finger-like electrode structure was evaporated on top. In this case we used aluminium as electrode and a thin MoO_x buffer layer in order to achieve sufficiently good charge carrier injection. In this case, silver is not chosen as electrode since the Ag 3s emission interferes with the F 1s peak, if a high pass energy is used and the analyser runs in constant energy mode. The finger structures were carefully connected at the edges with silver ink and clamps to the electrically separated screws of the sample holder in Figure 11.2a. With the help of an X-ray induced secondary electron imaging (SXI), the aluminium electrodes and the P3HT channels can be located showing a different contrast in Figure 11.2c, which is used to position the X-ray beam. The channel and the neighbouring contacts were scanned with a focused beam of 10 μm in diameter as sketched in Figure 11.2b.

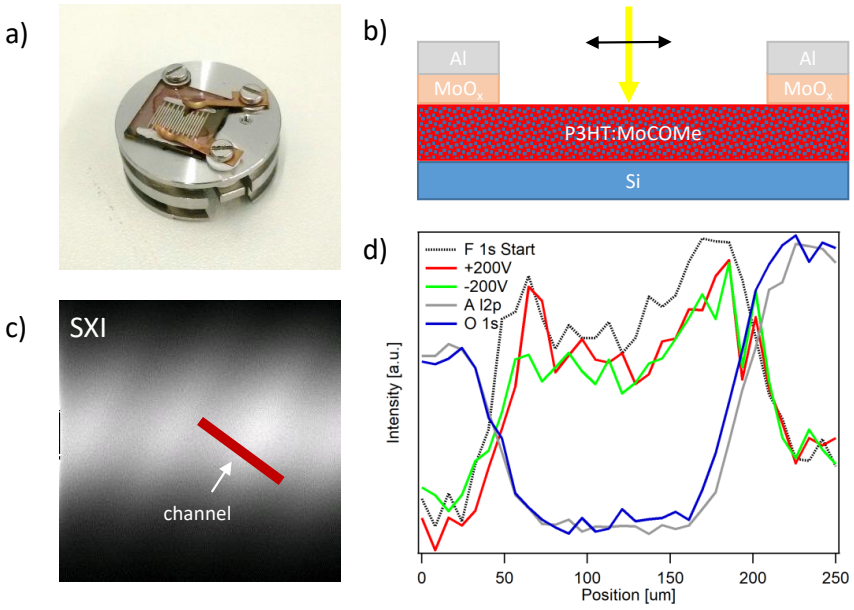

Figure 11.2: (a) Picture of the sample holder with doped P3HT film plus silver electrode connected via clamps. Sketch of the idea for this experiment in (b). X-ray induced secondary electron imaging (SXI) of the finger-like electrode structure in (c). The integrated intensity of the F 1s, Al 2p and O 1s emission as a function of the focused X-ray beam position in (d). The F 1s core-level was rescanned, as fast as possible, after a bias of +200 V (red) and -200 V (green) was applied.

For this purpose, the pass energy was set to 117.4 eV and spectra measured at constant binding energy at 688 eV using the channel electron multiplier to resolve the peak structure. The result of F 1s, Al 2p and O 1s integrated intensity as a function of position is depicted in Figure 11.2d. A clear pattern of the F 1s emission in between the Al 2p and O 1s signal, that is originating from the electrodes, can be distinguished matching the spacing of the evaporation mask of 200 μm. However a dependence of the F 1s signal on an externally applied voltage in red and green in Figure 11.2d was not observed. There has been a sequence of further attempts and tests to resolve the drift with XPS but which were not yet successful. It is possible, that the dopant concentration at the surface is not affected by the lateral current, or that only a few of the channels were active, since in the above setup all electrodes were run simultaneously. A vertical geometry, in which the voltage is applied between substrate and a surface electrode, was tested by evaporating a thin gold layer of a few nanometres onto P3HT, sought to be still transparent for XPS. The basic idea is to apply a voltage at the gold layer, while still being able to measure the core-level emission of the dopant beneath the gold layer. This attempt failed because a thin gold layer was found to be not conductive enough compared to doped P3HT. The current was therefore not distributed through the gold film, but running directly at the edges of the external contact into P3HT. The conductivity of the surface could not be increased by a fine copper grid, used for transmission electron microscopy (TEM).

Part III
Immobilization Approach

12 Anchoring and Activation

12.1 Spectroscopic studies on a model system

In order to study the linking process of small molecular dopants to organic semiconducting host matrices, a simple test molecule is chosen which bears a phenyl azide anchor and that is easy to synthesise. This molecule serves as a model for possible dopants and will not introduce a charge transfer. However, diffusion properties and interaction with its host matrix may be representative for suitable dopants. Within this model system one can additionally study and optimize film preparation processes and methods of activation such as UV-light and temperature. The body part is given by a naphthalene group, which is comparable in size to dopants like F4TCNQ or DMBI. For this study 2-((4-azidobenzyl)oxy)naphthalene (ABN) and its fluorine-substituted derivative 2-((4-azido-2,3,5,6-tetrafluorbenzyl)oxy)naphtalene (AF4BN) is used, which have been synthesised by S. Benneckendorf from OCI Heidelberg. Their structural formula is given in Fig. 12.1.

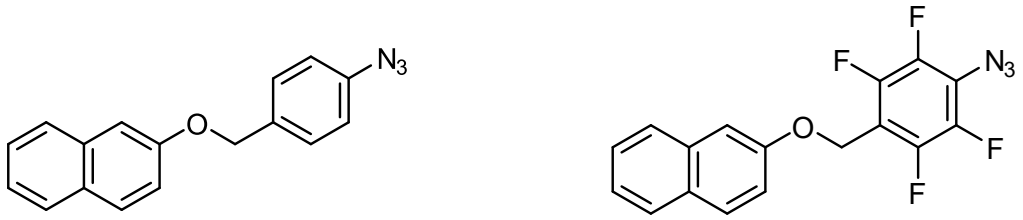

(a) ABN **(b)** F4ABN

Figure 12.1: The Figure shows the structural formula of the test molecules 2-((4-azidobenzyl)oxy) naphthalene (ABN) in (a) and 2-((4-azidobenzyl)oxy) naphthalene (AF4BN) in (b). Both molecules were synthesized by S. Benneckendorf from OCI Heidelberg.

As discussed in section 7.1 the fluorinated benzyl azide is expected to offer a higher yield of singlet nitrene insertion into alkyl chains or carbon-hydrogen bonds in general. Therefore, ABN and AF4BBN are investigated and compared by IR and XPS spectroscopy. Also UV-VIS Absorption measurements and microscopy imaging have been performed to further characterize the materials. The activation of the azide group by temperature or UV-light can be best detected by IR spectroscopy. To gain information on linking properties the azides have to be blended with suitable charge transport materials. In the following different concentrations were mixed with the p-type polymer P3HT and the n-tpye small molecule PCBM, which are solution-processable and offer different morphologies. From previous studies it is expected that polymers offer a higher diffusivity than small molecular hosts, which may also be present in this system.

12.1.1 Test Molecules ABN and AF4BN

Experimental Information: First, pure films of ABN and F4ABN were prepared by spin coating and drop casting on n-type silicon and on glass substrates cut into 1.5x1.5 cm^2 pieces. The azides dissolve readily in chlorobenzene already at room temperature. The materials were stirred on a hot plate at 50 °C as a test to increase solubility, but this did not affect the resulting film thickness. Depending on the measurement technique, the concentration of the solution was varied from 9 to 20 g L^{-1} in order to achieve a suitable film thickness. Spin coating was performed at 1000 rpm in a nitrogen glove box with an approximate humidity < 10 ppm. The samples were then shortly exposed to ambient conditions for carrying out all subsequent measurements.
An important step towards proving immobilization of the anchoring molecules is to track the azide's spectroscopic signature, which has to change upon activation. It is known from literature that reactions can be triggered by application of heat or UV light (250 nm).[205] For UV-activation of all azide containing films a mercury-vapor lamp GPH135T5L/4 from Peschl UV-products with a nominal UV-C power of 1.2 W at 254 nm was used. The penlight was mounted on a support above the sample at varying distance. In order to determine the total exposure, the light intensity at the sample position was measured using a Newport power-meter 1936-C equipped with a photo-diode 818-UV plus attenuator. The calibration measurement is shown in Figure 12.2 and follows a power law which agrees with an isotropic light source. Two fits have been made with either a strict x^{-2} or a general x^{-b} dependence on the distance to the sample x which both fit the data sufficiently well and yield a power factor of approximately 50 mW.

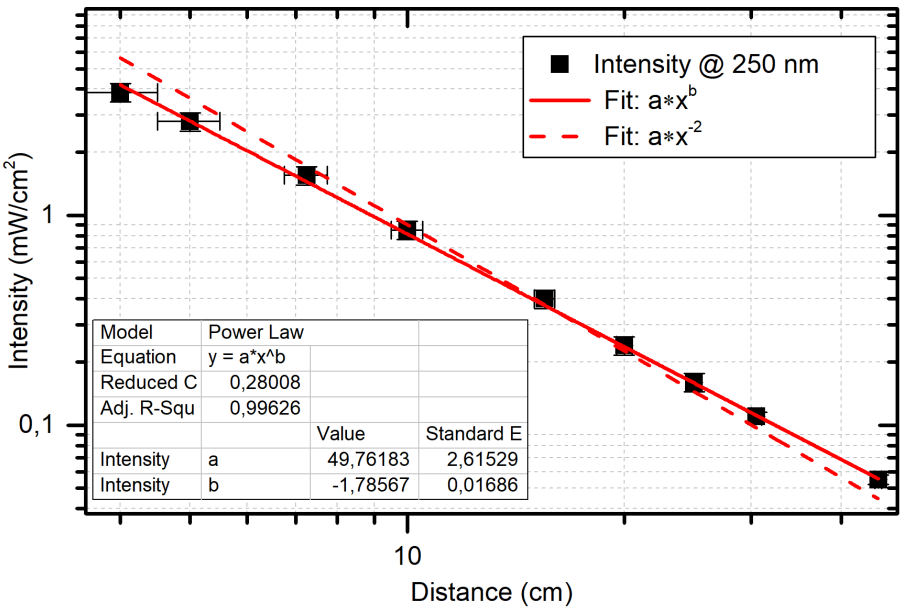

Figure 12.2: Intensity calibration of a discharge lamp, which is used to activate the azide inorganic thin films discussed below. The measured intensity is plotted versus the distance of the penlight to the sample position. From the fit we obtain a power factor of approx. 50 mW. The fit results are given in the inset for the model ax^b marked by a red line.

Results, Microscopy: Optical microscopy serves as a first tool to characterize the morphology of thin films on a macroscopic scale. Here, a Nikon Eclipse 80i reflected-light microscope with up to 100x objective magnification is used. Microscopy images of such films are shown in Figure 12.3. They exhibit a pronounced crystalline structure with crystal clusters of a few microns in size. The crystalline nature is further corroborated by cross-polarized light microscopy, where the directly reflected light is blocked by a polariser oriented at 90 degrees. The ABN crystals appear bright in the image, which arises form a slight rotation of polarization. Furthermore, de-wetting can be observed around dust particles. One can see holes in the film at higher magnification, which is likely connected to the material's tendency to from crystals. In addition, AF4BN was drop-casted from solution on silicon showing significantly larger crystals but also holes and ruptures, see Figure 12.3. In general the obtained azide layers are not compact or homogeneous and therefore disadvantageous for preparing pristine thin films. However, optimization of the film processing regarding solvent or substrate treatment was not conducted since the test molecules are not expected to act as a dopant and the precise energy levels are not of interest for this study. Optical transmission spectroscopy like IR or UV/Vis can still be reliably performed on such films but XPS and UPS are found to be challenging.

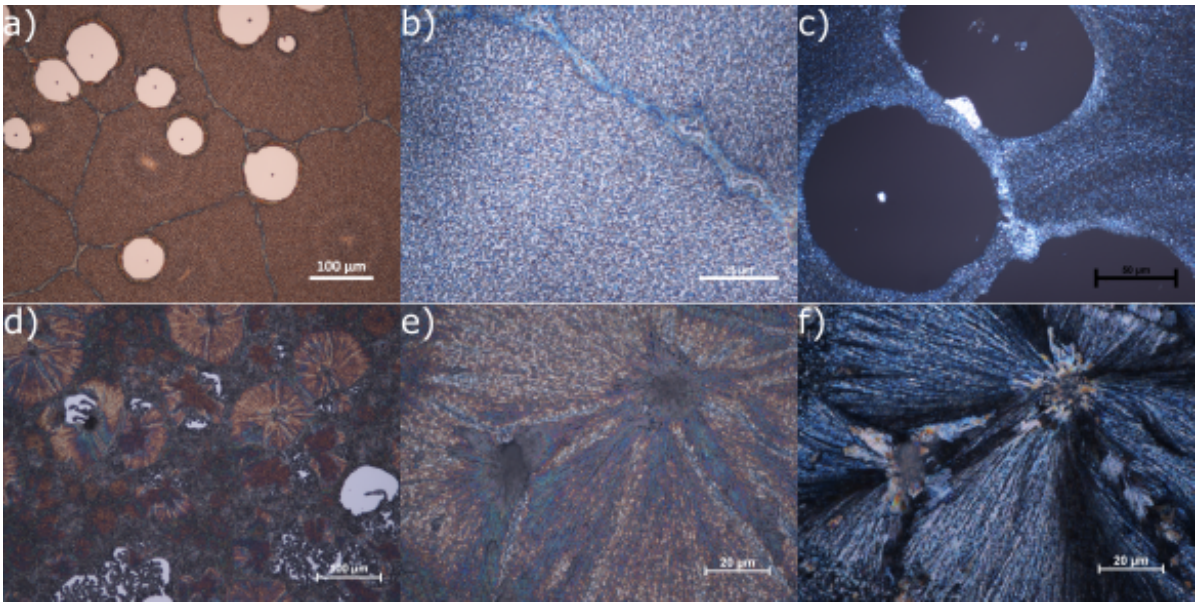

Figure 12.3: The Figure shows reflected-light microscopy images of a thin spin-cast ABN film in a), b) and under cross-polarization in c). ABN was cast on silicon from solution, which resulted in an approximate average film thickness of 35 nm. A film of AF4BN, which was drop-casted from solution, is given in d), e) and under cross-polarization in f). Scale bar: a) 100 µm, b) 25 µm, c) 50 µm, d) 100 µm, e) 20 µm and f) 20 µm.

Results, UV-Vis Absorption Spectroscopy: When pure films of ABN of AF4BN are activated in an inert atmosphere, complex reactions involving ketenimine expansion or triplet reaction are probably favoured compared to C-H insertion. Even partial polymerization or cross-linking is imaginable. Regardless of the mechanism, the transformed azide group can be seen as a marker of the reacted ABN molecules. Optical absorption is measured of pure acide films in Figure 12.4, using an Avantes AvaLight-DH-S-BAL light source and AvaSpec-ULS3648 spectrometer. From UV absorption measurements the absorption of the azide group is anticipated at about 250 nm (not visible in Figure 12.4), which triggers the photo-activation. In Figure 12.4 strong

absorption is observed in the UV and a tail extending into the visible and near infra-red. There are distinct bands at 300-350 nm, which are lost upon activation. These absorption bands can be related to the 2-methoxynaphthalene part of ABN and F4ABN.[262] In a cooled Argon matrix at 4 K or in the vapour phase of naphthalene comparable absorption bands have been measured at around 310 nm in literature.[263,264] These bands have been studied and assigned to an electronic long-axis polarized $^1B_{2u} \leftarrow {}^1A_g$ transition.[265,266] The possibly stronger absorption bands of naphthalene at 270 nm are not resolved in this spectrometer setup since the lower limit of the wavelength range is at 300 nm. The decrease in visibility of the naphthalene related absorption band is an indicator that the reactive azide group attacks the naphthalene body of neighbouring molecules. For pure ABN and F4ABN films possible insertion reactions are likely to involve the naphthalene group. It is important to compare them with absorption spectra of prototype matrix materials. For P3HT no significant absorption bands align with bands from ABN or AF4BN. For PCBM a distinct peak at ca. 335 nm, which is an orbitally allowed $^1T_{1u} \rightarrow {}^1A_g$ transition,[267,268] and a weak tail extending into the near-infrared overlaps with the spectral features of ABN and F4ABN. The absorption tail of PCBM is not expected to originate from artefacts but is related to intermolecular interactions.[269] A more detailed analysis on the activation reaction and molecular decomposition can be drawn from IR spectroscopy, testing ABN specific molecular vibrations.

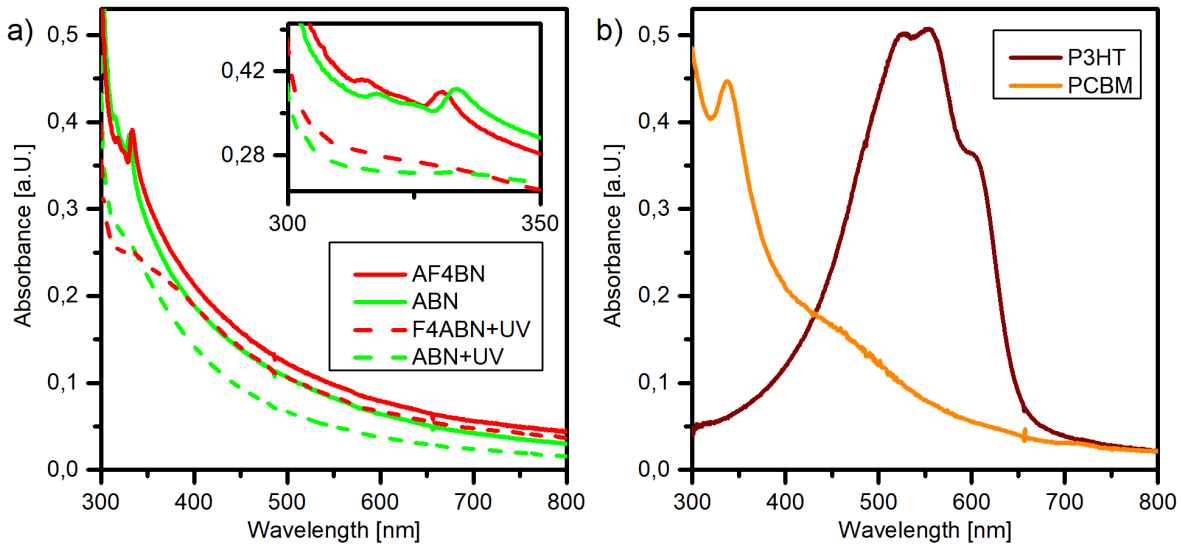

Figure 12.4: The Figure shows UV-Vis absorption spectra of ABN and AF4BN in comparison with the matrix materials P3HT and PCBM in (b). The UV-activated azide layers are represented by a dashed line in (a).

Results, IR-spectroscopy: Further insight into the activation process of the azide group in ABN and F4ABN is gained from IR spectroscopy. The subsequent IR measurements on the samples of this work were carried out and evaluated by H. Mager.[100] All samples have been measured on silicon in transmission geometry using unpolarized light at 7° incident angle. The spectra are recorded by a MCT detector averaging 200 scans. DFT calculations of ABN and F4ABN molecules in the gas phase are used to assign molecular vibrations to experimentally observed absorption bands. However, since the DFT calculation neglects inter-molecular interactions in the solid phase and is further dependent on the choice of exchange interaction and

basis set, it can not exactly predict peak strength and position. Nonetheless, an assignment of those absorption bands can be made which are influenced by the functional azide group. For both ABN and F4ABN the strong absorption band at about 2200 cm^{-1} is attributed to a pure stretching vibration band of the azide group. In addition there are vibrational modes from C-H bending vibration in the naphthalene body and the phenyl ring that seem to be influenced or affected by the azide group and its stretching mode. Such modes are expected to generate the strong absorption band of ABN at 1282 cm^{-1} and partially the very strong band of F4ABN at 1495 cm^{-1} (overlapping of two vibrational modes). A bending vibration of the azide group enters most likely at 791 cm^{-1} for ABN involving a bending vibration of C-H bonds in the naphthalene group. IR spectra of ABN and F4ABN are shown in Figure 12.5. The same sample is first measured directly after film preparation and is then activated by UV light in a glove box.

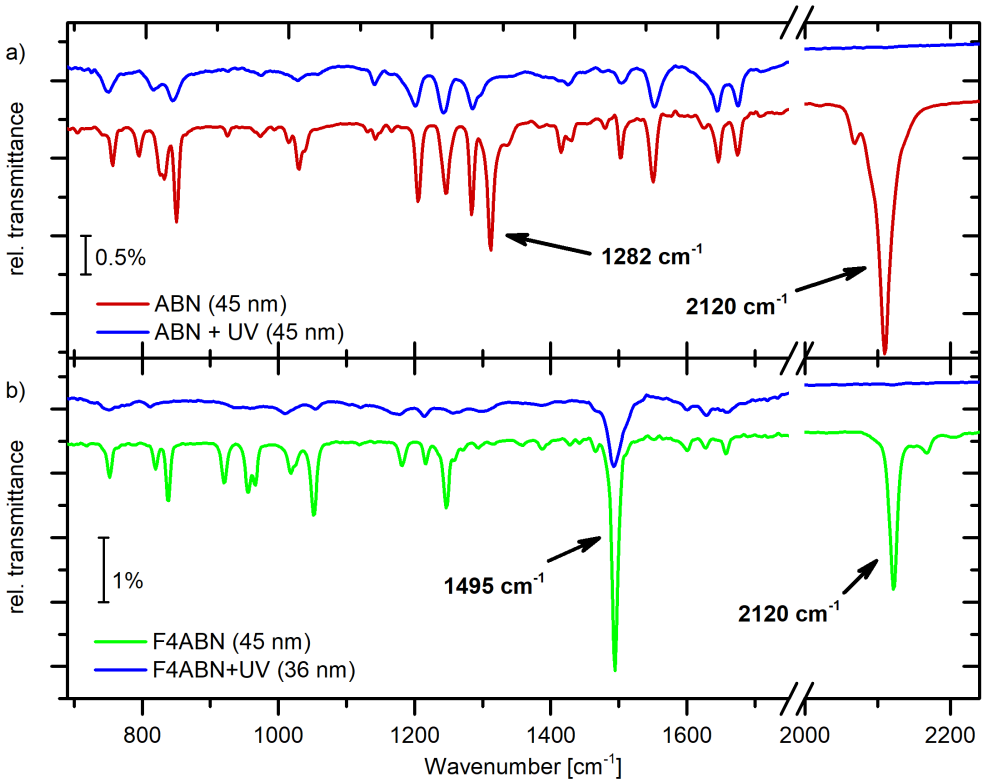

Figure 12.5: The Figure shows relative transmission spectra of ABN in red in (a) and of F4ABN in green in (b). The same film after UV activation is added in each sub-figure in blue. Thickness values in the legend are determined by ellipsometry. Important peaks are marked in the figure and are listed in Table B.1. The spectra have been measured and provided by H. Mager.[100]

After activation the peaks at 2200 cm^{-1} almost completely vanish and absorption bands that oscillate with the functional azide group are reduced in intensity, e.g. at 1282 cm^{-1} for ABN and at 1495 cm^{-1} for F4ABN. As a result, the reaction of the functional group within ABN and F4ABN can be clearly tracked. The samples have been measured before and after UV-activation using ellipsometry to determine the film thickness. Whereas the film thickness of ABN stayed approximately constant there seems to be a reduction of coverage for the F4ABN film as measured by ellipsometry and a suitable reflection model. In order to determine the proper order of magnitude for the UV-expose time, a step-wise activation was carried out. By

integrating the dominant vibration at ca 2100 cm^{-1} an estimate for the transformed fraction can be derived.

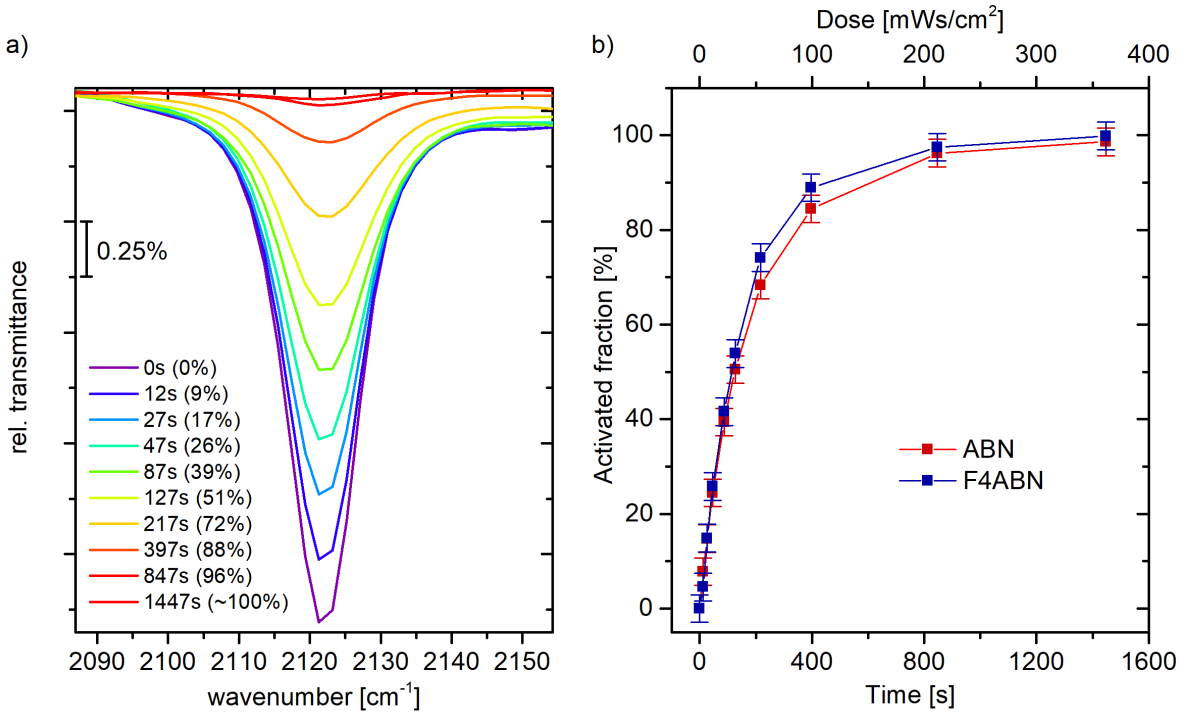

Figure 12.6: The Figure shows relative transmission spectra of F4ABN in the region of the azide's stretching vibration at 2100 cm^{-1} in (a) for various UV-exposure times. A continuous reduction in peak intensity can be verified. The normalized and integrated signal is plotted for ABN and F4ABN in (b). The spectra have been measured and provided by H. Mager.[100]

If the signal at time zero is taken as reference, a full transformation is achieved after 1500 s, which corresponds to a dose estimated from the penlight calibration to be about 0.6 J cm^{-2}. The progress of activation is plotted in Figure 12.6. By tendency a slightly faster activation is found for F4ABN compared to ABN. The peak integration can be further corroborated by a full oscillatory model (SCOUT) yielding similar results and can be followed in the Bachelor Thesis of H. Mager.[100] The precise reaction type or mechanism is however difficult to demonstrate. From Figure 12.5 one can see that there are no further absorption bands appearing which could have been assigned to new bonds or molecular states. The general loss in visibility and the broadening of peak shapes may indicate chemical reactions that involve new connections between molecules but also degradation in general. It should be noted that the spectrum of the pure activated F4ABN film shows much more broadening and reduced visibility than the corresponding activated ABN sample. Although this observation can not be clearly verified it agrees with the potentially higher reactivity of F4ABN which is assigned to the fluorine protected benzene anchor.

Results, Photoemission: As previously mentioned corresponding measurements with XPS and UPS are challenging, as pure ABN thin films are not stable under UHV conditions. To compensate for desorption to some extend, thicker layers have been processed from solutions with a concentration of up to 20 g L^{-1}. Since they are rather inhomogeneous and form islands (see Figure 12.3), partial charging and broadened line-shapes are difficult to avoid. This means

that they are not very reproducible concerning binding energy or absolute intensity. Therefore, the core-level spectra of ABN and F4ABN are not presented here (see Appendix Figure B.3) and merely principal observations are briefly summarized below for the sake of completeness.
If the film is exposed to UV radiation with a dose of 0.6 Ws cm^{-2} in an inert atmosphere, changes in the N 1s spectrum can provide a rough idea of the azide's signature. The N 1s peak shows a main component at 401 eV and a side-peak at 406 eV before activation. The two-peak structure is characteristic for the azide functional group, reported in literature.[179,185] The peak towards higher binding energies is assigned to the central electron-deficient nitrogen, whereas the main peak at 401 eV stems from the two lateral nitrogen atoms.[189] As a consequence the intensity ratio is expected to be 1:2, which roughly agrees with the data. After activation, the contribution at 406 eV vanishes and a single nitrogen peak remains that is likely originating from carbon-nitrogen bonds. Since intensity and exact binding energies are not meaningful, a change in overall peak intensity can not be correlated to a release of nitrogen. Nevertheless, the results indicate that the film is not activated by the X-ray's photo excitation. The O 1s emission is governed by SiO_2 from the native oxygen layer of the Si substrate. The covalently bonded oxygen of ABN is expected at about 533.5 eV and hardly visible for any sample. An oxygen component at a binding energy of about 536 eV may be assigned for the sample at highest coverage. This could be attributed to the covalently bonded oxygen, which suffers charging effects of the organic layer or generally to contaminations. The only reasonable contamination could be sodium with an Auger emission at 529 eV or 557.4 eV. Similar to ABN, the N 1s spectrum of AF4BN has a main component at 401 eV and shows a satellite at 405 eV vanishing after UV activation. It should be noted again, that at higher coverage, the spectral signatures are strongly shifted to higher binding energies making a clear analysis difficult. Significant for AF4BN is the strong fluorine emission and the carbon peak component at higher binding energies, which stems from carbon atoms bound to fluorine in the anchor group of F4ABN. Better spectra are obtained for F4ABN in blends for example with PCBM as shown in Figure 12.10. Due to a better film quality charging effects arising from inhomogeneity are not present in a suitable host matrix.

12.1.2 ABN and AF4BN blended with PCBM

Experimental Information: Blends of PCBM and the azide molecules have been prepared by mixing their respective solutions prior to spin-coating. PCBM was also dissolved in chlorobenzene and stirred on a hot plate at 50 °C for several hours. The preparation of the azide solution and film processing was conducted as described previously. Optical Microscopy revealed that a crystallization of the azide molecules occurs within the PCBM film if there is residual solvent present. Therefore the blends were annealed at 60-70 °C on a hotplate for 5 min in order to evaporate the remaining chlorobenzene. Quickly exposing the films to low vacuum was found to be working as well. The total concentration of 14 g L^{-1} for all mixing ratios was kept constant and resulted in a film thickness of ca. 45 nm, which was verified by profilometer measurements and ellipsometry.

Results, Microscopy: The crystalline azide molecules are found to segregate within PCBM thin films after spin coating under certain circumstances. From Figure 12.7 one can clearly see that the snow-flake like azide structures grow from seeds, which are caused by dust particles or other contaminations present in the film. The size of these structures depends on concentration but also varies with each sample. Furthermore cross-polarization microscopy highlight the patterns formed by the ABN crystals, because they are slightly changing the reflected light's polarization.

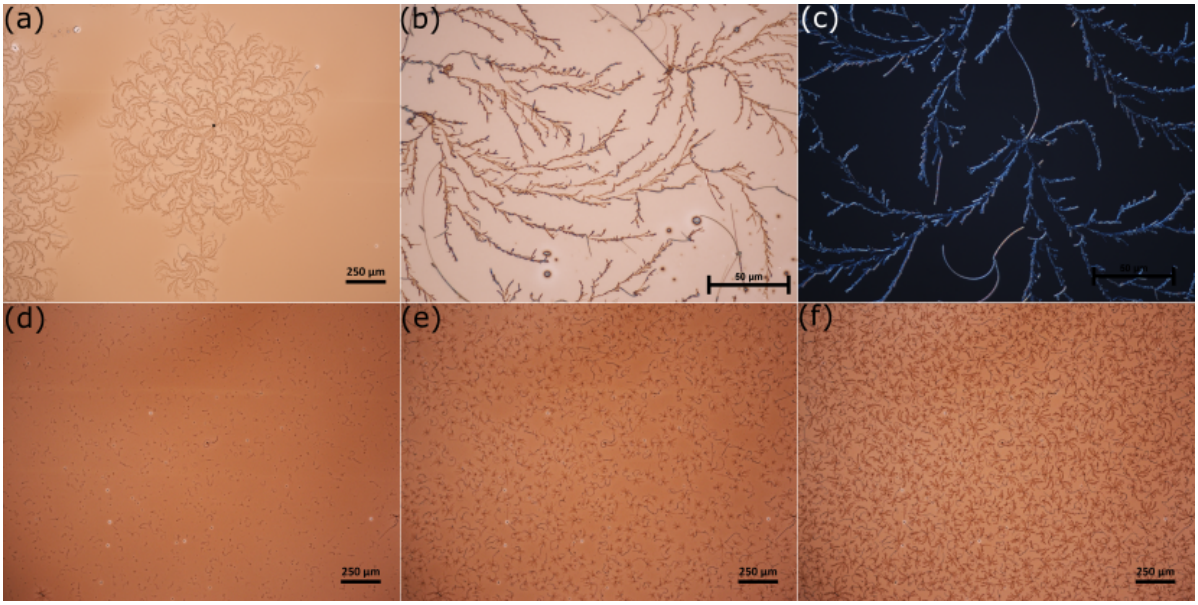

Figure 12.7: The Figure shows reflected-light microscopy images of PCBM mixed with ABN at a molar ratio of one. In (a) a very large structure is emerging from a black seed centered in the middle of the snow flake-like pattern. A zoom of (a) can bee seen with higher magnification in (b) and under cross-polarization in (c). The continuous growth of crystals in a single sample is depicted in (d)-(f). The Images (d)-(f) were taken ca. 5, 7 and 13 min after spin-coating. Scale bar: (a) 250 µm, (b)-(c) 50 µm and (d)-(f) 250 µm.

In particular, the continuous growth of the ABN structures on a very large scale can be nicely observed by microscopy. Here, the blended films were transferred from the glove-box directly to the microscope without annealing or vacuum treatment. The circular snow-flake patterns

then start to grow within minutes. This process predominantly occurs at high concentrations of ABN and is mediated by residual solvent in the film. This can be verified by comparing an annealed or vacuum treated film of similar concentration, which microscopically displays a neat film. The annealed film is further stable, at least for the observed period of a few hours, and does not develop any further crystalline structures. The few already formed crystals do not grow significantly. On the nano-scale, the morphology is of course completely unknown and may be composed of large clusters of ABN molecules.

Results, UV-Vis Absorption Spectroscopy: From the individual UV-Vis absorption spectra it could be presumed that all significant spectral features of PCBM and ABN are overlapping. however, as it can bee inferred from Figure 12.8, they are not distinctive in the blends. Interestingly the PCBM's π-π^* transition $^1T_{1u} \rightarrow {}^1A_g$ at ca. 335 nm decreases in the activated films.[268,270] A similar fading of characteristic absorption bands was also observed for the ABN bands at 300 - 350 nm of the pure materials since without host matrix present, the ABN molecules are likely to react with each other. This may be an indicator that PCBM undergoes a chemical reaction with ABN after UV activation. For pure PCBM a similar exposure with UV light leads only to a slight decrease in visibility of the $^1T_{1u} \rightarrow {}^1A_g$ transition[267,268] at ca. 335 nm, which may be related to polymerization or partial oxidation. However, there are no additional absorption bands arising in the blended films upon activation, see Figure 12.8. In any case, UV-triggered reactions of the PCBM blends can be verified by UV-Vis absorption spectroscopy that is likely occurring between PCBM and ABN or F4ABN.

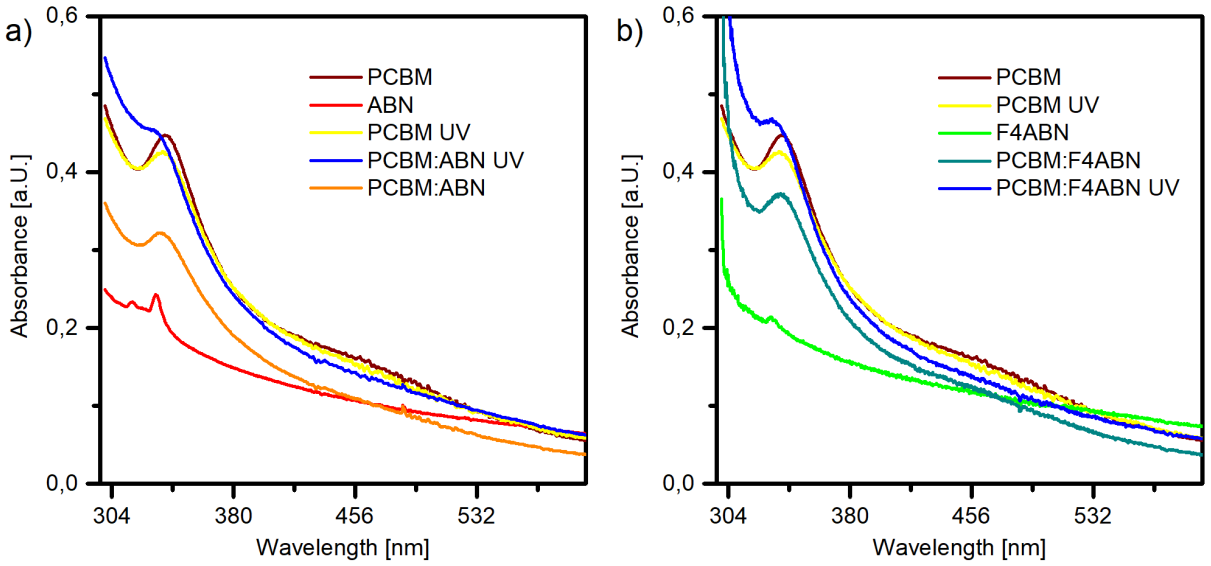

Figure 12.8: The Figure shows UV-Vis absorption spectra of ABN (a) and AF4BN (b) for the blends with PCBM at a concentration of 1 molar ratio (MR) for ABN and 0.5 MR for AF4BN. The activated layers are represented by a blue line. The spectra of PCBM and ABN or F4ABN are plotted for comparison. Different absolute absorption values can correlate with varying film thickness.

Results, IR-spectroscopy: Well defined films of high mixing ratio of ABN and F4ABN with PCBM have been investigated with IR spectroscopy by H. Mager and are plotted in Figure 12.9. The observed vibrational modes can be directly attributed to the spectra of pure PCBM and ABN or F4ABN in Figure 12.5 implying that there is no particular interaction between the

molecules before activation. Absorption strength and precise peak position of vibrational modes can slightly change as the azide stretching vibration of ABN at 2110 cm^{-1} in Table B.1 has shifted to 2113 cm^{-1}. Furthermore the C-O stretching vibration of PCBM at 1737 cm^{-1} is reduced in intensity compared to pure PCBM. Characteristic vibrational modes of ABN at 1282 cm^{-1} connected to the functional azide group can be found in the blended films as well. Similar observations can be made for F4ABN in PCBM, for example the F4ABN absorptions bands at 1495 cm^{-1} and 2120 cm^{-1} can be identified in spectra of Figure 12.9. Relative intensity ratios of vibrational modes are preserved in the blended films. If the blends are exposed to UV light in the glove-box an activation of the azide group can be verified. Vibrational modes linked to the functional azide group at 2110 cm^{-1} and 1282 cm^{-1} for ABN as well as at 1495 cm^{-1} and 2120 cm^{-1} for F4ABN are vanishing during UV exposure. PCBM related bands like the C-O stretching vibration at 1737 cm^{-1} remain unchanged after activation, which impedes making definite predictions or statements about azide reaction and immobilization.

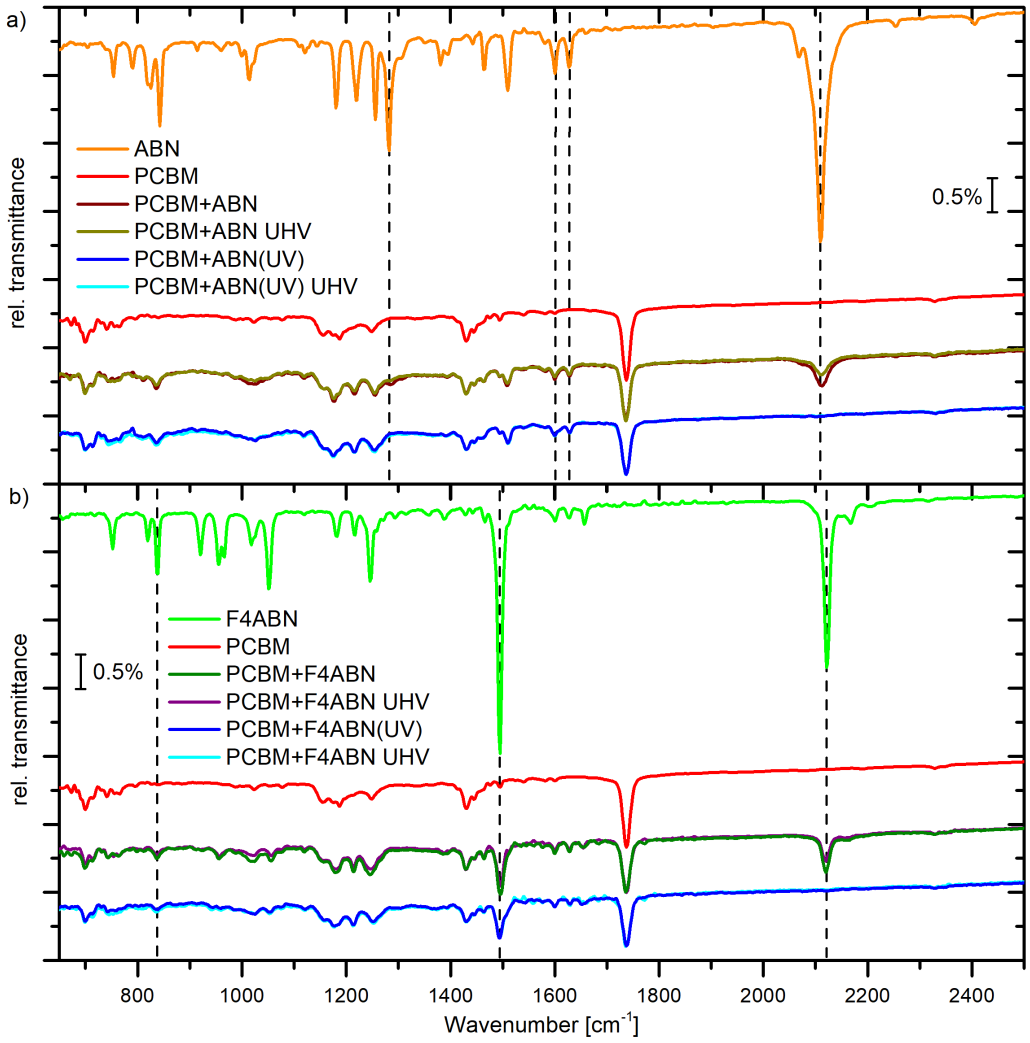

Figure 12.9: Relative transmission spectra of ABN blended with PCBM (a) and F4ABN in (b). The same film after UV activation is added in each sub-figure in blue. Important peaks are marked in the figure and can be compared with Table B.1. Each sample is remeasured after 22h UHV.The spectra have been measured and provided by H. Mager (Univ. Heidelberg).[100]

By integrating the absorption peak of the azide stretching vibration at around 2110 cm^{-1} the transformed ABN/F4ABN fraction can be estimated. After UV exposure for 5 min with an UV-power of 0.24 mW cm^{-2} about 47% of ABN and 67% of F4ABN molecules are activated. The converted fraction is much smaller compared to pure ABN films or mixed with P3HT. Since PCBM is strongly absorbing around 250 nm, it is believed that a higher UV-dose is required since PCBM is partially absorbing UV light to be used for activation. A full transformation of the azide is achieved after an additional 10 min exposure at 0.85 mW cm^{-2}. To test stability and volatility of ABN in PCBM the blended films are exposed to UHV conditions and measured again with IR spectroscopy to track ABN content. A decrease in ABN concentration is indeed observed for the non-activated films but corresponding IR spectra remain unchanged for activated films. This observation agrees with the following XPS measurements done under similar conditions. If it is assumed that only a negligible amount of azide is transformed at room temperature, one can use the strong absorption at around 2110 cm^{-1} to quantify ABN content. Under this assumption 19% of non-activated ABN has left the PCBM film in 2 hours and about 40 % after 22 hours showing significant desorption. Similar values are obtained for F4ABN.

Results, Photoemission: In contrast to the pure azide films, blends with PCBM can be properly characterized and analysed by XPS and UPS in various concentrations. In Figure 12.10 the spectra of PCBM mixed with ABN are plotted at a molar ratio ranging form 0.3 to 1 molar ratio (MR) before and after activation. The C 1s and O 1s emission is governed by PCBM and changes in these spectra are only observed at higher concentration of ABN after activation. Nitrogen exclusively occurs in ABN/f4ABN and can be used as a marker for activation. Before activating the film with UV-light, the N 1s spectrum clearly shows two distinct nitrogen species at an intensity ratio of 2:1.[179,185] In analogue to the pure ABN films the N 1s component at ca. 404.5 eV is attributed to the central electron deficient nitrogen atom and the main peak at 402 eV is assigned to the lateral nitrogen atoms.[189] The outer nitrogen atoms of the azide group differ slightly in binding energy, which can be anticipated by a little broader emission at 402 eV. Interestingly, the overall N 1s intensity before activation does not depend strongly on the concentration of ABN prepared in solution. In fact, after calculating the molar ratio of ABN according to Eq. 5.3 in Section 5.1 from the combined core-level spectra in Figure 12.10, it is found that the remaining ABN content is significantly lower. After activation, however, the ABN content agrees with the expected concentration assuming that the azide group has transformed into nitrene and released molecular nitrogen. The higher amount of ABN in the activated film can also be identified in the increase of the O 1s peak component towards lower binding energies stemming from C-O-C bonds present in the ABN molecule. For pure PCBM a small increase in the O 1s signal is found, mediated by UV-light which is due to an oxidation at the surface from residual oxygen in the glovebox. A decrease in the C 1s peak and a shoulder towards higher binding energies was observed for the sample with highest ABN content after activation. Furthermore, upon activation the peak component at 404.5 eV vanishes and a broader peak at about 399.5 eV emerges which is attributed to the formation of carbon-nitrogen bonds and consequently to a successful activation of the ABN molecule. From the N 1s emission one finds a complete ABN conversion for a dose of 1 J cm^{-2}, which agrees with results obtained from IR spectroscopy. The higher amount of ABN after activation can be assigned to an increase in stability of ABN in the film under vacuum conditions and therefore to a reduced volatility. Though it is not possible to determine if or how the ABN is connected with the PCBM matrix. The XPS core level spectra of F4ABN blended with PCBM are very similar to ABN mixed with PCBM (see Figure 12.10).

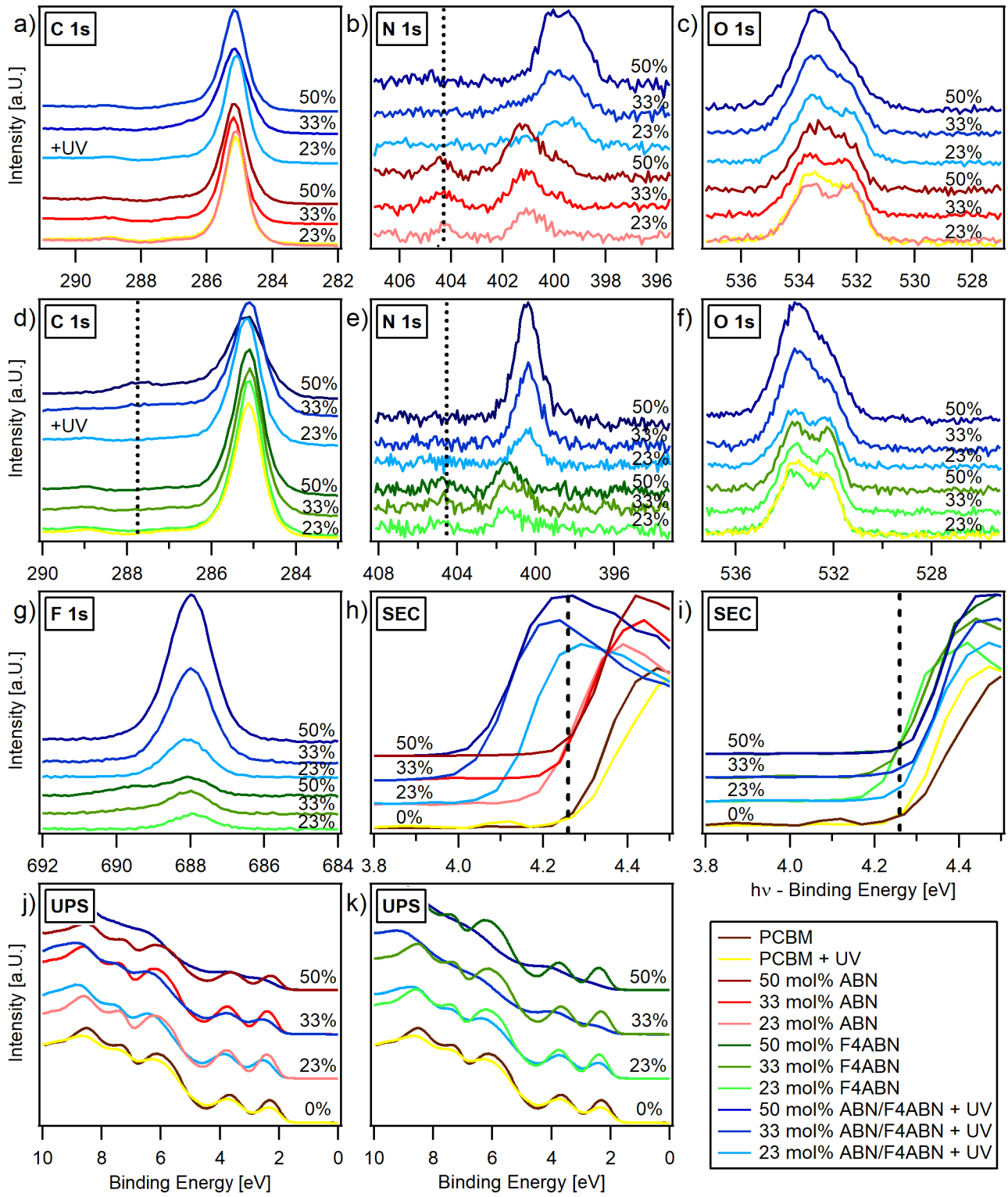

Figure 12.10: Core-level emission spectra of ABN in (a) - (c) and F4ABN in (d) - (g) blended with PCBM for various concentrations ranging from a molar ratio (MR) of 0.3 to 1.0 with respect to PCBM. The activated films are plotted in blue. The legend for all graphs can be found in the bottom. In (i) and (j) the secondary electron cut-off (XPS) is depicted for ABN and F4ABN, respectively. Corresponding UPS spectra are shown in (j) and (k).

The interpretation of the O 1s and N 1s emission series can be carried out as for F4ABN, which in principle possesses the same anchor group and anchoring mechanism. Correspondingly, a transformation of the azide group upon activation and an overall increase in F4ABN content is observed in the activated films. A larger F4ABN content in the activated films is attributed to a successful activation that prevents F4ABN molecules to leave the surface in UHV conditions since it is likely connected to neighbouring molecules. An indicator for this correlation is the much large N 1s peak at about 401 eV, which originates from C-N bonds and follows the initial concentration in intensity. In addition, the strong F 1s emission serves as a direct tracer for F4ABN molecules in the blend. Without activation only a small amount of F4ABN is detected which rarely depends on the F4ABN concentration in solution. In the detailed spectra of Figure 12.11, a peak analysis has been carried out to highlight changes in the N 1s emission upon activation. In the N 1s spectrum of the non-activated ABN sample a small peak component at 400.5 eV can be interpreted as a partial decay of the azide prior UV-activation.

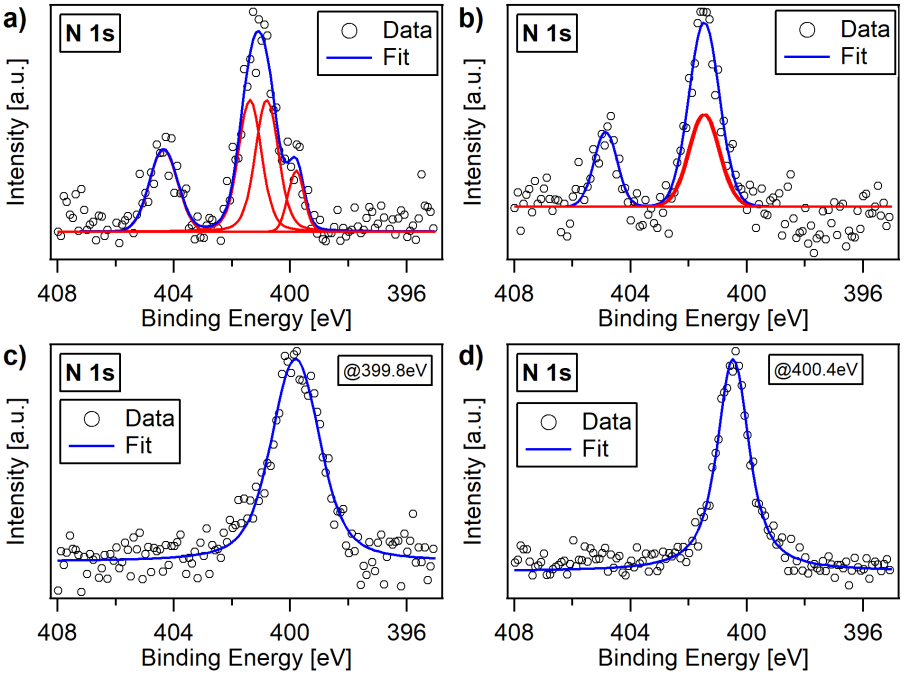

Figure 12.11: Fits of the N1s core level spectra of the PCBM blends with ABN in (a) and F4ABN in (b). The activated films are given in (c) and (d) for ABN and F4ABN, respectively. Single components are plotted in red and the total fit in blue.

A closer look at the F 1s spectrum for the non-activated films reveals a peak component at 689.5 eV which is not observed after activation for higher F4ABN content at comparable intensity ratios. If the azide group is exchanged with a N-H or C-H bond a strong shift of the F 1s level seems unlikely. A possible explanation involves intermolecular interactions. A first simulation provides indication for a shift of the F 1s core-level of 1 eV provided the fluorinated ring systems are directly stacking. If the F4ABN molecules are disordered within PCBM the F 1s emission is expected at 688 eV. This may be an explanation for the observed peak component at 698.5 eV for the non-activated PCBM:F4ABN films.

12.1.3 ABN and AF4BN blended with P3HT

Experimental Information: The P3HT films have been blended with ABN and F4ABN by mixing their respective solutions at a concentration of 14 g L^{-1}. Similar to the experiments conducted in the blends with PCBM, the materials were dissolved in chlorobenzene and stirred on a hotplate for several hours prior to spin-coating at 1000 rpm in a nitrogen glove box. After film deposition the just prepared thin films were directly annealed at 65 °C on a hot plate for 5 min in order to suppress segregation and crystallization of the ABN and F4ABN molecules in the polymer matrix. Unlike PCBM this post-treatment was not successful for P3HT since the segregation process already takes place during spin-coating, which is verified by Microscopy. Ellipsometry measurements on the P3HT films on silicon yield a film thickness of about 60 nm.

Results, Microscopy: In contrast to blends with PCBM, ABN and F4ABN are found to always segregate in P3HT regardless of the post-treatment. However, the degree of ABN and F4ABN crystallization is likely reduced by annealing of the P3HT film, which is shown for F4ABN in Figure 12.12 at a F4ABN content of 0.2 molar ratio (MR). For a content above 0.2 MR a thorough coverage of ABN and F4ABN crystals can be found even after an additional annealing step. The amount of ABN crystals above 0.2 MR seems to be much higher suggesting that at lower concentration not all ABN molecules have formed macroscopic structures.

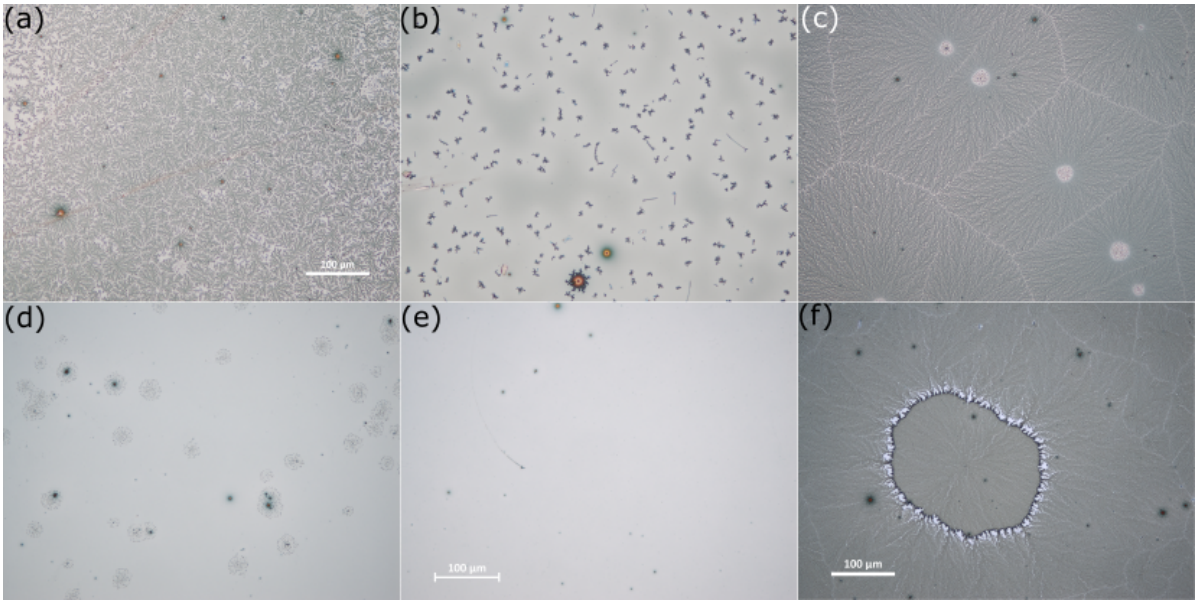

Figure 12.12: Reflected-light microscopy images of P3HT mixed with ABN and F4ABN. In (a) and (b) a film of F4ABN in P3HT at 0.2 molar ratio (MR) is shown where in (b) the film was annealed. In (c) and (d) a film of F4ABN in P3HT at 0.35 MR is exposed to UHV conditions. The film in (d) was activated by UV light before. In (e) a film of ABN in P3HT is shown at 0.1 MR and in (f) at 0.35 MR. Scale bar: (a) 100 µm, (e) 100 µm and (f) 100 µm.

The degree of segregation is difficult to quantify and furthermore not strictly reproducible as there have been films investigated at an ABN content of about 0.2 MR that varied in size and shape of ABN structures. By trend ABN seems to be more ready to form large structures than F4ABN for increasing content. In Figure 12.12 microscopy images are shown of F4ABN films which have been exposed to UHV conditions and which show a fading of the crystalline

structures. However, if the films have been activated with UV light before, these structures seem to persist and can be observed after retrieving the samples from UHV. Given the optically visible segregation, this suggests that the ABN molecules are immobilized because a partial polymerization or cross-linking between neighbouring ABN molecules has occurred, rather than with the P3HT matrix.

Results, UV-Vis Absorption Spectroscopy: The measured UV-Vis spectra for the blend in Figure 12.13 show ABN and F4ABN specific absorption since their spectral signatures do not overlap with those of P3HT. For example, unlike in PCBM the electronic long-axis polarized $^1B_{2u} \leftarrow {}^1A_g$ transition of naphthalene can clearly be identified between 200-300 nm similar to pure ABN films.[265,266] After activation these bands are reduced in visibility which is much more apparent for F4ABN, comparable to the spectra in Figure 12.4. Due to the fluorinated benzene ring a higher reactivity and potential CH-insertion efficiency of F4ABN is expected. From microscopy images considerable segregation is deduced, meaning a reaction of the nitrene radical with neighbouring ABN or F4ABN molecules seems likely. The UV-Vis spectra at higher wavelengths are dominated by the contribution of P3HT which rarely changes, if blended with ABN or after UV-activation. The shoulder at high wavelengths stays essentially unperturbed suggesting that the polymer order is maintained on the nano-scale. The peak structure above 500 nm is explained by a Franck-Condon coupled exciton-polaron series.[146] The lowest energy feature in the π-π^* range is associated with an inter-chain absorption and therefore benefits from domains of ordered P3HT forming weakly interacting H-aggregates.[144] Furthermore no polaronic feature is detected as it is known for electrochemical doping for example with F4TCNQ.

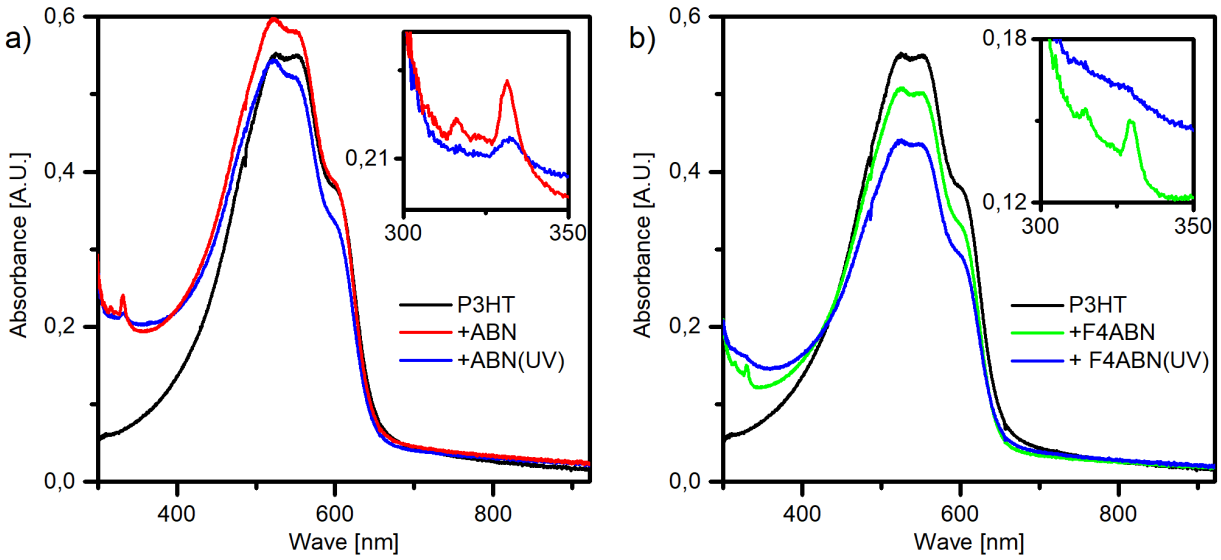

Figure 12.13: UV-Vis absorption spectra of ABN and AF4BN for the blends with P3HT at a concentration of approx. 0.2 molar ratio (MR). The activated layers are represented by a blue line.

Results, IR-spectroscopy: For the analysis of absorption bands in blends of ABN and F4ABN with P3HT thin films of about 55 nm have been measured in Figure 12.14 by H. Mager.[100] To increase visibility a rather high concentration of ca. 0.3 molar ratio of ABN/F4ABN was chosen for the presented spectra. As it is known from microscopy images ABN/F4ABN segregate at high concentrations forming large crystalline substructures which could not be prevented by

post-treatment with heat or vacuum to remove residual solvent. Identical measurements have been performed at lower concentration and homogeneous films, which led to corresponding absorption spectra with reduced strength of ABN/F4ABN bands agreeing with the initial ABN content. Consequently, for spectroscopy one has to make a trade-off between film quality and visibility of absorption bands. In Figure 12.14a each peak in the blend can be assigned to either P3HT or ABN with possibly small shifts that are due to a different dielectric background.

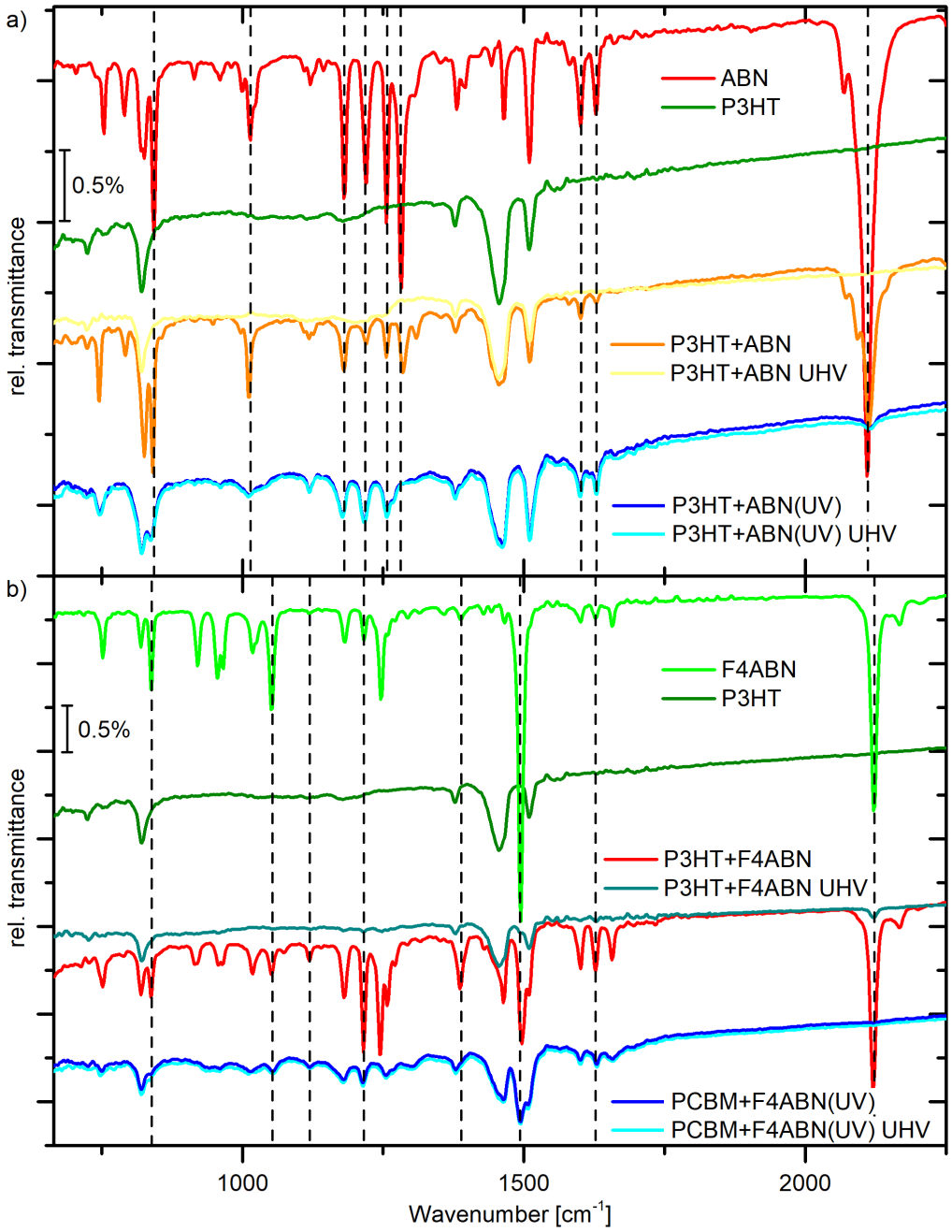

Figure 12.14: The Figure shows relative transmission spectra of ABN blended with P3HT (a) and F4ABN in (b). The blended film after UV activation is added in each sub-figure in blue. Important peaks are marked by a dashed line and can be compared with Table B.1. Each sample is further remeasured after 22h in UHV. The spectra have been measured and provided by H. Mager.[100]

Relevant peaks connected to the functional azide group of ABN at 1282 cm^{-1} and 2110 cm^{-1} can clearly be identified in the mixed films. Corresponding peaks can be found for F4ABN at 1495 cm^{-1} and 2122 cm^{-1} in Figure 12.14b. Remarkably, for F4ABN there are distinct peaks that are relatively gaining strength in the blend compared to the spectrum of a pure F4ABN film. They are located at 1118 cm^{-1}, 1386 cm^{-1}, 1600 cm^{-1}, 1625 cm^{-1} and at 1657 cm^{-1} as it can be inferred from the dashed markers in Figure 12.14. This increase in absorption of individual bands may be attributed to a different dielectric background leading to a modified electrostatic surrounding of F4ABN molecules favouring individual vibrations. In addition, the absorption band of P3HT at 1456 cm^{-1}, which is assigned to a stretching vibration of the thiophene ring,[238] seems to become asymmetric if blended with F4ABN. In the next step, thin films have been activated with UV-light at 254 nm with an approximate power of 0.24 mW cm^{-2} in a few cycles. The azide can be activated in P3HT which causes a disappearance of all azide-related vibration bands according to Table Appendix B.1 and a reduction of film thickness from e.g. 53 to 48 nm. For ABN there are some vibration bands showing an increased absorption upon UV-activation at 1220 cm^{-1}, 1510 cm^{-1} and at 1630 cm^{-1}. However, they can be assigned to C-H vibrations of the naphthalene group and therefore do not enable predictions about the precise anchoring mechanism. Since it is know that ABN crystallises at higher concentration, a reaction with neighbouring ABN seems more likely. But this means that an increasing ABN content does not give a better signal with regard to anchoring mediated changes of P3HT absorption. For F4ABN a general broadening and reduction in peak strength is observed similar to pure F4ABN thin films. With one exception, an increase in absorption upon activation can not be verified for F4ABN. A quantification of azide transformation is again made by integrating the strong stretching vibration of the azide group between 2046 cm^{-1} and 2170 cm^{-1}. A percentage of transformed ABN molecules of about 44% is obtained after one minute and of 89% after eight minutes UV-exposure. For F4ABN a significantly faster activation is found, where 90% are transformed after one minute. In general, the activation is slower compared to pure ABN/F4ABN films but much faster than for blends with PCBM. Consequently, the speed of activation depends on the UV-absorption of the host material. To test the stability of activated films, both UV treated and pristine blends were exposed to UHV conditions (10^{-8} mbar). Within limits of accuracy, all non-activated ABN/F4ABN molecules have evaporated from P3HT after approximately 20 h in UHV. It means that all ABN/F4ABN related absorption bands disappeared and the IR spectrum of a pure P3HT film is left in Figure 12.14. In contrast, the spectra of activated films essentially remained unperturbed and still held characteristic ABN/F4ABN features. It is concluded that if the blend was UV-activated, the ABN/F4ABN molecules are significantly less volatile and are ideally bound to neighbouring molecules. This was also observed for lower ABN/F4ABN concentrations of ca. 0.05 mol%, forming microscopically homogeneous films, for which a connection between P3HT and ABN/F4ABN is more likely. Moreover, ABN/F4ABN seems more diffusive in P3HT than in PCBM, where only about 40% of ABN molecules desorbed from PCBM under UHV conditions within the same time. For a more sensitive analysis blends of ca. 0.1 mol% were stored in the spectrometer at low vacuum of about 3 mbar for 75 hours. Here, a steady desorption of ABN/F4ABN was monitored, characterized by a decrease of significant vibration bands. Interestingly, after 72 hours significantly more ABN molecules (ca. 90%) left the P3HT film compared to F4ABN (ca. 20 %), which may be correlated to the higher tendency of ABN to segregate as seen by microscopy imaging.

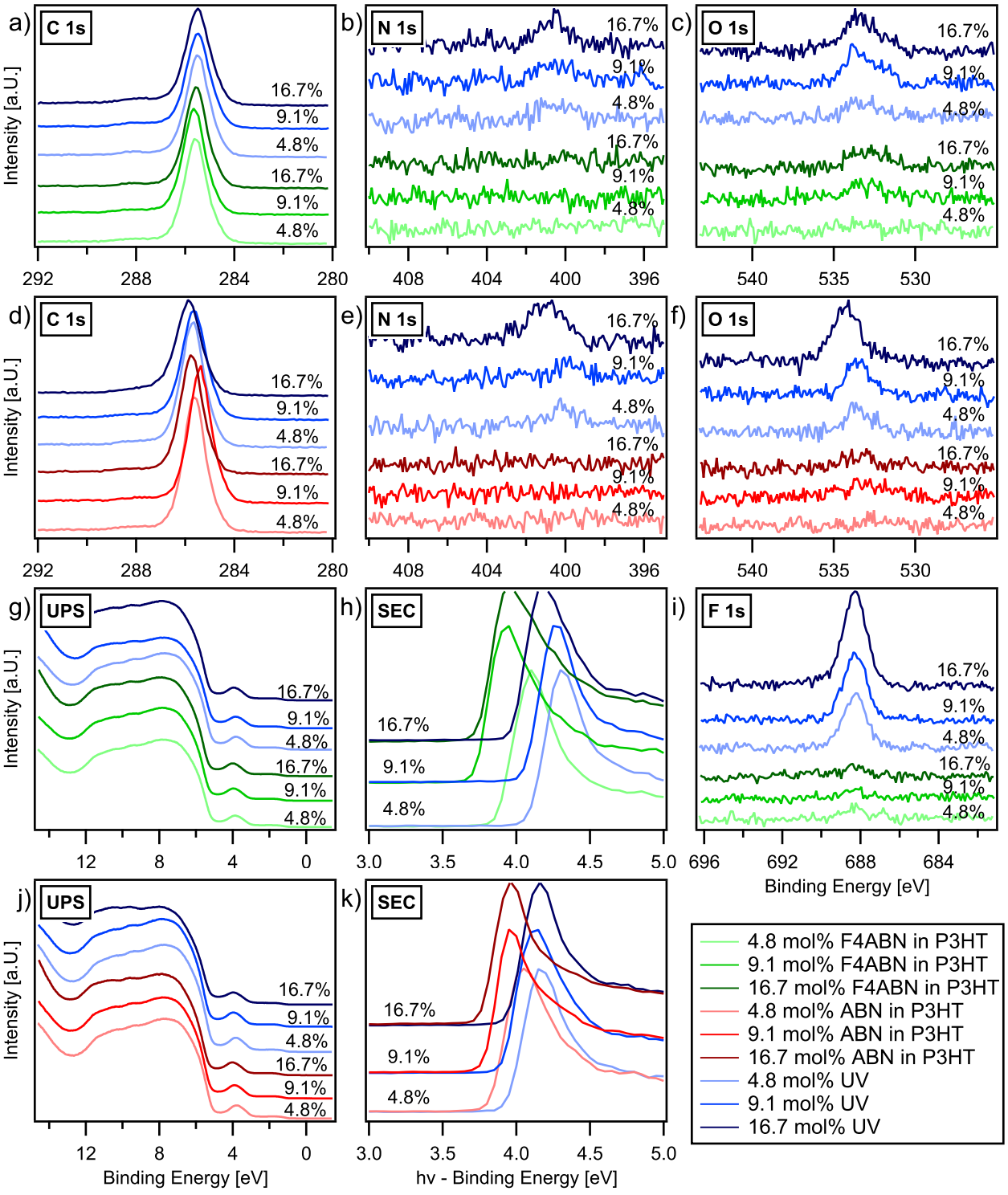

Figure 12.15: Core-level emission spectra of FABN in (a) - (c),(i) and ABN in (d) - (f) blended with P3HT for various concentrations ranging from a molar ratio (MR) of 0.05 to 0.2 with respect to a P3HT monomer. The activated films are plotted in blue. The legend for all graphs can be found in the bottom corner. In (h) and (k) the secondary electron cut-off (XPS) is depicted for F4ABN and ABN, respectively. Their energy axis is plotted as labelled in (k). Corresponding UPS spectra are shown in (g) and (j).

Results, Photoemission: Corresponding conclusions can be drawn from photoemission spectra of ABN/F4ABN blended with P3HT in Figure 12.15. The nitrogen N 1s and oxygen O 1s emissions serve as indicator to determine the presence of ABN/F4ABN since P3HT does not contain nitrogen nor oxygen. In the case of F4ABN there is additionally the strong F 1s emission present. For thin films which have not been activated by UV light only a little amount ABN/F4ABN can be detected at the surface in UHV. Without UV-activation the N 1s and F 1s signals are hardly detectable and further independent of the initial ABN/F4ABN concentration in solution. The loss of ABN/F4ABN is much more distinct for P3HT than for PCBM where a clear azide signature is measured showing that the functional group is intact. However, after UV-activation a single broad N 1s peak can be detected at ca. 400 eV stemming most likely from carbon nitrogen bonds for both ABN and F4ABN. After activation an O 1s peak at ca. 533.5 eV is measured, agreeing with the C-O-C bond connecting the naphthalene group and the benzene group. In case of F4ABN the additional F 1s emission at ca. 688 eV originates from C-F bonds in the benzene group. The molar concentration can be calculated according to to Eq. 5.3 in Section 5.1 and agrees, in the case of UV-activated films, with the concentrations prepared in solution. A shift in Fermi level position is not observed in neither UPS nor XPS spectra, meaning that ABN/F4ABN are not inducing a charge transfer or acting as a dopant for P3HT. A change of the work function in Figure 12.15h,k after UV-activation may also be explained by ABN/F4ABN being anchored to the surface. Consequently, the work function is not only determined by P3HT but is affected by ABN/F4ABN residing on the surface. This is not the case, if ABN/F4ABN evaporates from the surface without activation. On the other hand, the UPS spectra of the P3HT blends in Figure 12.15g,j do not show a distinct contribution of ABN/F4ABN. However, there are also no clear HOMO features observed for the UPS measurements of pure ABN/F4ABN in Figure Appendix B.3. In summary, it is believed that there are bound ABN/F4ABN molecules present in the P3HT film upon UV-activation. Without activation ABN/F4ABN tend to evaporate from the P3HT surface before the first measurement in UHV regardless of the initial concentration. Given the above results, the ABN/F4ABN test molecules seem to be more diffusive in P3HT than in PCBM, which is a small molecule forming an amorphous film that has probably less voids than a semi-crystalline polymer such as P3HT. The precise anchoring mechanism can not be deduced by XPS measurements. One can only state that there are new C-N bonds formed after activation. At high concentration a segregation of ABN/F4ABN suggests reactions with neighbouring ABN/F4ABN molecules, which could render them less volatile because dimers or oligomers of ABN/F4ABN will have a higher mass and more hindrance in diffusion or desorption.

13 PCBM doped with o-AzBnO-DMBI

In order to test doping and anchoring capabilities of o-AzBnO-DMBI with respect to the non-azide reference dopants *o*-BnO-DMBI and *o*-MeO-DMBI, the molecules have to be blended with a suitable host material. In principle, a n-type polymer yields a potentially higher diffusivity for small molecules. Most of the literature concerning DMBI reports on strong n-doping of PCBM or C60.[218–220,222,223,225,226] Naab et al. showed doping of the n-type polymer P(NDI2OD-T2)/N2200 with DMBI dimers to perform better than DMBI-H but still found an order of magnitude lower conductivities for P(NDI2OD-T2) compared to PCBM.[226] Moreover, the low doping efficiency for DMBI in P(NDI2OD-T2) was attributed to a poor miscibility of dopant and polymer, which can cause agglomeration or segregation during processing. To improve this, Kiefer et al. attached polar side chains to the copolymer p(gNDI-gT2), which is similar to P(NDI2OD-T2), increasing both miscibility and conductivity.[271] This also holds for a fullerene derivative with a hydrophilic triethylene glycol type side chain (PTEG-1).[272] Since there is no access to a modified n-type polymer for this work, the investigation is continued with PCBM as matrix material and not with P(NDI2OD-T2) even though a higher diffusivity could be expected in a polymer.

13.1 Conductivity Measurements

Doping of PCBM with DMBI or DMBI-N leads to a significant increase in conductivity. To verify that o-AzBnO-DMBI is doping PCBM at comparable conductivities, IV-measurements were carried out by M. Barf from TU Braunschweig on patterned finger-like silver contacts with different channel lengths.

Experimental Information: All dopants and PCBM have been solved in chlorobenzene at a total concentration of 10 g L^{-1} and were mixed right before spin-coating, which was done at 1000 rpm for 60 s in a nitrogen glovebox. Since the dopants are not particularly stable in solution they were dissolved for a period of 5 min before processing, whereas PCBM was stirred at 50 °C overnight. As substrate glass with finger-like structured silver contacts was used with channel lengths between 25 μm and 30 μm. Voltages were applied on these contacts using the Semiconductor Parameter Analyzer 4155C by Agilent Technologies, which reads out corresponding currents for conductivity measurement. Conductivities were then calculated from a set of at least three different samples. For UV-treatment a mercury discharge lamp is used at an intensity of 0.85 mW/cm^2 for 20 min in nitrogen atmosphere, calibrated in Section 12.1. Annealing of the samples was carried out on a hot-plate in the nitrogen glovebox at 75 °C for one hour. The molar doping ratio was set to 1:10 in solution.

Analysis: An increase of 5 orders of magnitude was found for PCBM films doped with o-AzBnO-DMBI and o-BnO-DMBI compared to pure PCBM, which translates to values of 10^{-5} S m^{-1} for PCBM rising up to 0.1 S m^{-1} of doped films in Table 13.1. If doped films are annealed at 75 °C for one hour, the conductivities rise further to 1 S m^{-1}. The increase in conductivity after annealing can be assigned to a temperature-induced hydride transfer, generating more DMBI radicals and thereby increasing the number of PCBM radical anions, which ideally generates also more free charge carriers. After UV-treatment, which is supposed to trigger azide

reactions, a clear decrease in conductivities is observed. Although UV-activation is done under nitrogen atmosphere, residual oxygen or water leads to an oxidation of the thin film surface, as evidenced by XPS in Section 13.3. However, after annealing the conductivity can be raised again to about 1 S m^{-1}, see Table 13.1. This trend can be observed for both *o*-AzBnO-DMBI and *o*-BnO-DMBI. There is also indication that activated *o*-AzBnO-DMBI offers improved elec-

Dopant	treatment	conductivity [S/m]
PCBM	-	$(1.03 \pm 0.44) \cdot 10^{-6}$
PCBM:*o*-MeO-DMBI	as cast	0.007 ± 0.002
PCBM:*o*-AzBnO-DMBI	as cast	0.07 ± 0.04
PCBM:*o*-AzBnO-DMBI	75 °C for 1h	0.9 ± 0.3
PCBM:*o*-AzBnO-DMBI	UV	0.015 ± 0.004
PCBM:*o*-AzBnO-DMBI	UV, 75 °C for 1h	1.0 ± 0.2
PCBM:*o*-BnO-DMBI	as cast	0.01 ± 0.004
PCBM:*o*-BnO-DMBI	75 °C for 1h	0.38 ± 0.2
PCBM:*o*-BnO-DMBI	UV	0.005 ± 0.002
PCBM:*o*-BnO-DMBI	UV, 75 °C for 1h	1.35 ± 0.1

Table 13.1: Conductivity of thin films of PCBM doped with o-AzBnO-DMBI and o-BnO-DMBI at a molar ratio of 1:10, measured by M. Barf (TU Braunschweig).

trical stability observed at very high field strengths. Similar to the drift experiments mentioned in Section 11, a non-linear increase in current paired with a subsequent hysteresis was measured for PCBM doped with *o*-BnO-DMBI or *o*-AzBnO-DMBI at high fields. A UV-treatment had no effect on o-BnO-DMBI doped samples, however, for UV-activated *o*-AzBnO-DMBI a trend towards linear IV-characteristic was found. The hysteresis can either be explained by contact modification/degradation, or by ionic movement, i.e. mobile dopants. Consequently, the suppressed hysteresis for UV-treated *o*-AzBnO-DMBI, at least supports a possible immobilization of dopants.

13.2 IR-Spectroscopy

IR-spectroscopy is the primary tool to check azide reaction in the bulk of the PCBM film by tracking the azide stretching vibration at 2109 cm^{-1}. When treating the sample with UV-light under nitrogen atmosphere, it is important to ensure that azide decomposition is not only triggered at the surface and reversely, that UV-induced oxidation does not affect the whole PCBM film, but only its surface. Details about the specific azide reaction products could not be elucidated with IR-spectroscopy. IR-measurements have been done by S. Beck (Univ. Heidelberg).

Experimental Information: The films were prepared similarly to the samples in the previous section, namely from a 10 g L^{-1} chlorobenzene solution with a doping ration of 1:10 and spin-cast at 1000 rpm for 60 s. After spin-coating, the substrate's backside was cleaned with chlorobenzene. As substrates ca. 1 mm thick cut n-type/intrinsic FZ silicon wafers ($\sigma > 6000\ \Omega$ cm) were used, which were pre-cleaned in an ultrasonic bath. Activation and annealing was carried out identical to Section 13.1 or 13.3.

Analysis: IR transmission measurements of PCBM doped with *o*-AzBnO-DMBI are given in Figure 13.1. The pure transmission spectrum of *o*-AzBnO-DMBI shows a distinct peak at 2109

cm^{-1} assigned to the stretching vibration of the azide group. This mode can also be identified in the blend with PCBM, which completely vanishes after UV-treatment, suggesting that the azide has almost fully transformed within the film. However, similar to the model system in Section 12.1, there are no other distinct features in the relative change in Figure 13.1 that could allow an in-depth interpretation of the reactions involved in the azide decomposition. Nonetheless, no severe degradation from UV-treatment is found for neither pure PCBM nor doped PCBM, which could be expected from the decrease in conductivity measured in Section 13.1 or oxidation of the entire thin film opposed to the surface oxidation identified in Section 13.3. This would have caused a visible increase in for example C-O stretching vibrations due to oxidation from residual water or oxygen in the nitrogen glovebox.

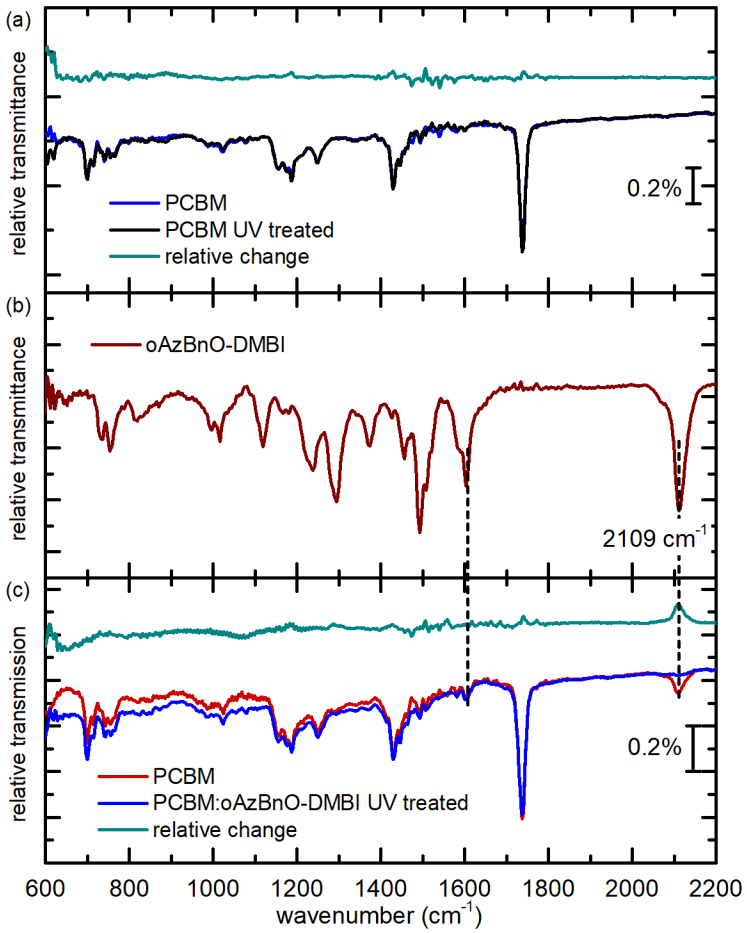

Figure 13.1: IR transmittance spectra of PCBM in (a), the dopant *o*-AzBnO-DMBI in (b) and the blend at a molar ratio of 1:10 in (c). The UV-treated films are plotted in blue in (a) and (c) together with their relative change to highlight UV induced changes. Most distinctive is the reduction at 2109 cm^{-1} of the azide stretching vibration. The data were measured and provided by S. Beck and R. Bäuerle (Univ. Heidelberg).

13.3 Photoelectron Spectroscopy

Photoelectron spectroscopy measurements are carried out on PCBM films doped with *o*-BnO-DMBI and *o*-AzBnO-DMBI at different concentrations. As a result, doping of PCBM by *o*-AzBnO-DMBI can be verified and their reaction mechanism classified. For sample preparation and azide activation, settings and methods are used as developed in Section 12.1 with test molecules ABN/F4ABN.

Experimental Information: Thin films were spin-cast from a 5 g L^{-1} chlorobenze solution on solvent cleaned silicon n^+-Si substrate. The dopants were dissolved shortly before deposition, whereas the PCBM solution was stirred at 50 °C overnight. For activation of the azide group, a mercury discharge penlight at 254 nm it used, mounted above the sample in a nitrogen glove-box. The UV dose was estimated to be about 1 J cm^{-2} given an intensity of 0.85 mW/cm^2 and an exposure time of 20 min. Optional annealing of the thin films was done on a hot plate in a nitrogen glove-box for one hour at 75 °C.

Results UPS: For PCBM films doped with both *o*-BnO-DMBI and *o*-AzBnO-DMBI one observes a Fermi level shift towards the LUMO of PCBM, which means that the HOMO in Figure 13.3a, b shifts to higher binding energies. This coincides with a reduction of the work function in Figure 13.3c, i and a shift of the C 1s and O 1s core level emission in Figure 13.4. These observations also agree with the significantly improved conductivity of doped PCBM films in Section 13.1. Furthermore, one finds a slightly larger Fermi level shift for *o*-BnO-DMBI compared to *o*-AzBnO-DMBI in Figure 13.3b, i suggesting that *o*-BnO-DMBI has a higher doping efficiency than *o*-AzBnO-DMBI. The measured Fermi level shift is summarized in Table 13.2. A slightly larger

Dopant	treatment	HOMO onset [eV]	Work function [eV]	C 1s [eV]
PCBM	-	1.85	4.2	285.2
o-AzBnO-DMBI	9 mol%	2.05 (0.2)	3.9 (0.3)	285.42 (0.22)
o-AzBnO-DMBI	9 mol%, UV	1.79 (-0.05)	4.13 (-0.07)	285.28 (0.08)
o-AzBnO-DMBI	9 mol%, 75°C	2.15 (0.3)	3.8 (0.4)	285.58 (0.38)
o-AzBnO-DMBI	9 mol%, UV+75°C	1.95 (0.1)	4.0 (0.2)	285.45 (0.25)
o-BnO-DMBI	9 mol%	2.2 (0.35)	3.8 (0.4)	285.6 (0.4)
o-BnO-DMBI	9 mol%, 75 °C	2.2 (0.35)	3.8 (0.4)	285.55 (0.35)
o-BnO-DMBI	9 mol%, UV+75 °C	1.95 (0.1)	3.95 (0.25)	285.45 (0.25)
o-AzBnO-DMBI	50 mol%	-	3.5 (0.7)	285.47 (0.27)
o-AzBnO-DMBI	50 mol, UV%	-	3.75 (0.45)	285.42 (0.22)
o-BnO-DMBI	50 mol%	-	3.43 (0.77)	285.43 (0.23)

Table 13.2: Determined energy positions for doped PCBM. The shift with respect to the PCBM reference in the first line is noted in brackets. The HOMO onset and work function values have been determined by linear extrapolation to zero at highest slope. Due to the strong HOMO broadening an extrapolation is not meaningful at concentrations around 50 mol%.

shift in the secondary electron cut-off (SEC) can be attributed to dopants at the surface, locally reducing the work function. For comparison, Naab et al. found a Fermi level shift of up to 500 meV, being slightly higher than the measured values in this work.[225] The measurement of Naab et al. was carried out on ITO as substrate and with *o*-MeO-DMBI as dopant, starting from a more

intrinsic PCBM layer which can depend on the substrate. As a consequence the precise value of the Fermi level shift is not as important as the movement of several 100 meV.

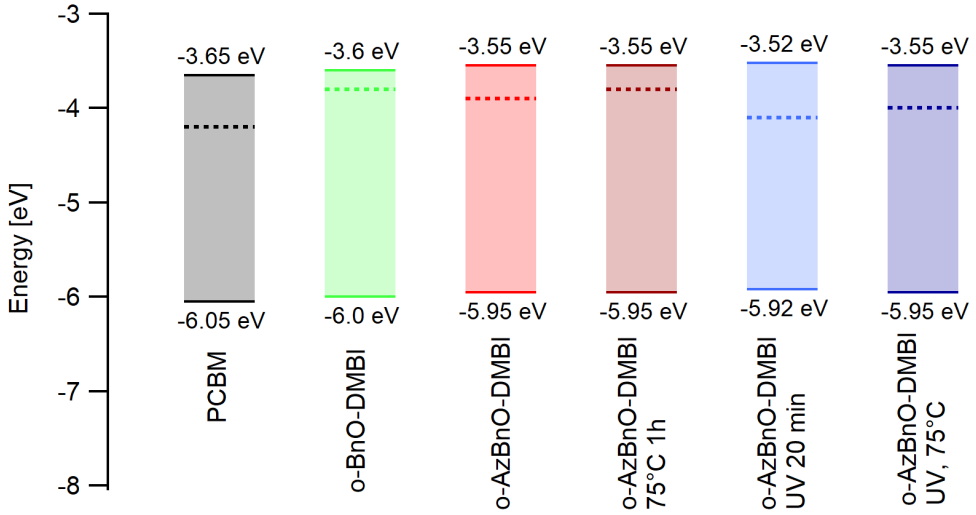

Figure 13.2: Presentation of energy diagram as calculated from Table 13.2 with constant band gap of 2.4 eV.

After UV-treatment, which is supposed to activate the azide and to engage anchoring of the dopant, a significantly reduction in visibility of the valence spectrum of *o*-AzBnO-DMBI is observed in Figure 13.3a, g. In addition, the doping effect seems to be weakened or revoked, i.e. the work function increases again in Figure 13.3c and the HOMO shifts back towards the position of pure PCBM in 13.3a. In principle this would suggest that the dopant is unusable for application if anchoring destroyed the doping capability. However, it is known from Section 13.1 that the conductivity reduces only about one order of magnitude upon UV-treatment. Therefore the observed changes in the surface sensitive photoemission experiments can indeed be correlated to an oxidation of the thin film surface from residual oxygen in the glovebox triggered by UV radiation. A reduced visibility of the HOMO line is also measured for pure PCBM without dopants, see Figure 13.3a. The O 1s emission in Figure 13.4j shows a distinct broadening and increase in peak intensity after UV treatment. The additional amount of oxygen in Figure 13.4j after activation seems to be higher in case of doped films meaning that n-doped PCBM films seem to be more prominent to oxidation. It is known from the data presented in Figure 13.4h that the UPS measurement itself partially triggers the azide decomposition but does not result in an increase of oxygen or additional broadening of line-shapes compared to *o*-BnO-DMBI as is evident from Figure 13.3b. As a consequence, reactions concerning the azide are likely much less harmful to the host than residual oxygen during the activation process. It can be inferred from IR-measurements that the bulk of PCBM is not strongly affected by oxygen, i.e. there is no occurrence of strong C-O vibrations after activation, indicating that only the surface is oxidized. Thermal annealing of doped films for one hour leads to an improved conductivity, which can be correlated with a small additional shift of the HOMO level and a further reduced work function. This is explicitly visible for *o*-AzBnO-DMBI in Figure 13.3j, k compared to as-cast films. Upon doping a broadening of the HOMO level is found that gives rise to an increase in tail states reaching into the band gap, which can be inferred from a log-scale plot in Figure 13.3d-13.3f.

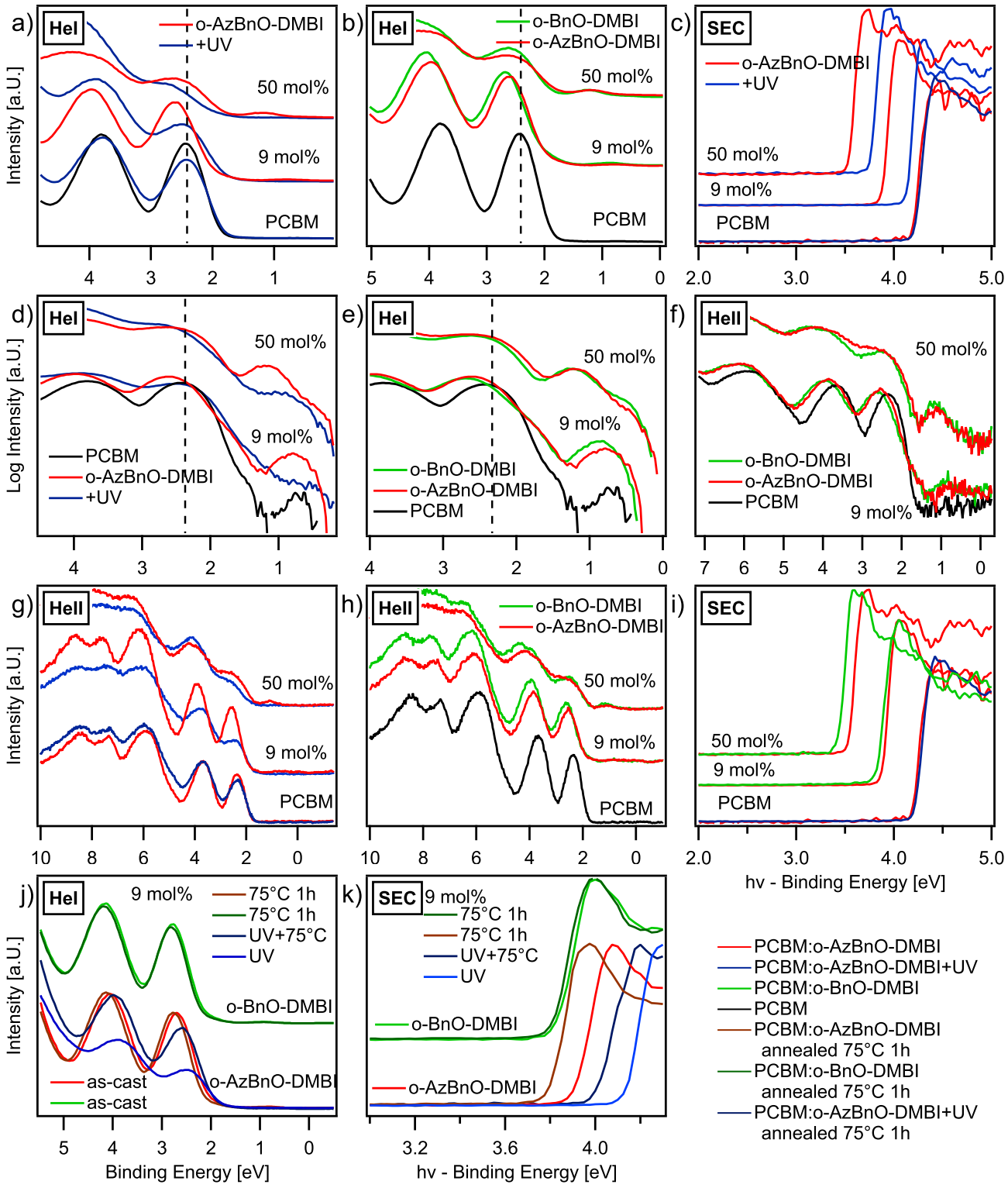

Figure 13.3: UPS measurements of PCBM doped with *o*-BnO-DMBI and *o*-AzBnO-DMBI at different doping concentrations. The secondary electron cut-off (SEC) in (c),(i),(k) was recorded with XPS. The effects of thermal annealing at 75 °C for one hour is presented in (j),(k) for both *o*-BnO-DMBI and *o*-AzBnO-DMBI as dopants. A logarithmic plot of (a),(b),(h) is given in (d),(e),(f) highlighting a HOMO broadening and emerging band gap states. A Fermi level shift can be observed for all doped samples, which is mitigated by UV treatment in (a),(c),(g).

This effect has been often observed in literature for dopant/matrix combinations and is mainly assigned to disorder.[273] Most interestingly, there seems to be a distinct state within the band gap emerging for doped PCBM. All UPS spectra are satellite corrected with the method described in Section 5.2. Pure PCBM is very similar in shape to the sample doped at 9 mol%, but does not exhibit a distinct peak at comparable strength. Furthermore, the band gap state is measured for both HeI and HeII excitation but also gains intensity with increasing doping concentration, which means the peak within the gap can be attributed to the doping of PCBM and not to ghost lines or artefacts. This distinct peak can either be attributed to negative polarons in PCBM or the highest occupied dopant cation state. Since the polaron shift is expected to be only about 200 meV and the band gap state increases with doping concentration, it is suspected that the observed emission at ca. 0.8 eV is indeed the charged DMBI. The dopant related band gap state can be also tracked in the UPS data published in literature for DMBI and a DMBI-dimer by Naab et al. found in the SI.[225,226] Indeed, there are other n-dopant systems which show a comparable emission within the band gap of the host.[274] Interestingly, a reduction in visibility is observed for air-unstable molecular n-dopant after air-exposure.[274] Upon UV-treatment in Figure 13.3d the dopant state also vanishes correlating with increased oxidation, reduced conductivity and most likely with a degradation of the dopant. After thermal annealing there is a small recovery observable in Figure 13.3f, if plotted on a log-scale.

Results XPS: XPS core-level measurement reveal both the activation mechanism of the functional azide group and possible charge transfer between host and the dopant. This conclusion is mainly based on the N 1s emission of *o*-AzBnO-DMBI and *o*-BnO-DMBI. In the previous part, the O 1s spectra in Figure 13.4j is already discussed which clearly shows an oxidation of the surface after UV-treatment. It is assumed that UV light also triggers a reaction with residual oxygen or water in the atmosphere of the nitrogen filled glovebox, even if its concentration is in the ppm range. The C 1s spectrum in Figure 13.4k shows an overall broadening of the main peak with increasing concentration and an emerging peak component at ca. 287 eV which can be either from additional C-O-C bonds or carbon nitrogen bonds of the dopant. A significant change upon UV-treatment is not observed for the carbon emission. However, most insight is gained from the N 1s spectrum, which is related to the dopant only, since PCBM does not contain nitrogen bonds. The dopant *o*-BnO-DMBI only has C-N bonds identical to DMBI and is therefore easier to interpret. The nitrogen bonded in DMBI is sketched in Figure 13.4a and is expected to cause an emission at ca. 400 eV. However, its cationic species in for example DMBI salt is known to exhibit a pronounced emission at ca. 402 eV. After hydride transfer the positive charge is most likely distributed evenly between the symmetric nitrogen atoms causing a shift to higher binding energies. The transformation from neutral to charged DMBI, or *o*-BnO-DMBI, can be initiated by temperature and is shown in Figure 13.4d. Initially at room-temperature, about 50% of the oBnO-DMBI molecules at the surface are charged. If heated to 100 °C, almost 90% of the dopant undergo hydride transfer. This does not mean that an equal number of free charge carriers are generated but a notable increase in conductivity was measured in Table 13.1. For lower concentration of 10 mol% only a minority of neutral DMBI is observed whereas an even amount of cations is found for large concentration in Figure 13.4g. For very high concentrations there might be clusters of *o*-BnO-DMBI and a charge transfer to PCBM does not occur as there are probably no neighbouring host molecules to interact with, unless the film is annealed to higher temperatures. One can speculate why there are further DMBI cations formed at 100 °C. A change in morphology upon annealing is possible, but heat induced hydrogen separation might be a simple explanation as well. The functional dopant *o*-AzBnO-DMBI shows the N 1s

signature of DMBI and its phenyl azide as a superposition, requiring peak analysis to understand reactions triggered by temperature or UV. The N 1s emission of pure azide can be found in Figure 12.11 of Section 12.1 or discussed based on calculations from literature in Figure 7.3. The three nitrogen atoms of the azide form a mesomeric state with an average charge distribution that leaves the central nitrogen atom electron deficient. The partial positive charge causes a noticeable peak shift to higher binding energies to around 405 eV. The N 1s levels of the lateral nitrogen atoms are only slightly separated in energy and can not be fully resolved which give rise to a combined larger peak at about 402 eV. If exposed to UV light the azide decomposes, releasing molecular nitrogen and forming an intermediate nitrene which is very reactive and can undergo CH-insertion (see Section 7.2 for details). As consequence the overall N 1s intensity reduces and the azide's distinct peak characteristic transforms to a single broad line at around 400 eV typical for C-N bonds. The expected peak structure and its conversion is depicted in Figure 13.4b. The combination or superposition of peak components from DMBI in Figure 13.4a and the azide in Figure 13.4b then yields the emission expected for *o*-AzBnO-DMBI. Here, charging of DMBI and azide decomposition should occur at sufficiently high temperature. Starting from the azide doublet (containing three nitrogen peaks) in light blue and neutral DMBI in light green, the charged and anchored *o*-AzBnO-DMBI is supposed to have a peak at 400 eV for newly formed C-N bonds (shown in dark blue) and the DMBI cation at ideally twice the intensity (in dark green), see Figure 13.4c. This has been presented in Figure 13.4e, which already shows charged DMBI at room temperature and, according to the fitted model, achieves an almost full transformation of the azide and charging of DMBI at 100 °C. In order to obtain a robust fit, the relative peak positions are fixed, as measured for *o*-BnO-DMBI and the azide of ABN in Section 12.1 and only one peak shape is used for all individual nitrogen components. As a result, a small absolute Fermi level shift, the shared peak shape of all components, the overall intensity and background is fitted. In addition, the fraction of converted DMBI and decomposed azide was adjusted respectively, for which the total amount of dopants is kept constant and the stoichiometric ratio of products is considered. For example, there are three nitrogen atoms in azide per molecule, but ideally only one after cleavage and always two nitrogen atoms in DMBI. The fitting procedure is also applied to UV treated *o*-AzBnO-DMBI doped PCBM in Figure 13.4f, which shows a full conversion of the azide but only a small change in the amount of DMBI cations. In Figure 13.4h the N 1s core-level is measured after the UPS measurement and UV-treatment, revealing that also UPS tends to activate the azide to some degree but a full azide conversion is reached after UV exposure within the margin of XPS sensitivity. To transform the azide via annealing, an activation temperature of ca. 130 °C is needed as determined by thermogravimetric analysis (TGA). Nonetheless, in UHV it is found that a considerable amount of azide has reacted at 100 °C within the surface region. On the other hand, an increase in cationic DMBI is achieved more effectively when annealed to higher temperatures than with irradiation of UV light. A full dependence of the N 1s emission with temperature is treated in detail in the next section. The stability of the azide in oAzBnO-DMBI is also tested by comparing as-cast films with samples that have been stored for 20 hours in either UHV (ca. 10^{-9} mbar) or HV (ca. 10^{-7} mbar). The samples were carried after preparation in a nitrogen glovebox to the vacuum chamber under ambient conditions and were subsequently transferred from the air-lock (HV) to the XPS chamber (UHV). After 20 h one observes a clear decrease in the peak component at 405 eV (azide) for samples in HV but only a minor decrease if the thin film was stored in UHV. An increase in O 1s peak intensity is also found for the sample in HV (not shown here), which indicates that the partial pressure of oxygen or water can influence the lifetime of the near-surface azide.

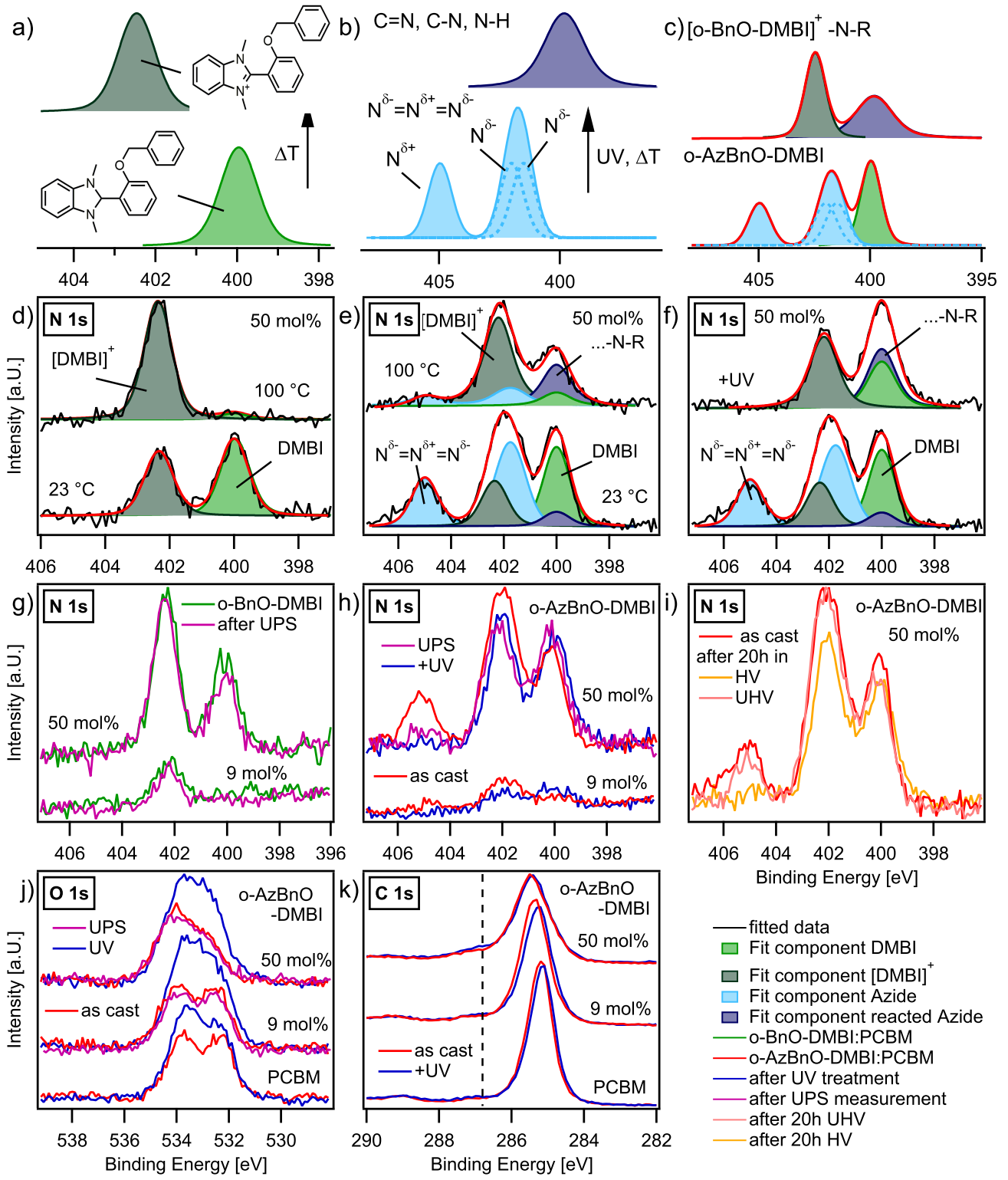

Figure 13.4: Composition and changes of N 1s core-level spectra of *o*-BnO-DMBI and *o*-AzBnO-DMBI are shown. The N 1s components of DMBI is sketched in (a), of phenyl azide in (b) and their combination present in *o*-AzBnO-DMBI in (c). They have been fitted to *o*-BnO-DMBI in (d) and to *o*-AzBnO-DMBI in (e),(f) at different temperatures and after UV treatment. XPS core-level spectra of varying doping concentration after UPS measurement or UV treatment for *o*-BnO-DMBI in (g) and *o*-AzBnO-DMBI in (h),(j),(k). Decay of the azide is studied in (i) in either UHV or HV.

13.4 Thermal Stability Measurement: XPS

For the purpose of testing the ability of anchoring the dopant by the covalent bonding between PCBM and *o*-AzBnO-DMBI, the temperature dependence of a doped PCBM film is investigated. Its composition is expected to change when heated to higher temperatures. If not covalently anchored to the host, dopants can evaporate or at least become more volatile within the blend. Although DMBI is not particular mobile in an amorphous small molecule host like PCBM, thermal activation may give additional information on the stability of activated *o*-AzBnO-DMBI. Therefore, XPS analysis is performed on a step-wise annealed thin film of doped PCBM and chemical properties of the materials as well as physical parameters like film thickness or doping concentration are evaluated. In principle, a thermogravimetric analysis of a thin film is carried out under vacuum conditions. However, in addition to mass loss, one can investigate activation mechanisms of both the dopant and the anchor group and identify possible decomposition reactions on a more "molecular level".

Experimental Information: Here, thin films of doped PCBM are processed on a strongly n-doped n^+-Si substrate. The silicon wafer is covered with a native oxide layer and has been cleaned with solvents prior to film preparation. The samples were spin-cast at 1000 rpm from chlorobenzene at a total concentration of 5 mg ml^{-1}. Since the functional dopants are not specifically stable in solution, they were added to the host briefly before spin-coating. All other steps have been performed identical to the samples prepared in the previous section. For this measurement a rather extreme doping concentration of 50 mol% is chosen, which may not be applicable in devices, but is required to achieve good visibility in XPS core-level spectra. The temperature dependence of the activation process and chemical composition or reactions is expected to be observable also at high concentration. The processing parameters were then tuned to obtain a film thickness of about 15 nm, at which the Si 2p emission can still be reliably detected. By comparing the damping of the Si 2p emission with a pristine silicon substrate, the nominal film thickness can be calculated, if an inelastic mean free path (IMFP) of electrons in PCBM is estimated, based on the models in Section 4.1. Changes in coverage then indicate desorption or decomposition. The samples were mounted on the Phi Versa Probe's hot-and-cold stage after being directly transferred to the measurement chamber in ambient conditions. The temperature was step-wise increased within one or two minutes and a full set of XPS core-level spectra was measured at constant temperature taking about 45 min.

Results, XPS: The recorded XPS core-level data for doped PCBM at room temperature and up to ca. 300 °C are depicted in Figure 13.6, 13.7 and 13.8. For better understanding, the interpretation based on the calculated coverage in Figure 13.5 is explained in advance and then spectral features and findings are discussed to substantiate the hypothesis. The initial film thickness of all samples is determined to be ca. 15 nm using the model described in Section 4.1. With increasing temperature the film thickness of pure PCBM stays constant, until the PCBM films becomes unstable and almost completely evaporates from the substrate at around 290 °C. At this temperature, there is a distinct drop in coverage which coincides with the melting point of PCBM at 280 °C. A clear difference can be observed for doped PCBM films, see Figure 13.5. If PCBM is doped with *o*-MeO-DMBI or *o*-BnO-DMBI the film becomes unstable at considerable lower temperature. The dopants are much more volatile than PCBM and, if not embedded in a stable matrix, tend to evaporate in UHV already at room temperature. Around 200 °C the dopants are no longer retained by PCBM and can evaporate from the blend, lowering the

threshold for some PCBM molecules to desorb as well. After the initial drop in coverage, that is ascribed to dopants, the remaining PCBM fraction evaporates at around 300 °C similar to pure PCBM, which results in a plateau between 200 and 300 °C in Figure 13.5. However, if PCBM is doped with *o*-AzBnO-DMBI, the films seem to be generally more stable even beyond 300 °C, meaning that the *o*-AzBnO-DMBI-doped film is more stable than a comparable pristine PCBM film. In this experiment the functional azide group of *o*-AzBnO-DMBI gets activated and possibly forms a reactive nitrene either during the annealing process at ca. 100°C or by UV-treatment before entering UHV. In any case it is anticipated that the anchor group of *o*-AzBnO-DMBI has reacted when approaching higher temperatures. Nonetheless, there is a small and continuous mass loss observed, when increasing the temperature that roughly starts at 180 °C. A closer look at Figure 13.5 reveals that *o*-BnO-DMBI seems to evaporate earlier than *o*-MeO-DMBI even though *o*-BnO-DMBI has a higher molar mass and is considered to be more bulkier. This discrepancy can be resolved and explained by the observation provided in the spectra of Figure 13.6 and 13.8. From N 1s and O 1s core-level spectra it is concluded, that the benzyl group is detaching from the DMBI body at about 180 °C. In case of *o*-BnO-DMBI, decomposition leads to a release of the phenyl group, which may cause the film to become unstable at even lower temperatures due to its higher volatility. This is a possible explanation for the here observed lower evaporation temperature of *o*-BnO-DMBI compared to *o*-MeO-DMBI. For *o*-AzBnO-DMBI a separation of DMBI body and anchor group allows the DMBI dopant to desorb from the film, while the anchor is still connected or interconnected with PCBM, which can be inferred from N 1s core-level components. A breaking of dopant-anchor connection is also able to explain the gradual mass loss for *o*-AzBnO-DMBI-doped samples at higher temperatures.

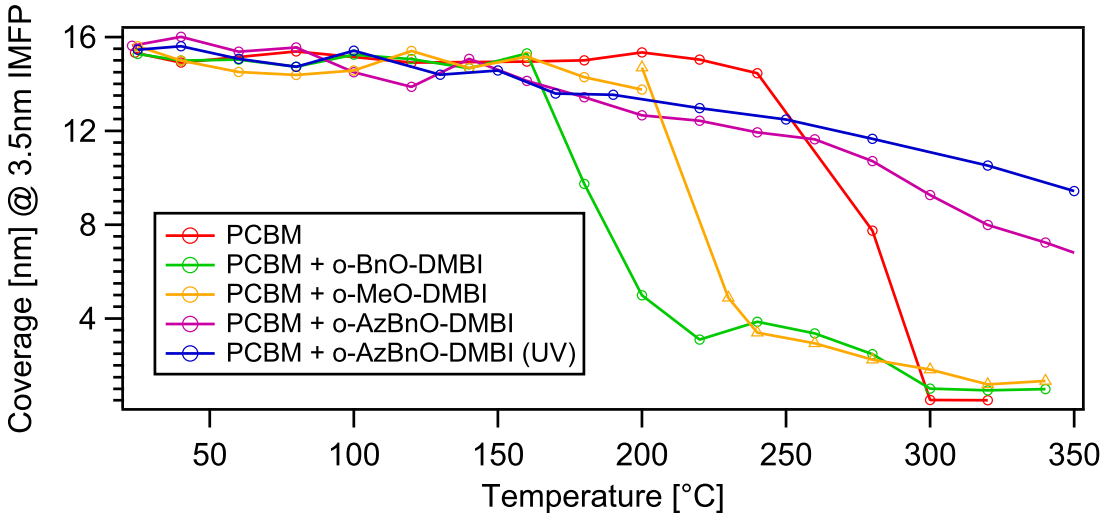

Figure 13.5: Substrate coverage in dependence of temperature for PCBM and PCBM doped with *o*-MeO-DMBI, *o*-BnO-DMBI and *o*-AzBnO-DMBI. The coverage is derived from the damping of the Si 2p substrate emission. We assume an electron IMFP of 3.5 nm to estimate the film thickness in nm. Most interestingly is the high coverage for samples doped with *o*-AzBnO-DMBI even beyond 300 °C.

This conclusion is based on N 1s and O 1s emission in Figure 13.6 and 13.8, which will be detailed in the following.

All doped samples show a Fermi level shift of up to 300 meV compared to pure PCBM at room-temperature. As mentioned in the previous section, N 1s core-level spectra of *o*-AzBnO-DMBI reveal a contribution of both the DMBI-dopant part and the functional azide group, transforming or reacting, if activated by heat or UV-light. The N 1s components can be separately analysed when comparing o-AzBnO-DMBI with *o*-BnO-DMBI, where *o*-BnO-DMBI only exhibits nitrogen peak components of DMBI located at 402.5 eV and 400 eV. The N 1s emission of the isolated azide functional group can be found in Figure 12.11 for the dummy molecules ABN and F4ABN mixed with PCBM. An extensive peak component analysis for the N 1s emission of *o*-AzBnO-DMBI and *o*-BnO-DMBI can also be found in Figure 13.4. N1s spectra of PCBM doped with *o*-BnO-DMBI in Figure 13.6a reveal that DMBI forms more charged species if annealed to higher temperatures, i.e. the peak component at 400 eV transforms into positively charged DMBI species at 402.5 eV. Here, it is assumed that the hydride or hydrogen radical transfer of DMBI is induced by temperature, causing the formation of DMBI cations. This also correlates with an increase in conductivity observed for annealed PCBM films doped with DMBI. A decline in the overall N 1s intensity is attributed to a loss of dopants, which occurs at ca. 220 °C for *o*-MeO-DMBI and 200 °C for *o*-BnO-DMBI in the blend (see Figure 13.6a,b). For *o*-AzBnO-DMBI the isolated peak at 405 eV is attributed to the central electron deficient nitrogen of the azide group and can be clearly identified in Figure 13.6c at room temperature. The lateral nitrogen peaks of the azide group (see Figure 12.11 for comparison) are expected to yield an emission between 400 eV and 402 eV. After UV activation, the changes of the N 1s emission of *o*-AzBnO-DMBI are best explained by the peak component fit in Figure 13.4f. In Figure 13.6 this can be seen by comparing the spectra at room temperature in Figure 13.6c with 13.6d (after UV activation). The peak from the central nitrogen of the azide group at 405 eV is lost and the peak ratio between the component at 402 eV and 400 eV shifts towards the peak at 400 eV. This indicates a decomposition of the azide group by UV-light and the formation of covalent bonds with carbon or hydrogen. With increasing temperature in Figure 13.6c, one observes both a decomposition of the azide at 80 to 140 °C, marked by the peak reduction at 405 eV, and an activation or cation formation of the DMBI part between 60 and 120 °C, causing a change of peak intensity ratio transferring from 400 eV to 402 eV (see Figure 13.6e or 13.4 for details). At high temperatures above 150 °C only charged DMBI species are expected at 402 eV and transformed azides at 400 eV. Ideally, the intermediate nitrene has formed covalent bonds with neighbouring molecules. For temperature above 240 °C, the N 1s component at 402 eV decreases significantly, which indicates that the DMBI part of *o*-AzBnO-DMBI is not bound any more and evaporates from the film. However, the component at 400 eV persists for temperatures higher than 300 °C, beyond the evaporation point of pure PCBM suggesting that the anchor is connected or even interconnected with PCBM. The separation of dopant and anchor means that the ether bond connecting the functional phenyl azide with the DMBI body is breaking apart. In mass spectroscopy data of annealed blends in Section 13.6 decomposition products of *o*-AzBnO-DMBI without the anchor can be found. Furthermore evidence is found in the O 1s emission in Figure 13.7. The O 1s signature of pure PCBM in Figure 13.7a is composed of two components at about 532.5 eV and 533.5 eV from the bindings sites of the carbonyl group and the methoxy group, respectively. The two components are well separated at room temperature and are of equal strength. For doped PCBM films, the ether bond in *o*-MeO-DMBI, *o*-BnO-DMBI and *o*-AzO-DMBI gives rise to an additional O 1s component at 534 eV, which causes an asymmetric double peak structure of the O 1s emission as shown in Figure 13.7b - 13.7d.

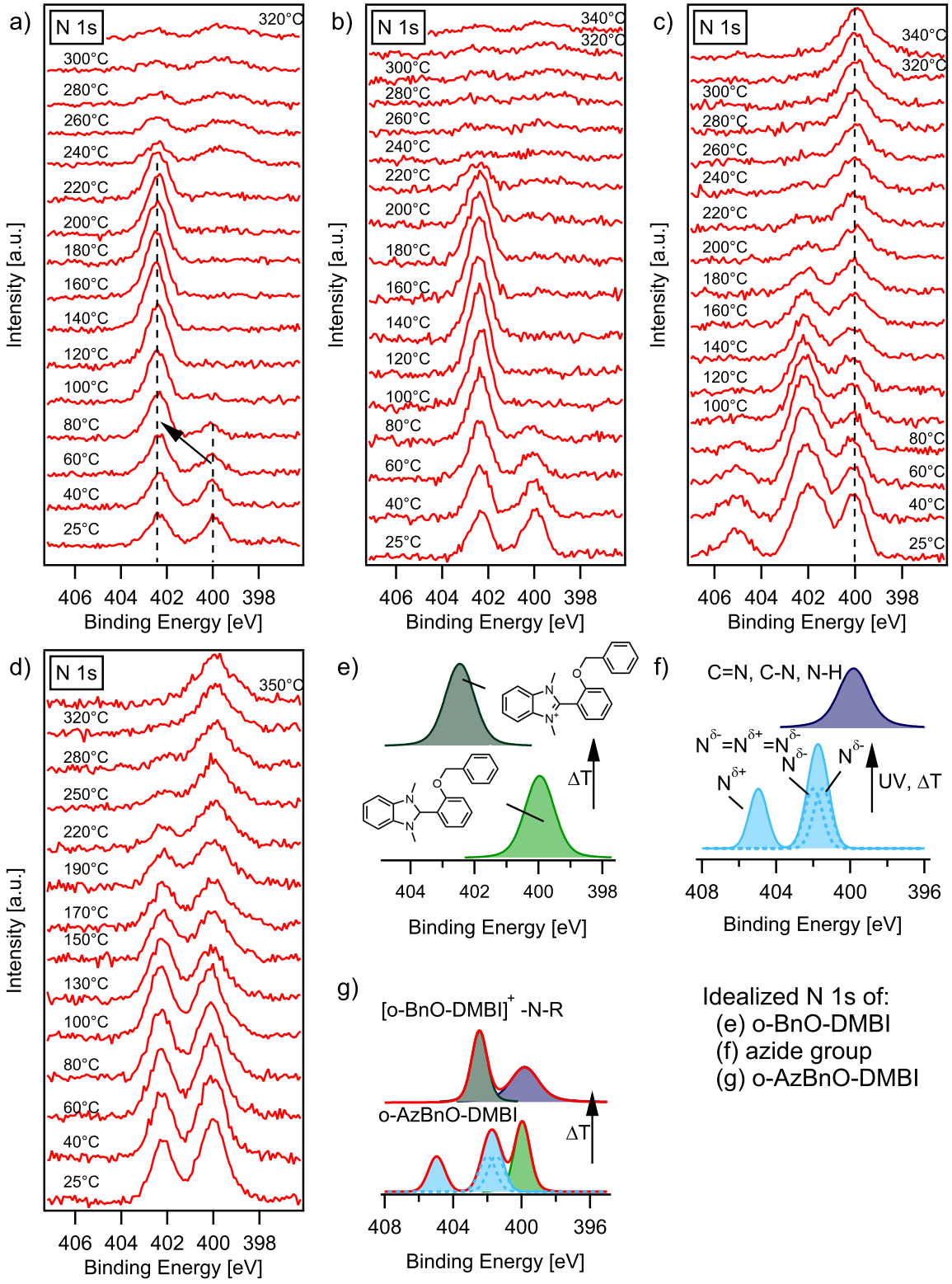

Figure 13.6: Temperature dependent N 1s core-level emission plotted for PCBM doped at 50 mol% with *o*-MeO-DMBI in (a), *o*-BnO-DMBI in (b), *o*-AzBnO-DMBI in (c) and for UV-activated oAzBnO-DMBI in (d). The single peak components and their transformation upon heating and UV-treatment is illustrated in (e). If heated or UV exposed the azide decomposes and the characteristic emission at 405 eV vanishes in (f). For the reaction mechanism please compare Figure 7.3, 7.4 and 8.1.

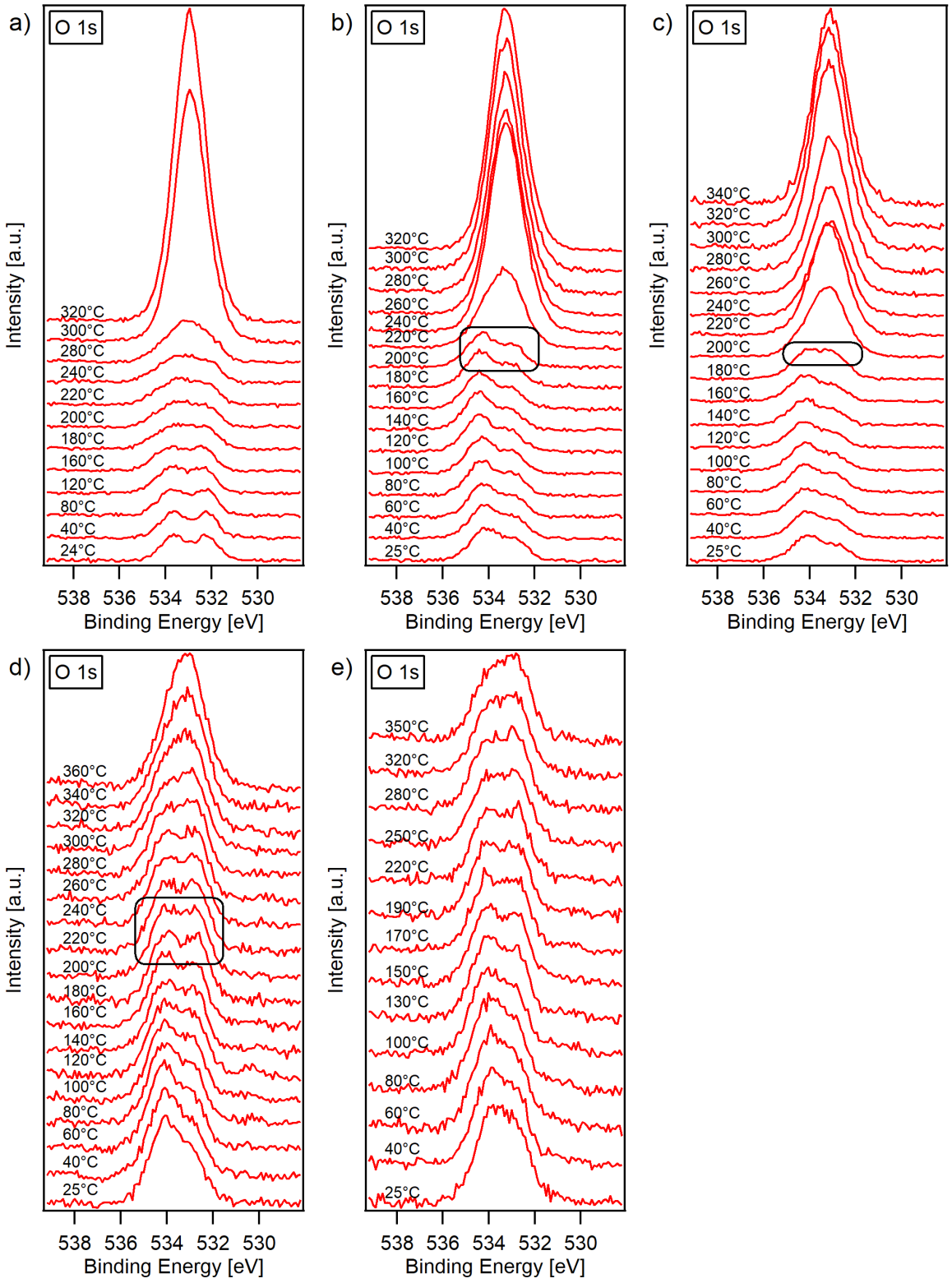

Figure 13.7: Temperature dependent measurements of the O 1s core-level emission of PCBM in (a) and doped at 50 mol% with *o*-MeO-DMBI in (a), *o*-BnO-DMBI in (c), *o*-AzBnO-DMBI in (d) and additionally UV-activated *o*-AzBnO-DMBI in (e). The spectra at highest temperature are marked by a circle in (b) and (c) right before the O 1s emission is dominated by SiO_X.

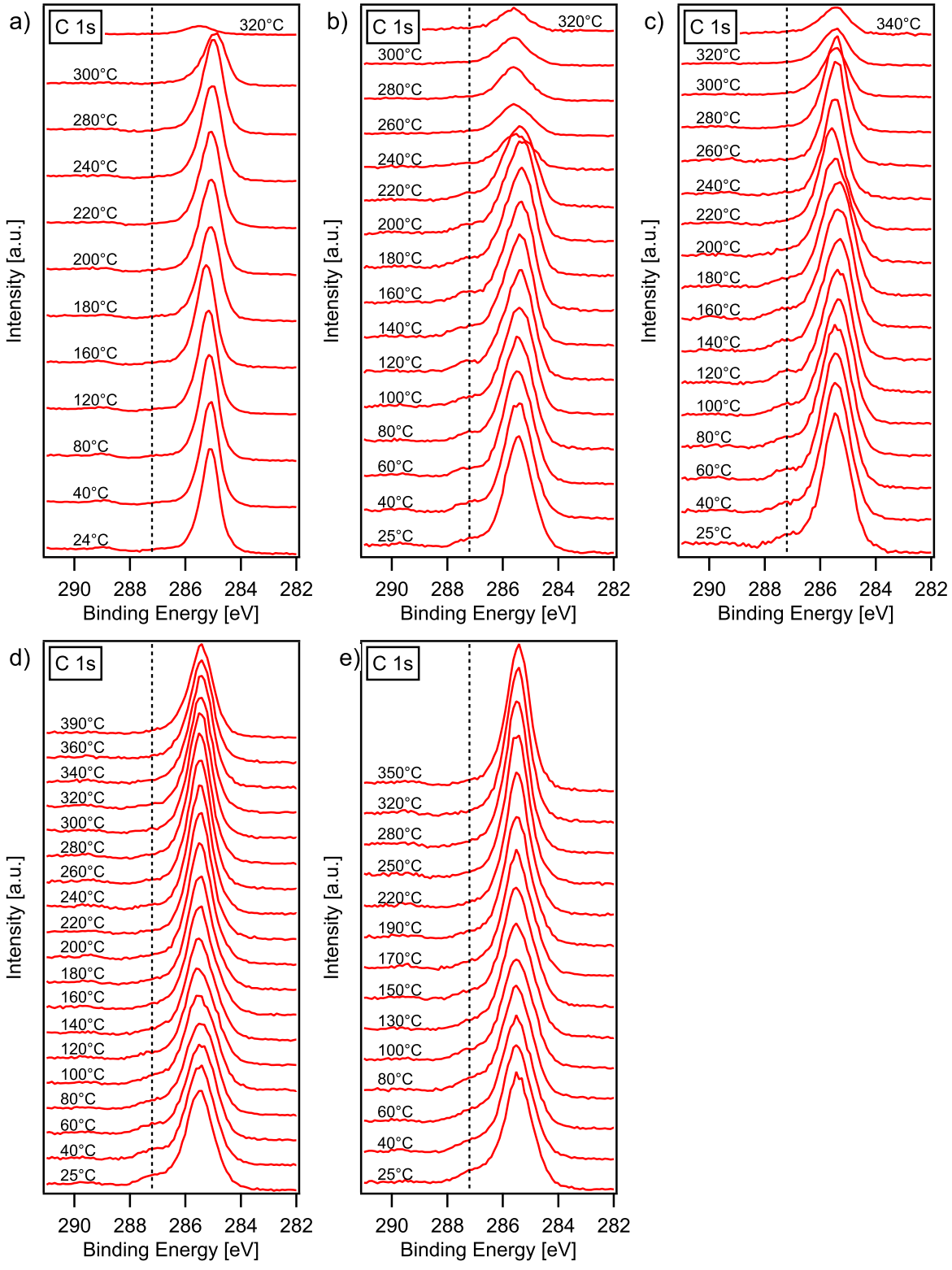

Figure 13.8: Temperature dependent measurements of the C 1s core-level emission of PCBM in (a) and doped at 50 mol% with *o*-MeO-DMBI in (b), *o*-BnO-DMBI in (c), *o*-AzBnO-DMBI in (d) and additionally UV-activated *o*-AzBnO-DMBI in (e). Compared to pure PCBM in (a) an additional shoulder around 287 eV can be observed for all doped samples which stems from C-N and C-O bonds of the dopant.

For UV-activated *o*-AzO-DMBI in PCBM the O 1s spectra in Figure 13.7e have to be analysed with care since UV-exposure was performed in a glove-box and an oxidation of the thin film surface from residual oxygen is pronounced. If the thin film has evaporated from the surface in UHV, the O 1s emission is dominated by the strong SiO_X peak from the substrate, which impedes tracking of the ether bond in DMBI for lower coverages. However, in Figure 13.7c and 13.7d a more or less symmetric O 1s peak is measured at 180 °C suggesting that the ether has dissociated and, most likely together with the DMBI body, evaporated from the blend. On the other hand, this is not observed for *o*-MeO-DMBI, which seems to maintain the ether bond, i.e. an asymmetric O 1s double peak, right up to 200 °C before leaving the film (marked by circles in Figure 13.7). For *o*-MeO-DMBI there is only a methoxy group attached to DMBI which is likely more stable than the phenol ring anchor of *o*-BnO-DBMI and *o*-AzBnO-DMBI. If the non-anchored benzene ring of oBnO-DMBI splits from the DMBI body and is not anchored to PCBM like in the case of *o*-AzBnO-DMBI, an immediate desorption of phenol is possible reducing the stability of the whole thin film compared to the example *o*-MeO-DMBI. This may be an explanation of the observed slightly higher stability of PCBM doped with *o*-MeO-DMBI compared to *o*-BnO-DMBI.

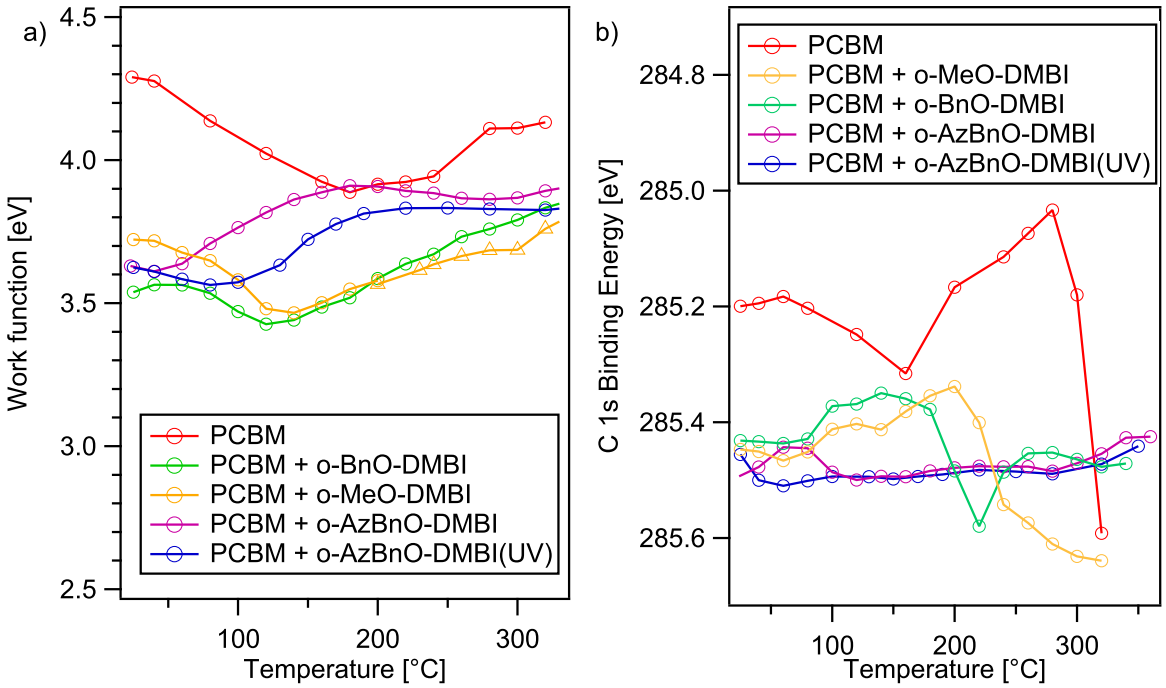

Figure 13.9: Binding energy of the C 1s emission extracted from Figure 13.8 in (b) and work function values derived from XPS secondary electron cut-off as a function of temperature in (a).

In addition one can track Fermi level shifts from C 1s peak maxima in Figure 13.8 and work function changes from the XPS secondary electron cut-off, which was recorded supplementary to core-level spectra for each temperature using a small bias in Figure 13.9. The fitted values are presented in Figure 13.9 as a function of temperature. At room-temperature a clear shift to higher binding energies and correspondingly to lower work functions is verified for all doped samples. In the temperature range between room-temperature and 100 °C there is no signifi-

cant change in binding energy observed for doped samples. Indeed one would rather expect an increase in doping efficiency meaning that energy levels shift further to higher binding energies. For temperature above 100 °C, however, an increase in work function is found for all doped samples, which can be assigned to dopants desorbing from the surface. An accumulation of residues during heat is also a possible explanation. For *o*-MeO-DMBI and *o*-BnO-DMBI a continuous decrease in C 1s binding energy above 100 °C is found until it rapidly rises again when the point is reached, at which the film has completely evaporated from the substrate. The remaining carbon adsorbed on the surface has a higher binding energy of about 286 eV and may contain of fragments of absorbed carbon hydrides or oxides, but it does differ from the C 1s emission of the thin film (see Figure 13.8). This variation in binding energy is not observed for films doped with *o*-AzBnO-DMBI, which exhibit a steady C 1s level with increasing temperature. For pure PCBM an initial decrease in work function and increase in C 1s binding energy up to 200 °C is observed and subsequently the reversed trend up to 300 °C. At 300 °C there is a prompt rise in C 1s binding energy; here the PCBM film has almost completely evaporated from the surface. One can not consistently explain the course of binding energies for pure PCBM with temperature. Possible explanations can be diffusion of residues or phase transitions of PCBM. Indeed, PCBM is known to have a phase transition at 245 °C, 273 °C and the melting point at 281 °C.[275] Additionally, Ngo et al. observed a mass-loss of ca. 1 wt% in the differential scanning calorimetry trace of PCBM, which was attributed to solvent residues leaving the film.[276]
The integrated and ASF-weighted intensity of combined N 1s, O 1s and C 1s spectra can be used to estimate the concentration of dopant molecules in the film by using the stoichiometric ratio of elements in dopant and matrix, respectively. According to Eq. 5.3 of Section 5.1, the molar ratio is calculated from least squares including confidence levels for prediction. The result is plotted in Figure 13.10.

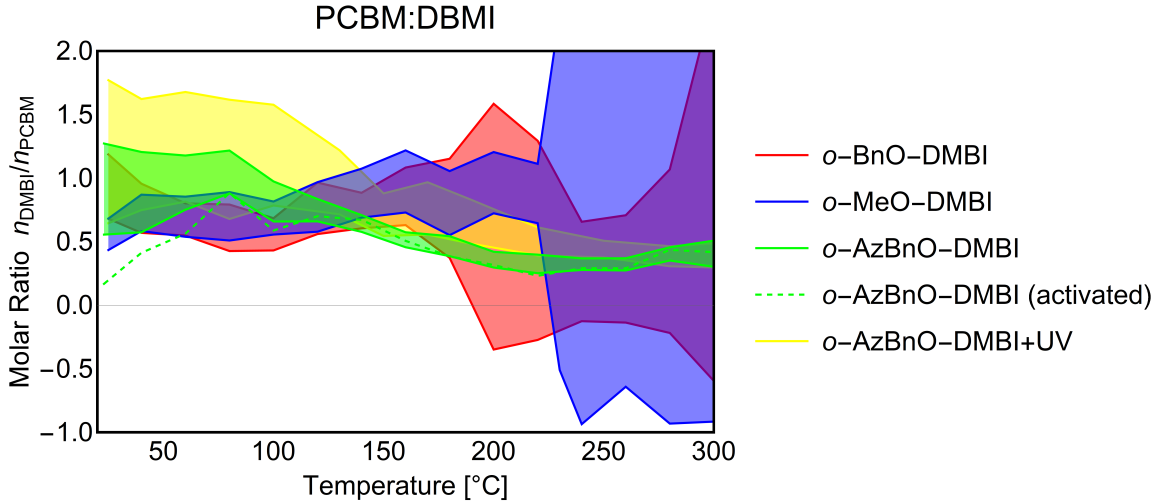

Figure 13.10: Calculated molar ratio of dopant molecules to PCBM as a function of temperature for *o*-MeO-DMBI, *o*-BnO-DMBI and *o*-AzBnO-DMBI. More precisely, the confidence interval for the calculated dopant concentration is plotted given the legend on the right. A molar ratio of one is expected from the prepared solution provided a homogeneous dopant distribution. An extremely large error bar means that the concentration could not be calculated reliably which indicates desorption or decomposition of the materials.

For finding the correct concentration, one further has to distinguish between decomposed and intact azide, since the number of nitrogen atoms per dopant molecule changes, if gaseous N_2 is released from the film. This has been done be separately integrating the N 1s peak at 405 eV and directly connecting its integral to the amount of non-reacted azide. A full peak component fit of the N 1s spectra (like in Figure 13.11) could also be used to identify the reacted *o*-AzBnO-DMBI for this plot. The coloured bands in Figure 13.10 mark trust-regions or confidence intervals of dopant concentration which start at a molar ratio of one agreeing with the concentration prepared in solution. Desorption or decomposition of dopant in the case of *o*-MeO-DMBI and *o*-BnO-DMBI translates to a sudden increase in error, which is reached at 200 °C for *o*-BnO-DMBI and at 230 °C for *o*-MeO-DMBI. In the case of *o*-AzBnO-DMBI, a steady decreasing concentration is found with a small error. This is valid for both thermally and UV-activated *o*-AzBnO-DMBI. The calculation confirms an activation of the azide with temperature, until a full conversion is obtained around 120 °C, i.e. the activated fraction agrees with calculated total concentration of *o*-AzBnO-DMBI in the margin of errors.

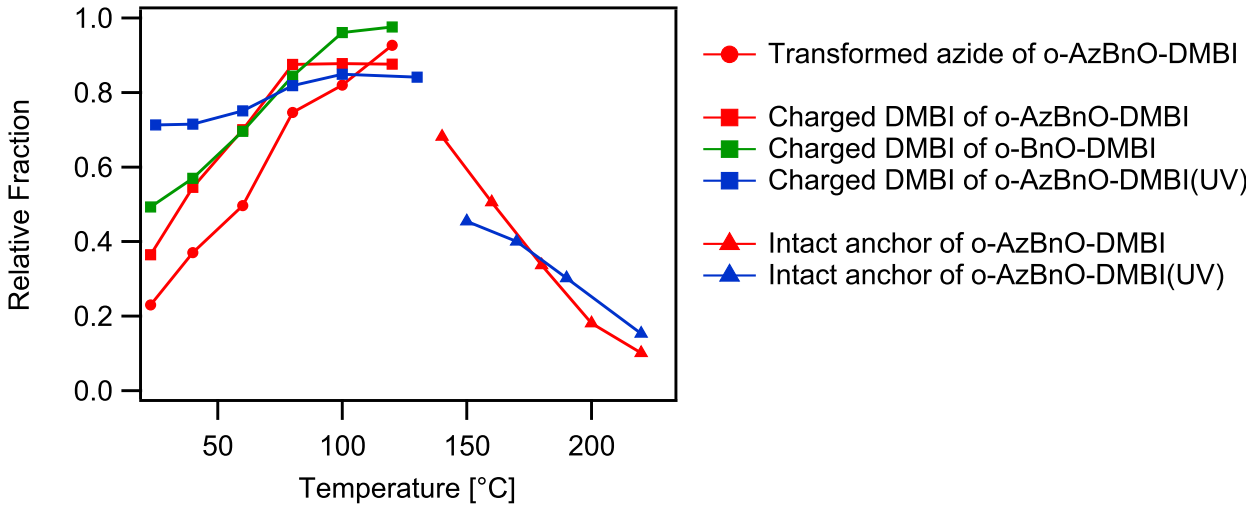

Figure 13.11: Fitted relative fraction of transformed azide as circles, charged DMBI as squares and the presumably broken DMBI-Anchor connection as triangles from the data in Figure 13.6 with the fit described previously. This is done for PCBM doped with *o*-BnO-DMBI in green, *o*-AzBnO-DMBI in red and UV-activated DMBI in blue. It should be noted, that this is a very constraint model fit, where a fixed peak relationship is implied for intact dopants below 150 °C and fully reacted molecules above 150 °C.

13.5 Sequential Deposition from Solution

Successful anchoring and a reduced mobility can be verified at room temperature by directly investigating the interface of host, i.e. PCBM, and the dopant *o*-AzBnO-DMBI. In Section 13.4 it is found that all DMBI derivatives are sufficiently stable in UHV at room temperature if blended with PCBM. However, the dopant itself is volatile under UHV conditions and is likely to desorb in considerable quantities if processed on top of PCBM. By comparing the coverage of oAzBnO-DMBI onto PCBM in UHV of as-cast with UV-activated films, a successful anchoring or at least a reduced volatility can be substantiated. To achieve a bilayer structure, dopant and matrix have to be sequentially deposited from orthogonal solvents, in order to avoid re-dissolution of the underlying matrix layer. The idea of this experiment is sketched in Figure 13.12.

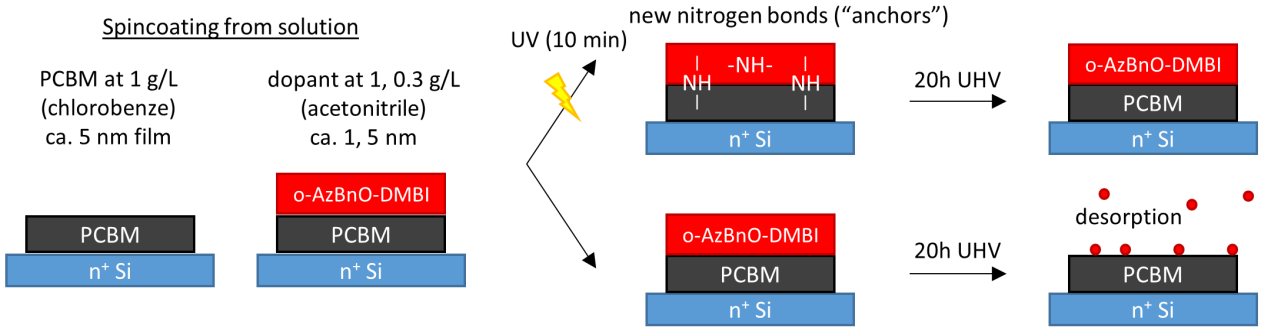

Figure 13.12: Sketch of the experiment to test anchoring of *o*-AzBnO-DMBI onto PCBM.

Experimental Information: PCBM films were spin-cast from a 1 g L^{-1} chlorobenzene solution at 1000 rpm on a solvent-cleaned n-doped n^+-Si silicon substrate, which is covered with a native oxide layer. After drying of the PCBM layer, the dopant oAzBnO-DMBI was deposited at 1000 rpm from a solution of acetonitrile. It should be noted, that *o*-AzBnO-DMBI is processed shortly after dissolving due to its stability issues in solution. To verify that acetonitrile does not dissolve PCBM, we mixed 10 mg of PCBM with 5 ml of acetonitrile and stirred the solvent at 50 °C overnight without visible change in colour or material being dissolved. However, we can not fully exclude that the dried PCBM film is not partially etched or the dopant penetrates into PCBM to some degree due to solvent swelling. We processed the dopant from a 1 g L^{-1} and 0.3 g L^{-1} solution which resulted in either a close to mono-layer coverage or a ca. 5 nm thick top-layer. Activation of *o*-AzBnO-DMBI was realized by UV exposure for 15 min.

Results: Measured XPS core-level are presented in Figure 13.13. From the damping of the Si 2p core-level (not shown here), the coverage was estimated with respect to a clean substrate. The results are listed in Table 13.3. After keeping the samples in UHV conditions for 20 h without interruption, the Si 2p and thus the film thickness was measured again, revealing a significant reduction of coverage for samples which were not activated with UV light prior entering the XPS chamber. On the other hand, samples irradiated with UV-light show perfectly constant coverage and hence no desorption. In addition, this can be nicely seen from the reduction in N 1s peak intensity in Figure 13.13a versus 13.13b and 13.13d versus 13.13e, indicating a loss of dopants at the surface for non-activated films. The O 1s emission is more difficult to interpret, since it is composed of contributions from the substrate's native oxygen layer, the methyl ester of PCBM and the ether of the dopant in Figure 13.13c, f.

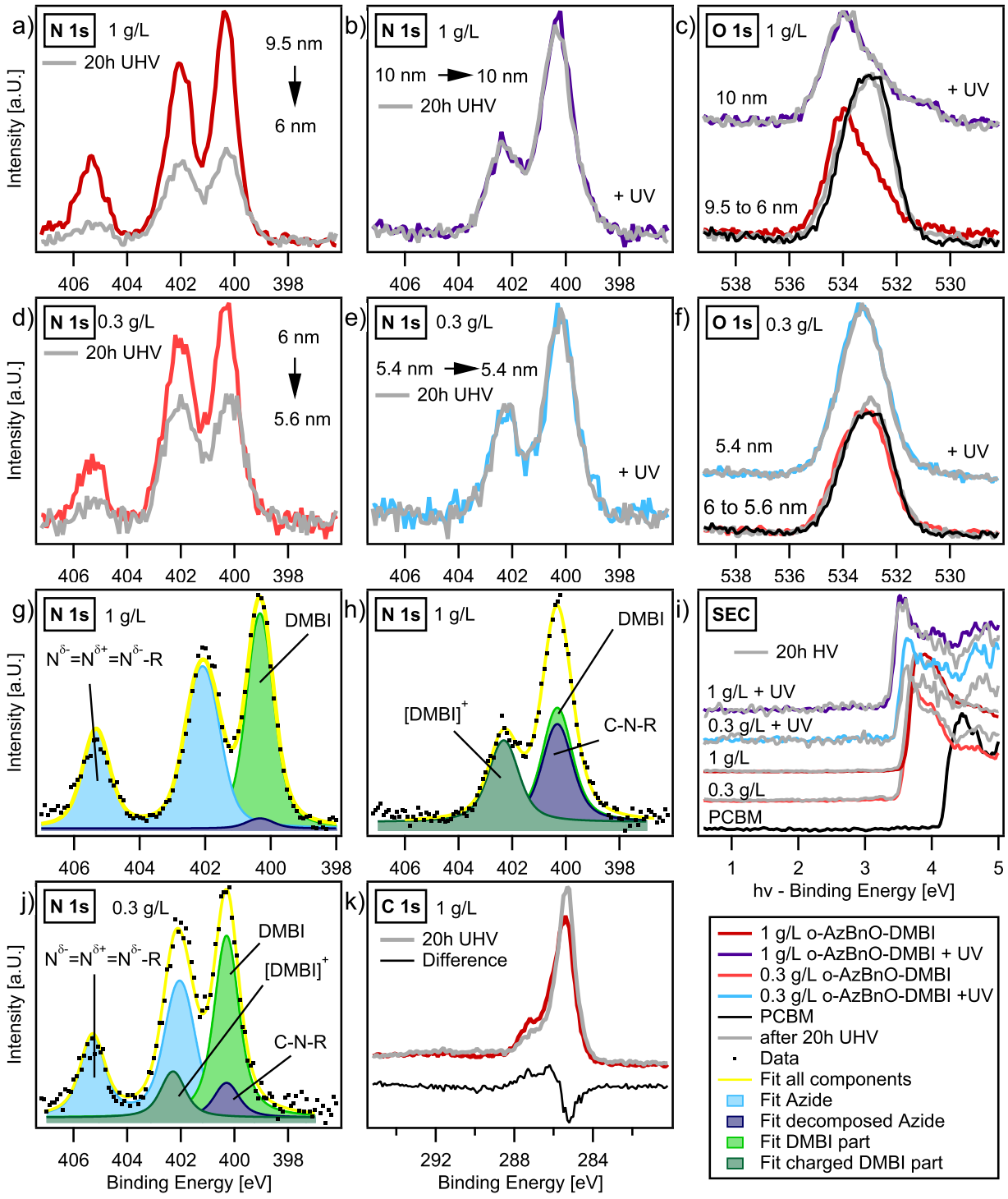

Figure 13.13: XPS spectra of a bilayer structure of PCBM and oAzBnO-DMBI. The dopant layer has been processed on PCBM at concentration of 1 g L^{-1} in (a)-(c),(g),(h),(k) and at 0.3 g L^{-1} in (d)-(f),(j). A clear decline in signal and coverage can be observed over 20 h in UHV for non-activated samples in (a),(d). The coverage stays constant if the dopant top-layer is activated with UV light prior entering the UHV chamber in (b),(e). A peak component fit is carried out in (g),(h),(j) with the assignment of Figure 13.4. Furthermore a decrease in work function can be observed for all samples compared to PCBM in (i). The O 1s emission is plotted for both activated and as-cast film in (c) and (f).

A change in the O 1s emission can only be observed for the sample with high dopant coverage in Figure 13.13c, i.e. processed from a solution with concentration of 1 g L^{-1}. A UV-related oxidation of the PCBM surface can be suspected for low dopant coverage in Figure 13.13f.
For this experiment we used a rather long UHV-storing time of about 20 h in order to ensure that all dopant molecules, which are not chemically bound to the matrix, have left the surface. However, it is found that most of the non-reacted *o*-AzBnO-DMBI molecules desorb considerably faster, most likely within minutes. For low coverage there is still a small remaining faction of *o*-AzBnO-DMBI with intact azide group physisorbed on PCBM, having found a local potential minimum. In addition, there are dopants which already transformed the functional azide group and possibly formed covalent bonds before entering UHV, which is why a full evaporation of all dopant molecules is not observed. Nonetheless, there is a clear trend that UV-treated samples show constant coverage regardless of the UHV-storing time, indicating that dopant molecules are chemisorbed on the surface. However, this is also the case for multilayers of dopant molecules, i.e. for the sample processed with 1 g L^{-1} solution and a total of 10 nm film thickness, from which it is concluded that *o*-AzBnO-DMBI can interconnect or polymerize yielding a reduced volatility as well.
A peak fit of the N 1s emission in Figure 13.13g,h shows that for the sample of high dopant coverage, which likely forms multilayers of *o*-AzBnO-DMBI, there is little charge transfer or charged DMBI ions. On the other hand, for low dopant coverage, processed from only 0.3 g L^{-1} solution, we find approximately 20% charged DMBI on the surface. This not surprising given that dopants can only transfer an electron at the interface to PCBM. For UV-treated films a larger fraction of charged dopants is found, regardless of the initial coverage, which is most likely due to radiation induced splitting of the hydride. For comparison, the amount of charged dopants in the blend for either very low concentration and/or annealed films can be close to 100%, which of course does not mean that there are equally many free charge carriers generated.

Sample, treatment	Charged DMBI	Thickness L	L after 20 h UHV
PCBM	-	6 nm	-
1 g/L *o*-AzBnO-DMBI	0 %	9.5 nm	6 nm
1 g/L *o*-AzBnO-DMBI + UV	40%	10 nm	10 nm
0.3 g/L *o*-AzBnO-DMBI	20%	6 nm	5.6 nm
0.3 g/L *o*-AzBnO-DMBI + UV	50%	5.4 nm	5.4 nm

Table 13.3: The layer thickness was determined from the damping of the Si 2p core-level spectrum. The fraction of charged DMBI species was estimated based on the peak component fit of Figure 13.13g-13.13j.

13.6 Mass Spectroscopy

Besides the indirect evidence for anchoring of the functional azide group with neighbouring molecules, a direct proof for *o*-AzBnO-DMBI covalently bonding to PCBM, was not found with the spectroscopic techniques of the previous section. With regard to the precise reaction mechanism, it is established that azides react with fullerenes in a 1,3-dipolar [3+2] cycloadditions forming triazolines,[277,278] which, upon thermal treatment, undergo a loss of nitrogen,[279,280] or [2+1] cycloaddition with nitrenes yielding aziridinofullerenes or azafulleroids.[281,282] Also CH-insertion into PCBM's alkyl chain may occur. Therefore, it is attempted to investigate doped PCBM films with high resolution mass spectroscopy. Electrospray-ionization (ESI) and matrix-assisted laser desorption/ionization (MALDI) high resolution mass spectrometry were employed to measure both activated and non-activated PCBM films in the mass spectroscopy facility at OCI Heidelberg under the supervision of Dr. J. Gross.

Experimental Information: Dopants and PCBM were mixed in a solution of chlorobenze similar to the thin film preparation in Section 13.1 at a molar ratio of 1:3 (*o*-AzBnO-DMBI:PCBM). The solution was subsequently dried in vacuum to yield a solid blend of dopant and PCBM deposited on the walls of the glass bottle. Activation of the azide by heat was carried out on a hotplate at 135 °C under nitrogen atmosphere by annealing the dried blend within the glass bottle. Additionally, small amounts of pure material were weighed for mass analysis without further conditioning. The vacuum-dried blend cannot be easily UV-activated in the bottle, because the UV-light does not deeply penetrate into PCBM powder. Therefore large glass substrates are spin-coated at 1000 rpm to prepare thin films of ca. 50 nm thickness, which were exposed to UV-light at 254 nm for 30 min. Afterwards the material was rinsed with chlorobenze and collected in a glass bottle to be dried by vacuum as well. The samples were then carried to the OCI Heidelberg for mass analysis. There the samples were stored in a fridge until they were further processed. The mass spectra were recorded using the following instruments: JEOL JMS-700 magnetic sector (EI); Bruker ApexQehy-brid 9.4 T FT-ICR (ESI, DART); Finnigan LCQquadrupole ion trap (DART); Bruker Autoflex Speed (MALDI).

Results: MALDI mass spectra of *o*-AzBnO-DMBI blended witch PCBM are shown in Figure 13.14 together with the assignment of important mass traces. Complementary ESI spectra are recorded showing similar results to the data obtained from MALDI measurements. For the non-activated pure blend in Figure 13.14 the main peak is located at mass 370.2 m/z which matches the cationic *o*-AzBnO-DMBI molecule with intact azide group [*o*-AzBnO-DMBI -H]$^+$. It is thus assumed that the MALDI excitation laser does not strongly trigger azide decomposition. Nonetheless, the possibility of laser desorption affecting the azide is a considerable concern,[283] which is why auxiliary ESI spectra were recorded (see Figure B.1). In the pure blend a small amount of amine product is detected at 344.2 m/z, that matches the mass of cationic *o*-AzBnO-DMBI for which the azide has transformed to an amine group [(*o*-AzBnO-DMBI) -H -N_3 +NH_2]$^+$. Relative to cationic *o*-AzBnO-DMBI, provided similar detection efficiency, only trace amounts of amine is expected to be present in the blend. Among all possible nitrene products, amine is the least favourable, since no further addition reaction can occur. PCBM with an estimated mass of 910 g mol$^-$ can only be found with a small signal in Figure 13.14a after averaging in high-resolution (not shown here). With better signal to noise a small peak from cycloaddition products can be found as well, which have formed during processing and transport or by laser desorption.

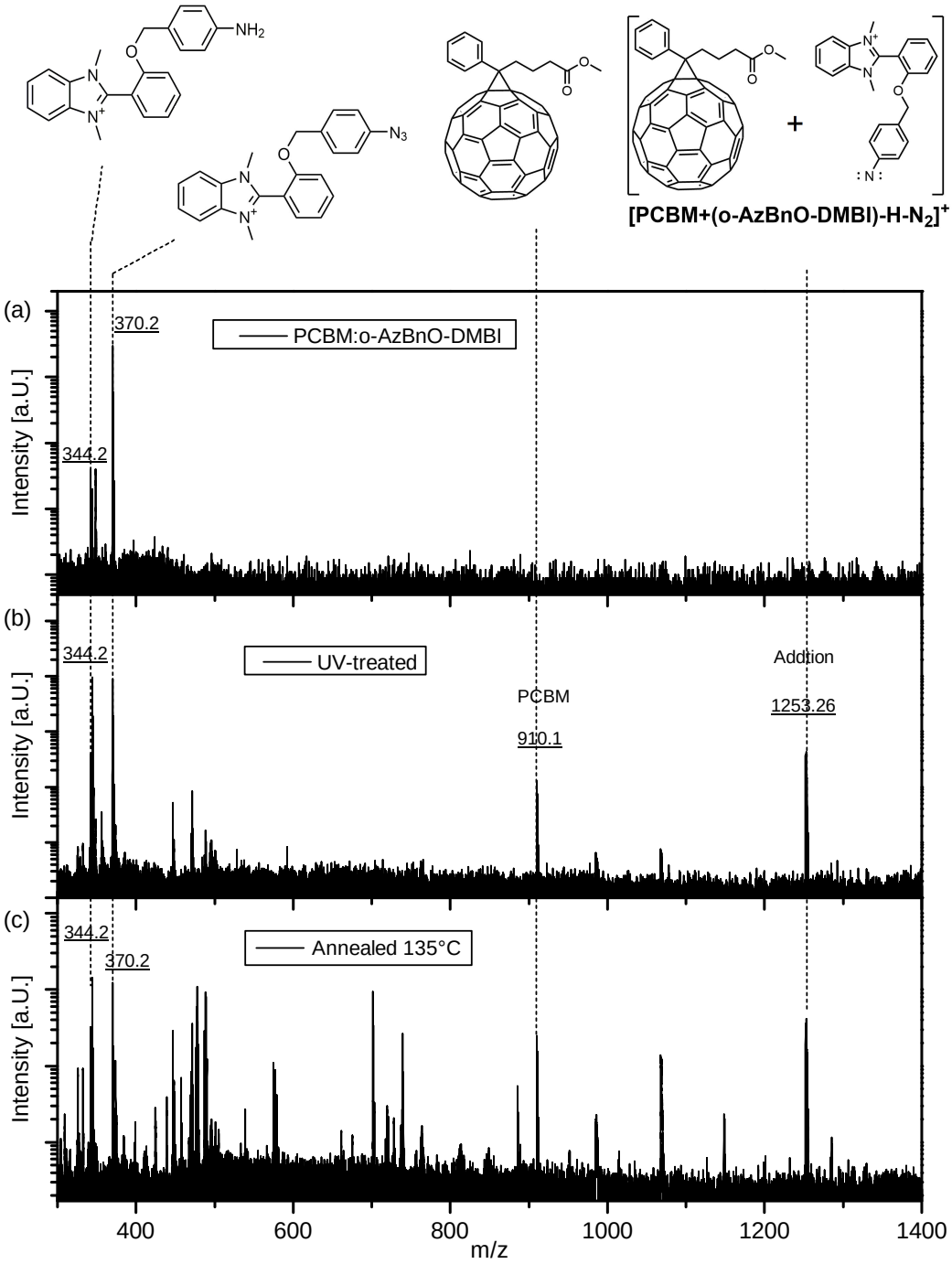

Figure 13.14: MALDI mass spectroscopy data of a blend of PCBM and *o*-AzBnO-DMBI at 25 mol% in (a) after UV-treatment in (b) and thermal annealing at 135 °C in (c) on a log-scale. The assignment of mass traces is depicted above. In principle, the MALDI desorption laser can cause azide decomposition but we observe a pronounced main peak at 370.2 m/z assigned to intact *o*-AzBnO-DMBI in (a). PCBM and CH insertion products are clearly visible in (b) with trace amounts of amine and *o*-AzBnO-DMBI. There are multiple fragments within the thermally activated blends in (c). The data were provided by the mass spectroscopy facility at OCI Heidelberg under the supervision of Dr. J. Gross.

Given the doping ratio in solution, PCBM seems to have a lower cross-section/detection-efficiency than the lighter dopant cation. Remarkably, for the UV-activated blend in Figure 13.14b a distinct peak at 1253.26 m/z is found, which can be assigned to the direct addition product: [PCBM+(*o*-AzBnO-DMBI)]$^+$ minus nitrogen [N_2] and a hydrogen atom [H] to be [PCBM+(*o*-AzBnO-DMBI)-H-N_2]$^+$. This is direct evidence for the cycloaddition of *o*-AzBnO-DMBI covalently connecting to PCBM supporting the picture of an anchoring dopant molecule. Beside the important cycloaddition product in Figure 13.14b, there is a peak assigned to PCBM and traces of un-activated *o*-AzBnO-DMBI cations and amine products at comparable strength. After UV-treatment ideally no un-reacted *o*-AzBnO-DMBI is supposed to be present in the thin film, as found by IR-measurements. Given the higher detection efficiency of the dopant relative to PCBM in Figure 13.14a, it is concluded that there are indeed only small amounts of amine and *o*-AzBnO-DMBI present in the film and that a major dopant fraction has undergone addition reactions. However, a real quantitative prediction with mass spectroscopy data is usually not possible. The thermally activated sample in Figure 13.14c shows the same products as for UV-treated samples but considerably more by-products which could not be assigned in detail. The results in Figure 13.14c show that UV-activation is still the more benign method to trigger nitrene generation. In ESI spectra towards lower mass (see Appendix), a peak at 239.1 m/z is found for the thermally activated blend, which can be attributed to *o*-AzBnO-DMBI having lost the phenyl anchor. The molecular weight matches the DMBI body plus the remaining O-H group but without the phenyl attachment: [DMBI +OH -H]$^+$. At higher temperatures a breaking of the ether bond was suspected from XPS analysis in Section 13.4 and is here corroborated via mass spectroscopy.

14 P3HT blended with o-AzBnO-DMBI

Due to the lack of suitable n-type polymers that could have offered a larger diffusivity for molecular dopants, a significant improvement for organic devices by potential immobilization of *o*-AzBnO-DMBI could not yet be demonstrated. To resolve this problem, *o*-AzBnO-DMBI is blended with the p-type polymer P3HT, for which F4TCNQ and Mo(tfd-CO_2Me)$_3$ were found to drift in an electrical field. Since DMBI derivatives are essentially used as strong electron donors or n-dopants, a doping effect in P3HT seems unlikely. However, they can be used to counter unintentional p-doping from oxygen or water to obtain more intrinsic P3HT. It is known from literature, that even if processed in a nitrogen glove-box, residual oxygen or water can cause P3HT to become unintentionally p-doped.[284,285] If P3HT is blended with DMBI, even processing in air may be possible without p-doping. An application was found by M. Barf (TU Braunschweig) for organic field effect transistors (OFET) made from P3HT, because a more intrinsic P3HT offers lower off-currents and a potentially higher on-off ratio. In addition, those OFETs were processed in air showing good overall performance. Furthermore, a suppressed hysteresis was found for UV-treated *o*-AzBnO-DMBI, but not for transistors build with *o*-BnO-DBMI regardless of UV-treatment, indicating a successful reduction of ionic contributions from drift or diffusion. This work will be published soon. Here, photoelectron spectroscopy measurements are reported, showing counter-doping of P3HT processed in air.

Experimental Information: The dopants were mixed with P3HT in a chlorobenzene solution at a concentration of 7.5 g L^{-1} and a molar mixing ratio of DMBI to P3HT monomers of 1:10. Similar to PCBM, the P3HT solution is stirred overnight at 50 °C in the glovebox and the dopants are solved right before processing, since they are not stable in solution. Spin-coating was done in air on ITO at 1000 rpm for 60 s. UV-activation was carried out in the nitrogen glovebox for 20 min similar to Section 13.1.

Results: The measured XPS and UPS of *o*-BnO-DMBI and *o*-AzBnO-DMBI blended with P3HT are presented in Figure 14.1. A clear Fermi level shift towards higher binding energies with respect to P3HT can be seen for both *o*-BnO-DMBI and *o*-AzBnO-DMBI in the core-level spectra in Figure 14.1e, g. This means that the DMBI-blended samples cause a Fermi level shift towards the LUMO level of P3HT, a behaviour typically observed for n-doping. The doping mechanism of DMBI is expected to proceed via hydride transfer forming, see Section 8.1. The SOMO level is anticipated to be at ca. -2.53 eV for *o*-MeO-DMBI$^{\cdot}$ by Bin et al.[286] which is not low enough to be doping P3HT with a LUMO of 2.13 eV efficiently.[77] Since an electron transfer to the LUMO level of P3HT is not possible, compensation-doping of a former p-doped P3HT or filling of band-gap states up to the charge neutrality level are possible explanations for the observed Fermi level shift. To verify that P3HT was indeed p-doped by oxygen, a band diagram was constructed based on UPS measurements assuming a common band gap, which can be estimated from literature values in Figure 14.2. From conductivity measurement it is known that P3HT blended with DMBI becomes about 4 orders of magnitude less conductive, which suggests a reduction of the free charge carrier density. However, due to the low conductivity of DMBI-blended P3HT, UPS spectra suffer from charging effects.

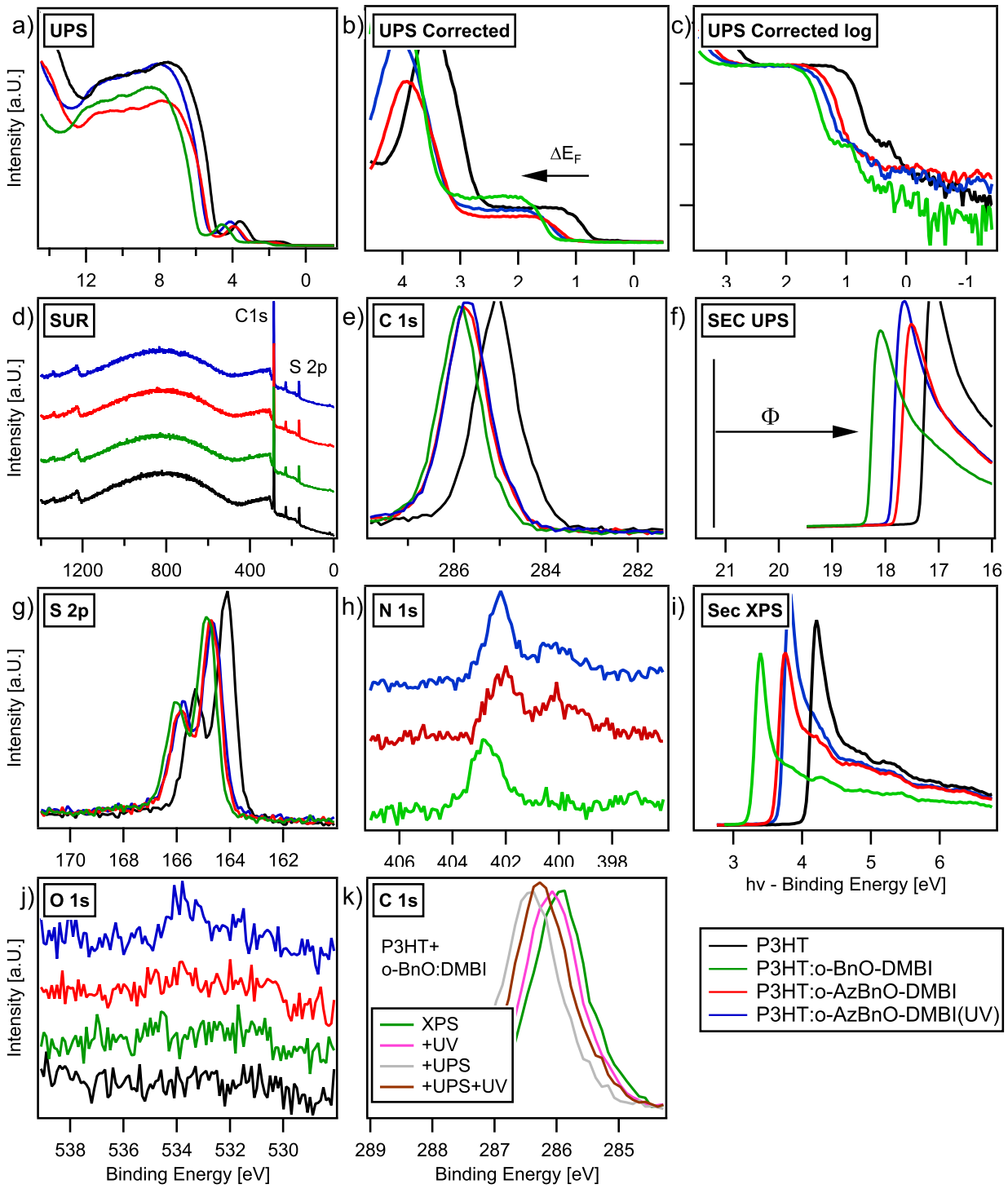

Figure 14.1: XPS and UPS spectra of P3HT in black, blended with *o*-BnO-DMBI in green and *o*-AzBnO-DMBI in red. UV treated films mixed with *o*-AzBnO-DMBI are plotted in blue. The legend for all figures, except of (k), are given in the right lower corner. The C 1s core-level emission is measured for P3HT:*o*-BnO-DMBI under different illumination to analyse effects of charging. In (b) and (c) a correction on the Fermi level position due to charging from UPS was applied, estimated based on C 1s shift under illumination as in (k). The spectra in (f) were measured under illumination of UV light at ca. 354 nm.

If the resistivity is too high, remaining positive charges from photoelectrons leaving the sample can not be fully compensated and build up an attractive surface potential. Photoelectrons then appear to have less kinetic energy and emission lines are shifted to higher binding energies, which can be confused with a Fermi level shift similar to n-doping. In order to verify that one indeed has a Fermi level shift from p-type to more intrinsic P3HT, the contribution from surface charging has to be considered. Since there is no significant broadening in line-shapes and only thin layers of P3HT are measured, it is assumed to have only a small additional energy shift in the UPS-spectra. For this purpose the C 1s core-level was measured with XPS under UV illumination from the UPS discharge lamp and a 364 nm photodiode in Figure 14.1k. The UPS-excitation causes a considerable shift to higher binding energies, whereas a small recovery is observed if the UV-photodiode is switched on. With a photon energy larger than the band gap of P3HT, the UV-photodiode photo-generates charge carriers in P3HT increasing its conductivity and reducing charging effects from UPS measurements. Since little to no influence of the photodiode on XPS and pure P3HT spectra is observed, it is assumed that they are not affected from charging. To account for this error, UPS spectra were charge-corrected by a constant energy shift, determined according to the difference from the XPS-only C 1s level in Figure 14.1k, to arrive at the spectra plotted in 14.1c. This systematic correction is not free of error, but not avoidable with our current set-up. Therefore, an additional systematic uncertainty must be kept in mind for the spectra in Figure 14.1k, c. The UPS secondary electron cutoff (SEC) depicted in Figure 14.1f was not corrected for charging, but measured under UV-illumination. For determining the work function, the secondary electron cutoffs measured by XPS in Figure 14.1i are used. From charge corrected UPS and XPS values in Table 14.1, the band diagram in Figure 14.2 was constructed assuming a constant band gap of $E_g = 1.9$ eV. Within the margin of errors, one finds a slightly p-doped pristine P3HT film, presumably from absorbed oxygen, and a more intrinsic Fermi level position if blended with *o*-AzBnO-DMBI. One can not identify an impact of UV-activation on the band substructure of *o*-AzBnO-DMBI:P3HT. On the other hand, the Fermi level position of P3HT mixed with *o*-BnO-DMBI appears to be shifted even further towards the LUMO in Figure 14.2, which is mainly due to a lower work function of the *o*-BnO-DMBI:P3HT sample. There is not a

Sample	Work function [eV]	HOMO corrected [eV]	C 1s [eV]
P3HT	4.05	0.7	285.12
P3HT:*o*-AzBnO-DMBI	3.64	1.05	285.47
P3HT:*o*-AzBnO-DMBI(UV)	3.67	1.2	285.65
P3HT:*o*-BnO-DMBI	3.2	1.4	285.75

Table 14.1: Work function, HOMO onset and C 1s peak maximum from spectra in Figure 14.1. The HOMO onset and secondary electron cutoff has been determined from linear extrapolation at highest slope. For the HOMO onset the charge corrected spectra in Figure 14.1b is used.

conclusive explanation for this observation but one can speculate that *o*-BnO-DMBI forms larger clusters on the surface region since *o*-BnO-DMBI tends to crystallize and does not mix with P3HT as well as *o*-AzBnO-DMBI. Nonetheless, the Fermi level shift measured for the C 1s level with respect to pure P3HT seems to be almost the same for both DMBI derivatives. Surprisingly, after spin-coating in air and UV-treatment in the glovebox, little to no oxygen is found in the O 1s region, which could have been suspected from comparable treatment of n-doped PCBM. After sufficient data accumulation for increasing the signal-to-noise ratio, one can resolve the N

1s signal for *o*-BnO-DMBI and *o*-AzBnO-DMBI, revealing a peak component at around 402.5 eV previously ascribed to charged DMBI. The N 1s emission of neutral DMBI at 400 eV is hardly visible for *o*-BnO-DMBI suggesting that most *o*-BnO-DMBI are existent as cationic species. Although a high fraction of charged DMBI was found for doping concentrations of 10 mol% for PCBM as well, charged DMBI in P3HT is interesting and proofs that DMBI is indeed undergoing charge transfer. This matches the observation of a Fermi level shift towards the intrinsic position of P3HT, if DMBI is countering unintentional p-doping. For *o*-AzBnO-DMBI most of the azide seems to be reacted during processing or measurement, since the emission at 405 eV of the central nitrogen peak of the azide group is not clearly visible. For both *o*-AzBnO-DMBI samples a broad peak component at 400 eV indicates the formation of carbon-nitrogen bonds after azide decomposition either by explicit UV treatment or during processing/measurement.

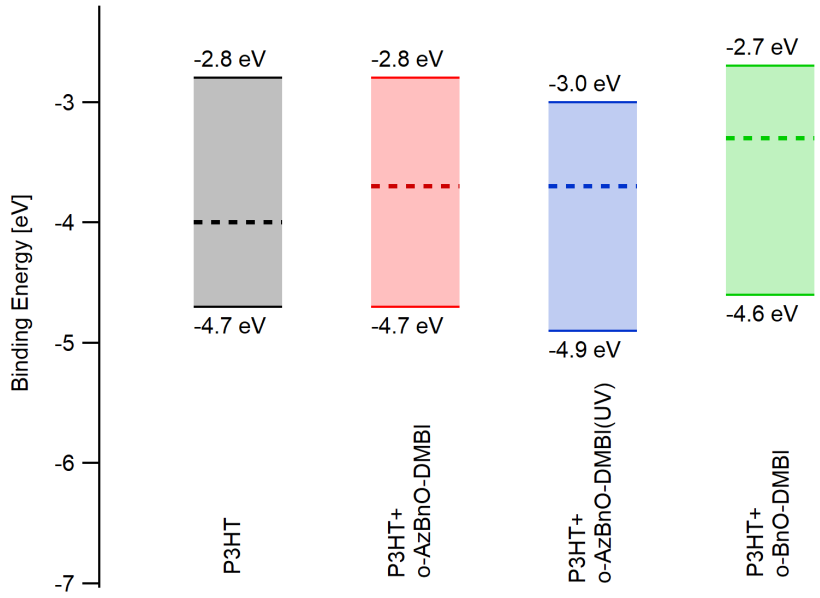

Figure 14.2: Band diagram for P3HT blended with *o*-AzBnO-DMBI and *o*-BnO-DMBI with values from Table 14.1 and a constant band gap of E_g = 1.9 eV.

15 Summary and conclusion

In this work, properties of molecular dopants in organic semiconductors are investigated aiming for a better understanding of their morphological stability. In the case of inorganic semiconductors, doping can be regarded as the key tool to control charge carrier density and energy level alignment at metal or semiconductor interfaces that ultimately give rise to a multitude of electronic devices. Typical examples are p-n junctions in diodes and bipolar junction transistors. Even in field effect transistors doping is heavily exploited in modern silicon technology for integrated circuits. However, in organic semiconductors doping efficiencies are much lower and the first devices like organic light emittind diodes (OLED) and photovoltaics (OPV) were exclusively built from intrinsic materials.[7,8,34] This is partly due to the high mobility of halides and alkali metals used as dopants. With emerging molecular dopants, stable doped layers are nowadays frequently employed as injection and transport layers in OLEDs and even p-n structures have been reported.[44,111] Nonetheless, dopants are known to cause exciton quenching[16] and there are material systems, especially among polymers, where a considerable diffusion of molecular dopants is observed.[14,15] Therefore a goal of this work was to study immobilization strategies for molecular dopants which are as little invasive as possible and at the same time universally applicable.

The first part of this thesis summarizes important basic considerations and provides an overview of relevant literature on the subject. In part II of this thesis, the well-known polymer poly(3-hexylthiophene) (P3HT) is doped with the soluble bulky molybdenum complex Mo(tfd-CO_2Me)$_3$, which represents a dopant-matrix system that can be studied with respect to different morphologies and processing methods. Since the regio-regularity of P3HT determines its crystallinity, regio-regular P3HT (rr-P3HT) features a high degree of order, whereas regio-random P3HT (rra-P3HT) forms fully amorphous thin films. Furthermore Mo(tfd-CO_2Me)$_3$ is derived from Mo(tfd)$_3$ to increase its solubility, which means that the dopant can be both deposited by thermal evaporation and mixed in solution. The diffusion of Mo(tfd-CO_2Me)$_3$ is comparatively studied in sequentially doped rr-P3HT and rra-P3HT films by means of Infrared and photoelectron spectroscopy. Thereby it is possible to differentially evaluate charge transfer in the bulk and at the surface. Sequential doping caught increasing interest recently, because introduction of dopants can be achieved on previously prepared polymer films offering the possibility of, at least in some cases, doped and highly ordered films.[118] With in-situ IR spectroscopy an immediate doping of the polymer film is verified that occurs during dopant deposition as evidenced by polaronic absorption bands. This suggests that Mo(tfd-CO_2Me)$_3$ quickly enters both rra-P3HT and rr-P3HT given the conditions of the thermal evaporation process. In a control experiment, corresponding doping on nitrogen-cooled rr-P3HT is not observed unless subsequently heated to room temperature accompanied by a much slower build up of absorption bands assigned to doping. With XPS core-level spectra recorded after deposition, neutral and charged dopants can be distinguished and the average dopant concentration at the surface can be calculated. This measurement is further instrumental in finding the maximum dopant capacity of such films, since a pure dopant ad-layer forms, if P3HT can no longer incorporate dopants. In fact, for lower cover-

ages the measured surface concentration implies that Mo(tfd-CO_2Me)$_3$ must have diffused into P3HT during deposition. The amount of charge transfer is inferred from the S 2p emission which was previously studied in fully solution-doped films. Interestingly, for low dopant coverage only charged dopants are present at the surface until a maximum number is reached and neutral dopants add to the surface. With XPS the dopant concentration is monitored as a function of time after deposition, revealing a slow decrease in the neutral dopant fraction, whereas the amount of charged dopants stays constant regardless of the coverage. This suggests that neutral dopants are more mobile than charged dopants, which are likely bound to the P3HT host by coulomb forces. Furthermore, the subsequent changes in surface concentration are much more prominent for rr-P3HT than for rra-P3HT and are numerically fitted by a model that describes adsorption, charging and diffusion of dopant molecules. Within this model, a higher dopant capacity is found in case of rr-P3HT compared to rra-P3HT and a lower limit of the diffusion constant at room-temperature can be estimated. Although there is no direct evidence, the data suggest that the semi-crystalline morphology, especially grain boundaries, may be an important factor aiding the diffusion of dopants.

A field-induced drift of dopants such as F4TCNQ and Mo(tfd-CO_2Me)$_3$ is observed by Müller at al.,[120] if a sufficiently high electrical voltage is applied to a doped P3HT film sandwiched between two electrodes in both vertical and lateral geometry. The movement of dopant is verified by optical fluorescence and infrared microscopy measured on a lateral channel and shows a distinct electrical hysteresis which can be correlated to optical microscopy data. Provided a high electrical field, dopant anions are pushed away from the cathode, causing a de-doped region of pure P3HT and leading to a fall-off in current. A proof of ion-migration is also attempted by means of in-situ XPS within this work. Here, a focused X-ray beam is moved along the channel after a voltage is applied to the electrodes inside the vacuum chamber. However, a conclusive evidence for dopant migration was not found, which may be due to the high surface sensitivity of XPS or the choice and layout of electrodes. To improve this experiment, a single lateral transistor channel should be chosen that can be controlled by the recently modified XPS sample holder. However, a vertical channel geometry, in which photoelectrons have to travel through the top electrode, was not suited for measuring the dopant drift at the contact. A thin gold layer of a few nanometres is not conductive enough compared to doped P3HT in order to distribute the current on the surface and still be sufficiently transparent for XPS.

Prior to the experiment on sequential deposition of Mo(tfd-CO_2Me)$_3$, the dopant and its properties were studied in solution-doped P3HT films. Efficient doping leads to a Fermi level shift of 0.5 - 1 eV towards to HOMO level of P3HT. Upon electron transfer the anionic species of Mo(tfd-CO_2Me)$_3$ is identified in the Mo 3d and S 2p core-level emission of doped films. A decrease in charge transfer efficiency is observed for higher doping concentrations as expected from previous studies. A comparison of the surface concentration with the intended doping concentrations in solution suggests a homogeneous dopant distribution. Additionally, a study of energy level alignment at the interface of a doped polymer film was attempted by systematically varying the doping concentration of the silicon substrate, on which doped P3HT was spin-cast from solution. In contrast to small molecular semiconductors, polymers can not be step-wise deposited and repeatedly measured with XPS in order to construct the band alignment at the substrate interface. Therefore, the idea was to vary the Fermi level position of a semiconducting substrate instead. However, conclusive results for a further-reaching study on band alignment

with respect to substrate properties could not be obtained, since intrinsic P3HT layers suffer from charging and the substrate surface properties, especially the work function and surface termination, are not sufficiently controlled. To improve this experiment in future studies, the layer thickness of P3HT should be chosen smaller to avoid charging and to detect the energy level position of the substrate emission. Furthermore, the native oxygen layer could be removed by etching and the P3HT film could be deposited on hydrogen-terminated silicon in an oxygen-free process and sample transfer. Alternatively, one could attempt a low and high film thickness by choosing two appropriate processing parameters in order to test the extent of the interface dipole and check for band bending in the silicon substrate. To guarantee a similar film quality for different thickness, which impacts the position of energy levels, the samples may need to be cross-validated with structural analysis. In the context of studying the drift of $Mo(tfd\text{-}CO_2Me)_3$ as described above, an interface study was conducted by evaporating silver on a doped P3HT film and by successively measuring photoemission. Silver was found to exhibit island growth on the doped P3HT films as inferred from core-level damping in XPS and scanning electron microscopy. At very low coverages a partial intercalation into the P3HT film is suspected. Since silver is exhibiting inhomogeneous growth conditions and organic residues are presumed to be floating on the growing silver layer, conclusions about the spacial extension of band alignment can not be made. However, a core-level shift of up to 0.5 eV is measured for P3HT upon silver deposition, whereas the F 1s level and the S 2p portion, attributed to charged dopants, does not shift accordingly and roughly stays constant regardless of the silver coverage. This can possibly be explained by isolated dopants or clusters of $Mo(tfd\text{-}CO_2Me)_3$ at the metal interface accepting an electron from silver.

In part III of this thesis, a new functionalized n-dopant is characterized which is expected to facilitate a controllable immobilization in a broad class of organic semiconductors. In this work, the primary strategy to suppress diffusion relies on a chemical reaction of the dopant with its host matrix forming covalent bonds which ultimately prevents the dopant from migrating. To achieve such an anchoring reaction, the dopant needs to be equipped with an additional "anchor" group that can be externally triggered by heat or light to engage a covalent bonding via click-chemistry. In this approach, concentration and processing can be freely adjusted and dopant immobilization initiated on the final blend by for example UV-light. In principle, this concept requires a complementary modification by functional groups of both dopant and matrix, which is not available so far with the known organic semiconductors. Therefore, reactive azides are chosen to fulfil the role of an universal "anchor" group, which ideally offers the possibility to attach to aliphatic C-H or olefinic C=C bonds present in almost any organic semiconductor by generating reactive singlet nitrenes upon photolysis. It is to note that azides have been previously reported as cross-linkers in desolubilization of semiconducting polymers.[184] To test chemical reactions and stability of a small molecule bearing a phenylazide group, the test molecules ABN and F4ABN were studied which possess a naphthalene body and can not induce doping but are comparable in size to e.g. F4TCNQ. The fluorine protected phenyl azide of F4ABN is expected to offer a higher yield of addition reactions compared to ABN. The spectroscopic signature of the azide group could be detected in blends with common host materials like P3HT and PCBM, and a controlled activation by UV-light is evidenced by IR spectroscopy. This is in agreement with XPS, where the transformation of the N 1s core-level emission upon UV-treatment suggests decomposition of azide and the formation of new C-N or N-H bonds. This is also observed for pure ABN and F4ABN films, for which a reaction with neighbouring ABN

or F4ABN molecules is to be expected. Problems of mixing and crystallization are observed for PCBM and P3HT in microscopic images, which at least in the case of PCBM can be avoided by an additional annealing step to remove residual solvent. With respect to immobilization and anchoring, it can be demonstrated that ABN and F4ABN films are not stable in vacuum conditions and even evaporate from P3HT and PCBM blends in considerable amounts, which can be almost completely prevented when the film is activated by UV-light. This suggests a linking or cross-linking of ABN and F4ABN upon UV-treatment, reducing their volatility in vacuum. However, the precise anchoring mechanism could not be analysed with IR or XPS measurements.

The new derivatives of the air-stable n-dopant DMBI are named *o*-BnO-DMBI and *o*-AzBnO-DMBI and possess a phenyl and phenyl-azide group in ortho-position. The dopant *o*-AzBnO-DMBI is exemplary studied with regard to both doping and anchoring capabilities, whereas *o*-BnO-DMBI and the literature-known *o*-MeO-DMBI serve as a non-immobilizable reference. The dopants were blended with PCBM and activated by UV light after solution processing. Electrical measurements show that both *o*-BnO-DMBI and *o*-AzBnO-DMBI are effectively doping PCBM leading to conductivities values similar to those reported for DMBI. After UV-activation a small decrease in conductivity is correlated to an oxidation of the thin film surface from residual oxygen or water as evidenced by XPS. An additional annealing step improves the conductivity again, which is attributed to a thermal generation of charged dopants, arriving at a total of about six orders of magnitude increase in conductivity. The doping of PCBM can be further verified by photoelectron spectroscopy revealing a shift in the Fermi level position as well as charged dopant species. The anchoring properties of *o*-AzBnO-DMBI are investigated by testing the thermal stability of a highly doped PCBM film in ultra-high-vacuum (UHV). Additionally a bilayer structure of only a few monolayers is measured by XPS with the dopant on-top of PCBM exposed to UHV at room temperature. It is shown that activated *o*-AzBnO-DMBI increases the evaporation temperature of the blend even beyond the 300 °C measured for pure PCBM. In contrast, a fast desorption at around 180 °C is observed for *o*-BnO-DMBI with the remaining PCBM evaporating at 300 °C. However, there is evidence that the ether bond of *o*-AzBnO-DMBI and *o*-BnO-DMBI starts to break at higher temperatures. In a bilayer-structure *o*-AzBnO-DMBI was found to leave the PCBM surface already at room temperature but resisted desorption, if the film is activated by UV-light before entering UHV. These conclusions are drawn from a detailed analysis of XPS core-level spectra mainly from the dopant's N 1s and the substrate's Si 2p emission. Within a careful peak analysis of the N 1s emission, contributions of the azide and the DMBI body of *o*-AzBnO-DMBI can be separated and followed as a function of temperature. The doping mechanism of DMBI involves a hydride transfer to the host or a hydrogen radical transfer with a subsequent electron transfer, which can be partially initiated by temperature. For *o*-BnO-DMBI two nitrogen species are observed assigned to neutral and charged dopants. The N 1s emission of azides was separately measured for the test molecules ABN and F4ABN. A peak fit of the N 1s core-level of *o*-AzBnO-DMBI reveals an activation of both the azide decomposition and the DMBI charge transfer with increasing temperature. A direct proof for the reaction of *o*-AzBnO-DMBI with PCBM is given by a mass-spectroscopy measurement of the activated redissolved PCBM film. Beyond the doping and reaction of PCBM, a counter-doping effect of *o*-AzBnO-DMBI in unintentionally p-doped P3HT is observed. This can be beneficently used in P3HT transistors exposed to air, reducing their off-currents.
If a similar functionalization of p-dopants is successful in the future, a wider scope of matrix materials, especially polymers, can be tested. With immobilization of both p- and n-dopants

applications such as p-n junctions and thermoelectric devices can be approached.

In conclusion, photoelectron spectroscopy was applied to study the diffusion of molecular dopants in organic semiconductors. Although microscopy methods are more suited to investigate migration of dopants by measuring their lateral diffusion profile, photoemission can be used to determine the change in doping concentration selectively at the surface due to its high surface sensitivity. This can be done indirectly based on changes of the Fermi level position or by directly identifying the characteristic core-level emission of charged and neutral species. In this approach, migration is observed on length scales that are more relevant to devices, where an undesired vertical diffusion can become detrimental for lifetime and performance. Chemical reactions such as the activation of the anchor group of *o*-AzBnO-DMBI are directly monitored in combination with charge transfer and doping, which makes XPS a unique tool to correlate chemical reactions with doping or diffusion properties.

To summarize this work, the dopant diffusion in a sequential doping process is studied non-destructively by XPS on device relevant length scales to better understand and to identify process parameters like saturation and charge transfer efficiency. With the characterization of *o*-AzBnO-DMBI a first step towards a universally anchoring dopant is made.

Bibliography

[1] H. Letheby, "XXIX. - On the production of a blue substance by the electrolysis of sulphate of aniline," *J. Chem. Soc.*, vol. 15, pp. 161–163, 1862.

[2] S. C. Rasmussen, "The Early History of Polyaniline: Discovery and Origins," *Substantia*, vol. 1, Oct. 2017.

[3] R. McNeill, R. Siudak, J. H. Wardlaw, and D. E. Weiss, "Electronic conduction in polymers. I. The chemical structure of polypyrrole," *Australian Journal of Chemistry*, vol. 16, no. 6, pp. 1056–1075, 1963.

[4] M. Pope, H. P. Kallmann, and P. Magnante, "Electroluminescence in Organic Crystals," *The Journal of Chemical Physics*, vol. 38, no. 8, pp. 2042–2043, 1963.

[5] W. Helfrich and W. G. Schneider, "Recombination Radiation in Anthracene Crystals," *Phys. Rev. Lett.*, vol. 14, pp. 229–231, Feb 1965.

[6] H. Shirakawa, E. J. Louis, A. G. MacDiarmid, C. K. Chiang, and A. J. Heeger, "Synthesis of electrically conducting organic polymers: halogen derivatives of polyacetylene, (ch)," *J. Chem. Soc., Chem. Commun.*, pp. 578–580, 1977.

[7] C. W. Tang and S. A. VanSlyke, "Organic electroluminescent diodes," *Applied Physics Letters*, vol. 51, no. 12, pp. 913–915, 1987.

[8] C. W. Tang, "Two-layer organic photovoltaic cell," *Applied Physics Letters*, vol. 48, no. 2, pp. 183–185, 1986.

[9] B. W. D'Andrade, S. R. Forrest, and A. B. Chwang, "Operational stability of electrophosphorescent devices containing p and n doped transport layers," *Applied Physics Letters*, vol. 83, no. 19, pp. 3858–3860, 2003.

[10] Y. Yamamoto, K. Yoshino, and Y. Inuishi, "Electrical Properties of Phthalocyanine-Halogen Complexes," *Journal of the Physical Society of Japan*, vol. 47, no. 6, pp. 1887–1891, 1979.

[11] N. T. Kalyani and S. Dhoble, "Organic light emitting diodes: Energy saving lighting technology - A review," *Renewable and Sustainable Energy Reviews*, vol. 16, no. 5, pp. 2696 – 2723, 2012.

[12] M. Pfeiffer, T. Fritz, J. Blochwitz, A. Nollau, B. Plönnigs, A. Beyer, and K. Leo, "Controlled doping of molecular organic layers: Physics and device prospects," in *Advances in Solid State Physics 39* (B. Kramer, ed.), (Berlin, Heidelberg), pp. 77–90, Springer Berlin Heidelberg, 1999.

[13] M. L. Tietze, L. Burtone, M. Riede, B. Lüssem, and K. Leo, "Fermi level shift and doping efficiency in p-doped small molecule organic semiconductors: A photoelectron spectroscopy and theoretical study," *Phys. Rev. B*, vol. 86, p. 035320, Jul 2012.

[14] W. Gao and A. Kahn, "Controlled p-doping of zinc phthalocyanine by coevaporation with tetrafluorotetracyanoquinodimethane: A direct and inverse photoemission study," *Applied Physics Letters*, vol. 79, no. 24, pp. 4040–4042, 2001.

[15] S. Duhm, I. Salzmann, B. Bröker, H. Glowatzki, R. L. Johnson, and N. Koch, "Interdiffusion of molecular acceptors through organic layers to metal substrates mimics doping-related energy level shifts," *Applied Physics Letters*, vol. 95, no. 9, p. 093305, 2009.

[16] P. Tyagi, S. Tuli, and R. Srivastava, "Study of fluorescence quenching due to 2,3,5,6-tetrafluoro-7,7',8,8'-tetracyano quinodimethane and its solid state diffusion analysis using photoluminescence spectroscopy," *The Journal of Chemical Physics*, vol. 142, no. 5, p. 054707, 2015.

[17] W. Brütting, ed., *Physics of Organic Semiconductors*. John Wiley & Sons, Ltd, 1 ed., 2005.

[18] J. Y. Lee, S. Roth, and Y. W. Park, "Anisotropic field effect mobility in single crystal pentacene," *Applied Physics Letters*, vol. 88, no. 25, p. 252106, 2006.

[19] A. Troisi and G. Orlandi, "Charge-Transport Regime of Crystalline Organic Semiconductors: Diffusion Limited by Thermal Off-Diagonal Electronic Disorder," *Phys. Rev. Lett.*, vol. 96, p. 086601, Mar 2006.

[20] H. Bässler, "Localized states and electronic transport in single component organic solids with diagonal disorder," *physica status solidi (b)*, vol. 107, no. 1, pp. 9–54, 1981.

[21] R. Schmechel, "Hopping transport in doped organic semiconductors: A theoretical approach and its application to p-doped zinc-phthalocyanine," *Journal of Applied Physics*, vol. 93, no. 8, pp. 4653–4660, 2003.

[22] A. Miller and E. Abrahams, "Impurity conduction at low concentrations," *Phys. Rev.*, vol. 120, pp. 745–755, Nov 1960.

[23] M. C. J. M. Vissenberg and M. Matters, "Theory of the field-effect mobility in amorphous organic transistors," *Phys. Rev. B*, vol. 57, pp. 12964–12967, May 1998.

[24] I. Hill, A. Kahn, Z. Soos, and J. R.A. Pascal, "Charge-separation energy in films of π-conjugated organic molecules," *Chemical Physics Letters*, vol. 327, no. 3, pp. 181 – 188, 2000.

[25] R. H. Boyd, "Relaxation processes in crystalline polymers: molecular interpretation - a review," *Polymer*, vol. 26, no. 8, pp. 1123 – 1133, 1985.

[26] S. Duhm, Q. Xin, S. Hosoumi, H. Fukagawa, K. Sato, N. Ueno, and S. Kera, "Charge Reorganization Energy and Small Polaron Binding Energy of Rubrene Thin Films by Ultraviolet Photoelectron Spectroscopy," *Advanced Materials*, vol. 24, no. 7, pp. 901–905, 2012.

[27] W. R. Salaneck, "Intermolecular Relaxation Energies in Anthracene," *Phys. Rev. Lett.*, vol. 40, pp. 60–63, Jan 1978.

[28] E. Tsiper, Z. Soos, W. Gao, and A. Kahn, "Electronic polarization at surfaces and thin films of organic molecular crystals: PTCDA," *Chemical Physics Letters*, vol. 360, no. 1, pp. 47 – 52, 2002.

[29] J. Sworakowski, "How accurate are energies of HOMO and LUMO levels in small-molecule organic semiconductors determined from cyclic voltammetry or optical spectroscopy?," *Synthetic Metals*, vol. 235, pp. 125 – 130, 2018.

[30] A. J. Heeger, "Charge Storage in Conducting Polymers: Solitons, Polarons, and Bipolarons," *Polymer Journal*, vol. 17, pp. 201–208, jan 2006.

[31] S. Kahmann, D. Fazzi, G. J. Matt, W. Thiel, M. A. Loi, and C. J. Brabec, "Polarons in Narrow Band Gap Polymers Probed over the Entire Infrared Range: A Joint Experimental and Theoretical Investigation," *The Journal of Physical Chemistry Letters*, vol. 7, no. 22, pp. 4438–4444, 2016. PMID: 27749079.

[32] R. Österbacka, C. P. An, X. M. Jiang, and Z. V. Vardeny, "Two-Dimensional Electronic Excitations in Self-Assembled Conjugated Polymer Nanocrystals," *Science*, vol. 287, no. 5454, pp. 839–842, 2000.

[33] R. Ghosh, C. M. Pochas, and F. C. Spano, "Polaron Delocalization in Conjugated Polymer Films," *The Journal of Physical Chemistry C*, vol. 120, no. 21, pp. 11394–11406, 2016.

[34] I. Salzmann, G. Heimel, M. Oehzelt, S. Winkler, and N. Koch, "Molecular Electrical Doping of Organic Semiconductors: Fundamental Mechanisms and Emerging Dopant Design Rules," *Accounts of Chemical Research*, vol. 49, no. 3, pp. 370–378, 2016. PMID: 26854611.

[35] S. Winkler, P. Amsalem, J. Frisch, M. Oehzelt, G. Heimel, and N. Koch, "Probing the energy levels in hole-doped molecular semiconductors," *Mater. Horiz.*, vol. 2, pp. 427–433, 2015.

[36] G. Heimel, "The Optical Signature of Charges in Conjugated Polymers," *ACS Central Science*, vol. 2, no. 5, pp. 309–315, 2016. PMID: 27280165.

[37] S. Hunklinger, *Festkörperphysik*. München: München Oldenbourg, 2. ed., 2009.

[38] S.-J. Yoo and J.-J. Kim, "Charge Transport in Electrically Doped Amorphous Organic Semiconductors," *Macromolecular Rapid Communications*, vol. 36, no. 11, pp. 984–1000, 2015.

[39] I. Salzmann and G. Heimel, "Toward a comprehensive understanding of molecular doping organic semiconductors (review)," *Journal of Electron Spectroscopy and Related Phenomena*, vol. 204, pp. 208 – 222, 2015. Organic Electronics.

[40] S. Torabi, F. Jahani, I. Van Severen, C. Kanimozhi, S. Patil, R. W. A. Havenith, R. C. Chiechi, L. Lutsen, D. J. M. Vanderzande, T. J. Cleij, J. C. Hummelen, and L. J. A. Koster, "Strategy for Enhancing the Dielectric Constant of Organic Semiconductors Without Sacrificing Charge Carrier Mobility and Solubility," *Advanced Functional Materials*, vol. 25, no. 1, pp. 150–157, 2015.

[41] S. Braun and W. R. Salaneck, "Fermi level pinning at interfaces with tetrafluorotetracyanoquinodimethane (F4-TCNQ): The role of integer charge transfer states," *Chemical Physics Letters*, vol. 438, no. 4, pp. 259 – 262, 2007.

[42] A. Mityashin, Y. Olivier, T. Van Regemorter, C. Rolin, S. Verlaak, N. G. Martinelli, D. Beljonne, J. Cornil, J. Genoe, and P. Heremans, "Unraveling the Mechanism of Molecular Doping in Organic Semiconductors," *Advanced Materials*, vol. 24, no. 12, pp. 1535–1539, 2012.

[43] P. Pingel and D. Neher, "Comprehensive picture of *p*-type doping of p3ht with the molecular acceptor $f_4$tcnq," *Phys. Rev. B*, vol. 87, p. 115209, Mar 2013.

[44] K. Walzer, B. Maennig, M. Pfeiffer, and K. Leo, "Highly efficient organic devices based on electrically doped transport layers," *Chemical Reviews*, vol. 107, no. 4, pp. 1233–1271, 2007. PMID: 17385929.

[45] T. Glaser, S. Beck, B. Lunkenheimer, D. Donhauser, A. Köhn, M. Kröger, and A. Pucci, "Infrared study of the MoO3 doping efficiency in 4,4'-bis(N-carbazolyl)-1,1'-biphenyl (CBP)," *Organic Electronics*, vol. 14, no. 2, pp. 575 – 583, 2013.

[46] W. Gao and A. Kahn, "Controlled p-doping of the hole-transport molecular material n,n'-diphenyl-n,n'-bis(1-naphthyl)-1,1'-biphenyl-4,4'-diamine with tetrafluorotetracyanoquinodimethane," *Journal of Applied Physics*, vol. 94, no. 1, pp. 359–366, 2003.

[47] S. Olthof, W. Tress, R. Meerheim, B. Lüssem, and K. Leo, "Photoelectron spectroscopy study of systematically varied doping concentrations in an organic semiconductor layer using a molecular p-dopant," *Journal of Applied Physics*, vol. 106, no. 10, p. 103711, 2009.

[48] E. Aziz, A. Vollmer, S. Eisebitt, W. Eberhardt, P. Pingel, D. Neher, and N. Koch, "Localized Charge Transfer in a Molecularly Doped Conducting Polymer," *Advanced Materials*, vol. 19, no. 20, pp. 3257–3260, 2007.

[49] H. Méndez, G. Heimel, S. Winkler, J. Frisch, A. Opitz, K. Sauer, B. Wegner, M. Oehzelt, C. Röthel, S. Duhm, D. Többens, N. Koch, and I. Salzmann, "Charge-transfer crystallites as molecular electrical dopants," *Nature Communications*, vol. 6, p. 8560, Oct 2015.

[50] K. P. O'Donnell and X. Chen, "Temperature dependence of semiconductor band gaps," *Applied Physics Letters*, vol. 58, no. 25, pp. 2924–2926, 1991.

[51] R. Pässler, "Dispersion-related description of temperature dependencies of band gaps in semiconductors," *Phys. Rev. B*, vol. 66, p. 085201, Aug 2002.

[52] Y. Varshni, "Temperature dependence of the energy gap in semiconductors," *Physica*, vol. 34, no. 1, pp. 149 – 154, 1967.

[53] D. Yan and A. Cuevas, "Empirical determination of the energy band gap narrowing in highly doped n^+ silicon," *Journal of Applied Physics*, vol. 114, no. 4, p. 044508, 2013.

[54] D. Yan and A. Cuevas, "Empirical determination of the energy band gap narrowing in p^+ silicon heavily doped with boron," *Journal of Applied Physics*, vol. 116, no. 19, p. 194505, 2014.

[55] S. E. Swirhun, Y. . Kwark, and R. M. Swanson, "Measurement of electron lifetime, electron mobility and band-gap narrowing in heavily doped *p*-type silicon," in *1986 International Electron Devices Meeting*, pp. 24–27, Dec 1986.

[56] J. del Alamo, S. Swirhun, and R. Swanson, "Measuring and modeling minority carrier transport in heavily doped silicon," *Solid-State Electronics*, vol. 28, no. 1, pp. 47 – 54, 1985.

[57] A. Schenk, "Finite-temperature full random-phase approximation model of band gap narrowing for silicon device simulation," *Journal of Applied Physics*, vol. 84, no. 7, pp. 3684–3695, 1998.

[58] G. L. Pearson and J. Bardeen, "Electrical Properties of Pure Silicon and Silicon Alloys Containing Boron and Phosphorus," *Phys. Rev.*, vol. 75, pp. 865–883, Mar 1949.

[59] P. P. Debye and E. M. Conwell, "Electrical Properties of *n*-Type Germanium," *Phys. Rev.*, vol. 93, pp. 693–706, Feb 1954.

[60] N. D. Arora, J. R. Hauser, and D. J. Roulston, "Electron and hole mobilities in silicon as a function of concentration and temperature," *IEEE Transactions on Electron Devices*, vol. 29, pp. 292–295, Feb 1982.

[61] D. Long, "Scattering of Conduction Electrons by Lattice Vibrations in Silicon," *Phys. Rev.*, vol. 120, pp. 2024–2032, Dec 1960.

[62] P. Norton, T. Braggins, and H. Levinstein, "Impurity and Lattice Scattering Parameters as Determined from Hall and Mobility Analysis in *n*-Type Silicon," *Phys. Rev. B*, vol. 8, pp. 5632–5653, Dec 1973.

[63] S. S. Li, "The dopant density and temperature dependence of hole mobility and resistivity in boron doped silicon," *Solid-State Electronics*, vol. 21, no. 9, pp. 1109 – 1117, 1978.

[64] S. S. Li and W. R. Thurber, "The dopant density and temperature dependence of electron mobility and resistivity in *n*-type silicon," *Solid-State Electronics*, vol. 20, no. 7, pp. 609 – 616, 1977.

[65] L. Terman, "An investigation of surface states at a silicon/silicon oxide interface employing metal-oxide-silicon diodes," *Solid-State Electronics*, vol. 5, no. 5, pp. 285 – 299, 1962.

[66] A. Goetzberger, V. Heine, and E. H. Nicollian, "Surface states in silicon from charges in the oxide coating," *Applied Physics Letters*, vol. 12, no. 3, pp. 95–97, 1968.

[67] F. G. Allen and G. W. Gobeli, "Work Function, Photoelectric Threshold, and Surface States of Atomically Clean Silicon," *Phys. Rev.*, vol. 127, pp. 150–158, Jul 1962.

[68] M. L. Tietze, P. Pahner, K. Schmidt, K. Leo, and B. Lüssem, "Doped Organic Semiconductors: Trap-Filling, Impurity Saturation, and Reserve Regimes," *Advanced Functional Materials*, vol. 25, no. 18, pp. 2701–2707, 2015.

[69] B. Maennig, M. Pfeiffer, A. Nollau, X. Zhou, K. Leo, and P. Simon, "Controlled p-type doping of polycrystalline and amorphous organic layers: Self-consistent description of conductivity and field-effect mobility by a microscopic percolation model," *Phys. Rev. B*, vol. 64, p. 195208, Oct 2001.

[70] M. Oehzelt, N. Koch, and G. Heimel, "Organic semiconductor density of states controls the energy level alignment at electrode interfaces," *Nature Communications*, vol. 5, p. 4174, dec 2014.

[71] H. Bässler, "Charge Transport in Disordered Organic Photoconductors a Monte Carlo Simulation Study," *physica status solidi (b)*, vol. 175, no. 1, pp. 15–56, 1993.

[72] R. Coehoorn, W. F. Pasveer, P. A. Bobbert, and M. A. J. Michels, "Charge-carrier concentration dependence of the hopping mobility in organic materials with gaussian disorder," *Phys. Rev. B*, vol. 72, p. 155206, Oct 2005.

[73] S. V. Novikov, D. H. Dunlap, V. M. Kenkre, P. E. Parris, and A. V. Vannikov, "Essential Role of Correlations in Governing Charge Transport in Disordered Organic Materials," *Phys. Rev. Lett.*, vol. 81, pp. 4472–4475, Nov 1998.

[74] S. Olthof, S. Mehraeen, S. K. Mohapatra, S. Barlow, V. Coropceanu, J.-L. Brédas, S. R. Marder, and A. Kahn, "Ultralow doping in organic semiconductors: Evidence of trap filling," *Phys. Rev. Lett.*, vol. 109, p. 176601, Oct 2012.

[75] P. Pahner, H. Kleemann, L. Burtone, M. L. Tietze, J. Fischer, K. Leo, and B. Lüssem, "Pentacene Schottky diodes studied by impedance spectroscopy: Doping properties and trap response," *Phys. Rev. B*, vol. 88, p. 195205, Nov 2013.

[76] J. Steiger, R. Schmechel, and H. von Seggern, "Energetic trap distributions in organic semiconductors," *Synthetic Metals*, vol. 129, no. 1, pp. 1 – 7, 2002.

[77] Z.-L. Guan, J. B. Kim, H. Wang, C. Jaye, D. A. Fischer, Y.-L. Loo, and A. Kahn, "Direct determination of the electronic structure of the poly(3-hexylthiophene):phenyl-[6,6]-C61 butyric acid methyl ester blend," *Organic Electronics*, vol. 11, no. 11, pp. 1779 – 1785, 2010.

[78] S. Ko, E. T. Hoke, L. Pandey, S. Hong, R. Mondal, C. Risko, Y. Yi, R. Noriega, M. D. McGehee, J.-L. Brédas, A. Salleo, and Z. Bao, "Controlled Conjugated Backbone Twisting for an Increased Open-Circuit Voltage while Having a High Short-Circuit Current in Poly(hexylthiophene) Derivatives," *Journal of the American Chemical Society*, vol. 134, no. 11, pp. 5222–5232, 2012. PMID: 22385287.

[79] M. Kröger, S. Hamwi, J. Meyer, T. Riedl, W. Kowalsky, and A. Kahn, "P-type doping of organic wide band gap materials by transition metal oxides: A case-study on molybdenum trioxide," *Organic Electronics*, vol. 10, no. 5, pp. 932 – 938, 2009.

[80] I. G. Hill and A. Kahn, "Energy level alignment at interfaces of organic semiconductor heterostructures," *Journal of Applied Physics*, vol. 84, no. 10, pp. 5583–5586, 1998.

[81] M. A. Baldo and S. R. Forrest, "Transient analysis of organic electrophosphorescence: I. Transient analysis of triplet energy transfer," *Phys. Rev. B*, vol. 62, pp. 10958–10966, Oct 2000.

[82] T. Chassé, C.-I. Wu, I. G. Hill, and A. Kahn, "Band alignment at organic-inorganic semiconductor interfaces: α-NPD and CuPc on InP(110)," *Journal of Applied Physics*, vol. 85, no. 9, pp. 6589–6592, 1999.

[83] A. Rajagopal, C. I. Wu, and A. Kahn, "Energy level offset at organic semiconductor heterojunctions," *Journal of Applied Physics*, vol. 83, no. 5, pp. 2649–2655, 1998.

[84] N. Koch, A. Kahn, J. Ghijsen, J.-J. Pireaux, J. Schwartz, R. L. Johnson, and A. Elschner, "Conjugated organic molecules on metal versus polymer electrodes: Demonstration of a key energy level alignment mechanism," *Applied Physics Letters*, vol. 82, no. 1, pp. 70–72, 2003.

[85] A. Kahn, W. Zhao, W. Gao, H. Vázquez, and F. Flores, "Doping-induced realignment of molecular levels at organic-organic heterojunctions," *Chemical Physics*, vol. 325, no. 1, pp. 129 – 137, 2006. Electronic Processes in Organic Solids.

[86] J. Meiss, A. Merten, M. Hein, C. Schuenemann, S. Schäfer, M. Tietze, C. Uhrich, M. Pfeiffer, K. Leo, and M. Riede, "Fluorinated Zinc Phthalocyanine as Donor for Efficient Vacuum-Deposited Organic Solar Cells," *Advanced Functional Materials*, vol. 22, no. 2, pp. 405–414, 2012.

[87] H. Jiang, P. Hu, J. Ye, Y. Li, H. Li, X. Zhang, R. Li, H. Dong, W. Hu, and C. Kloc, "Molecular Crystal Engineering: Tuning Organic Semiconductor from p-type to n-type by Adjusting Their Substitutional Symmetry," *Advanced Materials*, vol. 29, no. 10, p. 1605053, 2017.

[88] P. Schulz, E. Edri, S. Kirmayer, G. Hodes, D. Cahen, and A. Kahn, "Interface energetics in organo-metal halide perovskite-based photovoltaic cells," *Energy Environ. Sci.*, vol. 7, pp. 1377–1381, 2014.

[89] A. Krishna, D. Sabba, H. Li, J. Yin, P. P. Boix, C. Soci, S. G. Mhaisalkar, and A. C. Grimsdale, "Novel hole transporting materials based on triptycene core for high efficiency mesoscopic perovskite solar cells," *Chem. Sci.*, vol. 5, pp. 2702–2709, 2014.

[90] Y. Qi, T. Sajoto, S. Barlow, E.-G. Kim, J.-L. Brédas, S. R. Marder, and A. Kahn, "Use of a High Electron-Affinity Molybdenum Dithiolene Complex to p-Dope Hole-Transport Layers," *Journal of the American Chemical Society*, vol. 131, no. 35, pp. 12530–12531, 2009. PMID: 19678703.

[91] A. Dai, Y. Zhou, A. L. Shu, S. K. Mohapatra, H. Wang, C. Fuentes-Hernandez, Y. Zhang, S. Barlow, Y.-L. Loo, S. R. Marder, B. Kippelen, and A. Kahn, "Enhanced Charge-Carrier Injection and Collection Via Lamination of Doped Polymer Layers p-Doped with a Solution-Processible Molybdenum Complex," *Advanced Functional Materials*, vol. 24, no. 15, pp. 2197–2204, 2014.

[92] Y. Karpov, T. Erdmann, M. Stamm, U. Lappan, O. Guskova, M. Malanin, I. Raguzin, T. Beryozkina, V. Bakulev, F. Günther, S. Gemming, G. Seifert, M. Hambsch, S. Mannsfeld, B. Voit, and A. Kiriy, "Molecular Doping of a High Mobility Diketopyrrolopyrrole-Dithienylthieno[3,2-b]thiophene Donor-Acceptor Copolymer with F6TCNNQ," *Macromolecules*, vol. 50, no. 3, pp. 914–926, 2017.

[93] W. H. Gries, "A Universal Predictive Equation for the Inelastic Mean Free Pathlengths of X-ray Photoelectrons and Auger Electrons," *Surface and Interface Analysis*, vol. 24, no. 1, pp. 38–50, 1996.

[94] P. J. Cumpson and M. P. Seah, "Elastic Scattering Corrections in AES and XPS. II. Estimating Attenuation Lengths and Conditions Required for their Valid Use in Overlayer/Substrate Experiments," *Surface and Interface Analysis*, vol. 25, no. 6, pp. 430–446, 1997.

[95] S. Tougaard, "Universality Classes of Inelastic Electron Scattering Cross-sections," *Surface and Interface Analysis*, vol. 25, no. 3, pp. 137–154, 1997.

[96] C. Powell and A. Jablonski, "Progress in quantitative surface analysis by X-ray photoelectron spectroscopy: Current status and perspectives," *Journal of Electron Spectroscopy and Related Phenomena*, vol. 178-179, pp. 331 – 346, 2010. Trends in X-ray Photoelectron Spectroscopy of solids (theory, techniques and applications).

[97] S. Tanuma, C. J. Powell, and D. R. Penn, "Calculations of electorn inelastic mean free paths. II. Data for 27 elements over the 50-2000 eV range," *Surface and Interface Analysis*, vol. 17, no. 13, pp. 911–926, 1991.

[98] M. P. Seah, "The quantitative analysis of surfaces by XPS: A review," *Surface and Interface Analysis*, vol. 2, no. 6, pp. 222–239, 1980.

[99] A. Cros, "Charging effects in X-ray photoelectron spectroscopy," *Journal of Electron Spectroscopy and Related Phenomena*, vol. 59, no. 1, pp. 1 – 14, 1992.

[100] H. Mager, "Infrarotspektroskopische untersuchung der verankerung molekularer dotanten," Master's thesis, University Heidelberg, 2018.

[101] V. Sivanesan, "Infrarotspektroskopische Untersuchung der p-Dotierung von Poly(3-hexylthiophen)," Master's thesis, Kirchhoff-Institut für Physik, 2016.

[102] M. Pfeiffer, K. Leo, X. Zhou, J. Huang, M. Hofmann, A. Werner, and J. Blochwitz-Nimoth, "Doped organic semiconductors: Physics and application in light emitting diodes," *Organic Electronics*, vol. 4, no. 2, pp. 89 – 103, 2003. High Efficiency Light Emitters.

[103] Y. Shen, A. R. Hosseini, M. H. Wong, and G. G. Malliaras, "How To Make Ohmic Contacts to Organic Semiconductors," *ChemPhysChem*, vol. 5, no. 1, pp. 16–25, 2004.

[104] M. Gross, D. C. Müller, H.-G. Nothofer, U. Scherf, D. Neher, C. Bräuchle, and K. Meerholz, "Improving the performance of doped π-conjugated polymers for use in organic light-emitting diodes," *Nature*, vol. 405, no. 6787, pp. 661–665, 2000.

[105] C. Ganzorig and M. Fujihira, "Improved drive voltages of organic electroluminescent devices with an efficient p-type aromatic diamine hole-injection layer," *Applied Physics Letters*, vol. 77, no. 25, pp. 4211–4213, 2000.

[106] X. Zhou, M. Pfeiffer, J. Blochwitz, A. Werner, A. Nollau, T. Fritz, and K. Leo, "Very-low-operating-voltage organic light-emitting diodes using a p-doped amorphous hole injection layer," *Applied Physics Letters*, vol. 78, no. 4, pp. 410–412, 2001.

[107] W. Gao and A. Kahn, "Effect of electrical doping on molecular level alignment at organic-organic heterojunctions," *Applied Physics Letters*, vol. 82, no. 26, pp. 4815–4817, 2003.

[108] A. M. Glaudell, J. E. Cochran, S. N. Patel, and M. L. Chabinyc, "Impact of the Doping Method on Conductivity and Thermopower in Semiconducting Polythiophenes," *Advanced Energy Materials*, vol. 5, no. 4, p. 1401072, 2015.

[109] O. Bubnova, Z. U. Khan, A. Malti, S. Braun, M. Fahlman, M. Berggren, and X. Crispin, "Optimization of the thermoelectric figure of merit in the conducting polymer poly(3,4-ethylenedioxythiophene)," *Nature Materials*, vol. 10, p. 429, may 2011.

[110] K. Harada, A. G. Werner, M. Pfeiffer, C. J. Bloom, C. M. Elliott, and K. Leo, "Organic Homojunction Diodes with a High Built-in Potential: Interpretation of the Current-Voltage Characteristics by a Generalized Einstein Relation," *Phys. Rev. Lett.*, vol. 94, p. 036601, Jan 2005.

[111] K. Yamashita, Y. Kunugi, Y. Harima, and A.-N. Chowdhury, "Fabrication of an Organic p-n Homojunction Diode Using Electrochemically Cation- and Photochemically Anion-Doped Polymer," *Japanese Journal of Applied Physics*, vol. 34, pp. 3794–3797, jul 1995.

[112] J. Kido and T. Matsumoto, "Bright organic electroluminescent devices having a metal-doped electron-injecting layer," *Applied Physics Letters*, vol. 73, no. 20, pp. 2866–2868, 1998.

[113] G. Parthasarathy, C. Shen, A. Kahn, and S. R. Forrest, "Lithium doping of semiconducting organic charge transport materials," *Journal of Applied Physics*, vol. 89, no. 9, pp. 4986–4992, 2001.

[114] V. I. Arkhipov, E. V. Emelianova, and H. Bässler, "Quenching of excitons in doped disordered organic semiconductors," *Phys. Rev. B*, vol. 70, p. 205205, Nov 2004.

[115] V. I. Arkhipov, E. V. Emelianova, and H. Bässler, "On the role of spectral diffusion of excitons in sensitized photoconduction in conjugated polymers," *Chemical Physics Letters*, vol. 383, no. 1, pp. 166 – 170, 2004.

[116] A. J. Ferguson, N. Kopidakis, S. E. Shaheen, and G. Rumbles, "Quenching of Excitons by Holes in Poly(3-hexylthiophene) Films," *The Journal of Physical Chemistry C*, vol. 112, no. 26, pp. 9865–9871, 2008.

[117] J. Li, C. W. Rochester, I. E. Jacobs, S. Friedrich, P. Stroeve, M. Riede, and A. J. Moulé, "Measurement of Small Molecular Dopant F4TCNQ and C60F36 Diffusion in Organic Bilayer Architectures," *ACS Applied Materials & Interfaces*, vol. 7, no. 51, pp. 28420–28428, 2015. PMID: 26673846.

[118] K. Kang, S. Watanabe, K. Broch, A. Sepe, A. Brown, I. Nasrallah, M. Nikolka, Z. Fei, M. Heeney, D. Matsumoto, K. Marumoto, H. Tanaka, S.-i. Kuroda, and H. Sirringhaus, "2D coherent charge transport in highly ordered conducting polymers doped by solid state diffusion," *Nature Materials*, vol. 15, no. 8, pp. 896–902, 2016.

[119] G. K. Mor, D. Jones, T. P. Le, Z. Shang, P. J. Weathers, M. K. B. Woltermann, K. Vakhshouri, B. P. Williams, S. A. Tohran, T. Saito, R. Verduzco, A. Salleo, M. A. Hickner, and E. D. Gomez, "Contact Doping with Sub-Monolayers of Strong Polyelectrolytes for Organic Photovoltaics," *Advanced Energy Materials*, vol. 4, no. 13, p. 1400439, 2014.

[120] L. Müller, S.-Y. Rhim, V. Sivanesan, D. Wang, S. Hietzschold, P. Reiser, E. Mankel, S. Beck, S. Barlow, S. R. Marder, A. Pucci, W. Kowalsky, and R. Lovrincic, "Electric-Field-Controlled Dopant Distribution in Organic Semiconductors," *Advanced Materials*, vol. 29, no. 30, p. 1701466, 2017.

[121] Y. Qi, T. Sajoto, M. Kröger, A. M. Kandabarow, W. Park, S. Barlow, E.-G. Kim, L. Wielunski, L. C. Feldman, R. A. Bartynski, J.-L. Brédas, S. R. Marder, and A. Kahn, "A Molybdenum Dithiolene Complex as p-Dopant for Hole-Transport Materials: A Multitechnique Experimental and Theoretical Investigation," *Chemistry of Materials*, vol. 22, no. 2, pp. 524–531, 2010.

[122] G. A. Berriman, J. L. Holdsworth, X. Zhou, W. J. Belcher, and P. C. Dastoor, "Molecular versus crystallite PCBM diffusion in P3HT:PCBM blends," *AIP Advances*, vol. 5, no. 9, p. 097220, 2015.

[123] B. Watts, W. J. Belcher, L. Thomsen, H. Ade, and P. C. Dastoor, "A Quantitative Study of PCBM Diffusion during Annealing of P3HT:PCBM Blend Films," *Macromolecules*, vol. 42, no. 21, pp. 8392–8397, 2009.

[124] N. D. Treat, T. E. Mates, C. J. Hawker, E. J. Kramer, and M. L. Chabinyc, "Temperature Dependence of the Diffusion Coefficient of PCBM in Poly(3-hexylthiophene)," *Macromolecules*, vol. 46, no. 3, pp. 1002–1007, 2013.

[125] J. Li, C. Koshnick, S. O. Diallo, S. Ackling, D. M. Huang, I. E. Jacobs, T. F. Harrelson, K. Hong, G. Zhang, J. Beckett, M. Mascal, and A. J. Moulé, "Quantitative Measurements of the Temperature-Dependent Microscopic and Macroscopic Dynamics of a Molecular Dopant in a Conjugated Polymer," *Macromolecules*, vol. 50, no. 14, pp. 5476–5489, 2017.

[126] T. Mills, L. G. Kaake, and X.-Y. Zhu, "Polaron and ion diffusion in a poly(3-hexylthiophene) thin-film transistor gated with polymer electrolyte dielectric," *Applied Physics A*, vol. 95, pp. 291–296, Apr 2009.

[127] K. Kaneto, H. Agawa, and K. Yoshino, "Cycle life, stability, and characteristics of color switching cells utilizing polythiophene films," *Journal of Applied Physics*, vol. 61, no. 3, pp. 1197–1205, 1987.

[128] J. Hynynen, D. Kiefer, and C. Müller, "Influence of crystallinity on the thermoelectric power factor of P3HT vapour-doped with F4TCNQ," *RSC Adv.*, vol. 8, pp. 1593–1599, 2018.

[129] I. E. Jacobs, E. W. Aasen, J. L. Oliveira, T. N. Fonseca, J. D. Roehling, J. Li, G. Zhang, M. P. Augustine, M. Mascal, and A. J. Moulé, "Comparison of solution-mixed and sequentially processed P3HT:F4TCNQ films: effect of doping-induced aggregation on film morphology," *J. Mater. Chem. C*, vol. 4, pp. 3454–3466, 2016.

[130] J. Hynynen, D. Kiefer, L. Yu, R. Kroon, R. Munir, A. Amassian, M. Kemerink, and C. Müller, "Enhanced Electrical Conductivity of Molecularly p-Doped Poly(3-hexylthiophene) through Understanding the Correlation with Solid-State Order," *Macromolecules*, vol. 50, no. 20, pp. 8140–8148, 2017. PMID: 29093606.

[131] R. Fujimoto, Y. Yamashita, S. Kumagai, J. Tsurumi, A. Hinderhofer, K. Broch, F. Schreiber, S. Watanabe, and J. Takeya, "Molecular doping in organic semiconductors: fully solution-processed, vacuum-free doping with metal-organic complexes in an orthogonal solvent," *J. Mater. Chem. C*, vol. 5, pp. 12023–12030, 2017.

[132] J. Li, D. M. Holm, S. Guda, Z. I. Bedolla-Valdez, G. Gonel, I. E. Jacobs, M. A. Dettmann, J. Saska, M. Mascal, and A. J. Moulé, "Effect of processing conditions on additive DISC patterning of P3HT films," *J. Mater. Chem. C*, vol. 7, pp. 302–313, 2019.

[133] I. E. Jacobs, J. Li, S. L. Burg, D. J. Bilsky, B. T. Rotondo, M. P. Augustine, P. Stroeve, and A. J. Moulé, "Reversible Optical Control of Conjugated Polymer Solubility with Sub-micrometer Resolution," *ACS Nano*, vol. 9, no. 2, pp. 1905–1912, 2015. PMID: 25625435.

[134] M. Hedenqvist and U. Gedde, "Diffusion of small-molecule penetrants in semicrystalline polymers," *Progress in Polymer Science*, vol. 21, no. 2, pp. 299 – 333, 1996.

[135] H. L. Frisch and S. A. Stern, "Diffusion of small molecules in polymers," *Critical Reviews in Solid State and Materials Sciences*, vol. 11, no. 2, pp. 123–187, 1983.

[136] H. Fujita, "Diffusion in polymer-diluent systems," in *Fortschritte Der Hochpolymeren-Forschung*, (Berlin, Heidelberg), pp. 1–47, Springer Berlin Heidelberg, 1961.

[137] M. H. Cohen and D. Turnbull, "Molecular Transport in Liquids and Glasses," *The Journal of Chemical Physics*, vol. 31, no. 5, pp. 1164–1169, 1959.

[138] J. H. Petropoulos, "Quantitative analysis of gaseous diffusion in glassy polymers," *Journal of Polymer Science Part A-2: Polymer Physics*, vol. 8, no. 10, pp. 1797–1801, 1970.

[139] W. J. Koros and D. R. Paul, "CO2 sorption in poly(ethylene terephthalate) above and below the glass transition," *Journal of Polymer Science: Polymer Physics Edition*, vol. 16, no. 11, pp. 1947–1963, 1978.

[140] D. R. Paul and W. J. Koros, "Effect of partially immobilizing sorption on permeability and the diffusion time lag," *Journal of Polymer Science: Polymer Physics Edition*, vol. 14, no. 4, pp. 675–685, 1976.

[141] M. T. Dang, L. Hirsch, and G. Wantz, "P3HT:PCBM, Best Seller in Polymer Photovoltaic Research," *Advanced Materials*, vol. 23, no. 31, pp. 3597–3602, 2011.

[142] P. Vanlaeke, A. Swinnen, I. Haeldermans, G. Vanhoyland, T. Aernouts, D. Cheyns, C. Deibel, J. D'Haen, P. Heremans, J. Poortmans, and J. Manca, "P3HT/PCBM bulk heterojunction solar cells: Relation between morphology and electro-optical characteristics," *Solar Energy Materials and Solar Cells*, vol. 90, no. 14, pp. 2150 – 2158, 2006.

[143] K.-J. Baeg, D. Khim, D.-Y. Kim, J. B. Koo, I.-K. You, W. S. Choi, and Y.-Y. Noh, "High mobility top-gated poly(3-hexylthiophene) field-effect transistors with high work-function Pt electrodes," *Thin Solid Films*, vol. 518, no. 14, pp. 4024 – 4029, 2010.

[144] P. J. Brown, D. S. Thomas, A. Köhler, J. S. Wilson, J.-S. Kim, C. M. Ramsdale, H. Sirringhaus, and R. H. Friend, "Effect of interchain interactions on the absorption and emission of poly(3-hexylthiophene)," *Phys. Rev. B*, vol. 67, p. 064203, Feb 2003.

[145] W. R. Salaneck, O. Inganäs, B. Thémans, J. O. Nilsson, B. Sjögren, J. Österholm, J. L. Brédas, and S. Svensson, "Thermochromism in poly(3-hexylthiophene) in the solid state: A spectroscopic study of temperature-dependent conformational defects," *The Journal of Chemical Physics*, vol. 89, no. 8, pp. 4613–4619, 1988.

[146] M. C. Gurau, D. M. Delongchamp, B. M. Vogel, E. K. Lin, D. A. Fischer, S. Sambasivan, and L. J. Richter, "Measuring Molecular Order in Poly(3-alkylthiophene) Thin Films with Polarizing Spectroscopies," *Langmuir*, vol. 23, no. 2, pp. 834–842, 2007. PMID: 17209641.

[147] S. Ludwigs, ed., *P3HT Revisited - From Molecular Scale to Solar Cell Devices*, vol. 265 of *Advances in Polymer Science*. Springer, Berlin, Heidelberg, 2014.

[148] M. D. Irwin, D. B. Buchholz, A. W. Hains, R. P. H. Chang, and T. J. Marks, "p-Type semiconducting nickel oxide as an efficiency-enhancing anode interfacial layer in polymer bulk-heterojunction solar cells," *Proceedings of the National Academy of Sciences*, vol. 105, no. 8, pp. 2783–2787, 2008.

[149] T. Salim, J. Y. Lek, B. Bräuer, D. Fichou, and Y. M. Lam, "Polymer nanofibers: preserving nanomorphology in ternary blend organic photovoltaics," *Phys. Chem. Chem. Phys.*, vol. 16, pp. 23829–23836, 2014.

[150] X. Shen, W. Hu, and T. P. Russell, "Measuring the Degree of Crystallinity in Semicrystalline Regioregular Poly(3-hexylthiophene)," *Macromolecules*, vol. 49, no. 12, pp. 4501–4509, 2016.

[151] M. J. M. Wirix, P. H. H. Bomans, H. Friedrich, N. A. J. M. Sommerdijk, and G. de With, "Three-Dimensional Structure of P3HT Assemblies in Organic Solvents Revealed by Cryo-TEM," *Nano Letters*, vol. 14, no. 4, pp. 2033–2038, 2014. PMID: 24579985.

[152] J. A. Merlo and C. D. Frisbie, "Field Effect Transport and Trapping in Regioregular Polythiophene Nanofibers," *The Journal of Physical Chemistry B*, vol. 108, no. 50, pp. 19169–19179, 2004.

[153] D. T. Duong, C. Wang, E. Antono, M. F. Toney, and A. Salleo, "The chemical and structural origin of efficient p-type doping in P3HT," *Organic Electronics*, vol. 14, no. 5, pp. 1330 – 1336, 2013.

[154] K. J. Ihn, J. Moulton, and P. Smith, "Whiskers of poly(3-alkylthiophene)s," *Journal of Polymer Science Part B: Polymer Physics*, vol. 31, no. 6, pp. 735–742, 1993.

[155] I. Osaka and K. Takimiya, "Backbone orientation in semiconducting polymers," *Polymer*, vol. 59, pp. A1 – A15, 2015.

[156] D. T. Duong, M. F. Toney, and A. Salleo, "Role of confinement and aggregation in charge transport in semicrystalline polythiophene thin films," *Phys. Rev. B*, vol. 86, p. 205205, Nov 2012.

[157] S. K. Mohapatra, Y. Zhang, B. Sandhu, M. S. Fonari, T. V. Timofeeva, S. R. Marder, and S. Barlow, "Synthesis, characterization, and crystal structures of molybdenum complexes of unsymmetrical electron-poor dithiolene ligands," *Polyhedron*, vol. 116, pp. 88 – 95,

2016. Special Issue in Honour of Professor Malcolm L. H. Green on the occasion of his 80th Birthday.

[158] A. Dai, A. Wan, C. Magee, Y. Zhang, S. Barlow, S. R. Marder, and A. Kahn, "Investigation of p-dopant diffusion in polymer films and bulk heterojunctions: Stable spatially-confined doping for all-solution processed solar cells," *Organic Electronics*, vol. 23, pp. 151 – 157, 2015.

[159] K. Kanai, K. Akaike, K. Koyasu, K. Sakai, T. Nishi, Y. Kamizuru, T. Nishi, Y. Ouchi, and K. Seki, "Determination of electron affinity of electron accepting molecules," *Applied Physics A*, vol. 95, pp. 309–313, Apr 2009.

[160] A. L. Tenderholt, R. K. Szilagyi, R. H. Holm, K. O. Hodgson, B. Hedman, and E. I. Solomon, "Electronic Control of the "Bailar Twist" in Formally d0-d2 Molybdenum Tris(dithiolene) Complexes: A Sulfur K-edge X-ray Absorption Spectroscopy and Density Functional Theory Study," *Inorganic Chemistry*, vol. 47, no. 14, pp. 6382–6392, 2008. PMID: 18517189.

[161] W. Liu, L. Müller, S. Ma, S. Barlow, S. R. Marder, W. Kowalsky, A. Köhn, and R. Lovrincic, "Origin of the π-π Spacing Change upon Doping of Semiconducting Polymers," *The Journal of Physical Chemistry C*, vol. 122, no. 49, pp. 27983–27990, 2018.

[162] C. Rothe, "Electrical doping is paving the way for the implementation of OLEDs in consumer electronics," *Laser & Photonics Reviews*, vol. 1, no. 4, pp. 303–306, 2007.

[163] C. Sutton, C. Risko, and J.-L. Brédas, "Noncovalent Intermolecular Interactions in Organic Electronic Materials: Implications for the Molecular Packing vs Electronic Properties of Acenes," *Chemistry of Materials*, vol. 28, no. 1, pp. 3–16, 2016.

[164] J. Li, C. W. Rochester, I. E. Jacobs, E. W. Aasen, S. Friedrich, P. Stroeve, and A. J. Moulé, "The effect of thermal annealing on dopant site choice in conjugated polymers," *Organic Electronics*, vol. 33, pp. 23 – 31, 2016.

[165] H. Ishii, K. Sugiyama, E. Ito, and K. Seki, "Energy Level Alignment and Interfacial Electronic Structures at Organic/Metal and Organic/Organic Interfaces," *Advanced Materials*, vol. 11, no. 8, pp. 605–625, 1999.

[166] W. Chen, W. Jiao, D. Li, X. Sun, X. Guo, M. Lei, Q. Wang, and Y. Li, "Cross Self-n-Doping and Electron Transfer Model in a Stable and Highly Conductive Fullerene Ammonium Iodide: A Promising Cathode Interlayer in Organic Solar Cells," *Chemistry of Materials*, vol. 28, pp. 1227–1235, feb 2016.

[167] B. Russ, M. J. Robb, F. G. Brunetti, P. L. Miller, E. E. Perry, S. N. Patel, V. Ho, W. B. Chang, J. J. Urban, M. L. Chabinyc, C. J. Hawker, and R. A. Segalman, "Power factor enhancement in solution-processed organic n-type thermoelectrics through molecular design," *Advanced Materials*, vol. 26, pp. 3473–3477, jun 2014.

[168] A. Lobnik, I. Oehme, I. Murkovic, and O. S. Wolfbeis, "pH optical sensors based on sol-gels: Chemical doping versus covalent immobilization," *Analytica Chimica Acta*, vol. 367, no. 1, pp. 159 – 165, 1998.

[169] P. K. Dhal, G. N. Babu, S. Sudhakaran, and P. S. Borkar, "Immobilization of penicillin acylase by covalent linkage on vinyl copolymers containing epoxy groups," *Die Makromolekulare Chemie, Rapid Communications*, vol. 6, pp. 91–95, feb 1985.

[170] L. S. Shlyakhtenko, A. A. Gall, J. J. Weimer, D. D. Hawn, and Y. L. Lyubchenko, "Atomic Force Microscopy Imaging of DNA Covalently Immobilized on a Functionalized Mica Substrate," *Biophysical Journal*, vol. 77, no. 1, pp. 568 – 576, 1999.

[171] S. Bräse, C. Gil, K. Knepper, and V. Zimmermann, "Organische Azide - explodierende Vielfalt bei einer einzigartigen Substanzklasse," *Angewandte Chemie*, vol. 117, no. 33, pp. 5320–5374, 2005.

[172] J. H. Boyer and F. C. Canter, "Alkyl and Aryl Azides.," *Chemical Reviews*, vol. 54, no. 1, pp. 1–57, 1954.

[173] B. Schulze and U. S. Schubert, "Beyond click chemistry - supramolecular interactions of 1,2,3-triazoles," *Chem. Soc. Rev.*, vol. 43, pp. 2522–2571, 2014.

[174] W. Lwowski, "Nitrenes and the Decomposition of Carbonylazides," *Angewandte Chemie International Edition in English*, vol. 6, no. 11, pp. 897–906, 1967.

[175] B. L. Evans, A. D. Yoffe, and P. Gray, "Physics And Chemistry Of The Inorganic Azides," *Chemical Reviews*, vol. 59, no. 4, pp. 515–568, 1959.

[176] E. F. V. Scriven and K. Turnbull, "Azides: their preparation and synthetic uses," *Chemical Reviews*, vol. 88, no. 2, pp. 297–368, 1988.

[177] T. Curtius, "über Stickstoffwasserstoffsäure (Azoimid) N3H," *Berichte der deutschen chemischen Gesellschaft*, vol. 23, no. 2, pp. 3023–3033, 1890.

[178] F. Weygand and K. Hunger, "Acylierung von Aminosäuren mit pht-Methoxybenzyloxycarbonyl-azid," *Chemische Berichte*, vol. 95, no. 1, pp. 1–6, 1962.

[179] E. D. Stenehjem, V. R. Ziatdinov, T. D. P. Stack, and C. E. D. Chidsey, "Gas Phase Azide Functionalization of Carbon," *Journal of the American Chemical Society*, vol. 135, no. 3, pp. 1110–1116, 2013. PMID: 23301920.

[180] P. Van Roey, J. M. Salerno, W. L. Duax, C. K. Chu, M. K. Ahn, and R. F. Schinazi, "Solid-state conformation of anti-human immunodeficiency virus type-1 agents: Crystal structures of three 3'-azido-3'-deoxythymidine analogs," *Journal of the American Chemical Society*, vol. 110, no. 7, pp. 2277–2282, 1988.

[181] H. D. Fair and R. F. Walker, *Energetic Materials Volume 2: Technology of the Inorganic Azides*. Plenum Press, New York, 1977.

[182] "Information on azide compounds." Stanford University Environmental Health and Safety Departement.

[183] R.-Q. Png, P.-J. Chia, J.-C. Tang, B. Liu, S. Sivaramakrishnan, M. Zhou, S.-H. Khong, H. S. O. Chan, J. H. Burroughes, L.-L. Chua, R. H. Friend, and P. K. H. Ho, "High-performance polymer semiconducting heterostructure devices by nitrene-mediated photocrosslinking of alkyl side chains," *Nature Materials*, vol. 9, p. 152, dec 2009.

[184] N. Cho, H.-L. Yip, J. A. Davies, P. D. Kazarinoff, D. F. Zeigler, M. M. Durban, Y. Segawa, K. M. O'Malley, C. K. Luscombe, and A. K.-Y. Jen, "In-situ Crosslinking and n-Doping of Semiconducting Polymers and Their Application as Efficient Electron-Transporting Materials in Inverted Polymer Solar Cells," *Advanced Energy Materials*, vol. 1, no. 6, pp. 1148–1153, 2011.

[185] A. C. Gouget-Laemmel, J. Yang, M. A. Lodhi, A. Siriwardena, D. Aureau, R. Boukherroub, J.-N. Chazalviel, F. Ozanam, and S. Szunerits, "Functionalization of Azide-Terminated Silicon Surfaces with Glycans Using Click Chemistry: XPS and FTIR study," *The Journal of Physical Chemistry C*, vol. 117, no. 1, pp. 368–375, 2013.

[186] A. Devadoss and C. E. D. Chidsey, "Azide-Modified Graphitic Surfaces for Covalent Attachment of Alkyne-Terminated Molecules by "Click" Chemistry," *Journal of the American Chemical Society*, vol. 129, no. 17, pp. 5370–5371, 2007. PMID: 17425323.

[187] C. Radhakrishnan, M. K. F. Lo, M. V. Warrier, M. A. Garcia-Garibay, and H. G. Monbouquette, "Photocatalytic Reduction of an Azide-Terminated Self-Assembled Monolayer Using CdS Quantum Dots," *Langmuir*, vol. 22, no. 11, pp. 5018–5024, 2006. PMID: 16700589.

[188] N. Devaraj and J. Collman, "Copper Catalyzed Azide-Alkyne Cycloadditions on Solid Surfaces: Applications and Future Directions," *QSAR & Combinatorial Science*, vol. 26, no. 11-12, pp. 1253–1260, 2007.

[189] F.-F. Chen and F. Wang, "Electronic Structure of the Azide Group in 3'-Azido-3'-deoxythymidine (AZT) Compared to Small Azide Compounds," *Molecules*, vol. 14, no. 7, pp. 2656–2668, 2009.

[190] B. Cabral and M. Costa, "Density functional study of molecular properties of hydrazoic acid and methyl azide," *Journal of Molecular Structure: THEOCHEM*, vol. 343, pp. 31 – 41, 1995.

[191] C. J. Nielsen and C. E. S. gfogren, "The vibrational spectra, molecular structure and conformation of organic azides: Part IV. an ab initio study of hydrazoic acid, azidomethane, azidoethane, azidoethene and azidomethanal," *Journal of Molecular Structure: THEOCHEM*, vol. 150, no. 3, pp. 361 – 379, 1987.

[192] L. O. Brockway and L. Pauling, "The Electron-Diffraction Investigation of the Structure of Molecules of Methyl Azide and Carbon Suboxide," *Proceedings of the National Academy of Sciences*, vol. 19, no. 9, pp. 860–867, 1933.

[193] F. L. Hirshfeld, "Electron Density Distributions in Molecules," *Crystallography Reviews*, vol. 2, no. 4, pp. 169–200, 1991.

[194] E. Lieber, C. N. R. Rao, T. S. Chao, and C. W. W. Hoffman, "Infrared spectra of organic azides," *Analytical Chemistry*, vol. 29, no. 6, pp. 916–918, 1957.

[195] N. Hooper, L. J. Beeching, J. M. Dyke, A. Morris, J. S. Ogden, A. A. Dias, M. L. Costa, M. T. Barros, M. H. Cabral, and A. M. C. Moutinho, "A Study of the Thermal Decomposition of 2-Azidoethanol and 2-Azidoethyl Acetate by Ultraviolet Photoelectron Spectroscopy and

Matrix Isolation Infrared Spectroscopy," *The Journal of Physical Chemistry A*, vol. 106, no. 42, pp. 9968–9975, 2002.

[196] H. M. Badawi, "Theoretical study of the structure and vibrational spectra of formyl and methyl azides," *Journal of Molecular Structure: THEOCHEM*, vol. 583, no. 1, pp. 89 – 97, 2002.

[197] T. H. Lee, R. J. Colton, M. G. White, and J. W. Rabalais, "Electronic structure of hydrazoic acid and the azide ion from x-ray and ultraviolet electron spectroscopy," *Journal of the American Chemical Society*, vol. 97, no. 17, pp. 4845–4851, 1975.

[198] J. F. W. Keana and S. X. Cai, "New reagents for photoaffinity labeling: synthesis and photolysis of functionalized perfluorophenyl azides," *The Journal of Organic Chemistry*, vol. 55, no. 11, pp. 3640–3647, 1990.

[199] E. Leyva, M. J. T. Young, and M. S. Platz, "High yields of formal CH insertion products in the reactions of polyfluorinated aromatic nitrenes," *Journal of the American Chemical Society*, vol. 108, no. 26, pp. 8307–8309, 1986.

[200] S. Murase, K. Shibata, H. Furukawa, Y. Miyashita, and K. Horie, "Large photoinduced refractive index increase in polymer films containing phenylazide maintaining their transparency and thermal stability," *Polymer Journal*, vol. 35, pp. 203–207, feb 2003.

[201] R. Poe, K. Schnapp, M. J. T. Young, J. Grayzar, and M. S. Platz, "Chemistry and kinetics of singlet pentafluorophenylnitrene," *Journal of the American Chemical Society*, vol. 114, no. 13, pp. 5054–5067, 1992.

[202] A. Marcinek, M. S. Platz, S. Y. Chan, R. Floresca, K. Rajagopalan, M. Golinski, and D. Watt, "Unusually long lifetimes of the singlet nitrenes derived from 4-azido-2,3,5,6-tetrafluorobenzamides," *The Journal of Physical Chemistry*, vol. 98, no. 2, pp. 412–419, 1994.

[203] A. Reiser, L. J. Leyshon, and L. Johnston, "Effect of matrix rigidity on the reactions of aromatic nitrenes in polymers," *Trans. Faraday Soc.*, vol. 67, pp. 2389–2396, 1971.

[204] S. C. Reddington, P. J. Rizkallah, P. D. Watson, R. Pearson, E. M. Tippmann, and D. D. Jones, "Different photochemical events of a genetically encoded phenyl azide define and modulate gfp fluorescence," *Angewandte Chemie*, vol. 125, no. 23, pp. 6090–6093, 2013.

[205] S. X. Cai, D. J. Glenn, M. Kanskar, M. N. Wybourne, and J. F. W. Keana, "Development of Highly Efficient Deep-UV and Electron Beam Mediated Cross-Linkers: Synthesis and Photolysis of Bis(perfluorophenyl) Azides," *Chemistry of Materials*, vol. 6, no. 10, pp. 1822–1829, 1994.

[206] M. J. T. Young and M. S. Platz, "Polyfluorinated aryl azides as photoaffinity labelling reagents; the room temperature CH insertion reactions of singlet pentafluorophenyl nitrene with alkanes," *Tetrahedron Letters*, vol. 30, no. 17, pp. 2199 – 2202, 1989.

[207] A. Reiser and L. Leyshon, "Correlation between negative charge on nitrogen and the reactivity of aromatic nitrenes," *Journal of the American Chemical Society*, vol. 92, no. 25, pp. 7487–7487, 1970.

[208] F. S. Benneckendorf, *Verringerung des Kontaktwiderstandes von Metall-Halbleiterkontakten durch Modifikation der Interphase, sowie Entwicklung einer universellen Immobilisierung von Dotanden in Halbleitermaterialien*. PhD thesis, University Heidelberg, 2019.

[209] M. G. Mason, C. W. Tang, L.-S. Hung, P. Raychaudhuri, J. Madathil, D. J. Giesen, L. Yan, Q. T. Le, Y. Gao, S.-T. Lee, L. S. Liao, L. F. Cheng, W. R. Salaneck, D. A. dos Santos, and J. L. Brédas, "Interfacial chemistry of Alq3 and LiF with reactive metals," *Journal of Applied Physics*, vol. 89, no. 5, pp. 2756–2765, 2001.

[210] C. K. Chan, A. Kahn, Q. Zhang, S. Barlow, and S. R. Marder, "Incorporation of cobaltocene as an n-dopant in organic molecular films," *Journal of Applied Physics*, vol. 102, no. 1, p. 014906, 2007.

[211] C. K. Chan, W. Zhao, S. Barlow, S. Marder, and A. Kahn, "Decamethylcobaltocene as an efficient n-dopant in organic electronic materials and devices," *Organic Electronics*, vol. 9, no. 5, pp. 575 – 581, 2008.

[212] C. J. Bloom, C. M. Elliott, P. G. Schroeder, C. B. France, and B. A. Parkinson, "Low Work Function Reduced Metal Complexes as Cathodes in Organic Electroluminescent Devices," *The Journal of Physical Chemistry B*, vol. 107, no. 13, pp. 2933–2938, 2003.

[213] Y. Qi, S. K. Mohapatra, S. Bok Kim, S. Barlow, S. R. Marder, and A. Kahn, "Solution doping of organic semiconductors using air-stable n-dopants," *Applied Physics Letters*, vol. 100, no. 8, p. 083305, 2012.

[214] A. G. Werner, F. Li, K. Harada, M. Pfeiffer, T. Fritz, and K. Leo, "Pyronin B as a donor for n-type doping of organic thin films," *Applied Physics Letters*, vol. 82, no. 25, pp. 4495–4497, 2003.

[215] F. Li, A. Werner, M. Pfeiffer, K. Leo, and X. Liu, "Leuco Crystal Violet as a Dopant for n-Doping of Organic Thin Films of Fullerene C60," *The Journal of Physical Chemistry B*, vol. 108, no. 44, pp. 17076–17082, 2004.

[216] A. Werner, F. Li, K. Harada, M. Pfeiffer, T. Fritz, K. Leo, and S. Machill, "n-Type Doping of Organic Thin Films Using Cationic Dyes," *Advanced Functional Materials*, vol. 14, no. 3, pp. 255–260, 2004.

[217] D. Gebeyehu, B. Maennig, J. Drechsel, K. Leo, and M. Pfeiffer, "Bulk-heterojunction photovoltaic devices based on donor-acceptor organic small molecule blends," *Solar Energy Materials and Solar Cells*, vol. 79, no. 1, pp. 81 – 92, 2003.

[218] P. Wei, J. H. Oh, G. Dong, and Z. Bao, "Use of a 1H-Benzoimidazole Derivative as an n-Type Dopant and To Enable Air-Stable Solution-Processed n-Channel Organic Thin-Film Transistors," *Journal of the American Chemical Society*, vol. 132, no. 26, pp. 8852–8853, 2010. PMID: 20552967.

[219] P. Wei, T. Menke, B. D. Naab, K. Leo, M. Riede, and Z. Bao, "2-(2-Methoxyphenyl)-1,3-dimethyl-1H-benzoimidazol-3-ium Iodide as a New Air-Stable n-Type Dopant for Vacuum-Processed Organic Semiconductor Thin Films," *Journal of the American Chemical Society*, vol. 134, no. 9, pp. 3999–4002, 2012. PMID: 22324847.

[220] S. S. Kim, S. Bae, and W. H. Jo, "Performance enhancement of planar heterojunction perovskite solar cells by n-doping of the electron transporting layer," *Chem. Commun.*, vol. 51, pp. 17413–17416, 2015.

[221] C. Yang, S. Cho, A. Heeger, and F. Wudl, "Heteroanalogues of PCBM: N-Bridged Imino-PCBMs for Organic Field-Effect Transistors," *Angewandte Chemie International Edition*, vol. 48, no. 9, pp. 1592–1595, 2009.

[222] G. Kwon, K. Kim, B. D. Choi, J. Roh, C. Lee, Y.-Y. Noh, S. Seo, M.-G. Kim, and C. Kim, "Multifunctional Organic-Semiconductor Interfacial Layers for Solution-Processed Oxide-Semiconductor Thin-Film Transistor," *Advanced Materials*, vol. 29, no. 21, p. 1607055, 2017.

[223] S. Rossbauer, C. Müller, and T. D. Anthopoulos, "Comparative Study of the N-Type Doping Efficiency in Solution-processed Fullerenes and Fullerene Derivatives," *Advanced Functional Materials*, vol. 24, no. 45, pp. 7116–7124, 2014.

[224] M. Lu, H. T. Nicolai, G.-J. A. H. Wetzelaer, and P. W. M. Blom, "N-type doping of poly(p-phenylene vinylene) with air-stable dopants," *Applied Physics Letters*, vol. 99, no. 17, p. 173302, 2011.

[225] B. D. Naab, S. Guo, S. Olthof, E. G. B. Evans, P. Wei, G. L. Millhauser, A. Kahn, S. Barlow, S. R. Marder, and Z. Bao, "Mechanistic Study on the Solution-Phase n-Doping of 1,3-Dimethyl-2-aryl-2,3-dihydro-1H-benzoimidazole Derivatives," *Journal of the American Chemical Society*, vol. 135, no. 40, pp. 15018–15025, 2013. PMID: 24011269.

[226] B. D. Naab, S. Zhang, K. Vandewal, A. Salleo, S. Barlow, S. R. Marder, and Z. Bao, "Effective Solution- and Vacuum-Processed n-Doping by Dimers of Benzimidazoline Radicals," *Advanced Materials*, vol. 26, no. 25, pp. 4268–4272, 2014.

[227] M. Schwarze, B. D. Naab, M. L. Tietze, R. Scholz, P. Pahner, F. Bussolotti, S. Kera, D. Kasemann, Z. Bao, and K. Leo, "Analyzing the n-Doping Mechanism of an Air-Stable Small-Molecule Precursor," *ACS Applied Materials & Interfaces*, vol. 10, no. 1, pp. 1340–1346, 2018. PMID: 29236472.

[228] F. Ghani, A. Opitz, P. Pingel, G. Heimel, I. Salzmann, J. Frisch, D. Neher, A. Tsami, U. Scherf, and N. Koch, "Charge transfer in and conductivity of molecularly doped thiophene-based copolymers," *Journal of Polymer Science Part B: Polymer Physics*, vol. 53, no. 1, pp. 58–63, 2015.

[229] L. Müller, D. Nanova, T. Glaser, S. Beck, A. Pucci, A. K. Kast, R. R. Schröder, E. Mankel, P. Pingel, D. Neher, W. Kowalsky, and R. Lovrincic, "Charge-Transfer-Solvent Interaction Predefines Doping Efficiency in p-Doped P3HT Films," *Chemistry of Materials*, vol. 28, no. 12, pp. 4432–4439, 2016.

[230] L. Müller, *On The Correlation Between Structural Order And Molecular Doping In Semiconducting Polymers*. PhD thesis, Ruperto-Carola-University of Heidelberg, Germany, 2018.

[231] D. T. Scholes, P. Y. Yee, J. R. Lindemuth, H. Kang, J. Onorato, R. Ghosh, C. K. Luscombe, F. C. Spano, S. H. Tolbert, and B. J. Schwartz, "The Effects of Crystallinity on Charge

Transport and the Structure of Sequentially Processed F4TCNQ-Doped Conjugated Polymer Films," *Advanced Functional Materials*, vol. 27, no. 44, p. 1702654, 2017.

[232] C. Scharsich, R. H. Lohwasser, M. Sommer, U. Asawapirom, U. Scherf, M. Thelakkat, D. Neher, and A. Köhler, "Control of aggregate formation in poly(3-hexylthiophene) by solvent, molecular weight, and synthetic method," *Journal of Polymer Science Part B: Polymer Physics*, vol. 50, no. 6, pp. 442–453, 2012.

[233] S. Cook, A. Furube, and R. Katoh, "Mixed Solvents for Morphology Control of Organic Solar Cell Blend Films," *Japanese Journal of Applied Physics*, vol. 47, pp. 1238–1241, feb 2008.

[234] J. Li, G. Zhang, D. M. Holm, I. E. Jacobs, B. Yin, P. Stroeve, M. Mascal, and A. J. Moulé, "Introducing Solubility Control for Improved Organic P-Type Dopants," *Chemistry of Materials*, vol. 27, no. 16, pp. 5765–5774, 2015.

[235] J. Gao, B. W. Stein, A. K. Thomas, J. A. Garcia, J. Yang, M. L. Kirk, and J. K. Grey, "Enhanced Charge Transfer Doping Efficiency in J-Aggregate Poly(3-hexylthiophene) Nanofibers," *The Journal of Physical Chemistry C*, vol. 119, no. 28, pp. 16396–16402, 2015.

[236] C. Wang, D. T. Duong, K. Vandewal, J. Rivnay, and A. Salleo, "Optical measurement of doping efficiency in poly(3-hexylthiophene) solutions and thin films," *Phys. Rev. B*, vol. 91, p. 085205, Feb 2015.

[237] P. Pingel, M. Arvind, L. Kölln, R. Steyrleuthner, F. Kraffert, J. Behrends, S. Janietz, and D. Neher, "p-Type Doping of Poly(3-hexylthiophene) with the Strong Lewis Acid Tris(pentafluorophenyl)borane," *Advanced Electronic Materials*, vol. 2, no. 10, p. 1600204, 2016.

[238] Y. H. Kim, D. Spiegel, S. Hotta, and A. J. Heeger, "Photoexcitation and doping studies of poly(3-hexylthienylene)," *Phys. Rev. B*, vol. 38, pp. 5490–5495, Sept. 1988.

[239] T.-A. Chen, X. Wu, and R. D. Rieke, "Regiocontrolled Synthesis of Poly(3-alkylthiophenes) Mediated by Rieke Zinc: Their Characterization and Solid-State Properties," *Journal of the American Chemical Society*, vol. 117, no. 1, pp. 233–244, 1995.

[240] M. Meneghetti and C. Pecile, "Charge-transfer organic crystals: Molecular vibrations and spectroscopic effects of electron-molecular vibration coupling of the strong electron acceptor TCNQF4," *The Journal of Chemical Physics*, vol. 84, no. 8, pp. 4149–4162, 1986.

[241] P. Pingel, L. Zhu, K. S. Park, J.-O. Vogel, S. Janietz, E.-G. Kim, J. P. Rabe, J.-L. Brédas, and N. Koch, "Charge-Transfer Localization in Molecularly Doped Thiophene-Based Donor Polymers," *The Journal of Physical Chemistry Letters*, vol. 1, no. 13, pp. 2037–2041, 2010.

[242] J. S. Chappell, A. N. Bloch, W. A. Bryden, M. Maxfield, T. O. Poehler, and D. O. Cowan, "Degree of charge transfer in organic conductors by infrared absorption spectroscopy," *Journal of the American Chemical Society*, vol. 103, no. 9, pp. 2442–2443, 1981.

[243] A. Salmerón-Valverde, J. G. Robles-Martínez, J. García-Serrano, R. Gómez, R. M. Ridaura, M. Quintana, and A. Zehe, "A Study of the Degree of Charge Transfer in TTF Molecular

Complexes with Nitro-Carboxylated Fluorene Derivatives," *Molecular Engineering*, vol. 8, pp. 419–426, Dec 1999.

[244] J. C. Stires, IV, E. J. McLaurin, and C. P. Kubiak, "Infrared spectroscopic determination of the degree of charge transfer in complexes of tcne with methyl-substituted benzenes," *Chem. Commun.*, pp. 3532–3534, 2005.

[245] P. Reiser, L. Müller, V. Sivanesan, R. Lovrincic, S. Barlow, S. R. Marder, A. Pucci, W. Jaegermann, E. Mankel, and S. Beck, "Dopant Diffusion in Sequentially Doped Poly(3-hexylthiophene) Studied by Infrared and Photoelectron Spectroscopy," *The Journal of Physical Chemistry C*, vol. 122, no. 26, pp. 14518–14527, 2018.

[246] H. O. Seo, M.-G. Jeong, K.-D. Kim, D. H. Kim, Y. D. Kim, and D. C. Lim, "Studies of degradation behaviors of poly (3-hexylthiophene) layers by X-ray photoelectron spectroscopy," *Surface and Interface Analysis*, vol. 46, no. 8, pp. 544–549, 2014.

[247] J. Maibach, *Preparation and Characterization of Solution-Processed Organic Semiconductor Interfaces: Electronic Properties of Thiophene-Fullerene based Donor-Acceptor Systems*. PhD thesis, TU Darmstadt, 2014.

[248] S. J. N. Burgmayer, H. L. Kaufmann, G. Fortunato, P. Hug, and B. Fischer, "Molybdenum-Pterin Chemistry. 3. Use of X-ray Photoelectron Spectroscopy To Assign Oxidation States in Metal Complexes of Noninnocent Ligands," *Inorganic Chemistry*, vol. 38, no. 11, pp. 2607–2613, 1999.

[249] N. H. Turner and A. M. Single, "Determination of peak positions and areas from wide-scan XPS spectra," *Surface and Interface Analysis*, vol. 15, no. 3, pp. 215–222, 1990.

[250] H. Fujimoto, U. Nagashima, H. Inokuchi, K. Seki, Y. Cao, H. Nakahara, J. Nakayama, M. Hoshino, and K. Fukuda, "Ultraviolet photoemission study of oligothiophenes: π-band evolution and geometries," *The Journal of Chemical Physics*, vol. 92, no. 7, pp. 4077–4092, 1990.

[251] A. Opitz, J. Frisch, R. Schlesinger, A. Wilke, and N. Koch, "Energy level alignment at interfaces in organic photovoltaic devices," *Journal of Electron Spectroscopy and Related Phenomena*, vol. 190, pp. 12 – 24, 2013. Spectroscopy of Energy Materials.

[252] M. Beerbom, B. Lägel, A. Cascio, B. Doran, and R. Schlaf, "Direct comparison of photoemission spectroscopy and in situ kelvin probe work function measurements on indium tin oxide films," *Journal of Electron Spectroscopy and Related Phenomena*, vol. 152, no. 1, pp. 12 – 17, 2006.

[253] R. A. McKee, F. J. Walker, M. B. Nardelli, W. A. Shelton, and G. M. Stocks, "The Interface Phase and the Schottky Barrier for a Crystalline Dielectric on Silicon," *Science*, vol. 300, no. 5626, pp. 1726–1730, 2003.

[254] S. Miyazaki, J. Schäfer, J. Ristein, and L. Ley, "Surface Fermi level position of hydrogen passivated Si(111) surfaces," *Applied Physics Letters*, vol. 68, no. 9, pp. 1247–1249, 1996.

[255] M. Kühn, *Heterokontakte organischer Leuchtdioden: Schichtdickenabhängiges Strom-Spannungsverhalten*. PhD thesis, Technische Universität Darmstadt, 2017.

[256] L. Lozzi, S. Santucci, and S. La Rosa, "Au/CuPc interface: Photoemission investigation," *Journal of Vacuum Science & Technology A*, vol. 22, no. 4, pp. 1477–1481, 2004.

[257] Y. Hirose, A. Kahn, V. Aristov, P. Soukiassian, V. Bulovic, and S. R. Forrest, "Chemistry and electronic properties of metal-organic semiconductor interfaces: Al, Ti, In, Sn, Ag, and Au on PTCDA," *Phys. Rev. B*, vol. 54, pp. 13748–13758, Nov 1996.

[258] C. S. Lee and M. D. Dadmun, "Important thermodynamic characteristics of poly(3-hexyl thiophene)," *Polymer*, vol. 55, no. 1, pp. 4 – 7, 2014. Special issue: Porous Polymers.

[259] O. Shalev and M. Shtein, "Effect of crystal density on sublimation properties of molecular organic semiconductors," *Organic Electronics*, vol. 14, no. 1, pp. 94 – 99, 2013.

[260] A. Ogata, "Mathematics of dispersion with linear adsorption isotherm," tech. rep., 1964.

[261] S. Hugger, R. Thomann, T. Heinzel, and T. Thurn-Albrecht, "Semicrystalline morphology in thin films of poly(3-hexylthiophene)," *Colloid and Polymer Science*, vol. 282, pp. 932–938, Jun 2004.

[262] A. J. Berro, X. Gu, N. O'Connor, S. Jockusch, T. Nagai, T. Ogata, P. Zimmerman, B. J. Rice, E. Adolph, T. Byargeon, J. Gonzalez, N. J. Turro, and C. G. Willson, "Optical threshold layer and intermediate state two-photon PAG approaches to double exposure lithography," *Proc. SPIE*, vol. 7273, pp. 7273 – 7273 – 10, 2009.

[263] F. Bayrakçeken, O. J. Demir, L. Tunçyürek, and İpek Ş. Karaaslan, "Triplet triplet energy transfer from naphthalene to biacetyl in the vapor phase," *Spectrochimica Acta Part A: Molecular and Biomolecular Spectroscopy*, vol. 65, no. 1, pp. 27 – 31, 2006.

[264] F. Salama and L. J. Allamandola, "Electronic absorption spectroscopy of matrix isolated polycyclic aromatic hydrocarbon cations. I. The naphthalene cation ($C^{10}H_8^+$)," *The Journal of Chemical Physics*, vol. 94, no. 11, pp. 6964–6977, 1991.

[265] G. George and G. Morris, "The intensity of absorption of naphthalene from 30 000 cm^{-1} to 53 000 cm^{-1}," *Journal of Molecular Spectroscopy*, vol. 26, no. 1, pp. 67 – 71, 1968.

[266] D. P. Craig, J. M. Hollas, M. F. Redies, and J. S. C. Wait, "Analysis of the naphthalene vapour absorption bands at 3200Å. I. Naphthalene *h*-8," *Philosophical Transactions of the Royal Sociepe A*, vol. 253, no. 1035, pp. 543–568, 1961.

[267] S. Falke, P. Eravuchira, A. Materny, and C. Lienau, "Raman spectroscopic identification of fullerene inclusions in polymer/fullerene blends," *Journal of Raman Spectroscopy*, vol. 42, no. 10, pp. 1897–1900, 2011.

[268] S. Leach, M. Vervloet, A. Desprès, E. Bréheret, J. P. Hare, T. J. Dennis, H. W. Kroto, R. Taylor, and D. R. Walton, "Electronic spectra and transitions of the fullerene C60," *Chemical Physics*, vol. 160, no. 3, pp. 451 – 466, 1992.

[269] S. Cook, H. Ohkita, Y. Kim, J. J. Benson-Smith, D. D. Bradley, and J. R. Durrant, "A photophysical study of PCBM thin films," *Chemical Physics Letters*, vol. 445, no. 4, pp. 276 – 280, 2007.

[270] S. V. John, N. Mayedwa, C. Ikpo, L. Y. Molefe, M. M. Ndipingwi, N. R. Dywili, J. V. Wyk, S. F. Mapolie, P. Baker, and E. Iwuoha, "Photoluminescence quenching of poly(octylfluorenylbenzothiadiazole) luminophore by n-type cobalt(II) salicylaldimine metallodendrimer," *Synthetic Metals*, vol. 220, pp. 114 – 122, 2016.

[271] D. Kiefer, A. Giovannitti, H. Sun, T. Biskup, A. Hofmann, M. Koopmans, C. Cendra, S. Weber, L. J. Anton Koster, E. Olsson, J. Rivnay, S. Fabiano, I. McCulloch, and C. Müller, "Enhanced n-Doping Efficiency of a Naphthalenediimide-Based Copolymer through Polar Side Chains for Organic Thermoelectrics," *ACS Energy Letters*, vol. 3, no. 2, pp. 278–285, 2018.

[272] J. Liu, L. Qiu, G. Portale, M. Koopmans, G. ten Brink, J. C. Hummelen, and L. J. A. Koster, "N-Type Organic Thermoelectrics: Improved Power Factor by Tailoring HostâĂŞDopant Miscibility," *Advanced Materials*, vol. 29, no. 36, p. 1701641, 2017.

[273] V. I. Arkhipov, P. Heremans, E. V. Emelianova, and H. Bässler, "Effect of doping on the density-of-states distribution and carrier hopping in disordered organic semiconductors," *Phys. Rev. B*, vol. 71, p. 045214, Jan 2005.

[274] M. L. Tietze, F. Wölzl, T. Menke, A. Fischer, M. Riede, K. Leo, and B. Lüssem, "Self-passivation of molecular n-type doping during air exposure using a highly efficient air-instable dopant," *physica status solidi (a)*, vol. 210, no. 10, pp. 2188–2198, 2013.

[275] J. Maibach, T. Adermann, T. Glaser, R. Eckstein, E. Mankel, A. Pucci, K. Müllen, U. Lemmer, M. Hamburger, T. Mayer, and W. Jaegermann, "Impact of processing on the chemical and electronic properties of phenyl-C61-butyric acid methyl ester," *J. Mater. Chem. C*, vol. 2, pp. 7934–7942, 2014.

[276] T. T. Ngo, D. N. Nguyen, and V. T. Nguyen, "Glass transition of PCBM, P3HT and their blends in quenched state," *Advances in Natural Sciences: Nanoscience and Nanotechnology*, vol. 3, p. 045001, sep 2012.

[277] T. Grösser, M. Prato, V. Lucchini, A. Hirsch, and F. Wudl, "Ringexpansion des Fullerengerüstes durch hochregioselektive Bildung von Diazafulleroiden," *Angewandte Chemie*, vol. 107, no. 12, pp. 1462–1464, 1995.

[278] M. Cases, M. Duran, J. Mestres, N. Martín, and M. Solà, "Mechanism of the Addition Reaction of Alkyl Azides to [60]Fullerene and the Subsequent N2 Extrusion to Form Monoimino-[60]fullerenes," *The Journal of Organic Chemistry*, vol. 66, no. 2, pp. 433–442, 2001. PMID: 11429811.

[279] T. Grösser, M. Prato, V. Lucchini, A. Hirsch, and F. Wudl, "Ring Expansion of the Fullerene Core by Highly Regioselective Formation of Diazafulleroids," *Angewandte Chemie International Edition in English*, vol. 34, no. 12, pp. 1343–1345, 1995.

[280] A. Hirsch, "Addition Reactions of Buckminsterfullerene (C60)," *Synthesis*, vol. 1995, pp. 895–913, aug 1995.

[281] T. Nakahodo, M. Okada, H. Morita, T. Yoshimura, M. Ishitsuka, T. Tsuchiya, Y. Maeda, H. Fujihara, T. Akasaka, X. Gao, and S. Nagase, "[2+1] Cycloaddition of Nitrene onto

C60 Revisited: Interconversion between an Aziridinofullerene and an Azafulleroid," *Angewandte Chemie International Edition*, vol. 47, no. 7, pp. 1298–1300, 2008.

[282] A. B. Smith and H. Tokuyama, "Nitrene additions to [60]fullerene do not generate [6,5] aziridines," *Tetrahedron*, vol. 52, no. 14, pp. 5257 – 5262, 1996.

[283] A. El-Aneed, A. Cohen, and J. Banoub, "Mass Spectrometry, Review of the Basics: Electrospray, MALDI, and Commonly Used Mass Analyzers," *Applied Spectroscopy Reviews*, vol. 44, no. 3, pp. 210–230, 2009.

[284] M. S. A. Abdou, F. P. Orfino, Y. Son, and S. Holdcroft, "Interaction of Oxygen with Conjugated Polymers: Charge Transfer Complex Formation with Poly(3-alkylthiophenes)," *Journal of the American Chemical Society*, vol. 119, no. 19, pp. 4518–4524, 1997.

[285] A. Guerrero, P. P. Boix, L. F. Marchesi, T. Ripolles-Sanchis, E. C. Pereira, and G. Garcia-Belmonte, "Oxygen doping-induced photogeneration loss in P3HT:PCBM solar cells," *Solar Energy Materials and Solar Cells*, vol. 100, pp. 185 – 191, 2012. Photovoltaics, Solar Energy Materials, and Technologies: Cancun 2010.

[286] Z. Bin, J. Li, L. Wang, and L. Duan, "Efficient n-type dopants with extremely low doping ratios for high performance inverted perovskite solar cells," *Energy Environ. Sci.*, vol. 9, pp. 3424–3428, 2016.

[287] R. Huisgen, "Centenary Lecture 1,3-Dipolar Cycloadditions," *Proc. Chem. Soc.*, pp. 357–396, Oct. 1961.

[288] R. Huisgen, "Kinetics and Mechanism of 1,3-Dipolar Cycloadditions," *Angewandte Chemie International Edition in English*, vol. 2, no. 11, pp. 633–645, 1963.

[289] P. A. S. Smith, *The Curtius Reaction*, ch. 9, pp. 337–449. American Cancer Society, 2011.

[290] H. Staudinger and J. Meyer, "über neue organische Phosphorverbindungen III. Phosphinmethylenderivate und Phosphinimine," *Helvetica Chimica Acta*, vol. 2, no. 1, pp. 635–646, 1919.

[291] J. H. Boyer and J. Hamer, "The Acid-catalyzed Reaction of Alkyl Azides upon Carbonyl Compounds1," *Journal of the American Chemical Society*, vol. 77, no. 4, pp. 951–954, 1955.

[292] J. Aube and G. L. Milligan, "Intramolecular schmidt reaction of alkyl azides," *Journal of the American Chemical Society*, vol. 113, no. 23, pp. 8965–8966, 1991.

[293] J. Aube, G. L. Milligan, and C. J. Mossman, "Titanium tetrachloride-mediated reactions of alkyl azides with cyclic ketones," *The Journal of Organic Chemistry*, vol. 57, no. 6, pp. 1635–1637, 1992.

[294] H. Wolff, *The Schmidt Reaction*, ch. 8, pp. 307–336. American Cancer Society, 2011.

[295] K. F. Schmidt, "über den Imin-Rest," *Berichte der deutschen chemischen Gesellschaft (A and B Series)*, vol. 57, no. 4, pp. 704–706, 1924.

[296] H. Hemetsberger, D. Knittel, and H. Weidmann, "Synthese von α-Azidozimtsäureestern," *Monatshefte für Chemie / Chemical Monthly*, vol. 100, pp. 1599–1603, Sep 1969.

[297] F. P. Cossío, C. Alonso, B. n. Lecea, M. Ayerbe, G. Rubiales, and F. Palacios, "Mechanism and Stereoselectivity of the Aza-Wittig Reaction between Phosphazenes and Aldehydes," *The Journal of Organic Chemistry*, vol. 71, no. 7, pp. 2839–2847, 2006. PMID: 16555840.

[298] P. K. Dutt, H. R. Whitehead, and A. Wormall, "CCXLI.-The action of diazo-salts on aromatic sulphonamides. Part I," *J. Chem. Soc., Trans.*, vol. 119, pp. 2088–2094, 1921.

A Appendix: Related Publications

P. Reiser, L. Müller, S. Sivanesan, R. Lovrincic, S. Barlow, S. Marder, A. Pucci, W. Jaegermann, E. Mankel and S. Beck, "Dopant Diffusion in Sequentially Doped Poly(3-hexylthiophene) Studied by Infrared and Photoelectron Spectroscopy," *The Journal of Physical Chemistry C*, vol. 122, no. 26, pp. 14518-14527, 2018

P. Reiser, F. S. Benneckendorf, M. Barf, L. Müller, R. Bäuerle, S. Hillebrandt, S. Beck, R. Lovrincic, E. Mankel, J. Freudenberg, D. Jänsch, W. Kowalsky, A. Pucci, W. Jaegermann, U. H. F. Bunz and K. Müllen, "N-Type Doping of Organic Semiconductors: Immobilization via Covalent Anchoring," *Chemistry of Materials*, vol. 31, no. 11, p. 4213-4221, 2019

L. Müller, S. Rhim, V. Sivanesan, D. Wang, S. Hietzschold, P. Reiser, E. Mankel, S. Beck, S. Barlow, S. Marder, A. Pucci, W. Kowalsky and R. Lovrincic, "Electric-Field-Controlled Dopant Distribution in Organic Semiconductors," *Advanced Materials*, vol. 29, no. 30, p. 1701466, 2017

A. Klein, C. Lohaus, P. Reiser, L. Dimesso, X. Wang and T. Yang, "Energy band alignment of antiferroelectric (Pb,La)(Zr,Sn,Ti)O3," *Applied Surface Science*, vol. 407, pp. 99-104, 2017

M. Alt, M. Jesper, J, Schinke, S. Hillebrandt, P. Reiser, T. Rödlmeier, I. Angelova, K. Deing, T. Glaser, E. Mankel, W. Jaegermann, A. Pucci, U. Lemmer, U. H. F. Bunz, W. Kowalsky, G. Hernandez-Sosa, R. Lovrincic, and M. Hamburger, "The Swiss-Army-Knife Self-Assembled Monolayer: Improving Electron Injection, Stability, and Wettability of Metal Electrodes with a One-Minute Process," *Advanced Functional Materials*, vol. 26, no. 18, pp. 3172-3178, 2016

M. Ruscello, T. Sarkar, A. Levitsky, G. M. Matrone, N. Droseros, S. Schlisske, E. Sachs, P. Reiser, E. Mankel, W. Kowalsky, N. Banerji, N. Stingelin, G. L. Frey and G. Hernandez-Sosa, "Nanocomposite of nickel oxide nanoparticles and polyethylene oxide as printable hole transport layer for organic solar cells," *Sustainable Energy Fuels*, vol. 3, p. 1418-1426, 2019

M. Barf, P. Reiser, R. Bäuerle, F. Benneckendorf, W. Köntges, L. Müller, M. Pfannmöller, J. Freudenberg, D. Jänsch, S. Beck, E. Mankel, J. Tisserant, R. Lovrincic, R. Schröder, U. Bunz, K. Müllen, A. Pucci, W. Jaegermann, W. Kowalsky, "Compensation of Oxygen Doping in P-Type Organic Field-Effect Transistors Utilizing Immobilized N-Dopants", *in preparation*, 2019

B Appendix: Supporting Information

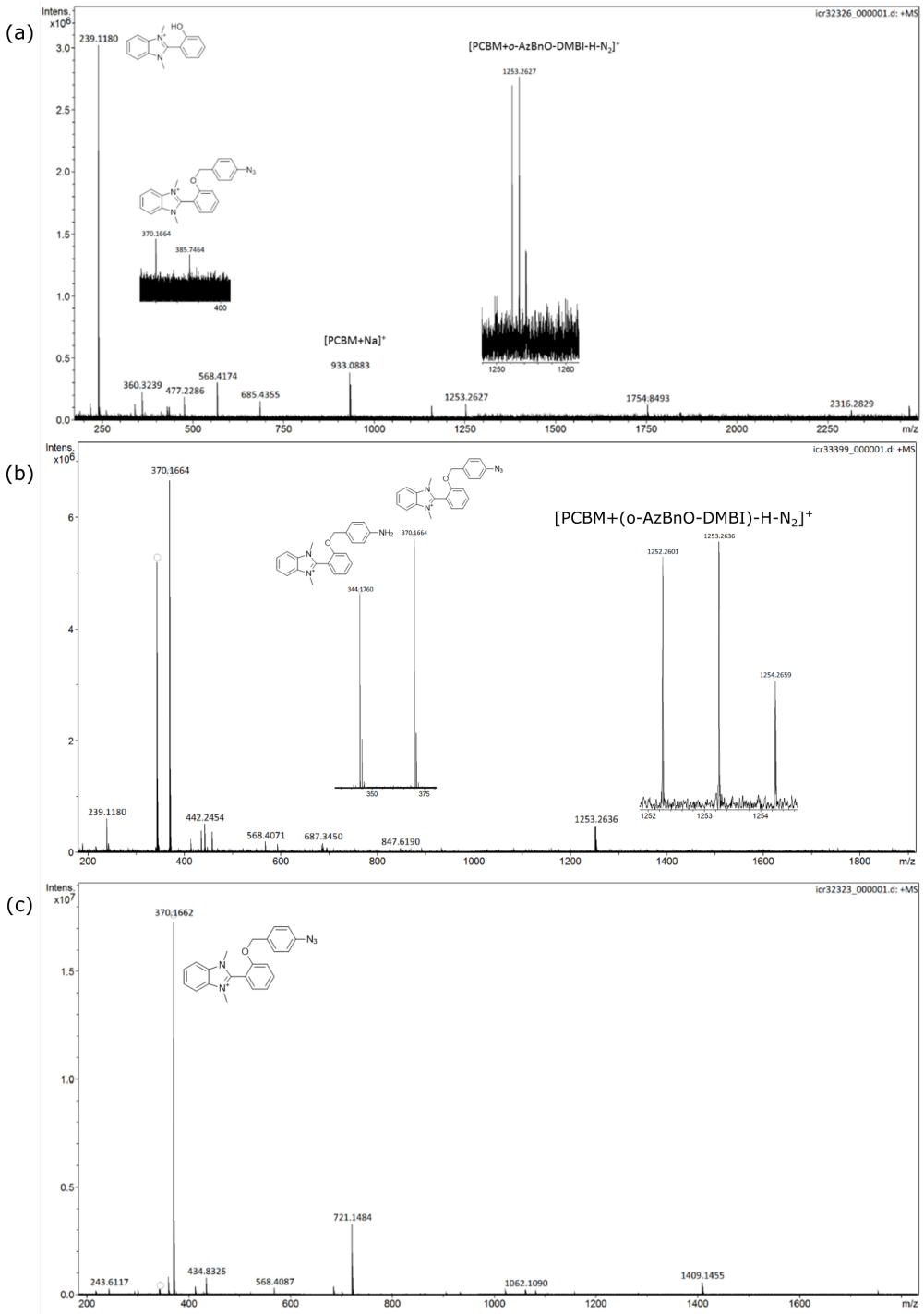

Figure B.1: ESI mass spectra of PCB doped with o-AzBnO-DMBI as blank in (c) after UV-treatment in (b) and annealed at 135 °C in (a). The data were provided by the mass spectroscopy facility at OCI Heidelberg under the supervision of Dr. J. Gross.

Results, Thermogravimetric Analysis: The activation by heat can be indirectly measured by a thermogravimetric analysis (TGA). A TGA measurement of ABN and F4ABN is shown in Figure B.2. Here, pure material is steadily heated and the probe's mass is continuously measured. Changes in weight indicates decomposition and in general reactions including release of by-products. At about 100 °C for ABN and 130 °C for F4ABN a clear spike in the heat flow marks the melting point of the two materials. A product of the azide activation is nitrogen which is released into the gas phase and should result in a mass-loss which starts at a temperature of about 130 °C and causes a peak in heat flow. The step between 140 °C and 180 °C for both ABN and F4ABN is therefore assigned to a transformation of the azide group. The generation of nitrene causes a weight loss of 10.2 % for ABN and 8.1 % for F4ABN, which is a little smaller than the observed shoulder centered at 185 °C and 165 °C for ABN and F4ABN, respectively. This is likely due a decomposition or sublimation yielding a steady mass loss starting at around 200 °C right after or probably during the azide activation and continuing up to 400 °C. As a consequence azide activation has to be carried out carefully at 140 °C since higher temperatures of >160 °C may already cause decomposition. However, a more efficient activation is rendered by irradiation with deep UV-light.

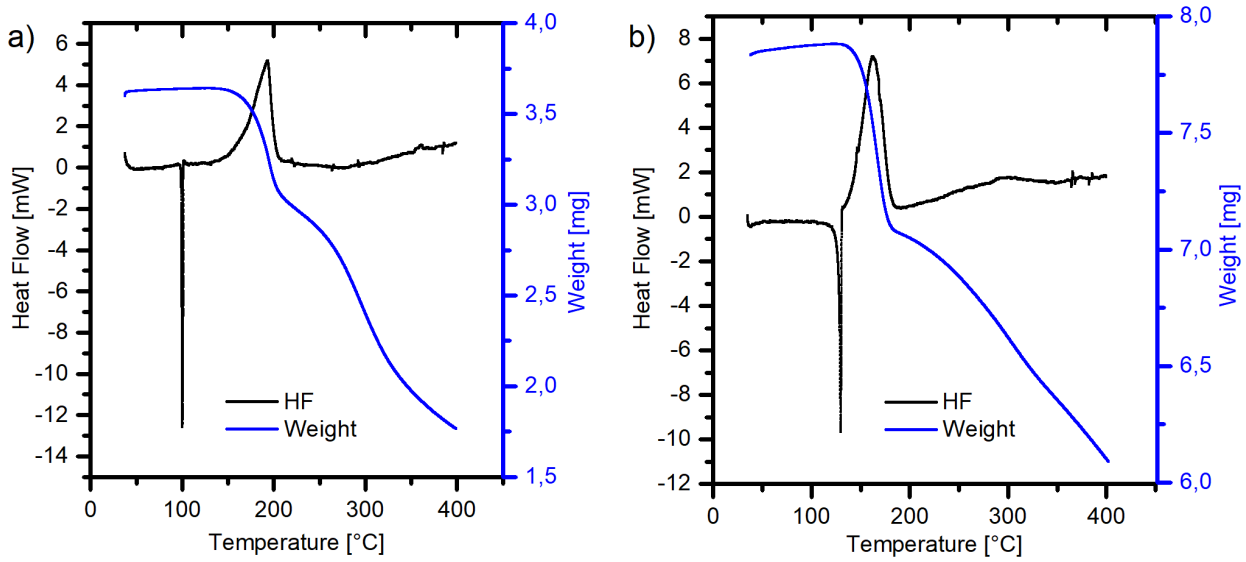

Figure B.2: Thermogravimetric analysis (TGA) of ABN and AF4BN in (a) and (b) respectively (measured and provided by S. Benneckendorf (Univ. Heidelberg)).[208]

Molecule	Exp. absorption [cm^{-1}]	Theo. absorption [cm^{-1}]	Vibrational mode
ABN	791	813	$\delta(\text{C-H})_{\text{naph}} + \delta(\text{N}_3)$
ABN	1020	1150	$\delta(\text{C-H})_{\text{naph}}$
ABN	1020	1157	$\delta(\text{C-H})_{\text{benz}} + \nu(\text{N}_3)$
ABN	1180	1193	$\delta(\text{C-H})_{\text{naph}}$
ABN	1282	1369	$\delta(\text{C-H})_{\text{benz,naph}} + \nu(\text{N}_3)$
ABN	2110	2248	$\nu(\text{N}_3)$
F4ABN	1052	078	$\delta(\text{C-H}) + \nu(\text{C-F})$
F4ABN	1246	1290	$\delta(\text{C-H})_{\text{naph}} + \nu(\text{N}_3)$
F4ABN	1495	1514	$\text{ring(C-C)}_{\text{benz}} + \nu(\text{N}_3)$
F4ABN	1495	1523	$\text{ring(C-C)}_{\text{benz}} + \nu(\text{C-N})$
F4ABN	2122	2270	$\nu(\text{N}_3)$

Table B.1: Assignment of theoretically calculated molecular vibrations for ABN and F4ABN to experimentally measured absorption peak positions carried out by H. Mager.[100] Only the modes which contain a contribution of the azide group are selected. Stretching, bending and ring deformation vibration are denoted by ν, δ and ring, respectively. The index naph or benz provides the oscillator's location in either the naphtalene or the benzyl group.

A list of named azide reactions: the Huisgen reaction, which refers to a 1,3-dipolar cycloaddition,[287,288] between for example an organic azide and an alkyene yielding a triazole; the Curtius rearrangement decomposing acyl azide to isocyanate that can be further transformed to amine and carbamate or urea derivatives;[177,289] Staudinger reaction with phosphine or phosphite to iminophosphorane or its modification the Staudinger ligation able to connect two molecules via an amide connection;[290] the Boyer-Schmidt-Aube rearrangement denotes the acid-mediated reaction of alkyl azides with aromatic aldehydes;[291–293] the Schmidt rearrangement in which a carbonyl group reacts with an organic azide forming amides;[294,295] the Hemetsberger-Knittel synthesis of indole-carboxylic ester;[296] for the synthesis of the Aza-Wittig reaction[297] and of heterocycles. There is also a variety of synthetic routes for organic azides, which commonly employ the displacement or nucleophilic aromatic substitution of e.g. halides at saturated or unsaturated sites by salts like sodium azide or trimethylsilyl azide. Azides can also be synthesized from alcohols, sulfonates and acetats, epoxides, amines or hydrazines, carboxylic acids and ketals. Other methods proceed via rearrangement, azo-transfer or the so-called Dutt-Wormall reaction.[176,298]

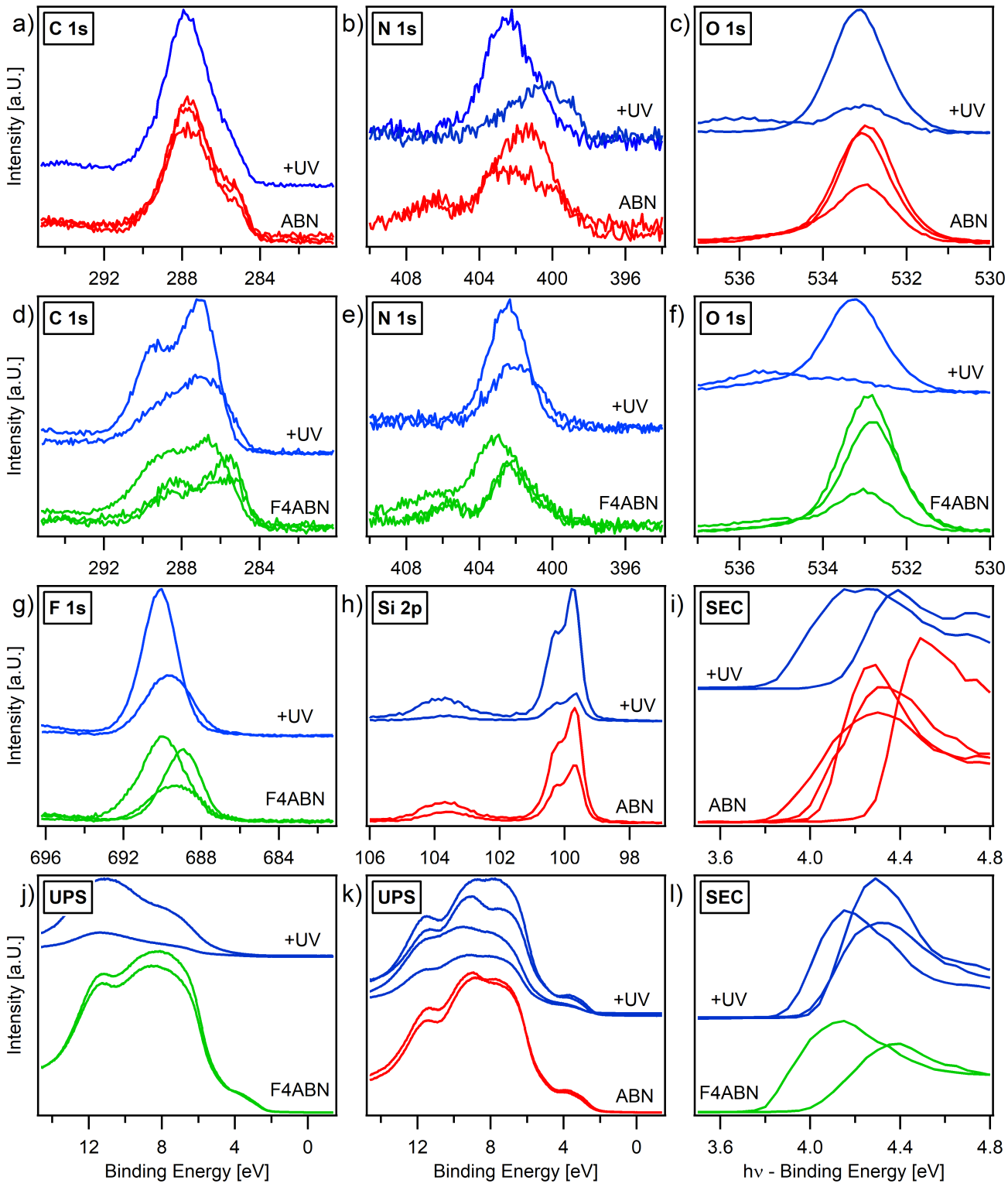

Figure B.3: Photoemission spectra of ABN in red and F4ABN in green. The spectra for UV activated films are displayed in blue. Multiple curves represent various samples and sample regions that differ in coverage. The Si 2p substrate emission is clearly visible (h). Since the thin films are of poor quality, binding energy and peak width are not reliable. The secondary electron cut-off (XPS) is shown in (i) and (l). UPS spectra of the azide film are given in (j) and (k). The O 1s spectra in (c) and (f) are plotted versus binding energy.

Emission	Theo. P3HT	Exp. P3HT	Theo. Mo(tfd-CO_2Me)$_3$	Exp. Mo(tfd-CO_2Me)$_3$
C 1s	91 %	89.1 %	40 %	38.07 %
S 2p	9 %	10.89 %	16.2 %	14.77 %
F 1s	-	-	24.3 %	28.14 %
Mo 3d	-	-	2.7 %	2.62 %
O 1s	-	-	16.2 %	16.4 %

Table B.2: Calculated elemental composition of P3HT and Mo(tfd-CO_2Me)$_3$. The experimental values are derived from the respective core-level emission by taking into account atomic sensitivity factors (see Section 4.1). The theoretical values are based on the structural formula of the materials. There is an agreement within the error range of 10-20 %. The F 1s intensity is slightly higher than expected. However, fluorine and oxygen are located on the outer moieties whereas sulphur and molybdenum form the core of the Mo(tfd-CO_2Me)$_3$ complex.

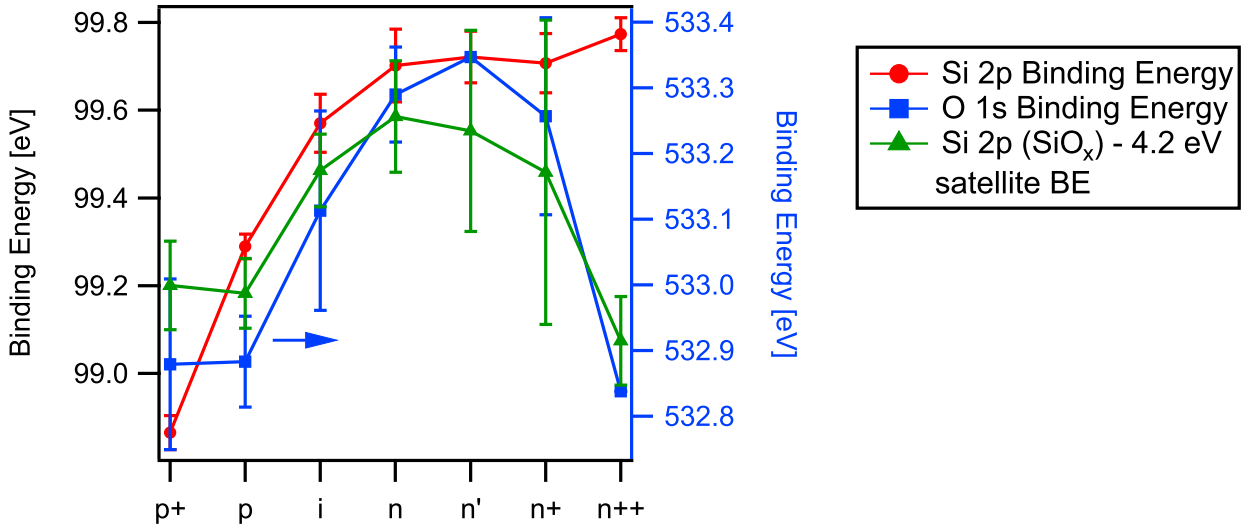

Figure B.4: Binding energy of the Si 2p (red) and O 1s emission (blue) of differently doped silicon substrates. The oxygen stems from the native oxide layer. The binding energy of the O 1s line is plotted on the right. The position of the SiO_x satellite (green) is shifted to lower binding energies (-4.2 eV) for comparison. The substrate of highest doping concentration n++ does not fit the trend of the Si 2p line. However, for n++ only one sample was measured which could have been an outlier. The error bar represents the standard deviation of multiple measurements.

Danksagung

Hiermit möchte ich mich bei allen bedanken, die mich während meiner Promotion unterstützt haben. Mein besonderer Dank gilt...

Herrn Prof. Wolfram Jaegermann für die Aufnahme in seine Arbeitsgruppe und die Möglichkeit meine Doktorarbeit am InnovationLab Heidelberg zu schreiben. Ich möchte mich für die interessante Aufgabenstellung sowie die wertvollen Ratschläge und Diskussionen während meiner Promotion bedanken,

Frau Prof. Annemarie Pucci für die Übernahme des Zweitgutachtens sowie die enge Kollaboration am InnovationLab Heidelberg,

Dr. Sebastian Beck für die erfolgreiche Zusammenarbeit zur Diffusion und Immobilisierung von Dotanden, die spannende Arbeit im Labor, die gemeinsame Zeit und die große Hilfe bei der Fertigstellung und Einreichung der Publikationen,

Dr. Eric Mankel für die Betreuung meiner Arbeit und die Unterstützung bei der Wartung und Reparatur der Spektroskopieanlagen im Labor. Auch möchte ich mich für die Diskussionen zu der theoretischen Beschreibung der Diffusion und Interpretation der Spektren bedanken,

Dr. Jan Freudenberg und Simon Benneckendorf für die Synthese und Bereitstellung der funktionalisierten Dotanden und der Testmaterialien. Bedanken möchte ich mich für die vielen Besprechungen und die Hilfe bei der Aufklärung des Reaktionsmechanismus der n-Dotanden,

Dr. Lars Müller, Marc-Michael Barf, Vipilan Sivanesan, Simon Benneckendorf und Heiko Mager für die gemeinschaftliche Laborarbeit an dem Themengebiet der molekularen Dotanden,

dem gesamten iL-Analytik Team und der Oberflächenforschungsgruppe für die harmonische Arbeitsatmosphäre und gegenseitige Hilfsbereitschaft, insbesondere Dr. Robert Lovrincic, Dr. Sebastian Hietzschold, Christian Willig, Dr. Sabina Hillebrandt, Dr. Michael Sendner, Paula Connor, Dr. Maybritt Kühn, Florian Ullrich, Valentina Rohnacher und Markus Frericks,

und meinen Eltern für die moralische Unterstützung während der letzten Jahre.

Erklärung

Hiermit versichere ich, die vorliegende Dissertation ohne Hilfe Dritter nur mit den angegebenen Quellen und Hilfsmitteln angefertigt zu haben. Alle Stellen, die aus Quellen entnommen wurden, sind als solche kenntlich gemacht. Diese Arbeit hat in gleicher oder ähnlicher Form noch keiner Prüfungsbehörde vorgelegen.

Darmstadt, den 20. Juli 2019

(Patrick Reiser)

Lebenslauf

Aus datenschutzrechtlichen Gründen nicht verfügbar.